



Title	An observational study of tropical cyclone intensity estimation, intensity change processes, and intensity forecast
Author(s)	嶋田, 宇大
Citation	北海道大学. 博士(環境科学) 乙第7038号
Issue Date	2017-12-25
DOI	10.14943/doctoral.r7038
Doc URL	http://hdl.handle.net/2115/68189
Type	theses (doctoral)
File Information	Udai_Shimada.pdf



[Instructions for use](#)

博士論文

**An Observational Study of Tropical Cyclone Intensity
Estimation, Intensity Change Processes, and
Intensity Forecast**

(熱帯低気圧の強度推定、強度変化プロセス及び
強度予報に関する観測的研究)

北海道大学大学院環境科学院

嶋田 宇大

Udai Shimada

November 2017

Copyright © Udai Shimada 2017

Abstract

An observational study of tropical cyclones (TCs) using radar and satellite data is made from the perspective of intensity estimation, intensity change processes, and intensity forecast with the aim of better understanding intensity change and further improving the accuracy of intensity forecast. First, a system using Doppler radar data is developed, where the TC wind field is retrieved and the central pressure is estimated at 5-min intervals. A verification of intensity estimates relative to the best track data shows that the accuracy of the system is comparable to or better than the accuracies of Dvorak and satellite microwave-derived estimates.

Next, by using satellite-derived rainfall data and radar data, the statistical relationship between TC rainfall structure and intensity change, and intensity change processes in two TCs are investigated. It is found that, during the development stage, the higher the axisymmetry (the degree of axial symmetry) of the rainfall distribution in the inner-core region, the larger the intensity change in the next 24 h, depending on the current intensity. The relative relationship between axisymmetric and asymmetric terms of rainfall shows that the larger the axisymmetric term and the smaller the asymmetric term, the larger the intensity change is.

Strong vertical wind shear causes the structure of the eyewall to become asymmetric and is generally a hostile environmental condition for TCs to intensify. However, Typhoon Noul (2015) reintensified with the formation of a symmetric eyewall despite vertical wind shear greater than 10 m s^{-1} . The reintensification began with convective bursts. The maximum azimuthal mean tangential wind at 2-km altitude increased from 30 to 50 m s^{-1} during only 5 h, associated with the increase in azimuthal mean reflectivity inside the radius of maximum wind (RMW). It was when the vortex vertically aligned through vortex precession upshear that a symmetric eyewall formed in strong shear. The radar analysis suggests that the vortex tilt, convective bursts, and subsequent intensification occurred triggered by the increase in shear in the presence of environmental conditions favorable for convection.

After the completion of an eyewall replacement cyclone (ERC), a TC often continues to intensify and in some cases rapid intensification (RI) occurs. However, RI processes after an ERC have not yet been investigated. An operational ground-based Doppler radar observed the RI of Typhoon Goni (2015) for 24 h immediately after it completed an ERC. This provides an

invaluable opportunity to examine Goni's RI processes in detail. Around the onset of RI, relatively strong outflow outside the RMW above the boundary layer was observed, which contributed to rapid contraction of the low-level RMW, causing the RMW to slope greatly outward with height. The radial profile of tangential wind became more peaked with time. During RI, the low-level outflow changed into inflow just outside the RMW and the secondary circulation became well established. An updraft peak and the radius of maximum reflectivity between 2- and 9-km altitudes were located inside the RMW.

Finally, the possibility of further improvement in TC intensity forecast is examined based on the findings that inner-core structural conditions govern subsequent intensity change. Five new predictors associated with rainfall distribution and structural features, including the axisymmetry of the rainfall distribution, are incorporated into a multiple regression model, which predicts intensity up to 5 days ahead. Results show that the model produces a 2–7% improvement in the forecast skill, compared against a model without these predictors.

Acknowledgements

I would like to express my deepest appreciation to my supervisor, Associate Prof. Takeshi Horinouchi of Hokkaido University. He kindly gave me insightful comments and thoughtful advice. Without his assistance, this dissertation would not have been possible. My appreciation also goes to Profs. Atsushi Kubokawa and Youichi Tanimoto, and Assistant Prof. Masayuki Kawashima for encouragement and suggestions for the improvement of this dissertation. I am deeply grateful to Associate Prof. Hironori Fudeyasu of Yokohama National University for his helpful advice and comments that have greatly improved the dissertation. I thank Mr. Yasutomo Kiyohara of Naval Oceanography Antisubmarine Warfare Center Yokosuka for useful suggestions on this dissertation.

All studies in this dissertation were carried out after I moved to the Meteorological Research Institute (MRI) of the Japan Meteorological Agency (JMA), the Typhoon Research Department in 2013. Special thanks are given to Prof. Emeritus Koji Yamazaki of Hokkaido University, Associate Prof. Hiroyuki Yamada of University of the Ryukyus, Drs. Naoko Kitabatake, Akiyoshi Wada, Munehiko Yamaguchi, and Masahiro Sawada for their guidance and support. They provided me with great opportunities to work on studies of tropical cyclones. Additionally, I would like to express my gratitude to my colleagues, Dr. Kazumasa Aonashi, Mr. Shingo Yamada, Mr. Yoshiaki Takeuchi, Mr. Isao Takano, Dr. Kozo Okamoto, Mr. Ryo Oyama, Dr. Wataru Yanase, Mr. Tomoaki Sakuragi, Mr. Masaru Kunii, Dr. Sho Yokota, Dr. Kohei Yoshida, and Dr. Masahiro Kazumori. Gratitude is also extended to my colleagues at the Regional Specialized Meteorological Center (RSMC) Tokyo. Furthermore, I would like to express my gratitude to Drs. Hisayuki Kubota, Masuo Nakano, Ryuji Yoshida, and Hiroki Tsuji for fruitful discussions on tropical cyclones.

The study of Chapter 2 was the development of an intensity estimation system using Doppler radar data. Currently, this system is in an experimental use in the JMA. In the processes of the development, I appreciate many advice from Dr. Wen-Chau Lee of the National Center for Atmospheric Research (NCAR), Prof. Ben Jong-Dao Jou of National Taiwan University, Drs. Frank D. Marks Jr., Paul Reasor, and Shirley T. Murillo of the National Oceanic and Atmospheric Administration (NOAA)/Hurricane Research Department (HRD), and Dr. Paul R. Harasti of the U.S. Naval Research Laboratory (NRL). I used

the "DRAFT" Doppler radar analysis tool of MRI. I am deeply grateful to Mr. Hiroshi Yamauchi, Mr. Eiichi Sato, and Mr. Nobuhiro Nagumo for their helpful advice. This study was funded by Ministry of Education, Culture, Sports, Science and Technology (MEXT) KAKENHI Grant 25400468. The study was published in the Monthly Weather Review of American Meteorological Society Journal; doi:10.1175/MWR-D-15-0254.1.

The study of Chapter 3 was funded by the 8th Precipitation Measuring Mission (PMM) of Japan Aerospace Exploration Agency (JAXA). In this mission, I thank Dr. Takuji Kubota of JAXA for his advice. I am also deeply grateful to Dr. Yoshiaki Miyamoto of University of Miami for fruitful discussions and assistance. This study was published in the Monthly Weather Review of American Meteorological Society Journal; doi:10.1175/MWR-D-16-0244.1.

In the study of Chapter 5, special thanks are given to Assistant Prof. Kosuke Ito of University of the Ryukyus, Mr. Satoki Tsujino and Dr. Sachie Kanada of Nagoya University, Dr. Robert Rogers of NOAA's HRD and Associate Prof. Michael M. Bell of Colorado State University for insightful comments and encouragement. This work was supported by the Ministry of Education, Culture, Sports, Science and Technology (MEXT) KAKENHI Grant 16H04053. This study was published in the Journal of the Atmospheric Sciences of American Meteorological Society Journal; doi:10.1175/JAS-D-17-0042.1.

The study of Chapter 6 was carried out in the framework of a project that aims to improve TC intensity forecast at JMA. I thank the project members including Dr. Munehiko Yamaguchi, Mr. Norihisa Koide, Ms. Hiromi Owada, and Mr. Takeshi Iriguchi. This study was funded by the 8th Precipitation Measuring Mission (PMM) of JAXA. In addition, I thank Dr. Mark DeMaria of NHC, Dr. Buck Sampson of NRL, Drs. John Kaplan and Jason P. Dunion of NOAA's HRD, and Dr. Kate Musgrave of Colorado State University for kindly providing JMA/MRI with the SHIPS developmental code and valuable comments.

Finally, I would like to thank my wife for her support and encouragement.

Table of Contents

Abstract	i
Acknowledgements	iii
Table of contents	v
Chapter 1: Introduction	1
1.1. Basic structure of tropical cyclones	4
1.2. Current status of tropical cyclone intensity estimation	7
1.3. Current understanding of tropical cyclone intensity change processes	9
1.3.a. Theoretical understanding of intensification	9
1.3.b. Observational understanding of intensification	12
1.3.c. Transition processes to intensification	14
1.3.d. Intensity change associated with internal processes	15
1.3.e. Intensity change by vertical wind shear	17
1.4. Current status of tropical cyclone intensity forecast	22
1.5. Purpose of this study	24
Chapter 2: Intensity estimation using Doppler radar observations	25
2.1. Data, cases, and methodology	25
2.1.a. Data	25
2.1.b. Cases	27
2.1.c. Methodology	29
2.2. Simulation experiment	33
2.2.a. Simulation settings	33
2.2.b. Results and verification	36
2.3. Estimation results	38
2.3.a. Overall statistical verification	38

2.3.b. Classification of the individual cases	40
2.4. Discussion	47
2.4.a. Comparison with conventional methods	47
2.4.b. Additional statistical verification	47
2.4.c. Utility of the DR intensity estimation method	50
2.5. Summary	52
Chapter 3: Intensity change and axisymmetry	54
3.1. Data and method	54
3.2. Results	58
3.2.a. Case study	58
3.2.b. Relationship between TC intensity changes and axisymmetry	63
3.3. Discussion	72
3.4. Summary	74
Chapter 4: Reintensification and eyewall formation in strong shear: A Case Study of Typhoon Noul (2015)	76
4.1. Motivation	76
4.2. Data, method and accuracy evaluation	79
4.3. Overview of Typhoon Noul	82
4.4. Results	84
4.4.a. Axisymmetric structure	84
4.4.b. Asymmetric structure	86
4.5. Discussion	94
4.5.a. Vortex Precession	94
4.5.b. Comparison with other intensifying storms in shear	95
4.6. Summary	97

Chapter 5: Rapid Intensification of Typhoon Goni (2015) After Eyewall Replacement	99
5.1. Motivation	99
5.2. Data and methodology	100
5.2.a. Wind dataset	100
5.2.b. Data quality	101
5.3. Overview of Goni	103
5.3.a. Storm history and environmental conditions	103
5.3.b. Intensity analysis	104
5.3.c. Structural evolution	105
5.4. Goni's RI	109
5.4.a. RI onset	110
5.4.b. RI phase	114
5.4.c. Mature stage	115
5.4.d. Absolute angular momentum budget	117
5.5. Discussion	121
5.6. Summary	123
 Chapter 6: Further Improvement in the SHIPS Using Rainfall and Structural Information	125
6.1. Motivation	125
6.2. Data and methodology	127
6.2.a. Data	127
6.2.b. New predictors	130
6.2.c. Forecast experiments and their verification	134
6.3. Results	137
6.3.a. Forecast performance	137

6.3.b. Case study	141
6.3.c. Realtime forecast	144
6.4. Summary	145
Chapter 7: Conclusions	147
Appendix A. GBVTD technique	151
A.1. GBVTD formulation	151
A.2. Limitations of the GBVTD technique	154
Appendix B. Definition of RI for WNP TCs	155
Appendix C. Basic formula	157
List of reference papers	158
References	159

Chapter 1: Introduction

Observational, modeling, and theoretical studies have been conducted to investigate tropical cyclone (TC) intensity change from various perspectives including intensification processes, air-sea interactions, external forcing such as vertical wind shear, extratropical transition, and forecasting, and have improved our understanding of TCs. However, there still remain some important issues to be addressed in this field. In studying TC intensity (i.e., central pressure and maximum sustained wind), the following issues should be pointed out.

First, best track data are not necessarily correct. Best track data provide intensities at 6-h intervals, which are estimates primarily analyzed by an empirical method from satellite cloud patterns. This method depends on the resolution of satellite data and the skill of analysts, and does not consider dramatic intensity changes such as eyewall replacement cycles (ERCs).

Second, numerical models do not satisfactorily reproduce realistic structures and intensity changes. The skill of model's reproduction of TCs depends on horizontal resolution, physical parameterizations, and boundary and environmental conditions. No matter how exactly the intensity is simulated, the three-dimensional structure of the TC is not guaranteed. In addition, there is little ground truth for numerical simulations of TCs in the western North Pacific basin. As a result of such poor model performance, the skill of intensity forecast in the Japan Meteorological Agency (JMA) has not been improved at least for the last decade (Ito 2016).

Third, the TC pressure field adjusts to the TC wind field (Wu et al. 2006; Ito 2007). This is from the geostrophic adjustment argument (Schubert et al. 1980). According to the estimates by Wu et al. (2006), the horizontal scale of the eyewall L , where latent heat is released, is typically smaller than the Rossby deformation radius $L_R \equiv NH/I$, where N is the static stability (Brunt–Väisälä frequency), H is the vertical scale, I is the inertial stability (see Appendix C) (Table 1.1). In this scaling argument, pressure field adjusts to wind field. Therefore, the following pathway to TC intensification is doubtful; the decrease in the central pressure leads to the increase in low-level inflow and, as a result, the increase in the tangential wind. This adjustment argument is very important when we consider the efficiency of energy retained as wind kinetic energy to the injected heat energy.

A TC experiences a lifecycle of its formation, intensification, and

dissipation. According to the JMA, the mean longevity of TCs classified as tropical storm is 5.3 days (JMA 2017a). Figure 1.1 shows the evolution of the intensity of Typhoon Goni (2015), and also shows the evolution of sea surface temperature (SST) and vertical wind shear along the track. Goni was a relatively long-lived TC (more than 11 days), during which it underwent rapid intensification (RI), an ERC, landfall, and extratropical transition. During the weakening stage, it was affected by strong vertical shear greater than 10 m s^{-1} in the region of relatively low SSTs below 28°C .

One of the important issues during the lifecycle of a TC is RI. It is difficult to predict whether and when RI will occur. In fact, in the case of Goni, the JMA failed to forecast RI just after an ERC. One of the reasons for the difficulty of predicting RI is that internal processes leading to RI remain unclear. Aircraft observations, which provide a snapshot of a TC at best every few hours, have revealed what is happening with TCs. However, the time scale of internal processes leading to RI can be considered to be shorter than that of aircraft observations. This may prevent us from fully understanding TCs. To resolve this issue and to improve the skill of intensity forecast, further studies using higher-temporal observations are needed. The use of ground-based Doppler radar data and hourly satellite-derived rainfall products is a promising way to study rapid intensity change, but an evaluation of their accuracy and utility is needed before hand, because there are some intrinsic limitations in the use of them.

Based on the current issues regarding TC intensity discussed above, what to do by using high-temporal observations is sorted into three categories: intensity analysis, intensity change processes, and intensity forecast. In the rest of this chapter, we review the basic structure of TCs, the current status of intensity analysis, the current understanding of intensity change processes, and the current status of intensity forecast. Finally, we describe the purpose of this study.

Table 1.1: Estimation of L and L_R . Adapted from Wu et al. (2006). N is the static stability, H is the vertical scale, and V_{max} is the maximum surface wind.

	Case 1	Case 2	Hurricane Georges (1998)	Hurricane Fran (1996)
Latitude	22°N	22°N	18°N	23°N
N	0.015 s ⁻¹	0.015 s ⁻¹	0.015 s ⁻¹	0.015 s ⁻¹
H	10 km	10 km	10 km	10 km
V_{max}	13 m	45 m	20 m	12 m
L	330 km	150 km	230 km	280 km
L_R	1120 km	230 km	680 km	1050 km
L/L_R	0.29	0.65	0.34	0.27

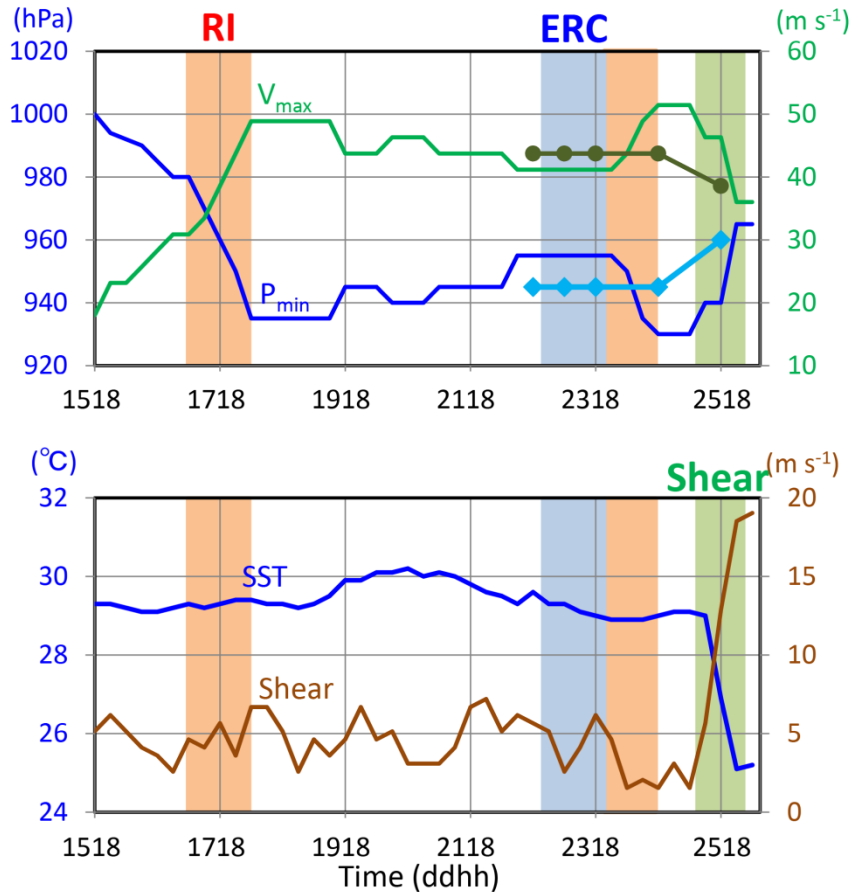


Fig. 1.1: (a) Best track intensity of Typhoon Goni (2015): green line, V_{max} ; blue line, P_{min} . The light blue line and the dark green line show JMA intensity forecasts for $ft = 12$ h, 24 h, 48 h, and 72 h initialized at 1800 UTC 22 August 2015. (b) Vertical wind shear (brown line) between 200 and 850 hPa averaged within 1000 km from the center and SST (blue line). The vertical orange bar indicates the period focused on in this study. The vertical orange bar indicates a rapid intensification (RI) period, the blue bar indicates an eyewall replacement cycle (ERC) period, and the green bar indicates the period of interaction with strong vertical wind shear.

1.1. Basic structure of tropical cyclones

Before reviewing intensity, here we review the basic structure of TCs. Figure 1.2a indicates a radius–height plot of azimuthal mean tangential wind for typical intense TCs. This schematic is based on a boundary layer theory by Kepert and Wang (2001). Note that the y-axis is shown in logarithm scale. In general, the azimuthal mean tangential wind above the boundary layer (generally defined as strong inflow layer) lies approximately in gradient wind balance, where the radial pressure gradient force, the centrifugal force, and the Coriolis force are balanced,

$$\frac{\bar{v}^2}{r} + f\bar{v} = \frac{1}{\rho} \frac{\partial p}{\partial r}, \quad (1.1)$$

where \bar{v} is azimuthal mean tangential wind, r is the radius from the TC center, f is the Coriolis parameter, ρ is density, and p is pressure. Willoughby (1990) verified using aircraft in situ observations that the gradient wind balance is a good approximation for \bar{v} in the free atmosphere of TCs. Within the boundary layer, there is a peak of \bar{v} near the top of the boundary layer, where \bar{v} is supergradient,

$$\frac{\bar{v}^2}{r} + f\bar{v} > \frac{1}{\rho} \frac{\partial p}{\partial r}.$$

In areas where wind is supergradient, air parcels are forced radially outward. Below the peak of \bar{v} , tangential flow is smaller than the corresponding gradient flow, which is calculated from the pressure gradient, due to surface friction. A composite analysis of dropsonde observations (Fig. 1.3) shows that azimuthal mean radial wind, \bar{u} , is inflow in the boundary layer, and its peak is just above the surface. Above the boundary layer, outflow exists around the radius of maximum wind (RMW), and weak inflow exists outside the $2 \times$ RMW.

Because absolute angular momentum \bar{M} ($\bar{M} = (1/2)fr^2 + r\bar{v}$) is, to good approximation, materially conserved except in the BL, examining changes in the distribution of \bar{M} through the secondary circulation is useful for understanding the evolution of a TC vortex. Thus, in this study, we often show a distribution of \bar{M} . Figure 1.2b shows that \bar{M} increases with increasing radius. This condition is inertially stable. \bar{M} surfaces are displaced inward toward the center in the supergradient region.

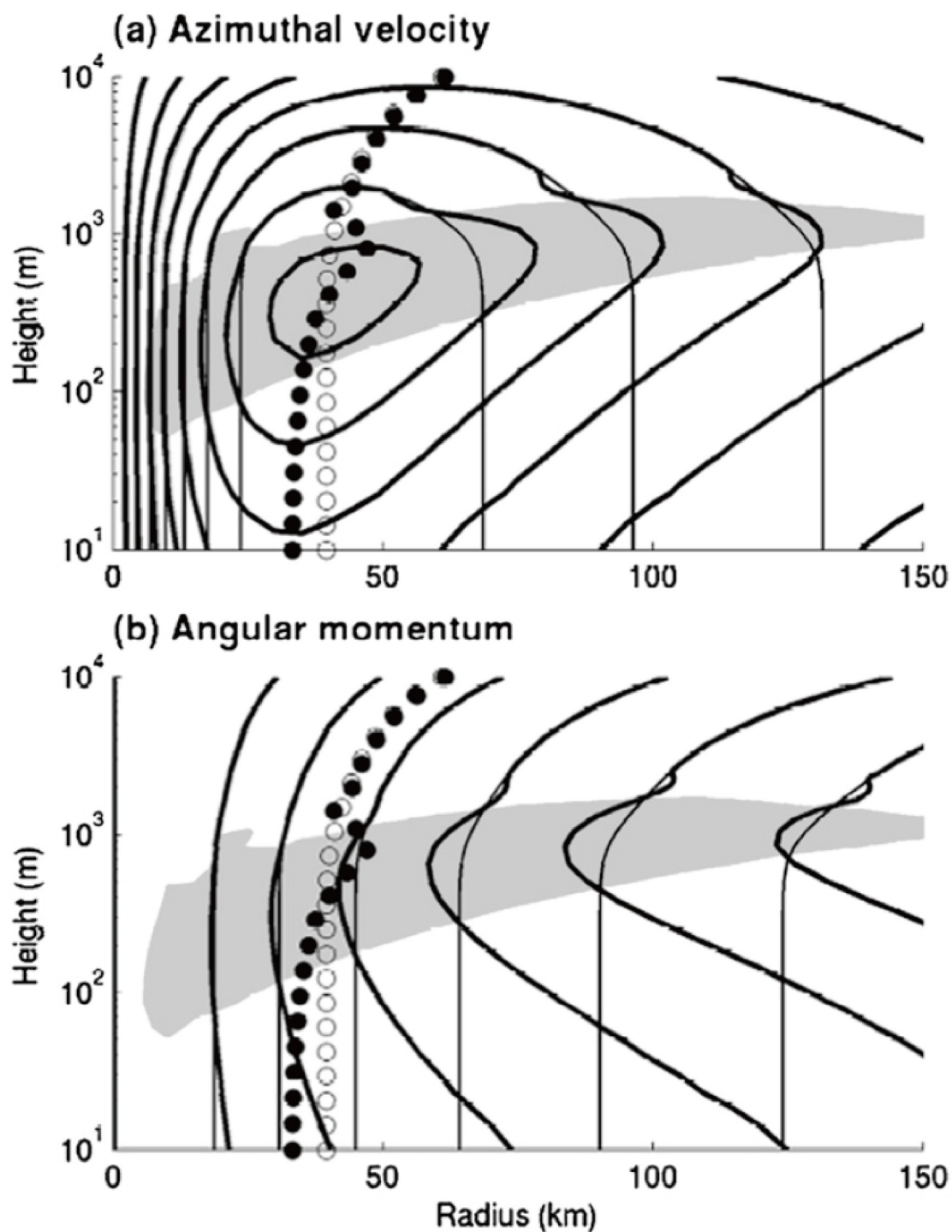


Fig. 1.2: Schematic radius–height cross sections of (a) the tangential wind (thick contours) and the gradient wind (thin contours) and (b) the angular momentum with (thick contours) and without (thin contours) the influence of friction. The region of the supergradient winds is shaded. The filled circles indicate the radius of maximum tangential wind and the open circles indicate the radius of maximum gradient wind. Adapted from Powell et al. (2009).

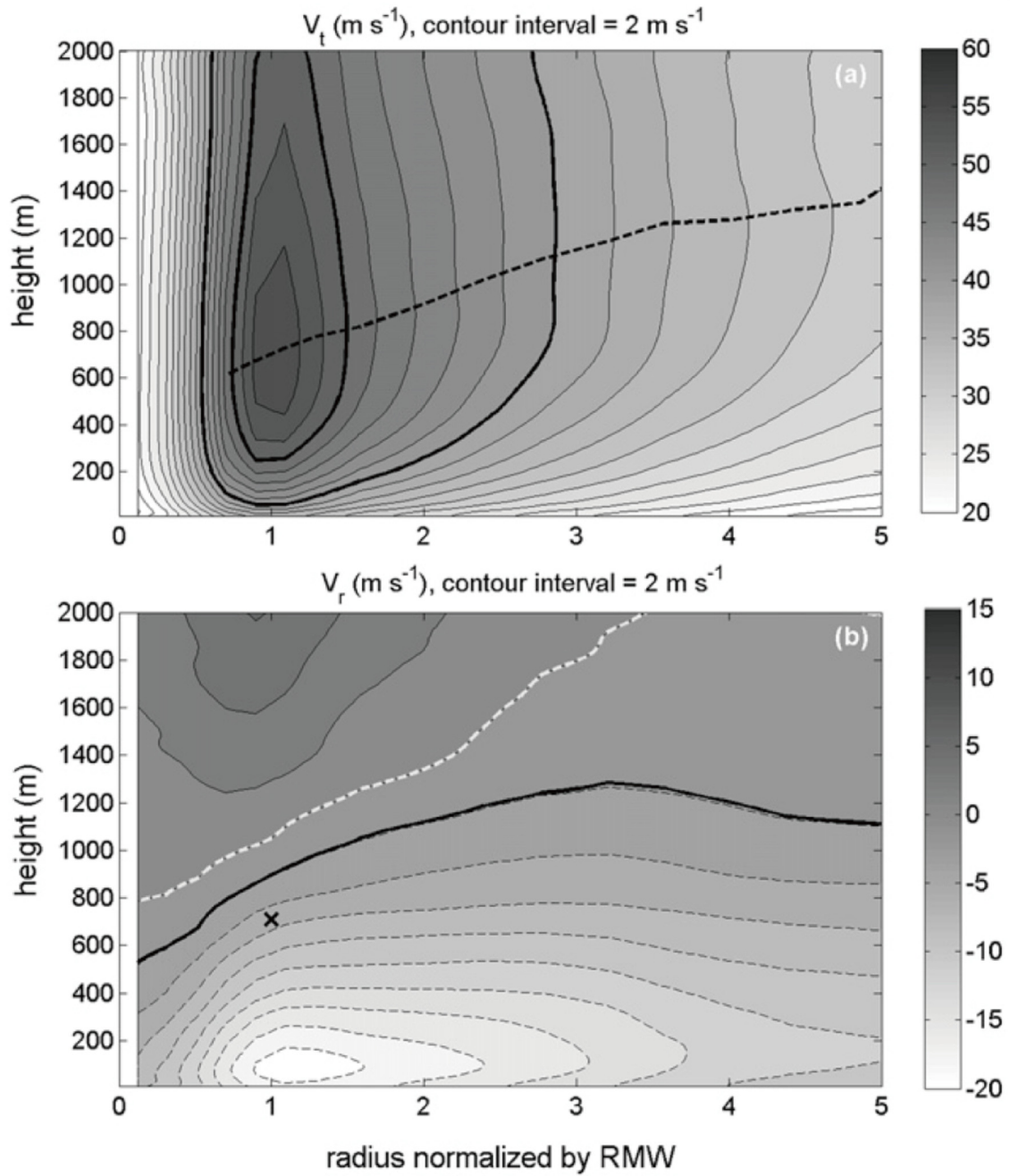


Fig. 1.3: Radius–height plots of (a) the tangential wind and (b) the radial wind based on the dropsonde composite analysis. The abscissa axis is normalized by the RMW. The dashed line in (a) indicates the height of the maximum tangential wind speed at each radius. The thick black line in (b) indicates the height of the inflow layer determined by 10% of the peak inflow and the white dashed line indicates the zero contour of the radial wind. The X mark indicates the location of the maximum tangential wind speed. Adapted from Zhang et al. (2011).

1.2. Current status of tropical cyclone intensity estimation

It is of great importance to analyze TC intensity (i.e., central pressure and maximum sustained wind) with high accuracy and frequency, not only from the perspective of improving scientific understanding of various phenomena associated with TCs, but also for disaster prevention and mitigation. TC intensity estimates are generally made using infrared (IR) satellite data, for example, by the Dvorak technique (e.g., Dvorak 1975, 1984; Koba et al. 1990; Velden et al. 1998; Olander et al. 2004; Olander and Velden 2007), satellite microwave sounding data (Brueske and Velden 2003; Herndon and Velden 2004; Demuth et al. 2004; Oyama 2014), satellite microwave imager data (Bankert and Tag 2002; Hoshino and Nakazawa 2007; Sakuragi et al. 2014), and all other available observations.

The Dvorak technique is an empirical method based on past reconnaissance observations and the subjective classification of cloud patterns, but the advanced Dvorak technique is a fully automated method (Olander and Velden 2007). Methods using satellite microwave sounding and imager data are entirely objective, but in the western North Pacific basin, satellite methods refer to best track data as truth. Because these data are based mainly on the Dvorak technique, the uncertainty of the satellite methods includes the estimation error associated with the Dvorak technique. The Dvorak technique is generally used at 6-h intervals by operational centers, and does not consider rapid fluctuations in intensity. In addition, these conventional methods estimate TC intensity from relevant physical values such as cloud patterns and upper level warm core anomalies, rather than by using a straightforward physical equation that describes pressure distributions. Therefore, conventional estimates have a large margin of error with a standard deviation of 7–19 hPa (Koba et al. 1990). Although it is not realistically possible at present to obtain the central pressure (P_{min}) of TCs from dropsonde observations in the western North Pacific basin, it is still necessary to estimate TC intensities with as much accuracy and frequency as possible, particularly for TCs that change intensity rapidly.

One method of addressing this problem is to estimate P_{min} by using a physical equation, namely, the gradient wind equation. Lee et al. (2000) proposed a method that uses data from a single ground-based Doppler radar (DR) (hereafter, the “DR method”). In this method, the ground-based Velocity Track Display (GBVTD) technique (Lee et al. 1999, Appendix A) is used to retrieve \bar{v} of a TC from the Doppler radial velocities, V_D , under the

assumption that there is one primary circular vortex around the TC center and that the asymmetric radial wind is much smaller than the corresponding tangential wind. Then, P_{min} is estimated at 5-min intervals by using an axisymmetric pressure deficit deduced by applying the retrieved \bar{v} to the gradient wind equation and using a sea level pressure (SLP) observation around the TC as an anchor for pressure measurement. Because the DR method calculates the P_{min} by using a physical equation related to the TC wind field, the estimated P_{min} is expected to have higher accuracy than that derived from cloud patterns and upper-level warm core anomalies, although the DR method is applicable only to TCs that approach radar locations. To apply the DR method, it is essential to retrieve \bar{v} from V_D with high accuracy. Because the GBVTD technique has been successfully used to retrieve \bar{v} for many TCs (Lee et al. 2000; Harasti et al. 2004; Lee and Bell 2007; Zhao et al. 2008, 2012, 2016), the DR method is promising.

The DR method has already been implemented by the National Hurricane Center (NHC) (Harasti et al. 2007), where it is called Vortex Objective Radar Tracking and Circulation (VORTRAC), but the accuracy with which the DR method estimates the P_{min} and the scientific utility of the DR method have not yet been clarified comprehensively, probably owing to the lack of sufficient TC examples. Thus, it is essential to examine the accuracy of the P_{min} estimates and their suitability for monitoring TC intensity at 5-min intervals. In addition, in-depth examinations of the DR method's reliability, strengths, weaknesses, and limitations are needed. We develop our own system to retrieve the TC wind field and to estimate the P_{min} in Chapter 2.

1.3. Current understanding of tropical cyclone intensity change processes

We here review previous studies of TC intensity change including RI, secondary eyewall formation, ERC, and the effect of vertical wind shear from the view of both theories and observations. We focus on internal processes related to our observational study using radar and satellite data. Thus, we do not review the interaction between the ocean and TCs, although it is a very important process.

a. Theoretical understanding of intensification

Theoretical studies have examined the mechanisms of TC vortex intensification in terms of the response to heat sources. In the case of a radially located heat source, Shapiro and Willoughby (1982) and Pendergrass and Willoughby (2009) have demonstrated that diabatic heating inside the RMW leads to a rapid increase in tangential wind speed (Fig. 1.4). They also showed that eyewall heating causes more rapid strengthening of the tangential wind as the maximum wind speed increases. Schubert and Hack (1982) and Vigh and Schubert (2009) found that diabatic heating inside the RMW is more efficient for the formation of a warm core than diabatic heating outside the RMW. When the heat source is distributed azimuthally, Nolan and Grasso (2003) and Nolan et al. (2007) showed that the axisymmetric component of diabatic heating is much more efficient for the vortex intensification than the asymmetric component; in fact, asymmetric heating can contribute directly to the weakening of a TC vortex. Nolan et al. (2007) also showed that the ratio of energy retained as wind kinetic energy to the injected heat energy increases as the maximum wind speed increases.

Smith and Montgomery (2016) illustrated vortex spinup and spindown by considering how the distribution of \bar{M} is changed by forced diabatic heating. Figure 1.5 shows the secondary circulation (radial and vertical flows) induced by radial gradient of diabatic heating and the resultant tangential wind tendency, which is dependent on the radial location of the imposed heating. With diabatic heating located inside the RMW, the radial gradient of potential temperature negatively increases around the RMW, which induces the secondary circulation for a vortex to satisfy thermal wind balance. Then, the circulation advects \bar{M} inward outside the heating region, leading to the increase in the tangential wind around the RMW. With diabatic heating located outside the RMW, the tangential wind around the RMW decreases.

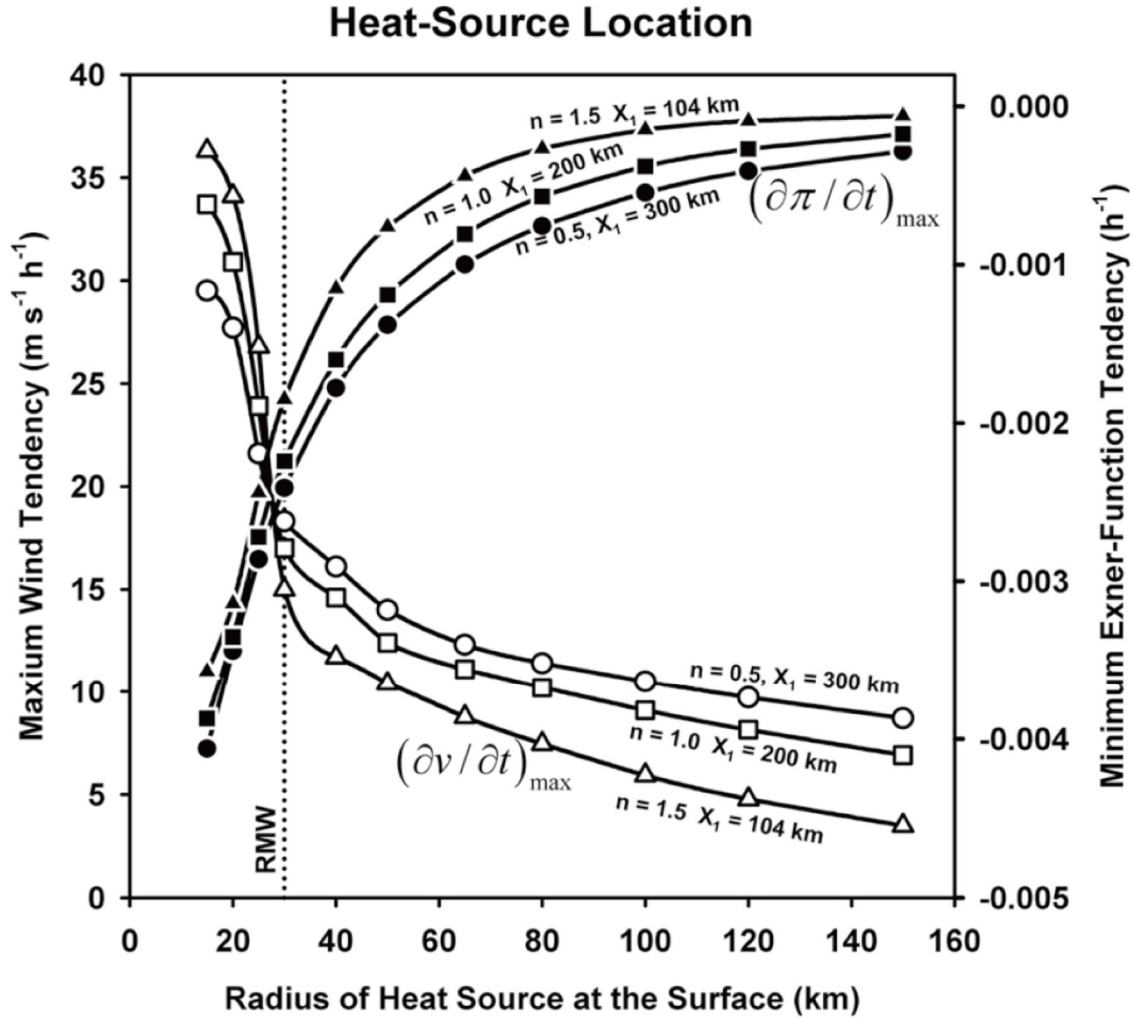


Fig. 1.4: Pendergrass and Willoughby (2009) solved the Sawyer–Eliassen equation on a balanced basic vortex to examine the maximum tangential wind tendency, $(\partial v/\partial t)_{\max}$, and the minimum Exner function tendency, $(\partial \pi/\partial t)_{\min}$, in response to the imposed diabatic heating. The abscissa axis is the radius of heat source imposed at the surface.

The shape of the balanced basic vortex is parameterized by n and X_1 . n is a parameter to determine the wind field inside the RMW so that the wind speed is proportional to the n th power of radius. X_1 is the horizontal scale of the vortex and the wind speed outside the RMW decays exponentially with X_1 . A sharp vortex wind profile is given by $n = 1.5$ and $X_1 = 104$ km, a medium vortex wind profile is given by $n = 1.0$ and $X_1 = 200$ km, and a broad vortex wind profile is given by $n = 0.5$ and $X_1 = 300$ km. The RMW is located at 30 km.

The more inside the RMW the heating is located, the larger the magnitude of $(\partial v/\partial t)_{\max}$ and $(\partial \pi/\partial t)_{\min}$. As the heat source moves outward outside the RMW, the magnitude of $(\partial v/\partial t)_{\max}$ and $(\partial \pi/\partial t)_{\min}$ becomes small. Adapted from Pendergrass and Willoughby (2009).

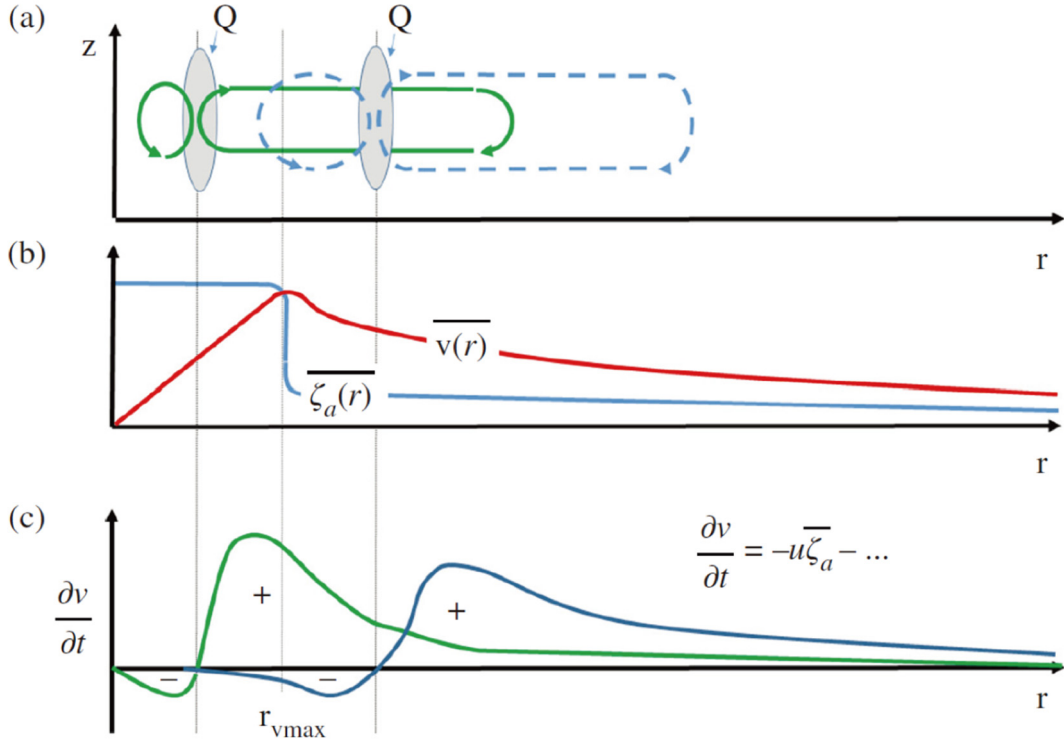


Fig. 1.5: Schematic diagrams illustrating vortex spinup and spindown caused by diabatic heating depending on the radial location. Panel (a) shows the secondary circulation induced by imposed diabatic heating. The horizontal scale of the circulation is determined by the local Rossby deformation radius ($L_R \equiv NH/D$). Panel (b) shows a balanced basic vortex. Panel (c) shows the tendency of tangential wind ($\frac{\partial v}{\partial t}$) by the advection of angular momentum due to the induced secondary circulation. In (a) and (c), when diabatic heating is located inside the RMW, the response is indicated by the green color, and when diabatic heating is located outside the RMW, the response is indicated by the blue color. Adapted from Smith and Montgomery (2016).

Conventionally, the mechanism of vortex spinup has been considered in a balanced vortex framework as described above (e.g., Nolan et al. 2007; Pendergrass and Willoughby 2009; Vigh and Schubert 2009; Fudeyasu and Wang 2011), but recent theoretical studies have emphasized the role of the boundary layer (BL) in vortex spinup (Smith et al. 2009; Montgomery and Smith 2014; Frisius and Lee 2016). Smith et al. (2009) and Smith and Montgomery (2016) proposed a hypothesis that boundary layer spinup with supergradient flow is important for a vortex to spin up. Schmidt and Smith (2016) concluded using a minimal axisymmetric model that eyewall spinup occurs by upward advection of \bar{M} from the BL where the tangential wind is supergradient. Frisius and Lee (2016) examined the impact of gradient wind imbalance on intensification by using Ooyama's three-layer model (Ooyama 1969) with some modifications. They demonstrated that the intensification

rate is larger when the unbalanced boundary layer dynamics is permitted in the lowest model layer than when the unbalanced boundary layer is not permitted. Although mechanisms described above are from the view of axisymmetric vortex spinup, which is referred to an axisymmetric mode (Reasor et al. 2009; Guimond et al. 2016), there is an asymmetric mode where eddy momentum fluxes contribute to the increase in the mean flow. The latter mode is associated with the axisymmetrization of potential vorticity anomalies represented as vortex Rossby waves (e.g., Montgomery and Kallenbach 1997; Wang 2002). While the axisymmetric mode largely contributes to vortex intensification, the asymmetric mode plays a nonnegligible role in intensification (Nolan et al. 2007; Reasor et al. 2009; Persing et al. 2013).

b. Observational understanding of intensification

Observational studies have examined inner-core structures favorable for intensification of TCs, such as the distribution of inertial stability, axial symmetry, vortex tilt, and the radial location of deep convection and diabatic heating (e.g., Rogers et al. 2013, 2015, 2016; Jiang and Ramirez 2013; Zagrodnik and Jiang 2014; Stevenson et al. 2014; Susca-Lopata et al. 2015; Tao and Jiang 2015; Zawislak et al. 2016).

Rogers et al. (2013) performed composite analyses of airborne Doppler measurements to compare inner-core structural differences between intensifying and steady-state hurricanes. They showed that intensifying hurricanes are characterized by convective bursts (deep, vigorous convection) that preferentially occur inside the RMW (see the left panel of Fig. 1.6). Rogers et al. (2015), who used airborne observations to investigate Hurricane Earl (2010), also emphasized the role of asymmetric convective bursts during RI. Guimond et al. (2016) examined convective bursts during the RI of Hurricane Karl (2010) using aircraft observations and showed that mesovortices in the eye helped deep convective bursts inside the RMW, and downdrafts located radially inward of the convective bursts assisted to warm and dry the eye.

Rogers et al. (2013) also showed in composite analyses that intensifying hurricanes have a ring-like vorticity structure inside the RMW and greater azimuthal precipitation coverage in the eyewall compared with steady-state hurricanes (see the right panel of Fig. 1.6). Zagrodnik and Jiang (2014) investigated the distribution of rainfall and diabatic heating by using Tropical Rainfall Measuring Mission (TRMM) Precipitation Radar (PR) data and showed that both distributions become more axisymmetric immediately before the onset of RI, whereas the rainfall area extends farther on the

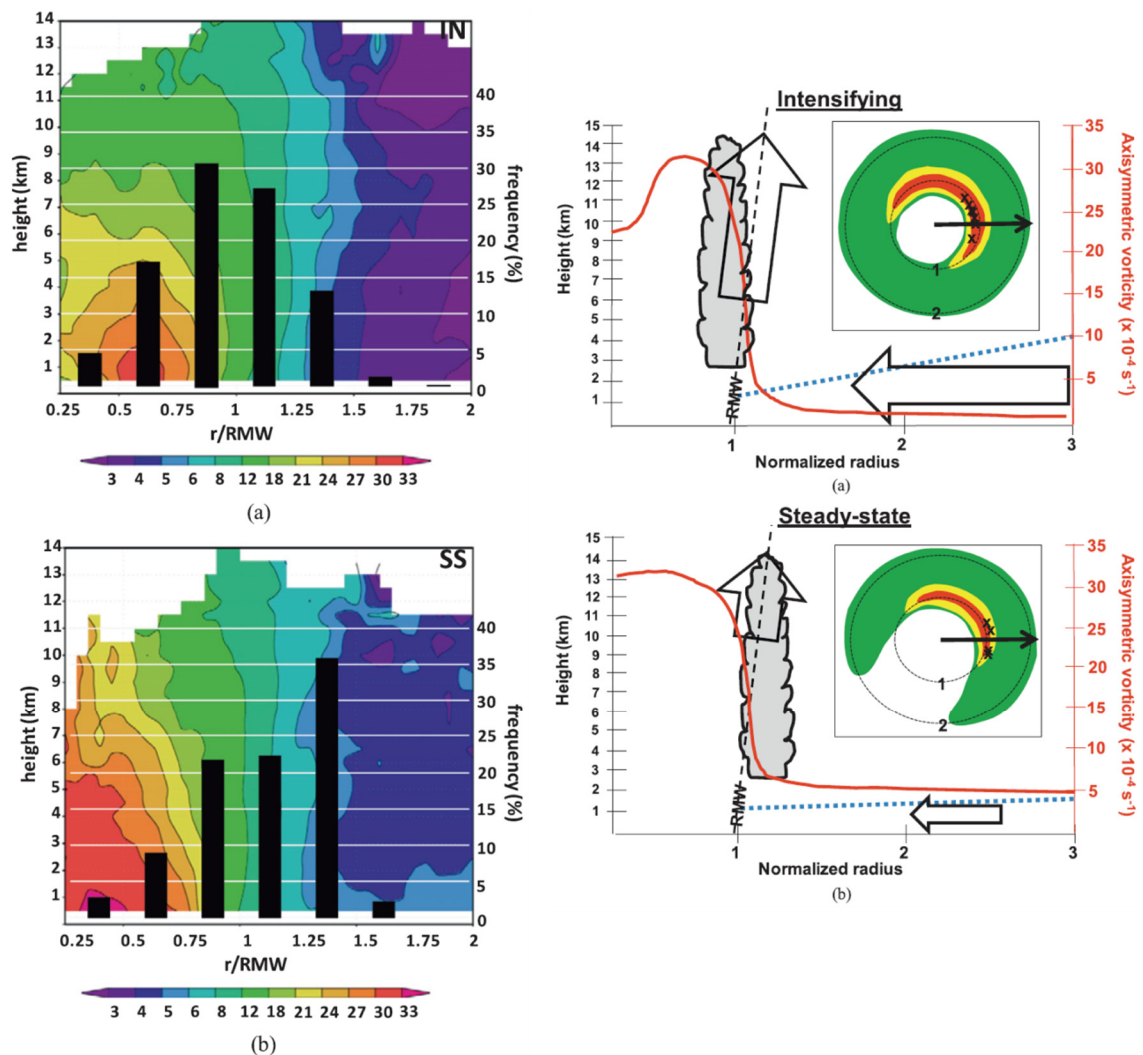


Fig. 1.6: (left) Frequency of convective burst points as a function of radius normalized by the RMW for (left top) intensifying TCs and (left bottom) steady-state TCs. The composite-mean axisymmetric vertical vorticity (10^{-4} s^{-1}) is color shaded.

(right) Schematic of the differences in inner-core structure between (left top) intensifying TCs and (left bottom) steady-state TCs. Black dashed line indicates the RMW, red line represents axisymmetric vertical vorticity ($\times 10^{-4} \text{ s}^{-1}$) at 2-km altitude, and thick arrows indicate axisymmetric radial and vertical flow. Blue dotted line denotes inflow layer. Cloud cartoon represents the radial location of convective bursts. Insets show reflectivity distribution at 2-km altitude (color shaded) and typical location of convective bursts (\times marks). Black arrow in inset is 850-200-hPa shear vector.

Adapted from Rogers et al. (2013).

upshear side during RI. Kieper and Jiang (2012) reported that the existence of an eyewall ring on the Naval Research Laboratory (NRL) 37 GHz passive microwave composite product that consists of low-level water clouds and warm rain is important for RI. Meanwhile, Jiang (2012) used TRMM data to show that strong convection is neither a necessary nor a sufficient condition for RI, although they found a statistically significant relationship between convective

intensity in the inner core and TC intensity changes. Also using TRMM data, Jiang and Ramirez (2013) found that rainfall in the inner core is at least moderate to heavy (i.e., total raining area $> 3000 \text{ km}^2$, total volumetric water $> 5000 \text{ mm h}^{-1} \text{ km}^2$) and convection in the inner core is at least moderate (i.e., maximum near-surface radar reflectivity $> 40 \text{ dBZ}$, maximum 20-dBZ (40 dBZ) echo height > 8 (4) km, minimum 85-GHz polarization-corrected brightness temperature (PCT) $< 235\text{K}$, and minimum 10.8-mm brightness temperature $< 220\text{K}$) in TCs before the onset of RI, but intense asymmetric convection is not a necessary condition for the onset of RI.

Rogers et al. (2015) examined structural differences between Hurricane Earl (2010), a rapidly intensifying TC, and Hurricane Gustav (2008), a steady-state TC, and showed that inertial stability was higher inside and lower outside the RMW, and that inflow in the BL was deeper and stronger in Earl than in Gustav, leading to a preference for deep vigorous convection inside the RMW in Earl.

c. Transition processes to intensification

It has recently been revealed that the intensification rate of tropical cyclones (TCs) is not determined by environmental conditions only but is also controlled by dynamical and thermodynamical processes in the TC's inner core. Hendricks et al. (2010) showed that there is little difference in environmental conditions between TCs that rapidly intensify and those that intensify at a normal rate. They concluded that the intensification rate is controlled mostly by internal dynamical processes, provided that environmental conditions are relatively favorable. Miyamoto and Takemi (2013) performed an idealized numerical simulation that showed the importance of internal processes in achieving RI. A TC vortex becomes axisymmetric, and inertial stability substantially increases, before the onset of RI. The large inertial stability increases the residence time of air parcels in the inner core, which enhances convective available potential energy (CAPE) within the radius of maximum wind (RMW). Then an eyewall forms by consuming the enhanced CAPE, and the intensification rate rapidly increases. Kieu et al. (2014) performed idealized numerical simulations and hypothesized that an upper level warm core, high humidity in the inner core, and sufficient low-level tangential flow are necessary for the onset of RI. The findings of these studies suggest that no matter how favorable environmental conditions are, a TC cannot intensify unless favorable internal conditions have been realized.

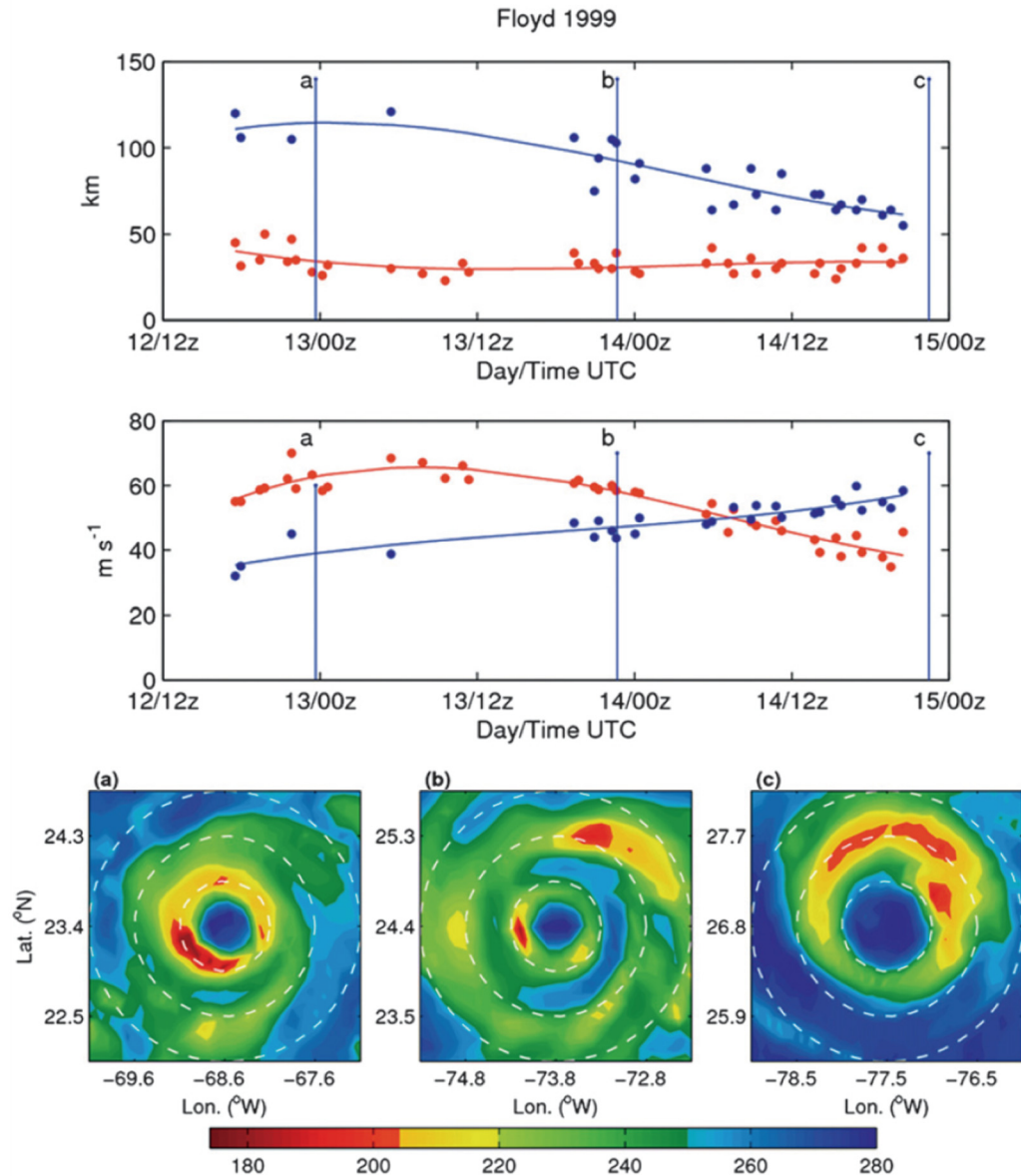


Fig. 1.7: Example of an ERC for Hurricane Floyd (1999). (top) The time evolution of the radius of an inner maximum wind (r_1 , red) and an outer maximum wind (r_2 , blue). (bottom) The time evolution of the maximum wind at r_1 (red) and the maximum wind at r_2 (blue). (a–b) 85-GHz brightness temperatures (K) from the Special Sensor Microwave Imager (SSM/I) polar-orbiting microwave satellite. The time of each imagery corresponds to the time of each imagery in the top two panels. White dashed rings indicate radial distances from the storm center of 50, 100, and 150 km. Adapted from Sitkowski et al. (2011).

d. Intensity change associated with internal processes

Intensity change occurs with drastic structural change. As representative phenomena of internal processes associated with intensity change, here we review the current understanding of secondary eyewall formation (SEF) and ERC.

To date, several views of SEF processes have been proposed. Whereas some studies emphasize the importance of persistent diabatic heating outside the primary eyewall for SEF (e.g., Rozoff et al. 2012; Menelaou et al. 2014; Zhu and Zhu 2014), others consider supergradient flow within the BL to be more important in the initiation of SEF (Huang et al. 2012; Bell et al. 2012; Abarca and Montgomery 2013, 2014, 2015; Abarca et al. 2016). Huang et al. (2012) proposed that unbalanced dynamics in the BL is essential for SEF. First, supergradient winds occur in the BL outside the primary eyewall after the outward expansion of the tangential wind field, and then air parcels in the supergradient winds are propelled outward, converge in the BL, and move upward. This forced ascent contributes to deep convection in the presence of convective instability, leading to SEF. Meanwhile, Kepert (2013) and Kepert and Nolan (2014) have pointed out that although the BL assists SEF, it does not initiate SEF, because “the BL is, to good approximation, slaved to the rest of the cyclone”. Kepert (2013) hypothesized that SEF occurs as a result of positive feedback between nonlinear responses in the BL to a local vorticity maximum outside the RMW in the free atmosphere and convection in the incipient secondary eyewall. Furthermore, Rozoff et al. (2012) demonstrated that the radially outward expansion of the high inertial stability region prior to SEF results in an increase in the efficiency of secondary eyewall development to imposed diabatic heating.

Sitkowski et al. (2011) extracted 24 ERC events of 14 hurricanes that were observed by aircraft and examined the climatological characteristics of changes in intensity and structure associated with the ERCs. An example of a representative ERC event is shown in Fig. 1.7. Their study revealed that after ordinary intensification, an outer wind maximum is observed in the incipient secondary eyewall on average 9 h prior to a suspension of intensification. Then, during the period from the local intensity maximum to the local intensity minimum, wind speed around the inner eyewall decreases by 10 m s^{-1} on average, whereas wind speed around the outer eyewall increases. A re-intensification period follows, during which the wind speed in the outer eyewall becomes greater than that in the inner eyewall and the wind peak around the inner eyewall gradually disappears, signaling the completion of the ERC. This re-intensification takes 11 h on average. The RMW associated with the secondary eyewall rapidly contracts during the ERC. After the completion of the ERC, the TC often continues to intensify and in some cases RI occurs.

e. Intensity change by vertical wind shear

Vertical wind shear vector is defined as the difference between vectors of the low-level and upper-level environmental winds. Vertical wind shear is one of the most important factors that explain changes in the structure and intensity of a tropical cyclone (TC). TCs form, intensify and weaken in the presence of shear. Thus, the effect of vertical shear on TCs has been studied in many papers including theoretical, modeling and observational studies so far.

For structural changes, observation-based composite studies (Reasor et al. 2013; DeHart et al. 2014) showed that for TCs in shear, eyewall convection is initiated associated with low-level deep inflow in the downshear-right quadrant. Intense updrafts grow hydrometeors downshear, causing radar reflectivity to be highest in the downshear-left quadrant. Intense downdrafts, which are associated with small-scale deep convection downshear-left dominate in the upshear-left quadrant in the upper level. Eyewall convection on the upshear side is suppressed associated with upper-level inflow and low-level outflow there. Black et al. (2002) analyzed radar echoes in the eyewall of two hurricanes in sheared environments and detailed asymmetric eyewall structure accompanied by small-scale, cyclonically rotating convective cells, which formed downshear and reached maturity on the left of shear. Corbosiero and Molinari (2002, 2003) showed that lightning locations in the inner-core of TCs are preferentially distributed in the downshear-left quadrant. Reasor et al. (2013) demonstrated through a composite of observations that TC vortices tend to be tilted downshear and to the left of the shear vector. Shear is a dominant determinant of asymmetric structure not only for mature storms, but also for transitioning storms (Foerster et al. 2014) and very intense TCs such as Typhoon Haiyan (2013) (Shimada et al. 2017b) and Hurricane Patricia (2015) (Rogers et al. 2017).

Reasor (2004) established a theory regarding vortex resilience in shear (Fig. 1.8). In sheared environments, differential advection by the vertical shear flow can cause a TC vortex to be tilted and can cause the vortex to shear apart (Fig. 1.8b). However, Jones (1995) and Reasor et al. (2004) demonstrated that a TC vortex intrinsically has dry dynamics that resists shear to keep its vortex vertically aligned. The tilted potential vorticity (PV) column of a TC can be projected onto an azimuthal mean PV and a wavenumber-1 PV anomaly (Reasor and Montgomery 2001). When the vortex scale is much smaller than the Rossby deformation radius, the wavenumber-1 PV asymmetry behaves as a vortex Rossby wave called a tilt mode (Fig. 1.8c, Reasor and Montgomery 2015), which is similar to an edge wave on a Rankin vortex (Lamb 1932), and

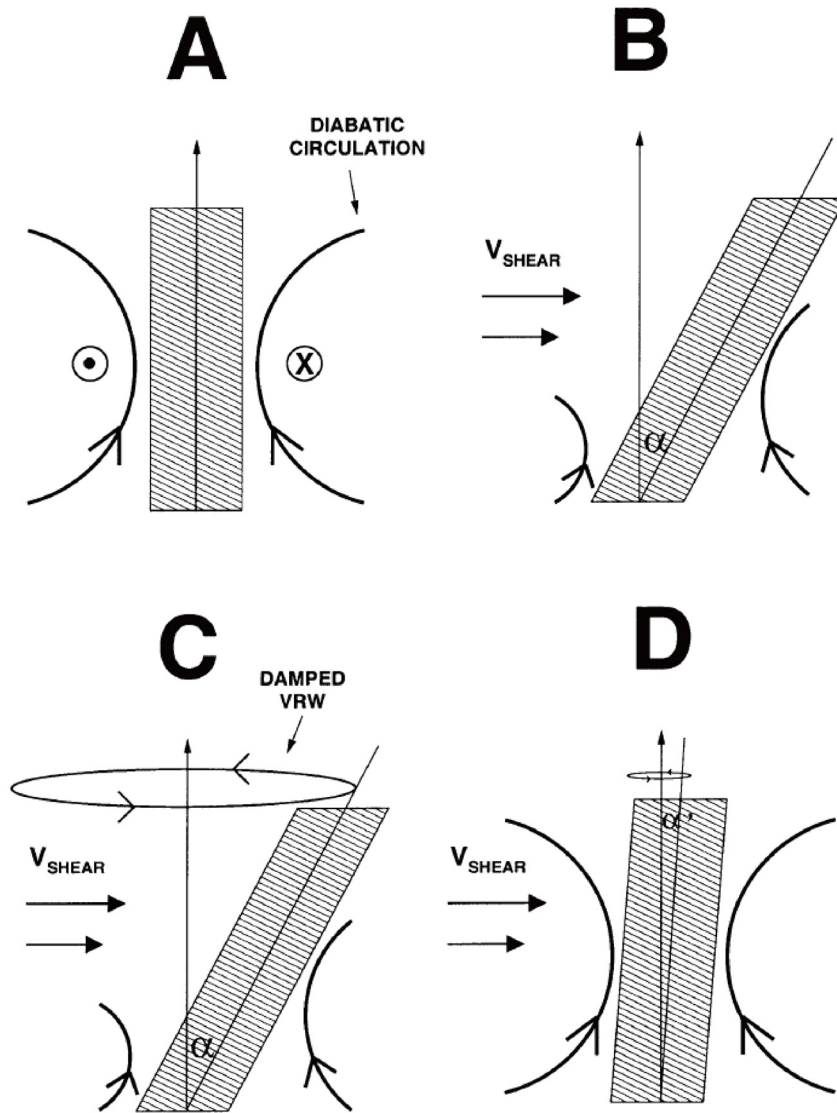


Fig. 1.8: Schematic of the vortex tilt, vortex Rossby wave damping, and vortex alignment in vertical shear flow. (a) A TC vortex (indicated by a rectangular shape) vertically aligned with the axisymmetric secondary circulation driven by diabatic heating. (b) In sheared environments, differential advection by the vertical shear flow can cause a TC vortex to be tilted. For a tilted vortex by the vertical shear to remain thermal wind balance, adiabatic upward motion is induced to cause a negative temperature anomaly downtilt and adiabatic downward motion is induced to cause a positive temperature anomaly uptilt. (c) The tilted potential vorticity (PV) column of a TC can be projected onto an azimuthal mean PV and a wavenumber-1 PV anomaly. The wavenumber-1 PV asymmetry behaves as a vortex Rossby wave called a tilt mode and the vortex precesses. (d) The amplitude of the tilt mode is reduced by the resonant damping mechanism. For sufficiently strong VRW damping, the vortex can be realigned.

the vortex precesses (Jones 1995). The amplitude of the tilt mode is reduced by the resonant damping mechanism (Fig. 1.8d, Schechter et al. 2002; Schechter and Montgomery 2003). Whether the mode damps or not is determined by radial PV gradient in sign at a critical radius where the phase speed of the

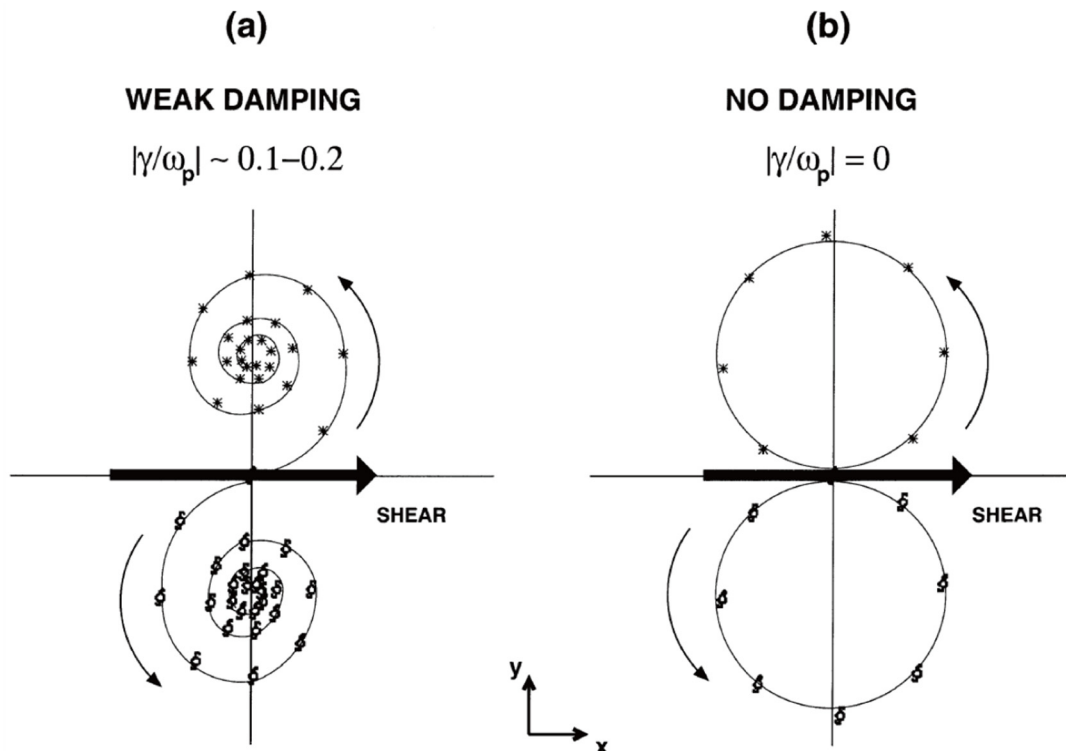


Fig. 1.9: Schematic of the vortex tilt evolution when (a) the vortex damping occurs and the vortex reaches an equilibrium tilt 90° to the left of shear, (b) the vortex damping does not occur and the vortex experiences tilting downshear, a cyclonic precession upshear, and a realignment repeatedly. In this schematic, the vortex is initially tilted by westerly vertical shear. Then, the vortex centers at upper level (the stars) and at lower level (the hurricane symbols) move to the direction indicated by each thin arrow.

vortex Rossby wave and tangential wind speed are the same. For TC vortices, the damping occurs with the gradient negative at the radius, whereas the vortex shears apart with the gradient positive at the radius (Schechter et al. 2002). With the tilt damping, the vortex reaches an equilibrium tilt 90° to the left of shear (Fig. 1.9a, Reasor et al. 2004). In addition, stronger vortices are more resilient to shear (Reasor et al. 2004). Meanwhile, when the PV gradient is 0 at the critical radius, the vortex undergoes tilting downshear, a cyclonic precession upshear, and a realignment repeatedly with half the angular velocity of the corresponding vortex Rossby wave (tilt mode) (Fig. 1.9b, Reasor et al. 2004; Reasor and Montgomery 2015).

For a tilted vortex by the vertical shear to remain in thermal wind balance, adiabatic upward motion is induced to cause a negative temperature anomaly downtilt (in the direction of the tilt vector, which is defined as the horizontal distance between the upper-level and low-level vortex centers) and adiabatic downward motion is induced to cause a positive temperature anomaly uptilt (Jones 1995; Wang and Holland 1996; Frank and Ritchie 1999;

Ueno 2007). With moist convective processes, upward and downward motions are distributed so that the vorticity advection associated with the storm-relative flow is balanced by the vorticity stretching or compression (e.g., Bender 1997; Frank and Ritchie 1999, 2001). In the low-level, negative vorticity advection associated with the low-level inflow is balanced by the vorticity stretching where upward motion is present, and positive vorticity advection due to the low-level outflow is balanced by the vorticity compression where downward motion is present. Maximum upward motion in the eyewall is located in the downtilt direction (Rogers et al. 2003; Zhu et al. 2004; Wu et al. 2006; Braun et al. 2006; Braun and Wu 2007; Ueno 2008; Riemer et al. 2010; Reasor and Eastin 2012; Reasor et al. 2013). A cold temperature anomaly is also consistent with upward motion (Wu et al. 2006; Braun et al. 2006; Reasor and Eastin 2012). Braun et al. (2006) simulated Hurricane Bonnie (1998) and concluded through the analysis results that the vortex tilt is linked with asymmetric convection and that the location of upward motion is closely related to that of the low-level inflow and convergence. As a result, the direction of the vortex tilt is confined to the location of low-level storm-relative inflow, instead of 90° to the left of shear described in Reasor et al. (2004). Furthermore, Braun et al. (2006) and Braun and Wu (2007) examined the relationship between eyewall mesovortex activity and vertical wind shear, and showed that strong updraft associated with a mesovortex occurs on the downshear side, where the outflow associated with the eyewall mesovortex and the low-level inflow associated with shear converge. In the upshear quadrant, vorticity anomalies associated with mesovortices move around the eyewall, but they are not accompanied by strong updrafts.

Vertical shear is known to be an unfavorable factor for intensification. The statistical relationship between shear and intensity change indicates that intensifying TCs were in weaker shear than non-intensifying TCs (Kaplan and DeMaria 2003). A predictor of shear in statistical dynamical models works for weakening (DeMaria and Kaplan 1994, 1999; Knaff et al. 2005; DeMaria 2009; Kaplan et al. 2010). Paterson et al. (2005) and Wang et al. (2015) statistically showed that 200–850-hPa wind shear greater than $\sim 10 \text{ m s}^{-1}$ tends to contribute to weakening. Explanations of the negative influence of shear on intensity include i) ventilation of a TC warm core and high PV caused by relatively strong upper level environmental wind (Frank and Ritchie 2001), ii) strong downdrafts bring mid-level low θ_e air into the boundary layer, leading to the decrease in the work done by the Carnot cycle during the life cycle of air parcels (Riemer et al. 2010), and iii) intrusion of mid-level dry air into the

eyewall (Tang and Emanuel 2010). In addition, effect of shear on intensity change is not dependent only on its magnitude, but also on vortex strength (DeMaria 1996; Riemer et al. 2013; Rios-Berrios and Torn 2017).

However, some studies have shown that strong shear can contribute to intensification through the occurrence of vigorous deep convections inside the radius of maximum wind (RMW) on the downshear side (Molinari et al. 2006; Musgrave et al. 2008; Reasor et al. 2009; Molinari and Vollaro 2010; Nguyen and Molinari 2012). Molinari and Vollaro (2010) and Nguyen and Molinari (2012) discussed that the asymmetric intensification can occur through the axisymmetric response to azimuthal mean diabatic heating inside the RMW, based on theoretical studies of Nolan and Grasso (2003), Nolan et al. (2007), Shapiro and Willoughby (1982) and Pendergrass and Willoughby (2009). Meanwhile, Reasor et al. (2009) showed that Hurricane Guillermo (1997) intensified rapidly with asymmetric strong convections downshear left under a shear of $\sim 7\text{-}8\text{ m s}^{-1}$ and emphasized the nonnegligible contribution of the eddy momentum fluxes. Although shear sometimes makes a positive impact on intensification, how a relatively strong shear and associated asymmetric deep convection can contribute to intensity changes has not been fully understood yet.

Even under a same moderate shear environment, there exist intensifying TCs and non-intensifying TCs. The difference between intensifying TCs and non-intensifying TCs has been investigated. Rogers et al. (2016) examined the structural change of Hurricane Edouard (2014) in terms of azimuthal distribution of convection and showed that Edouard had deep vigorous convections in the upshear-left quadrant during intensification, whereas there was little deep convection there during its maturity. Rios-Berrios and Torn (2017) demonstrated through a composite analysis of intensifying TCs and non-intensifying TCs under moderate shear conditions ($4.5\text{--}11.0\text{ m s}^{-1}$) that midlevel relative humidity and surface latent heat fluxes are larger for intensifiers, in particular, on the upshear side than for non-intensifiers. Intensifiers also have stronger tangential wind, and have stronger midlevel inflow downshear and stronger midlevel outflow upshear. However, we lack sufficient knowledge of what causes the difference in the inner-core structure under shear conditions. One of the reasons for this may result from insufficient observational studies so far, because those processes occur over the ocean, where even aircraft reconnaissance cannot necessarily observe them timely.

1.4. Current status of tropical cyclone intensity forecast

The skill of tropical cyclone (TC) intensity forecast has been steadily improved over the past two decades (DeMaria et al. 2014), though the improvement rate is slower than that of TC track forecast. There are some reasons for the slower rate; dynamical and thermodynamical processes of intensity change of TCs are so complicated, because of various factors involved in, that they have not been fully understood, and current numerical models do not necessarily reproduce TC structures and intensity changes. In such situations, the advent of skillful statistical dynamical model has contributed to the improvement of TC intensity forecast. The Statistical Hurricane Intensity Prediction Scheme (SHIPS, DeMaria and Kaplan 1994, 1999; DeMaria et al. 2005) is one of the statistical dynamical models used for intensity forecast.

The SHIPS is a multiple regression equation that predicts changes in intensity. Explanatory variables (hereafter, predictors) used in the regression model include climatology and persistency associated with initial intensity and intensity change in the past 12 h, environmental conditions such as vertical wind shear and SSTs, which are computed along the forecast TC track, and infrared (IR) satellite information around the TC at the initial forecast time. The SHIPS model provides the information of the degree to which each predictor contributes to intensity change. The number of predictors has been increased, and the skill of forecast has been steadily improved. Currently, SHIPS is one of the most skillful intensity forecast models in the world. Because of these reasons, SHIPS is widely used in operational centers around the world as the most reliable guidance for TC intensity forecast (e.g., Sampson and Knaff 2014).

In addition to SHIPS, forecast skill of the Hurricane Weather Research and Forecasting (HWRF) model has recently been improved since operationalized in 2007. The HWRF model is an atmosphere-ocean coupled regional numerical model focused on TCs on the basis of Weather Research and Forecasting (WRF) model with triple nest (18, 6 and 2 km) mainly developed by the Environmental Modeling Center (EMC), the National Centers for Environmental Prediction (NCEP) (Tallapragada et al. 2014; NCEP EMC 2017). Various enhancements including vortex initialization, data assimilation, and physics have been made to the HWRF model. Forecast is run for all TCs around the world up to 5 days ahead. Model output is plotted and opened on the web site in real time. However, there still remain issues in

HWRF. The HWRF model is still not good at predicting RI, tends to overforecast intensity for weak TCs, and sometimes gives rise to vortex spindown unnaturally. Recently, the improvement rate has been slowed down.

In the western North Pacific (WNP) basin, the Statistical Typhoon Intensity Prediction Scheme (STIPS, Knaff et al. 2005), which is similar to SHIPS, was developed and was used at the Joint Typhoon Warning Center (JTWC). Recently, it was replaced with SHIPS at the JTWC (Schumacher 2013). Meanwhile, the Meteorological Research Institute (MRI), the Japan Meteorological Agency (JMA) has recently set up SHIPS that predicts P_{min} as well as maximum wind speed (V_{max}) of TCs in the WNP basin using output from the JMA global spectral model (GSM). The forecast results confirmed that the accuracy of SHIPS with the GSM output was 20–25 % better than that of the Statistical Hurricane Intensity Forecast (SHIFOR; Jarvinen and Neumann 1979; Knaff et al. 2003), which is a statistical model using climatology and persistency and is often used as a benchmark for the evaluation of intensity forecast skill. As of 2017, SHIPS is in an experimental use in the Regional Specialized Meteorological Center (RSMC) Tokyo.

1.5. Purpose of this study

In this study, we stick to high-temporal observations of radars and satellites. The purpose of this study is

- i) to construct an intensity estimation system by using Doppler radar data and to evaluate the accuracy and utility of the method,
- ii) to examine the statistical relationship between TC structure and intensity change, and to investigate intensity change processes in two TCs by using high-temporal observations, and
- iii) to examine a possibility to further improve the skill of TC intensity forecasts.

In Chapter 2, we describe the DR method and evaluate estimate results. The development of an intensity estimate system, which provides the TC wind field and P_{min} , enables us to investigate dramatic structural and intensity changes of real TCs from Chapter 4 to 5. In Chapter 3, we examine the statistical relationship between axisymmetry (the degree of axial symmetry) derived from hourly satellite-based rainfall estimates and future intensity change. In Chapter 4, we conduct a case study of a TC that intensified in the presence of relatively strong shear, and in Chapter 5 we perform another case study of a TC that experienced RI just after an ERC. These TCs are worth examining in detail because they underwent large intensity changes with dramatic structural changes within several hours. Such characteristics have been rarely documented so far. We focus on key processes that lead to intensification. In Chapter 6, we examine the possibility of further improvement in TC intensity forecast based on the findings in this study. Finally, in Chapter 7, we summarize our results.

Chapter 2: Intensity estimation using Doppler radar observations

The conventional intensity estimation methods cannot capture rapid intensity changes. To capture them, we developed an intensity estimation system at 5-min intervals by using Doppler radar data.

Many strong TCs approach and make landfall in Japan. In particular, many TCs approach southwestern Japan, including the Okinawa Islands, where there is no topography effect on the TC structure. Therefore, TCs approaching this region are ideally suited for ground-based Velocity Track Display (GBVTD) retrievals and for studying intensity change. The JMA upgraded all radars in its observation network to Doppler radars between 2006 and 2013, and the new Doppler radars have collected data on many TCs since their installation.

The goal of this chapter is to estimate the central pressure, P_{min} , of TCs by using the accumulated Doppler radar data and to evaluate the accuracy and utility of the Doppler radar (DR) method. Before the estimation of TC intensities, we perform a preliminary experiment with pseudo-Doppler velocity data obtained by numerical simulation to confirm that the method can reasonably estimate P_{min} .

2.1. Data, cases, and methodology

a. Data

Doppler velocity, V_D , data observed by JMA C-band operational Doppler radars are used. Figure 2.1 shows the radar locations used and the observational range of 2-km, constant-altitude plane position indicator (CAPPI) data (~ 200 km) for each location. The Doppler observation parameters of the Okinawa radar, which is representative of the JMA radars, are listed in Table 2.1. Both high and low dual-pulse repetition frequency (dual-PRF) data for the lowest elevation plane position indicator (PPI) are used in order to see out to ~ 200 -km range at the 2-km altitude. Before 2009, the radars observed V_D at 10-min intervals, and since 2009 the observation interval has been 5 min. In this study, dealiasing of V_D by the Hybrid Multi-PRI (HMP) method (Yamauchi et al. 2006) and by a correction method that assumes there is a wavenumber-1 V_D pattern around a radar location

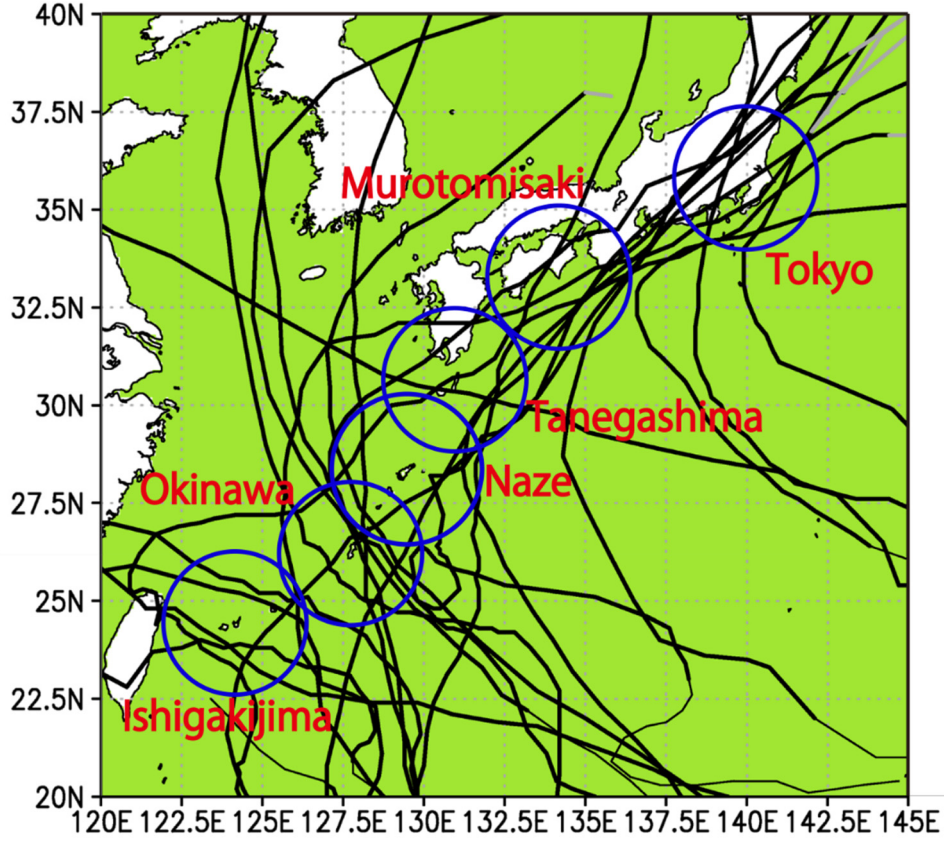


Fig. 2.1: Locations of the JMA operational Doppler radars and tracks of the TCs used in this study. The circles show the observation ranges of all radars (~ 200 km) for CAPPI data at 2-km altitude. Thick lines indicate TCs with maximum sustained (10-min average) surface winds of greater than 17 m s^{-1} (i.e., tropical storms), thin lines indicate TCs with maximum sustained surface winds of 17 m s^{-1} or less (i.e., tropical depressions), and gray lines indicate extratropical cyclones. The data are the JMA best track data.

Table 2.1: Doppler observation parameters of the Okinawa operational C-band radar.

	Lowest elevation angle	Other elevation angles
	0.4°	$1.8, 3.3, 5.0, 7.0, 10.0, 14.0, 19.0, 25.0^\circ$
Frequency	5350 MHz	
Pulse repetition frequency	940/752 Hz, 600/480 Hz	940/752 Hz
Unambiguous velocity	$\pm 52.7 \text{ m s}^{-1}$, $\pm 33.6 \text{ m s}^{-1}$	$\pm 52.7 \text{ m s}^{-1}$
Unambiguous range	160 km, 250 km	160 km
Pulse length	1 μs	
Range resolution	250 m	
Rotation rate	4 rpm	

influenced by TC circulation is performed automatically. Additionally, noise caused by dealiasing failure and sea clutter is removed from the data automatically by various quality control (QC) procedures. Although problems associated with the dealiasing correction of V_D can greatly affect the accuracy of TC intensity estimates, describing how to cope with these problems is beyond the scope of this study. Therefore, we examine the accuracy of the estimated P_{min} based on the premise that the Doppler velocity data have been dealiased and that most noise has been removed.

In addition to the V_D data, sea level pressure (SLP) data observed at weather stations at 10-min intervals are used. To verify our results, best track data and Dvorak P_{min} data from the Regional Specialized Meteorological Center (RSMC) Tokyo are used. The best track data from the RSMC Tokyo are based on both Dvorak P_{min} data and observations. These Dvorak P_{min} data are obtained by using the Dvorak technique to obtain current intensity (CI) numbers, which are then converted into P_{min} values by referring to the conversion table of Koba et al. (1990). When the radar data are available at 5-min intervals, all other data are interpolated linearly to 5-min intervals.

b. Cases

We use two criteria to select TC cases for estimation: the TC center has to be located within the 2-km altitude range (~ 200 km) of a Doppler radar, and we have to be able to subjectively identify the TC center from the V_D pattern (an indication that, in general, radar coverage is sufficient). The circulation of a TC is generally depicted by a dipole pattern of positive (away from the radar) and negative (toward the radar) V_D across the TC center, with a wavenumber-1 velocity pattern surrounding the radar location. We select 22 including TCs that struck southern Japan and strong TCs that passed over the Okinawa Islands (Fig. 2.1, Table 2.2). If the same TC is observed by two or more radars, then the observations of each radar are treated as a case, and the cases are distinguished by appending the letters A, B, or C to the TC name. Therefore, in total we estimate the intensity of 28 cases. The estimated duration of each case is about 9 h on average. Although this number of TC cases may not be a large enough sample size for statistical verification, it enables us to test the DR method on a variety of TCs.

Table 2.2: Cases used for the intensity estimation.

Case (Name)	Radar Site	Estimation Period [UTC]	Duration [hour]
T0607 (Maria)	Tokyo	0000 09 Aug – 0300 09 Aug 2006	3 h
T0709 (Fitow)	Tokyo	1600 06 Sep – 2300 06 Sep 2007	7 h
T0813 (Sinlaku)	Tanegashima	0200 18 Sep – 1500 18 Sep 2008	13 h
T0911 (Krovanh)	Tokyo	0600 31 Aug – 1000 31 Aug 2009	4 h
T1007 (Kompasu)	Okinawa	0200 31 Aug – 1300 31 Aug 2010	11 h
T1011 (Fanapi)	Ishigakijima	0500 18 Sep – 1900 18 Sep 2010	14 h
T1109 (Muifa)	Okinawa	1800 04 Aug – 1200 05 Aug 2011	18 h
T1115 (Roke)	Murotomisaki	2300 20 Sep – 0100 21 Sep 2011	2 h
T1204 (Guchol)	Okinawa	1000 18 Jun – 1500 18 Jun 2012	5 h
T1210 (Damrey)	Tanegashima	0100 01 Aug – 0900 01 Aug 2012	8 h
T1215 (Bolaven)	Okinawa	0400 26 Aug – 1700 26 Aug 2012	13 h
T1216 (Sanba)	Okinawa	1300 15 Sep – 0300 16 Sep 2012	14 h
T1217 (Jelawat)	Okinawa	1950 28 Sep – 0645 29 Sep 2012	10 h 55 min
T1307 (Soulik)	Ishigakijima	0700 12 Jul – 1600 12 Jul 2013	9 h
T1312 (Trami)	Ishigakijima	1800 20 Aug – 0700 21 Aug 2013	13 h
T1318 (Man-yi)	Murotomisaki	1300 15 Sep – 1900 15 Sep 2013	6 h
T1323 (Fitow)	Ishigakijima	1300 05 Oct – 0200 06 Oct 2013	13 h
T1324A (Danas)	Okinawa	0200 07 Oct – 1000 07 Oct 2013	8 h
T1324B (Danas)	Naze	0500 07 Oct – 1200 07 Oct 2013	7 h
T1408A (Neoguri)	Ishigakijima	1900 07 Jul – 0110 08 Jul 2014	6 h 10 min
T1408B (Neoguri)	Okinawa	0100 08 Jul – 0410 08 Jul 2014	3 h 10 min
T1411A (Halong)	Naze	0200 08 Aug – 1300 08 Aug 2014	11 h
T1411B (Halong)	Tanegashima	1500 08 Aug – 0500 09 Aug 2014	14 h
T1411C (Halong)	Murotomisaki	1000 09 Aug – 2345 09 Aug 2014	13 h 45 min
T1418A (Phanfone)	Naze	1700 04 Oct – 0400 05 Oct 2014	11 h
T1418B (Phanfone)	Tanegashima	0300 05 Oct – 1100 05 Oct 2014	8 h
T1418C (Phanfone)	Murotomisaki	1330 05 Oct – 1930 05 Oct 2014	6 h
T1419 (Vongfong)	Okinawa	0300 11 Oct – 1200 11 Oct 2014	9 h

c. Methodology

The primary procedures used for the DR intensity estimates are based on Lee et al. (1999, 2000), Lee and Marks (2000), and Bell and Lee (2012). There are six steps in the procedures (Fig. 2.2). After the dealiasing procedure and the removal of sea clutter and other noise (step 1), PPI data less than the elevation angle of 10.0° are interpolated to CAPPI data (step 2). After this step, the 2-km CAPPI data are used because at that altitude radar coverage for V_D is the most extensive over the longest period, and the TC wind fields are generally approximately in gradient wind balance (Willoughby 1990; Bell and Montgomery 2008). Note that for radar ranges greater than ~ 130 km, V_D from the lowest elevation PPI scan whose height is between 2-km and 4-km is just projected onto the 2-km CAPPI. Because vertical profiles of wind speed for TCs show a general increase from 3-km down to below 1-km (e.g. Franklin et al. 2003), there is a possibility that this CAPPI method contributes to positively biased P_{min} estimates when the TC center is far from the radar. Then, by using the GBVTD-simplex center-finding algorithm (Lee and Marks 2000; Bell and Lee 2012), where a radius of maximum wind (RMW) and its possible range are subjectively given, TC center positions at 5-min intervals are detected from the first-guess center positions interpolated linearly to 5-min intervals from center positions subjectively determined at 1-h intervals while viewing radar reflectivity imagery (step 3). Then, using the detected centers, the 2-km CAPPI data are interpolated to TC cylindrical coordinates with an azimuthal resolution of $\sim 0.7^\circ$ and a radial resolution of 500 m (step 4). After the retrieval of \bar{v} by the GBVTD technique (step 5), the \bar{v} data are substituted into the gradient wind equation,

$$\bar{\rho}_s \left(\frac{\bar{v}^2}{r} + f\bar{v} \right) = \frac{\partial \bar{p}_s}{\partial r}, \quad (2.1)$$

where r is the radius from the TC center, f is the Coriolis parameter corresponding to the latitude of each radar location, \bar{p}_s is the axisymmetric SLP, and $\bar{\rho}_s$ is the environmental air density at sea level. The value of $\bar{\rho}_s$ is assumed as 1.15 kg m^{-3} , which corresponds to the density in a tropical environment with a virtual temperature of 30.0°C at 1000 hPa. At the second decimal place, this value may be a little higher than that in the TC inner environment, which would make the radial SLP gradient calculated from the gradient wind balance with Eq. (2.1) slightly steeper than the actual gradient. When one or more SLP observations are available within radii of the deduced SLP gradient, the axisymmetric SLP deficits of the TC are obtained by integrating the radial SLP gradient (the right-hand side of Eq. (2.1)) inward

DR Intensity Estimate Procedures

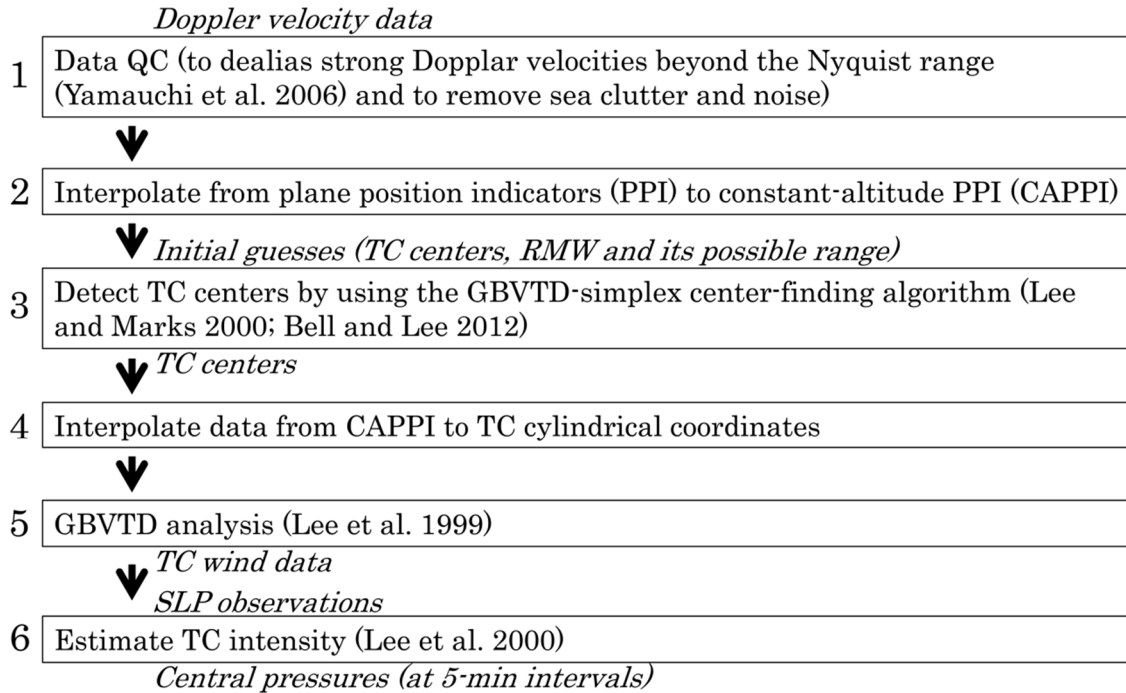


Fig. 2.2: The procedures used for the Doppler radar intensity estimation. Input and output data for each step are indicated in italics. Before (since) 2009, the estimate is performed at 10-min (5-min) intervals.

from each observation point toward the center of the TC (Lee et al. 2000). Finally, P_{min} is estimated by adding each SLP deficit to the corresponding SLP observation (step 6). When a SLP observation point is located within 15 km outside the GBVTD outer-most ring, P_{min} is estimated by extrapolating the SLP gradient over the distance from the observation point. As many P_{min} values are estimated as there are observations. Note that the DR method assumes that asymmetric components of the pressure distribution have little impact on the estimation results.

To stably estimate P_{min} , we modify the original DR method in four primary ways. First, the GBVTD-simplex center-finding method is modified by restricting the center-finding area to within a 5-km radius of the first guess point and confining the first-guess RMW to that associated with the primary eyewall (hereafter, P-RMW). These modifications enable a reasonable center to be identified around the guess point at all times; if there is no limitation placed on the simplex, it is difficult to detect a reasonable center for a dissipating TC or a TC with poor radar coverage, as described by Murillo et al. (2011). In addition, the latter modification enables more accurate \bar{v} to be

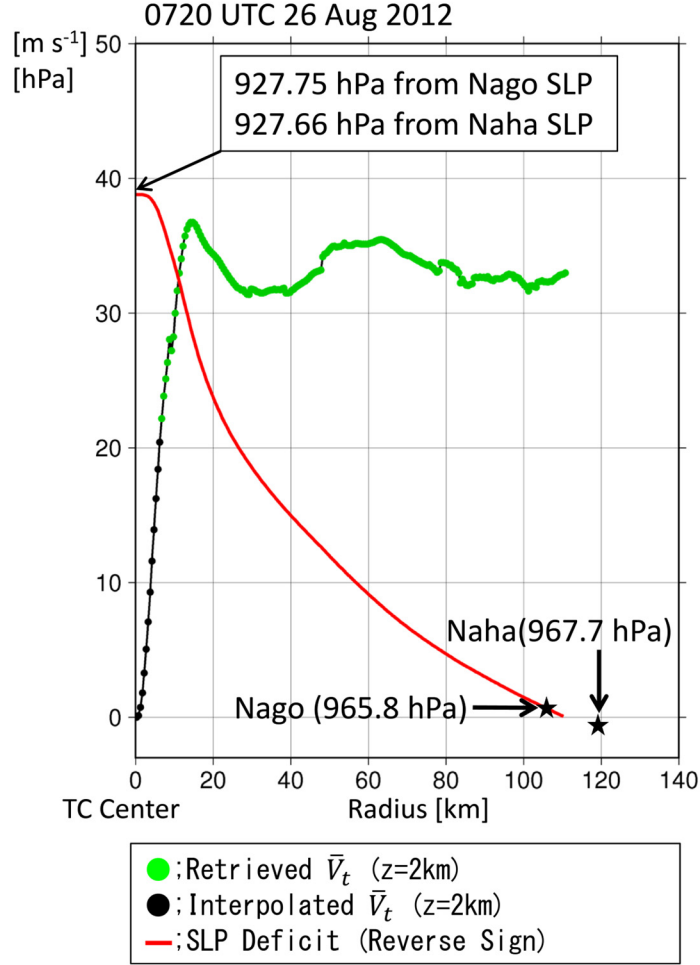


Fig. 2.3: Radial profiles of retrieved \bar{V}_t , interpolated \bar{V}_t , and SLP anomalies (with the sign reversed) for T1215. SLPs observed at Nago and Naha weather stations, which are used for the P_{min} estimation, are shown along with the estimated P_{min} . P_{min} from Naha is estimated by extrapolating the SLP gradient over the distance from Naha.

retrieved around the P-RMW. This is important because the SLP gradient calculated from Eq. (2.1) is sensitive to the magnitude of \bar{v} around the P-RMW. Second, we fill in missing values of \bar{v} by using a spline function with the assumption that $\bar{v} = 0 \text{ m s}^{-1}$ at the TC center. However, when the spline function produces a negative \bar{v} or an artificial local \bar{v} maximum in the eye region, a quadratic function instead of the spline function is applied. In this way, the radial distribution of \bar{v} within the eye region is deduced (Fig. 2.3). Third, the TC translational speed is used as a proxy for $V_{M\perp}$ in the GBVTD technique. One weakness of the GBVTD technique is that, in principle, it cannot retrieve the component of the mean environmental wind perpendicular to a line connecting the TC center and the radar location (hereafter, the cross-beam component of the mean environmental wind, $V_{M\perp}$). Instead, $V_{M\perp}$ is aliased into \bar{v} , which leads to the decrease of the retrieval accuracy of \bar{v} at

outer TC radii (Lee et al. 1999; Harasti et al. 2004; Chen et al. 2013). To resolve this aliasing problem, $V_{M\perp}$ must be obtained from an independent source. The Hurricane Volume Velocity Processing (HVVP) technique, which provides $V_{M\perp}$ by using a single Doppler radar (Harasti 2014; Chen et al. 2013), is one possibility, but the results of our preliminary examination showed that the use of the HVVP technique is not suitable for stable provision of $V_{M\perp}$ owing to occasional poor radar coverage (not shown). Hence, we use the cross-beam component of the TC translational speed as a proxy for $V_{M\perp}$ to resolve the aliasing problem. The effect of using this proxy is described in subsections 2.2b and 2.3a. Fourth, two QC procedures into the GBVTD retrieval are introduced:

- 1) Retrieved \bar{v} are rejected when associated asymmetric tangential winds with an amplitude of more than 25 m s^{-1} are retrieved, because such a large asymmetry is, in general, unlikely for TCs and likely to be a retrieval failure due to, for example, noise contamination.
- 2) To assess the accuracy of the GBVTD-retrieved winds, the root mean square difference (RMSD) between the V_D resampled from the GBVTD-retrieved winds and the observed V_D is computed at each radius, following Zhao et al. (2012). If the RMSD is more than 8 m s^{-1} inside the P-RMW and the TC has a maximum absolute V_D of more than 60 m s^{-1} with a single, closed eyewall, the wind retrieval accuracy is extremely poor, and the corresponding \bar{v} are rejected.

There are other limitations inherent in the GBVTD technique. First, the GBVTD technique has a weakness that the wavenumber-1 tangential wind can bias \bar{v} via the nonlinear azimuthal coordinate system employed by the technique, particularly when the radar is around the radius of the GBVTD analysis ring (see in Fig.13a of Lee et al. 1999). This can lead to poor P_{min} estimations especially when the distance between the TC center and the weather station whose sea level pressure is used as an anchor of pressure measurement is close to that from the radar to the TC center. Second, the GBVTD-simplex center-finding algorithm cannot detect centers when the radar is inside the P-RMW. In this case, we use the first-guess center positions as centers although in most of the cases the GBVTD technique also fails to retrieve \bar{v} because of few scatterers in the eye region. In this study, T0813 and T1217 fall under this situation. Third, the GBVTD technique assumes that radial winds are much weaker than tangential winds. When this assumption is violated, the retrieval accuracy of \bar{v} decreases.

2.2. Simulation experiment

In this section, we describe the preliminary experiment and present its results. To assess the accuracy with which the DR method can estimate P_{min} of TCs of known intensity, we use data obtained by numerical simulation. In particular, we verify two points of the procedures. First, we will confirm whether the use of 2-km \bar{v} and surface air density in the gradient wind equation yields reasonable P_{min} estimates. Second, we will confirm whether retrieval accuracy is improved by using TC motion as a proxy for the mean wind to correct an inherent bias in GBVTD-retrieved \bar{v} . Here, we describe the settings of the simulation and present the estimation verification results.

a. Simulation settings

We perform simulations of Typhoon Bolaven (2012), Typhoon Neoguri (2014), and Typhoon Vongfong (2014) with the JMA Non-Hydrostatic Model (JMA-NHM) (Saito et al. 2006, 2007). The physical parameterizations are mostly the same as those used by JMA's operational mesoscale model (JMA 2017b). The horizontal grid spacing of the simulation is 2.5 km, and results are output at 5-min intervals.

For simplicity, we construct pseudo- V_D data at 2-km altitude corresponding to each radar location from the simulated winds at 2-km altitude without considering the effects of radar-beam width and zenith angle. We regard only grid points with a non-zero mixing ratio of rain, snow, and graupel at 1-km altitude as the grid points where V_D at 2-km altitudes are observed, because a check for the presence of non-zero mixing ratios at 2-km altitude do not provide a sufficient V_D distribution. As in the real TCs, there are no pseudo- V_D observations around the TC center. Although the grid of the simulation is coarser than the radar resolution (Table 2.1), this is unlikely to be a serious problem for the results because the resolution of the radar data is reduced through the averaging and interpolation procedures. The tracks of the simulated TCs deviate from the observed tracks, so the simulated tracks are adjusted by displacing them parallel to the observed tracks. In addition, to increase the number of estimated cases, we prepare two virtual cases by parallel displacement of the simulated data. Because the simulated TCs are over the ocean, where there is no topography effect, this displacement has no disadvantage for the experiment. In total, we prepare six simulated TCs in this experiment (Fig. 2.4, Table 2.3).

Simulated Typhoon Bolaven (2012) has a RMW of ~ 46 km, about 3

times the observed RMW, and a typical TC structure. The simulated track is almost the same as the observed track, but the TC location is approximately 2 h ahead of the observation. The intensity of the simulated Bolaven is estimated for two cases, along the actual track of the simulated TC (S1215A) and along a second track displaced southwestward from S1215A (S1215B, blue line in Fig. 2.4). Simulated Typhoon Neoguri (2014) has a RMW of ~ 60 km, which is larger than the observed RMW of 35-40 km. Because the simulated track of Neoguri deviates southwestward from the observed track, the location of the simulated Neoguri is displaced northeastward (0.4415° east, 0.5379° north). The intensity of the simulated Neoguri is estimated for both T1408A (observed from the Ishigakijima radar, S1408A) and T1408B (observed from the Okinawa radar, S1408B). In the S1408A case, the coverage of the Ishigakijima radar is limited to the western part of Neoguri, and in the S1408B case, the coverage of the Okinawa radar is limited to its eastern part. In addition, we prepare a third track for the simulated Neoguri displaced northeastward (1.0415° east and 0.5379° north) from the simulated track; this S1408C case (yellow line in Fig. 2.4) has better coverage from the Okinawa radar than that of the S1408B case. Simulated Typhoon Vongfong (2014) (S1419) has a disappearing eyewall. Because such TCs frequently approach Japan, it is important to verify how accurately the DR method can estimate P_{min} of such TCs. In this case, we are not concerned about how well the numerical simulation can reproduce the observed TC structures, including their vertical structures.

For simplicity, we do not address the problem of the accuracy of the center-finding algorithm here. So, this experiment starts from step 4 in Fig. 2.2. TC centers used by the GBVTD technique are centroid centers of the pressure field calculated by applying a 1-2-1 smoothing filter 500 times (Nolan et al. 2009). Note that in this experiment, the true P_{min} is not the SLP at the centroid center but the lowest SLP within the eye region in the simulated TCs. We extract pseudo-SLP observations at points corresponding to surface weather stations from each simulation.

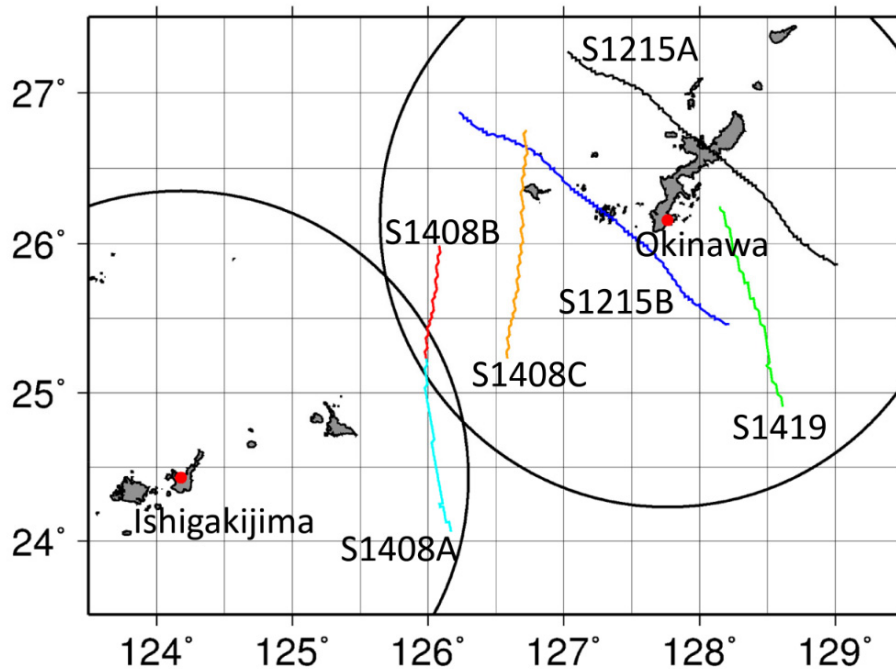


Fig. 2.4: Tracks of the six simulated TCs used in the preliminary experiment. Black circles indicate the ranges, ~ 200 km, of the Ishigakijima and Okinawa radars (red dots). Each color represents one simulated case.

Table 2.3: The six TCs used in the simulation experiment.

Name (Radar Site)	Outline	Model Initial Time [UTC]	Estimation Period [UTC]
S1215A (Okinawa)	A simulation of T1215	0600 25 Aug 2012	0200 26 Aug – 1500 26 Aug
S1215B (Okinawa)	The same as S1215A except the track is displaced southwestward (0.8° west and 0.4° south) from S1215A	0600 25 Aug 2012	0200 26 Aug – 1500 26 Aug
S1408A (Ishigakijima)	A simulation of T1408. The track is displaced northeastward (0.4415° east and 0.5379° north) from the simulated track	1200 06 Jul 2014	1900 07 Jul – 0110 08 Jul
S1408B (Okinawa)	The same as S1408A except the estimation period	1200 06 Jul 2014	0100 08 Jul – 0410 08 Jul
S1408C (Okinawa)	A simulation of T1408. The track is displaced northeastward (1.0415° east and 0.5379° north) from the simulated track	1200 06 Jul 2014	0100 08 Jul – 0700 08 Jul
S1419 (Okinawa)	A simulation of T1419. The track is displaced northward (0.0111° east and 0.1497° north) from the simulated track	0000 11 Oct 2014	0300 11 Oct – 1200 11 Oct

b. Results and verification

We perform P_{min} estimates using pseudo- V_D at 5-min intervals. Table 2.4 shows the estimates in the preliminary experiment compared with the true values in the simulated TCs. The RMSE of the estimated P_{min} relative to the true P_{min} is 2.84 hPa, and the bias is -0.77 hPa, although individual results can have a large effect because of the small number of TCs included. The incorporation of the cross-beam component of TC motion as a proxy for $V_{M\perp}$ helps to improve the biases of the TCs. For example, the bias of S1408B is improved by ~ 5 hPa, from -8.54 hPa to -3.55 hPa, though the negative bias is not eliminated. Figure 2.5a shows the axisymmetric radial distributions of the retrieved and true \bar{v} in S1408B averaged over the estimation period. The difference between the retrieved and true \bar{v} is quite small on average, except near the TC center, where the retrieved \bar{v} are interpolated by a spline function, resulting in slightly weak estimates, but the difference has little effect on the SLP field (not shown). Figure 2.5b shows the axisymmetric radial distributions of SLPs in S1408B averaged over the estimation period. The differences between the true and deduced SLPs show that at outer radii of more than 50 km, the pressure gradient is slightly steeper than the true gradient. In contrast, the pressure gradient is slightly shallower than the true gradient within the RMW. On the whole, a negative bias is evident. In S1419, the effect of the spline interpolation within the eye region leads to a positive P_{min} bias (not shown). The trends of the pressure distributions are similar in the other cases. Thus, the results of the preliminary experiment confirm that the DR method using V_D data at 2-km altitude and the cross-beam component of TC motion as a proxy for $V_{M\perp}$ can reasonably reproduce P_{min} , as reported by Harasti et al. (2004).

Table 2.4: Estimation accuracy of the six TCs in the simulation experiment. The P-RMW was determined from the retrieved \bar{V}_t after step 5 in Fig. 2.2 within a possible range of the subjectively determined P-RMW. The P-RMW values and central pressures were averaged over the estimation periods shown in Table 2.3.

	N	RMSE [hPa]	Bias [hPa]	Corr elati on	P-RMW (z=2 km) [km]	Central Pressure [hPa]	
						Estima ted	True
Overall with $V_{M\perp}$	931	2.84	-0.77	0.95	-	-	-
Overall without $V_{M\perp}$	934	4.93	-0.76	0.90	-	-	-
S1215A with $V_{M\perp}$ (without $V_{M\perp}$)	251 (253)	1.65 (2.55)	-0.25 (1.78)	-	46.00	933.61	933.86
S1215B with $V_{M\perp}$ (without $V_{M\perp}$)	230 (231)	2.13 (2.84)	-0.82 (-1.78)	-	45.54	932.55	933.37
S1408A with $V_{M\perp}$ (without $V_{M\perp}$)	134 (134)	3.06 (3.32)	-1.50 (2.14)	-	62.34	929.46	930.97
S1408B with $V_{M\perp}$ (without $V_{M\perp}$)	78 (78)	4.24 (9.32)	-3.55 (-8.54)	-	61.33	924.96	928.51
S1408C with $V_{M\perp}$ (without $V_{M\perp}$)	146 (146)	2.95 (7.24)	-1.96 (-5.70)	-	60.75	926.22	928.18
S1419 with $V_{M\perp}$ (without $V_{M\perp}$)	92 (92)	4.47 (5.94)	3.28 (5.06)	-	62.57	950.10	946.81

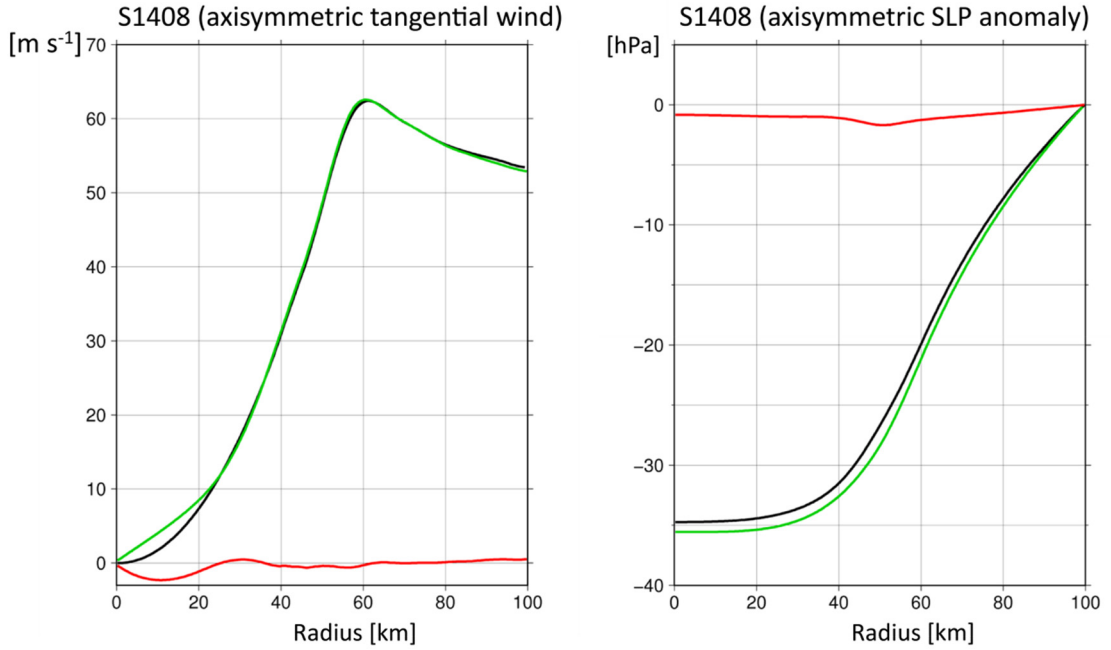


Fig. 2.5: Radial distributions of (a) axisymmetric tangential winds, \bar{V}_t , and (b) axisymmetric SLP anomalies of S1408B averaged over the estimation period. In (a) the black line is the true \bar{V}_t , the green line is the retrieved \bar{V}_t , and the red line is the difference between them. In (b) the black line represents the true SLP anomalies, the green line the deduced SLP anomalies, and the red line the difference between them.

2.3. Estimation results

In this section, we present the estimation results for the real TC cases. We first describe the overall statistical verification results; then we classify the TC cases into four groups according to the estimation results and describe the characteristics of the individual cases in each of the four groups in detail.

a. Overall statistical verification

A scatter diagram of the estimated and best-track P_{min} in the 28 cases shows that, despite large errors in the estimated P_{min} , most data points are concentrated in the vicinity of the 1:1 line (Fig. 2.6). The RMSE, bias, and correlation coefficient between the estimated and best track P_{min} are 8.37 hPa, 1.51 hPa, and 0.87, respectively. The P_{min} estimate error is within ± 5 hPa (± 10 hPa) in 60.3% (84.1%) of all estimates. In contrast, for the best track P_{min} of 960 hPa, the estimated P_{min} values are distributed from 975 hPa to 908 hPa. Most of these large differences are attributed to T1007, which is discussed in the next subsection.

The use of the cross-beam component of translational speed as a proxy for $V_{M\perp}$ in the GBVTD technique is remarkably effective. The P_{min} values estimated using the $V_{M\perp}$ proxy have RMSEs smaller than 94% and positive biases smaller than 55% of those of the P_{min} values estimated without using the $V_{M\perp}$ proxy (Table 2.5). Although for most of the TCs, biases are positive (not shown), incorporation of $V_{M\perp}$ in the GBVTD technique generally reduces this positive bias. This result is consistent with the results of the preliminary simulation experiment (section 2.2).

Therefore, P_{min} can be reasonably estimated from V_D at 2-km altitude by using TC motion as a proxy for $V_{M\perp}$. Differences in the accuracy of the estimates under several specific conditions are discussed in subsection 2.4b.

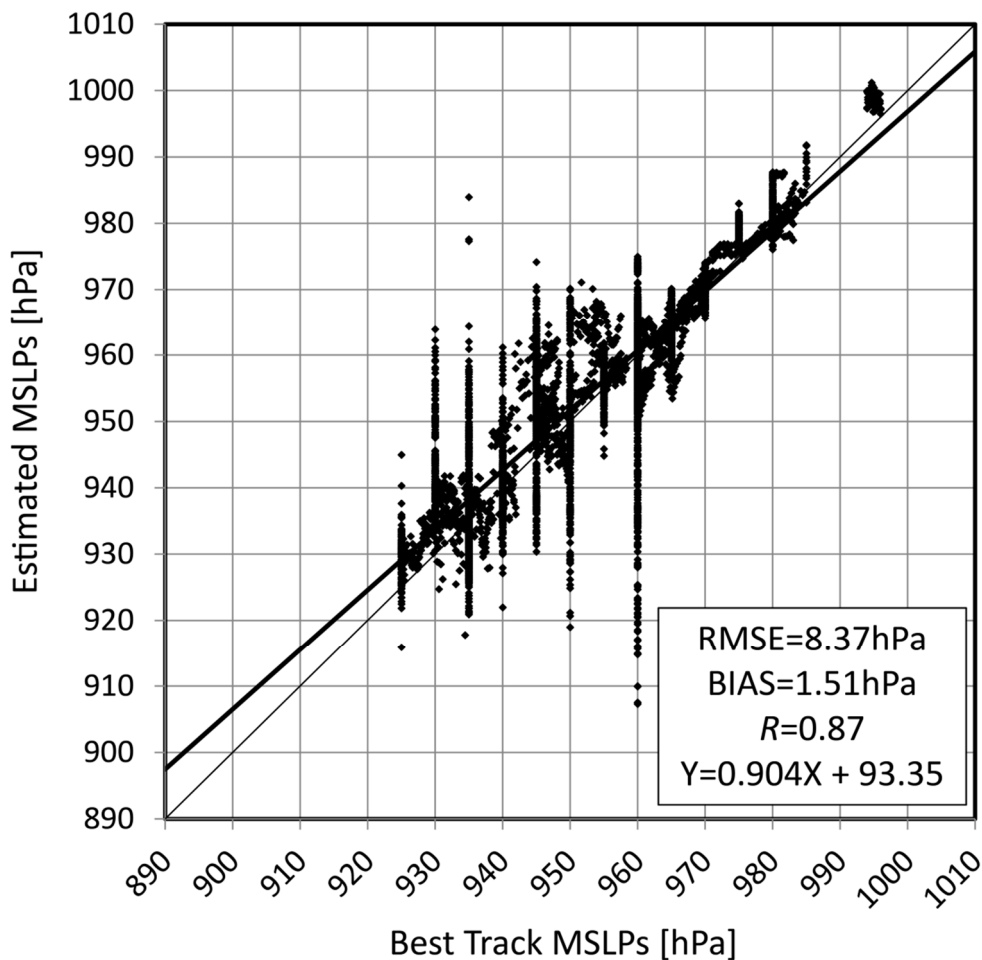


Fig. 2.6: Scatter diagram comparing the estimated P_{min} values with the best track P_{min} values. The corresponding RMSE, bias, and correlation coefficient, R , are also shown.

Table 2.5: Overall accuracy of the DR intensity estimates for the 28 TC cases. The results are shown both with and without incorporation of $V_{M\perp}$. The overall accuracy excluding T1007 is given in parentheses.

	N	RMSE [hPa]	Bias [hPa]	Correlation
Overall with $V_{M\perp}$ (excluding T1007)	5574 (5317)	8.37 (7.13)	1.51 (2.41)	0.87 (0.91)
Overall without $V_{M\perp}$ (excluding T1007)	5604 (5347)	8.94 (8.14)	2.77 (3.57)	0.86 (0.90)

b. Classification of the individual cases

We group the P_{min} estimates of the 28 cases into the following four groups: excellent P_{min} estimates; large differences between the DR and best track P_{min} values; a consistent positive bias relative to the best track; and erratic fluctuations.

We define an estimate as excellent if the RMSE is less than 4 hPa and the bias is within ± 4 hPa. Ten cases meet these criteria: T0709, T0813, T1115, T1215, T1307, T1312, T1323, T1408A, T1408B, and T1411B. We show the characteristics of T1312 in Fig. 2.7 as an example of an excellent estimate. The estimated P_{min} and its trend correlated well with that of the best track (Fig. 2.7a). Figures 2.7b and c show the Doppler velocity field and radial distribution of the retrieved axisymmetric tangential wind and axisymmetric SLP deficit at 2225 UTC on 20 August 2013. Although radar coverage is not very dense, the P_{min} values estimated from the SLPs at both Miyakojima (49.3 km from the TC center) and Ishigakijima (107.5 km from the TC center) are almost the same as the best track P_{min} at that time. The accuracies of all 10 cases are listed in Table 2.6. One of our most important findings here is that the DR method can provide almost the same P_{min} as the best track at 5-min intervals, whereas the accuracy of estimates made by the Dvorak method is not necessarily good.

For T1007, large differences are found between the DR and best track P_{min} values (Fig. 2.8). In the first half of the estimation period, T1007 has a negative V_D minima of about -70 m s⁻¹ and a positive V_D maximum of about 55 m s⁻¹ near the 12-km radius at 2-km altitude (Fig. 2.8b). The DR method retrieves \bar{v} greater than 60 m s⁻¹, and the P_{min} estimates are around 930 hPa on average (Figs. 2.8a, c), although they fluctuate somewhat erratically. As the TC approaches Okinawa Island, \bar{v} decreases rapidly. At the time of the TC's nearest approach to Nago on Okinawa Island, when the SLP is 965.1 hPa (Fig. 2.8a, blue star), Nago is located just within the RMW (~ 13 km from the TC center) and the retrieved \bar{v} is 47 m s⁻¹. The DR method provides P_{min} estimates that are more than 10 hPa below the SLP at Nago. In contrast, the best track P_{min} is consistently 960 hPa (black line in Fig. 2.8a), and the Dvorak P_{min} is consistently 947 hPa (dashed blue line in Fig. 2.8a) during the estimation period. Considering the fact that the \bar{v} at around the RMW (~ 12 km) changes from ~ 63 m s⁻¹ to ~ 47 m s⁻¹ during the estimation period and the observed SLP is 965.1 hPa around the RMW during the second half of the period, the P_{min} estimates obtained by the DR method seem more plausible than the best track data. This suggests that the DR method can capture some

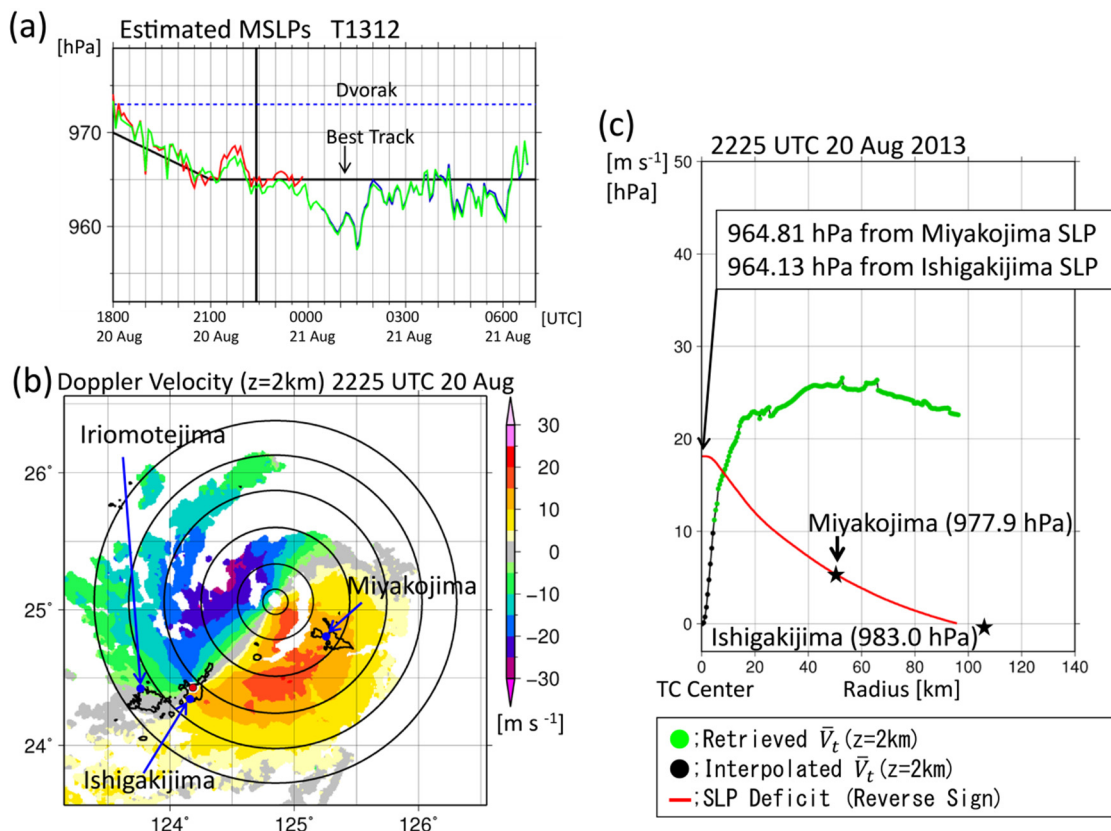


Fig. 2.7: (a) Time evolutions of the DR P_{min} (color lines), best track P_{min} (black line), and Dvorak P_{min} (blue dashed line) for T1312. The vertical black line indicates the time of the radar observation shown in (b). The red line indicates P_{min} derived from SLP at Miyakojima, the green line indicates P_{min} derived from SLP at Ishigakijima, and the blue line indicates P_{min} derived from SLP at Iriomotejima. (b) Doppler radial velocity of the 2-km CAPPI observed from the Ishigakijima radar (red dot) at 2225 UTC on 20 August 2013. The circles show the radii at 10, 30, 60, 90, 120, and 150 km from the TC center. (c) Same as Fig. 2.3, except for T1312 at 2225 UTC on 20 August 2013.

TC intensity changes on a short time scale (less than 6 h) that the conventional methods failed to capture. If T1007 is removed from the overall statistical verification described in subsection 2.3a, the RMSE improves to 7.13 hPa (Table 2.5). Other cases in this group, with similarly large differences between the DR and best track P_{min} values, are T1204 and T1419 (not shown).

The estimates of five TC cases show consistent positive biases: T1109, T1217, T1318, T1418A, and T1418B. Figure 2.9a shows the time evolution of the P_{min} of Typhoon Phanfone (T1418A, T1418B, and T1418C). T1418A shows a significant positive bias during the last 2 h of the estimation period (around 0300 UTC on 05 October 2014) compared with the prior and subsequent estimates. This bias is caused by poor radar coverage (not shown). Except for that period, however, the DR estimates of Typhoon Phanfone seem reasonable because the retrieved \bar{v} structure corresponds well to the V_D distribution and

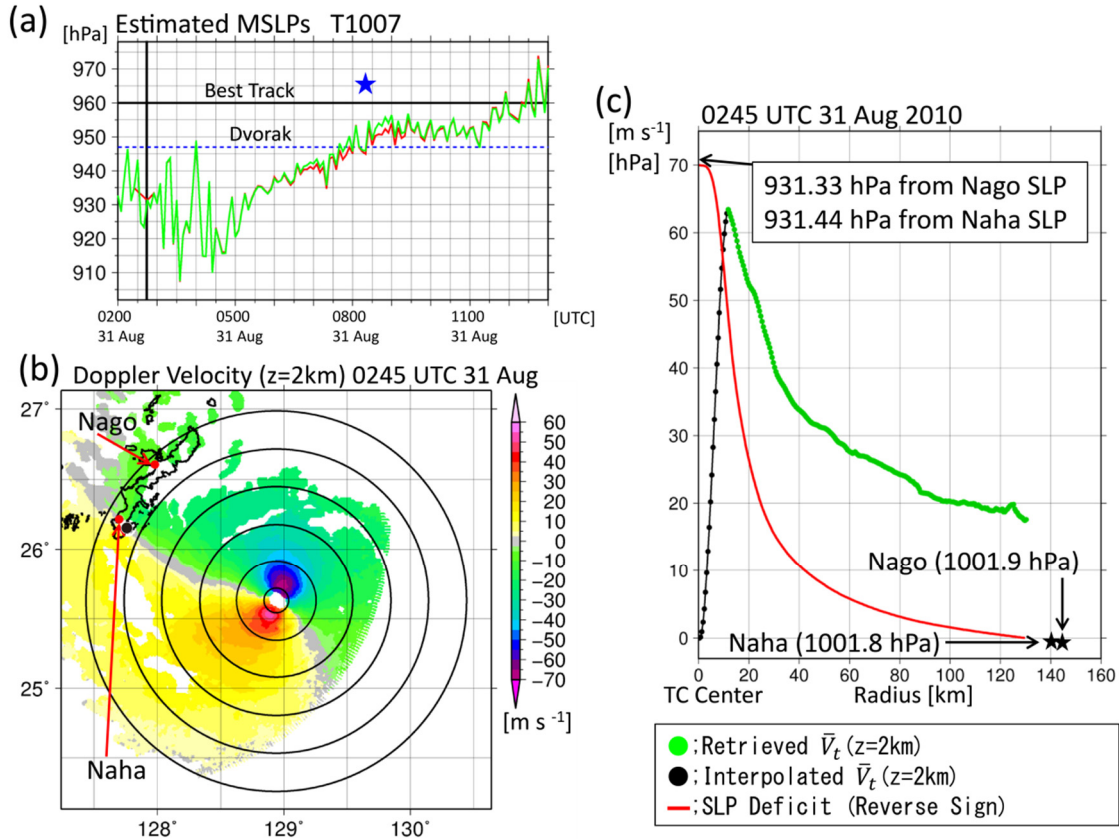


Fig. 2.8: (a) Same as Fig. 2.7a, except for T1007. The blue star is the SLP (965.1 hPa) observed at Nago, 13.2 km from the TC center. The vertical black line indicates the time of the observation shown in (b). The green line indicates P_{min} derived from SLP at Naha, and the red line indicates P_{min} derived from SLP at Nago. (b) Doppler radial velocity of the 2-km CAPPI observed from the Okinawa radar (black dot) at 0245 UTC on 31 August 2010. The circles show the radii at 10, 30, 60, 90, 120, and 150 km from the TC center. (c) Same as Fig. 2.3, except for T1007 at 0245 UTC on 31 August 2010.

because \bar{v} are retrieved in the eye region (Fig. 2.9b and c). One possible reason for the consistent positive biases of the DR estimates, compared with the best track, is that if the wavenumber-1 asymmetry is caused by a vortex Rossby wave and then it may be stationary near the eye region (e.g. Lamb 1932), it can potentially cause a constant bias to the GBVTD-retrieved \bar{v} (see subsection 2.1c), resulting in consistent P_{min} biases. However, because this possibility can lead to both positive and negative biases and because there is no case with a consistent negative bias, it may not be the reason for the consistent positive biases. Another possible reason is that the radial SLP structure inside the P-RMW assumed in the best track analysis is different from that deduced from the DR method. Table 2.7 shows the accuracies and the P-RMWs of the TCs in this group. Except for T1318, the P-RMW is more than 70 km. When the P-RMW is large, the effect of the difference between the SLP structures inside the P-RMW assumed in the best track analysis and

Table 2.6: Accuracy of the 10 cases with excellent estimation results. The P-RMW was determined from the retrieved \bar{V}_t after step 5 in Fig. 2.2 within its possible range used in the GBVTD-simplex center-finding algorithm. The P-RMW values and central pressures were averaged over the estimation periods shown in Table 2.2.

Case (Name, Alias)	N	Central Pressure [hPa]			RMSE [hPa]	Bias [hPa]	P-RMW (z=2 km) [km]
		Estimated	Best Track	Dvorak			
T0709 (Fitow)	226	974.76	974.55	974.44	2.21	0.22	49.12
T0813 (Sinlaku)	106	980.72	981.12	981.92	2.17	-0.41	18.83
T1115 (Roke)	49	951.05	949.12	926.86	3.77	1.94	23.19
T1215 (Bolaven)	314	931.66	929.12	948.46	3.88	2.54	14.07
T1307 (Soulik)	203	948.19	948.02	965.00	3.79	0.17	30.89
T1312 (Trami)	299	964.87	965.58	973.00	2.30	-0.70	40.64
T1323 (Fitow)	325	963.32	961.33	968.13	2.84	2.00	73.78
T1408 (Neoguri, T1408A)	141	940.33	940.00	947.00	3.27	0.33	39.99
T1408 (Neoguri, T1408B)	78	939.70	940.37	947.00	3.12	-0.67	35.21
T1411 (Halong, T1411B)	260	956.29	955.32	972.63	3.00	0.97	47.22

Table 2.7: As in Table 2.6, but for the five cases with consistent positive biases.

Case (Name, Alias)	N	Central Pressure [hPa]			RMSE [hPa]	Bias [hPa]	P-RMW (z=2 km) [km]
		Estimated	Best Track	Dvorak			
T1109 (Muifa)	243	951.95	945.32	956.00	6.94	6.64	71.68
T1217 (Jelawat)	148	949.92	931.89	947.08	18.87	18.03	85.80
T1318 (Man-yi)	140	968.34	960.00	975.75	8.81	8.34	45.10
T1418 (Phanfone, T1418A)	189	957.21	943.18	953.68	14.99	14.03	92.22
T1418 (Phanfone, T1418B)	167	957.11	945.50	956.00	11.88	11.61	85.55

deduced from the DR method on P_{min} estimates may be large. Interestingly, the DR P_{min} estimates are better correlated with the Dvorak P_{min} estimates than with the best track P_{min} values in this group (Fig. 2.9a and Table 2.7). Considering these findings, the P_{min} estimates of these cases characterized as having consistent positive biases may not be wrong, although we do not have true P_{min} data with which to compare them.

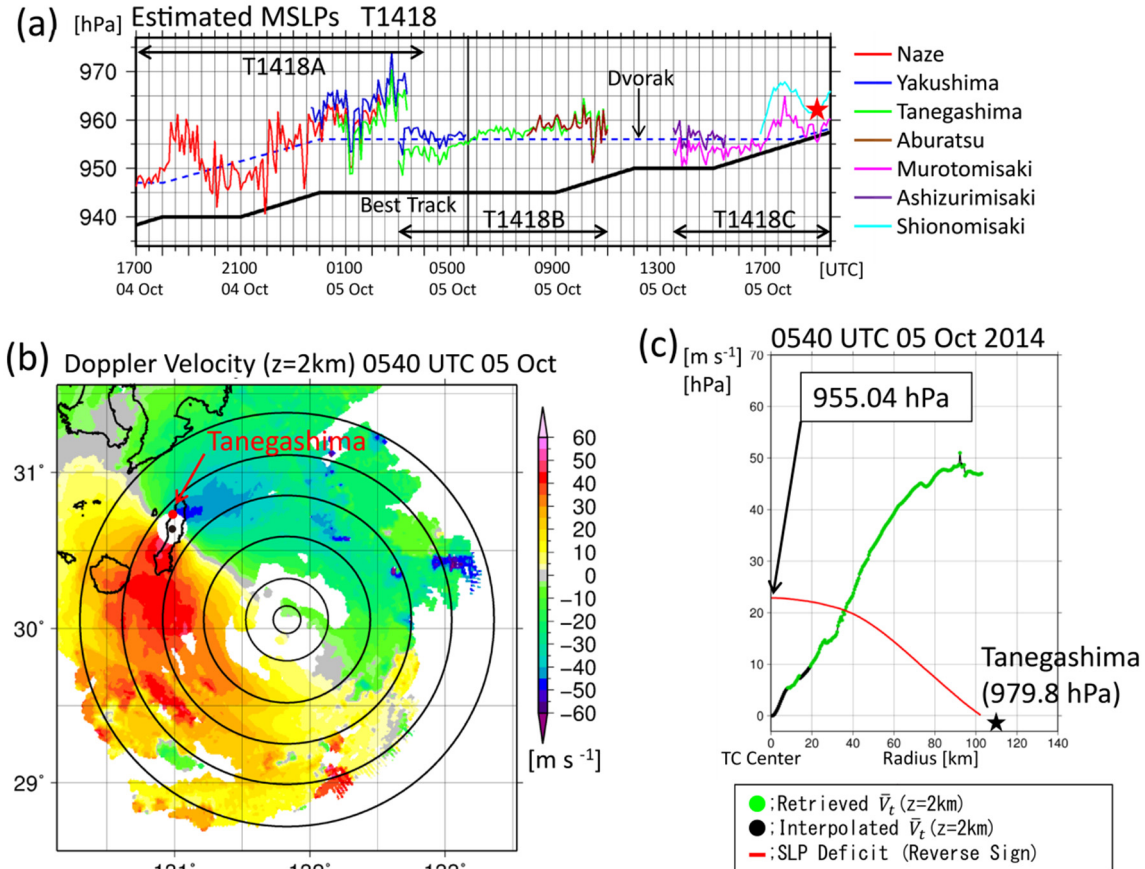


Fig. 2.9: (a) Same as Fig. 2.7a, except for T1418. The red star is the SLP (962.1 hPa) observed at Shionomisaki, which was 6.2 km from the TC center. The vertical black line indicates the time of the observation shown in (b). (b) The Doppler radial velocity of 2-km CAPPI observed from the Tanegashima radar (black dot) at 0540 UTC on 05 October 2014. The circles show the radii at 10, 30, 60, 90, 120, and 150 km from the TC center. (c) Same as Fig. 2.3, except for T1418 at 0540 UTC on 05 October 2014.

The estimated P_{min} fluctuates erratically in some cases, as they also did in some results of the simulation experiment (not shown). According to Harasti et al. (2004), unreasonable TC center finding by the simplex method is one reason for such erratic fluctuations, and we identify four additional reasons for erratic fluctuations. First, noise contamination caused by failure of the dealiasing correction sometimes results in violent fluctuations with amplitudes of 5–15 hPa, for example, in T1011 (Fig. 2.10a), T1216, and T1324B (not shown). In those cases, noisy data in small areas are not fully removed by the automatic processes. Second, in some cases the GBVTD assumption that radial winds are much weaker than tangential winds is apparently not valid inside the eyewall. If there are active mesovortices inside the P-RMW, there is no assurance that asymmetric radial winds are negligible, and the wind retrieval accuracy would not be good. The P_{min} estimates of

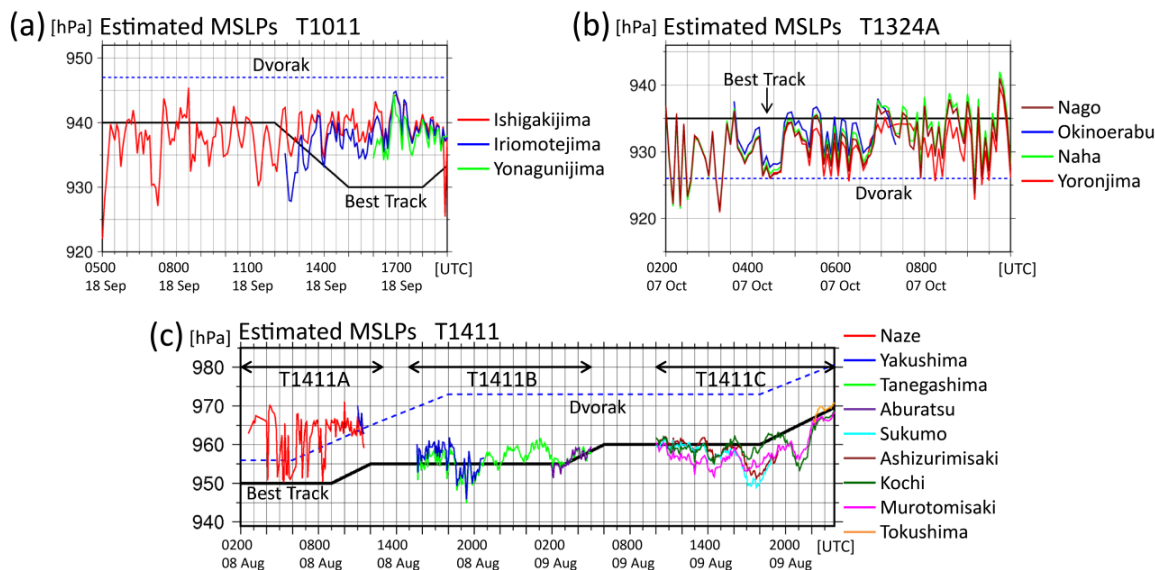


Fig. 2.10: Same as Fig. 2.7a, except for (a) T1011, (b) T1324A, and (c) T1411.

T1007 in the first half of the estimation period (Fig. 2.8a) and of T1324A (Fig. 2.10b) fluctuate with an amplitude of 5–15 hPa for this reason, because in these two cases, RMSDs between the V_D resampled from the GBVTD-retrieved winds and the observed V_D are sometimes quite large inside the P-RMW. Although the QC procedures described in subsection 2.1c remove retrieved winds with large RMSDs, the results can be problematic. When too many retrieved winds are rejected by the QC procedure, the estimated P_{min} tends to be too high. With insufficient rejection, the retrieved \bar{v} tends to be too strong in the eye region, and the estimated P_{min} becomes too low. As a result, the P_{min} shows erratic fluctuations. The third reason is illustrated by T1411A (Fig. 2.10c), for which the P_{min} fluctuates violently between two extremes. When the radar coverage is sufficient for wind retrieval around the disappearing eyewall, the estimated P_{min} is about 950 hPa, which is consistent with the best track. In contrast, poor radar coverage around the disappearing eyewall leads to a P_{min} of around 965 hPa. Fourth, the aliasing of wavenumber-2 radial winds into \bar{v} in the GBVTD retrieval formula (see details in Lee et al. 1999; Murillo et al. 2011) probably causes wavy fluctuations with a period of a couple of hours, as seen in T1204, T1215, T1411B (Fig. 2.10c), and T1411C (Fig. 2.10c). If wavenumber-2 radial winds are dominant within the eye region and their distribution moves around the eyewall cyclonically together with mesovortices (e.g., Kossin and Schubert 2004; Braun et al. 2006) or vortex Rossby waves (e.g., Montgomery and Kallenbach 1997; Wang 2002), the radial winds could bias the retrieved \bar{v}

with a period of a few hours.

Given these characteristics of our estimation results, we recommend using a running mean of DR P_{min} values of a few hours.

2.4. Discussion

In this section, we compare the accuracy of the DR method with conventional estimation methods, examine additional statistical verification results, and discuss the utility of DR intensity estimates.

a. Comparison with conventional methods

Koba et al. (1990) have reported that the standard deviation of Dvorak P_{min} estimates in the western North Pacific is 7–19 hPa relative to the JMA best track data; Martin and Gray (1993) have reported that the standard deviation of Dvorak P_{min} estimates in the western North Pacific is ~9 hPa relative to aircraft reconnaissance observations, and Velden et al. (2007) have reported that the RMSE of Dvorak P_{min} estimates is ~12 hPa relative to aircraft reconnaissance observations. According to Oyama (2014), Advanced Microwave Sounding Unit (AMSU) P_{min} estimates in the western North Pacific have a RMSE of ~10 hPa relative to the JMA best track data, and according to Velden et al. (2007), the RMSE of the AMSU method using the Cooperative Institute for Meteorological Satellite Studies (CIMSS) algorithm is ~8 hPa and that using the Cooperative Institute for Research in the Atmosphere (CIRA) algorithm is ~10 hPa, relative to aircraft reconnaissance observations. These error statistics indicate that the accuracy of the P_{min} estimates obtained by our DR method is comparable to or better than the accuracies of the Dvorak and AMSU methods.

We stress that the DR intensity estimates are totally independent of the past best track. We can now obtain plausible P_{min} at 5-min intervals by a method other than aircraft reconnaissance observations that is different from that used to obtain the best track. The use of DR estimates would be a new paradigm of TC intensity analysis in the western North Pacific, where aircraft observations are not available.

b. Additional statistical verification

We further compare the difference between the estimated P_{min} values and the best track P_{min} values with respect to several specific conditions (Fig. 2.11). Note, however, that because we use only 22 TCs for the estimations, the statistical results for some specific conditions may be dependent on extreme cases. The RMSEs are, in general, smaller when the distance between the TC center and the radar location is shorter, and the estimates exhibit a positive bias when the distance is large. The positive bias may result from the CAPPI

method as described in subsection 2.1c. Similarly, RMSEs are smaller when the distance between the TC center and the weather station whose sea level pressure is used as an anchor for pressure measurement is shorter. One reason for this similarity is likely the fact that the best track analysis uses the same weather station observations, and weather stations are near the radar locations.

The RMW is determined from all of the retrieved \bar{V}_t values after step 5 in Fig. 2.2. For TCs with a RMW of 20–70 km, the P_{min} estimates have a RMSE of 5.55 hPa and show a bias of 0.69 hPa. In contrast, for TCs with a RMW of 75–120 km, the estimates have a large positive bias of 5.23 hPa, as indicated in subsection 2.3b. Large RMWs greater than 120 km may contain false RMWs. Bell and Lee (2012) stated that missing data outside the radar range can cause a false RMW at a large radius. Thus, large errors accompanying large RMWs may be due in part to the false RMWs, more specifically lack of radar data.

Because the above results suggest that the pressure gradients retrieved by the DR method have a systematic error, we examine the relationship between the observational SLP gradient when there are multiple SLP observations around a TC and the corresponding retrieved SLP gradient. Figure 2.12 shows the result schematically: the retrieved SLP gradient is on average 0.55 hPa steeper than the observational SLP gradient over a 44.3 km interval. This result is apparently inconsistent with the positive biases of the P_{min} estimates described above. However, given that most of the weather stations are outside of the RMW, these findings suggest that the SLP gradient retrieved from outside the RMW is steeper than the true gradient, and that the SLP gradient inside the RMW, where some of the \bar{v} are interpolated by using a spline function, is shallower than the gradient inferred from the best track. These features are consistent with those of the average SLP gradient in the preliminary experiment (Fig. 2.5b). The radial SLP gradient error is attributed to (1) \bar{v} retrieval errors associated with the use of the TC motion as a proxy for $V_{M\perp}$ and several limitations inherent in the GBVTD technique, (2) the improper use of a value for surface air density that is a little too high and \bar{v} at 2-km altitude in the gradient wind equation (1), and (3) an interpolation error by the spline function. The development of a method for interpolating \bar{v} within the TC eye in a plausible way is a topic for future work.

In addition, the estimated P_{min} tends to be more consistent with the best track P_{min} when radar coverage is denser and wind retrieval accuracy is better (Figs. 2.11d, e).

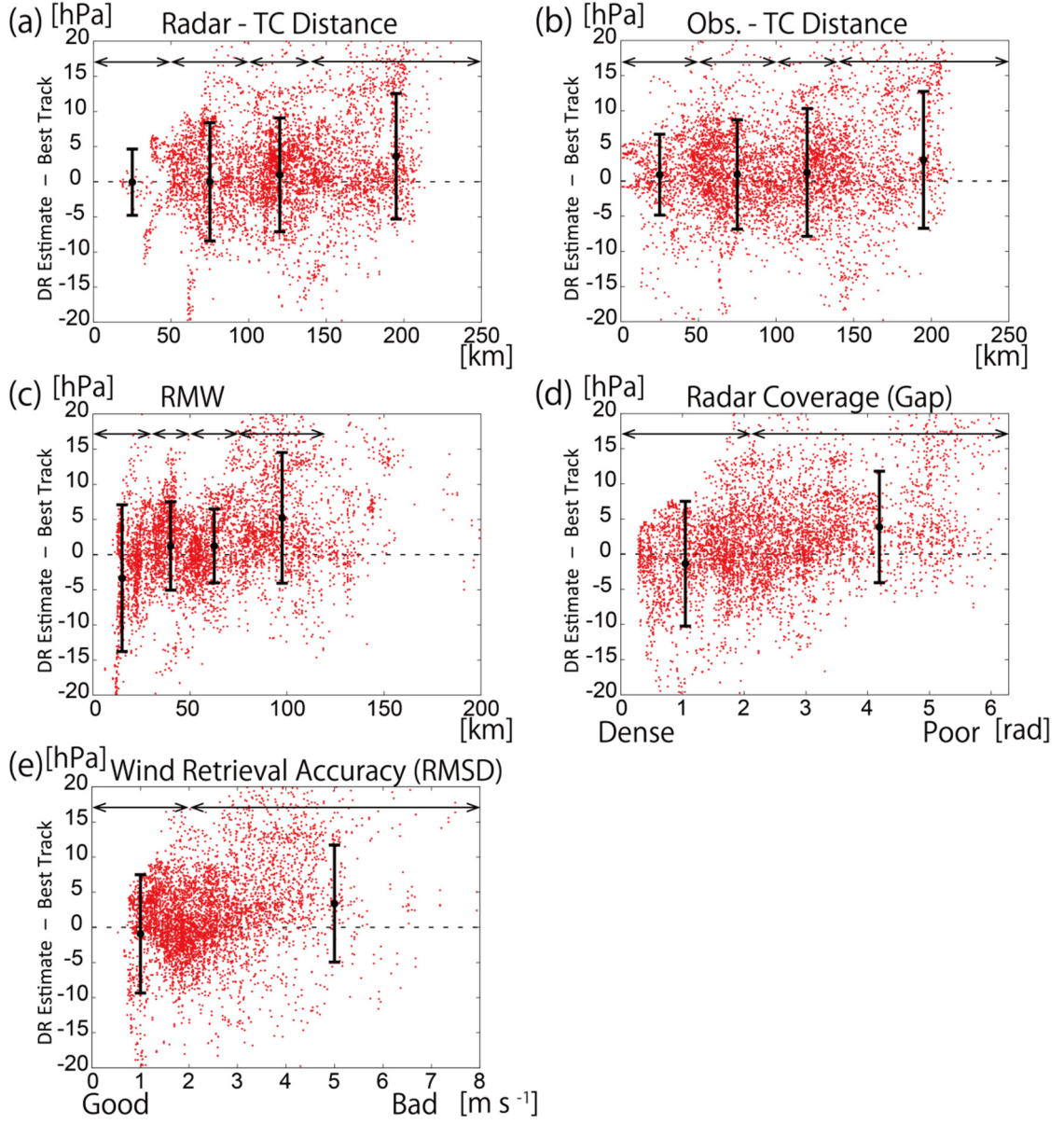


Fig. 2.11: Scatter diagrams comparing the difference between the estimated P_{min} values and the best track P_{min} values (y-axis) with (a) the distance between the radar location and the TC center, (b) the distance between the weather station and the TC center, (c) the RMW at 2-km altitude, (d) radar coverage, and (e) the GBVTD wind retrieval accuracy (x-axis). The RMWs are determined from all the GBVTD-retrieved \bar{V}_t from step 5 in Fig. 2.2. The radar coverage is defined as the radial average of the maximum azimuthal gap (rad) at each radius on the GBVTD-specified coordinate system. The wind retrieval accuracy is defined as the overall average of the RMSD between the V_D resampled from the GBVTD-retrieved winds and the observed V_D , identical to the RMSE shown in Fig. 3 of Zhao et al. (2012). The error bars show the bias and the RMSE within the range indicated by the double-headed arrows.

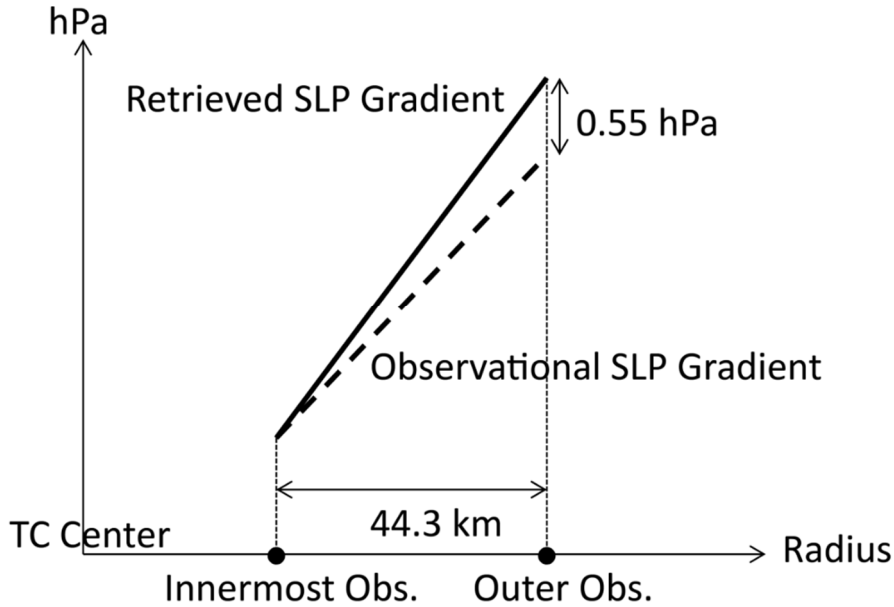


Fig. 2.12: Schematic diagram of retrieved and observed SLP gradients. The values are calculated when data from multiple SLP observations around the TCs are available. To obtain as many SLP gradients in the inner region of TCs as possible, when three or more SLP observations are available, only SLP gradients relative to the innermost observation point are calculated.

c. Utility of the DR intensity estimation method

Estimation of P_{min} by the DR method has three advantages. First, the DR method can provide P_{min} at 5-min intervals with an accuracy comparable to or better than that of conventional methods. As a result, we can monitor a TC at shorter intervals than is possible with conventional methods, which allow monitoring at 6-h intervals or several times per day. Second, the DR method can, in principle, estimate the intensity of any TC, as long as radar coverage is sufficient. In contrast, the Dvorak technique cannot handle rapid intensity changes, and the AMSU techniques, because of the coarse resolution of the instrument, are not suitable for estimating the P_{min} of a TC with a small eye (Oyama 2014). Third, in recent years the DR method could have been applied to four-to-five TCs each year according to Table 2.2. In particular, intense TCs approaching the vicinity of the Okinawa Islands, where there is no topography effect on the TC structure, are ideally suited for GBVTD retrievals. Therefore, the DR method will be beneficial for studying TCs that change intensity rapidly.

However, DR intensity estimates also have some limitations. Compared with the lifetime of a TC, the estimation period is extremely limited; only 9 h on average. The DR method also uses some parameters, such

as initial guess centers, the P-RMW and its possible range, that must be subjectively determined beforehand. In addition, the method cannot estimate P_{min} unless V_D can be successfully dealiased. Furthermore, the GBVTD technique has several inherent limitations as described previously. The dealiasing problem should be addressed by improving dealiasing and noise-removal methods. Because some other techniques to relax limitations of the GBVTD technique have been proposed (e.g. Jou et al. 2008; Wang et al. 2012; Chen et al. 2013), it may be possible to further improve the DR method.

2.5. Summary

It is of great importance to analyze TC intensity with high accuracy and frequency, particularly for rapidly intensifying and weakening TCs. However, conventional methods of TC intensity estimation, such as the Dvorak technique, which estimates P_{min} and maximum sustained wind speed from cloud patterns, and the AMSU technique, which estimates P_{min} from the magnitude of the upper-level warm core anomaly retrieved from satellite microwave sounding data, have limitations with regard to analysis accuracy and frequency. Furthermore, observing P_{min} in a straightforward way, such as by using dropsondes, is, for now, not a practical solution in the western North Pacific basin. However, because from 2006 to 2013 JMA upgraded all its operational radars to Doppler radars, Doppler velocity observations are available for the many TCs that have passed near these radars. If axisymmetric tangential winds retrieved from the Doppler velocities and the gradient wind equation can reasonably be used to infer a TC's pressure field, then P_{min} can be estimated from the Doppler velocities with high accuracy and frequency. A set of procedures proposed by Lee et al. (1999, 2000), Lee and Marks (2000), and Bell and Lee (2012) for estimating TC intensity by using the GBVTD technique to retrieve axisymmetric tangential winds from Doppler velocities showed promising results.

In this chapter, before estimating the intensity of real TCs, we performed a preliminary experiment using pseudo-Doppler velocities obtained from numerical simulations to confirm that the set of intensity estimation procedures could provide reasonable estimates of P_{min} . In particular, we assessed the effect of using the cross-beam (normal to the line connecting the radar with the TC center) component of the mean environmental wind, $V_{M\perp}$, assumed from the TC translational speed, to correct for the aliasing effect of the GBVTD algorithm. The results showed that when Doppler velocities at 2-km altitude and the assumed $V_{M\perp}$ were used, the estimated P_{min} had a RMSE of 2.84 hPa and a bias of -0.77 hPa. In addition, the incorporation of $V_{M\perp}$ assumed from the TC motion in the GBVTD algorithm decreased the bias and improved the accuracy of the estimate very well. We also confirmed that the DR method could reasonably estimate the P_{min} by using Doppler velocities at 2-km altitude.

On the basis of these preliminary results, we have evaluated the accuracy of this method by estimating the P_{min} of 28 TC cases, have identified some limitations, strengths, and weaknesses of the method, and have

evaluated its utility for studying TCs. We have used Doppler velocity data at 2-km altitude and the cross-beam component of the TC translational speed as $V_{M\perp}$. Compared with the best track data of RSMC Tokyo, the RMSE, bias, and correlation were 8.37 hPa, 1.51 hPa, and 0.87, respectively. The P_{min} estimation error was within ± 5 hPa (± 10 hPa) for 60.3% (84.1%) of the total number of estimates. This estimation accuracy is comparable to or better than the accuracies of the Dvorak and AMSU methods. Additionally, we confirmed that the accuracy was poor if the $V_{M\perp}$ was not incorporated into the GBVTD algorithm. Two distance metrics are defined, 1) the distance between the TC center and the radar location, and 2) the distance between the TC center and the surface weather station whose sea level pressure was used as an anchor for pressure measurement. The P_{min} estimated here tended to be more consistent with the best track P_{min} when the distance metrics were shorter, when the wind retrieval accuracy was better, and when the radar coverage was denser. For TCs with a RMW of 20–70 km, the estimated P_{min} had a RMSE of 5.55 hPa and showed a bias of 0.69 hPa relative to the best track. Examination of cases with large differences between the best track and DR method P_{min} values suggested that the DR method can capture TC intensity changes over a shorter time scale (less than 6 h) than is possible with the conventional methods. This suggests that the DR method can be used for studying rapidly intensifying and weakening TCs.

Chapter 3: Intensity change and axisymmetry

The results of previous observational studies reviewed in Chapter 1 contain two views about conditions favorable for intensification from the perspective of azimuthal distributions: the axisymmetric component of diabatic heating is important, as is asymmetric intense convection. Although relationships between inner-core structures and TC intensity changes have been investigated both theoretically and observationally, the relative contribution of axisymmetric and asymmetric components to intensity changes still remains a matter of debate. Further clarification is needed.

In this chapter, we investigate the relationship between TC intensity changes and axisymmetry deduced from hourly Global Satellite Mapping of Precipitation (GSMaP) data (Kubota et al. 2007, 2009), a satellite-derived rainfall product. We define axisymmetry as a metric positively correlated with the magnitude of the axisymmetric component of the rainfall rate and negatively correlated with the magnitude of the asymmetric component (see section 3.1). Because the magnitude of the rainfall rate can be assumed to be correlated with the magnitude of diabatic heating in the low- to middle-level troposphere, this metric is hypothesized to have a relationship with the TC intensity change. Previous studies using satellite data investigated TC features in relation to RI, whereas in this study we examine the intensification rate in relation to differences in rainfall structures.

3.1. Data and method

We use hourly GSMaP data composed of high-resolution (0.1°) satellite-based rainfall rate (mm h^{-1}) estimates. These data are processed and provided by the Japan Aerospace Exploration Agency (JAXA) (JAXA 2017a). The spatially and temporally high-resolution GSMaP dataset is constructed in two steps.

In the first step, the rainfall rate is estimated by a retrieval algorithm developed by Aonashi and Liu (2000), Aonashi et al. (2009) and Shige et al. (2009) from microwave satellite data from the TRMM Microwave Imager (TMI), the Advanced Earth Observing Satellite-II (ADEOS-II) Advanced Microwave Scanning Radiometer (AMSR), the Aqua AMSR for Earth Observing System (AMSR-E), the Global Change Observation Mission 1st - Water (GCOM-W) AMSR2, the Defense Meteorological Satellite Program

(DMSP) Special Sensor Microwave Imager Sounder (SSMIS) series, the National Oceanic and Atmospheric Administration (NOAA) Advanced Microwave Sounding Unit series (AMSU), and the Meteorological Operational Satellite Program of Europe (MetOp) AMSU series, the Global Precipitation Measurement Core Spacecraft (GPM-Core) GPM Microwave Imager (GMI). The use of these microwave satellite data enables the satellite-retrieved rainfall dataset to have a temporal resolution of about 3 to 6 h at each point and to cover the area from 60°S to 60°N; however, the rainfall rate is not retrieved in areas of expected surface temperatures below 0 °C, as snowfall is expected.

In the second step, hourly rainfall rate estimates are obtained from the satellite-retrieved rainfall data by means of two temporal interpolation methods. The first is the morph method (Joyce et al. 2004), in which the movement of precipitation areas retrieved from microwave satellite data is estimated by using migration vectors derived from geostationary satellite infrared (IR) imagery. The second is rainfall correction by a Kalman filter, which uses the statistical relationship between geostationary satellite IR brightness temperatures (TBs) and precipitation (Ushio et al. 2009). Details of the GSMaP dataset are given by Kubota et al. (2009) and the GSMaP web site (JAXA 2017a). Although the microwave satellites used to obtain the GSMaP data orbit the earth so as to generally cover the entire GSMaP region at intervals of no more than 3 to 6 h, quality degradation due to the temporal interpolation of precipitation may affect the axisymmetry of TCs. We will quantify this impact in subsection 3.2a.

GSMaP data are available since 2000. In this study, we use the GSMaP reanalysis product (version 6 algorithm without the gauge correction) for the period from 2000 to 2015.

We use the metric of axisymmetry, γ , defined by Miyamoto and Takemi (2013). First, a variable, ϕ , is divided into the azimuthal mean (axisymmetric component, denoted by an overbar) and the deviation from the azimuthal mean (asymmetric component, denoted by a prime),

$$\phi(r, \lambda, z, t) = \bar{\phi}(r, z, t) + \phi'(r, \lambda, z, t), \quad (3.1)$$

where r , λ , and z are the radial, tangential, and axial direction, and t is time, respectively. Axisymmetry is then defined as follows,

$$\gamma(r, z, t) \equiv \frac{\bar{\phi}(r, z, t)^2}{\bar{\phi}(r, z, t)^2 + \int_0^{2\pi} \phi'(r, \lambda, z, t)^2 d\lambda / 2\pi} \quad (3.2).$$

γ depends on the magnitude of the axisymmetric component as well as on that of the asymmetric component. γ lies between 0 and 1, and is largest when the

asymmetric component is zero all the way around the circle.

Although Miyamoto and Takemi (2013) used potential vorticity (PV) as ϕ in their definition of axisymmetry, we use the rainfall rate from the GSMaP dataset. First γ is calculated at each radius, and then γ is averaged from the TC center to the 100 km radius, in the same way as in Miyamoto and Takemi (2013). We choose 100 km as the outermost radius from which to obtain the mean axisymmetry in the inner core of a TC because the RMW is smaller than 100 km for most TCs (e.g., Stern et al. 2015). Miyamoto and Takemi (2013) showed that a distinct eyewall forms and RI begins several hours after the distribution of PV becomes axisymmetric. The use of precipitation data instead of PV might make it difficult to capture the axisymmetrization of TCs several hours before the start of intensification in a similar way to the PV field.

We prepare a dataset for this study consisting of all 380 TCs that occurred in the western North Pacific (WNP) basin (from the equator to 60°N and from 100°E to 180°E) from 2000 to 2015. Because the temporal resolution of the GSMaP data is hourly, we can obtain a sufficient number of samples for the investigation in the WNP basin. To obtain TC centers and current intensities [in terms of both central pressure and maximum sustained wind (10-min mean)], we use the best track data of the Regional Specialized Meteorological Center (RSMC) Tokyo, which are linearly interpolated to 1-h intervals. Although the GSMaP data can be used to investigate TCs all over the world, which is one of the advantages of this dataset, we mainly analyze TCs in the WNP basin because the success of our approach depends greatly on the quality of the best track data used. The TC dataset includes TCs classified as tropical storms (maximum sustained wind speed, 34–47 kt, 1 kt = 0.514 m s⁻¹), severe tropical storms (48–63 kt), and typhoons (>64 kt) in the best track data, and excludes TCs during the tropical depression stage (<34 kt), because the best track data do not provide maximum sustained wind data during that stage. However, if a TC decays into a tropical depression and then reintensify into a tropical storm, this tropical depression period is, exceptionally, included in the dataset to simplify data handling.

As intensity, we evaluate both central pressure and maximum sustained wind speed. We use knots (kt) as the units for maximum sustained wind speed because the best track data are reported in knots. We investigate the intensification rate (a short-term intensity change) at different times as well as the intensity change in the next 12 h, 24 h, 36 h and 48 h (a long-term intensity change) to determine causality between γ and TC intensification.

The intensification rate is calculated as the centered difference between 3 h before and 3 h after each time point, because most of intensities in the best track data used are available at 6-h intervals. We perform the investigation by dividing the TC data according to two TC stages: the development stage and the decay stage. The development stage is defined as a period from the time that the TC is first classified as a tropical storm to the latest time that the TC reaches its maximum intensity during its lifecycle. However, data in which the change of central pressure (maximum sustained wind) is positive (negative) owing to temporary weakening and landfall are excluded from the development stage dataset. The decay stage is defined as a period from 1 h after the development stage to the last time that the TC is classified as a tropical storm, including periods of reintensification and landfall. In the case of TCs that enters the WNP basin from the central Pacific basin, we determine both the development and decay stages for the entire period covered by the best track data (i.e., while the TC is in the WNP basin).

Finally, we bin the dataset into 5 hPa and 5 kt intervals of current intensity and 0.02 intervals of current γ .

3.2. Results

a. Case study

First, we examine whether γ is correlated to intensity changes in specific cases, while quantifying uncertainties in γ deduced from the hourly GSMaP data. To exclude the possibility that the results obtained are strongly dependent on the best track data, we select examples in the North Atlantic basin, along with best track data provided by the National Hurricane Center (NHC), as well as examples from the WNP basin. The NHC's best track data, which are based on in situ observations by aircraft and obtained by dropsonde as well as on satellite data, are expected to be more reliable than data from other centers. Note that the maximum sustained wind speed in the NHC's best track is a 1-min average, whereas that in the RSMC Tokyo's best track is a 10-min average.

We examine two typhoons, Typhoon Noul (2015) and Typhoon Dolphin (2015) (Fig. 3.1), and two hurricanes, Hurricane Earl (2010) and Hurricane Igor (2010) (Fig. 3.2). In the time evolution of each case, hourly γ shows erratic fluctuations. These fluctuations have several causes: 1) inaccurate TC center locations, when the TC center interpolated from the best track data deviates from the actual location (Fig. 3.1e); 2) different data resolutions among microwave satellites (Figs. 3.1e and 3.1f); 3) quality differences due to the use of the temporal interpolation method (Figs. 3.1b and 3.1c); and 4) biases in rainfall rate estimates among microwave satellites. We quantify uncertainties in γ associated with these causes (Table 3.1 and 3.2). As for the first cause of the erratic fluctuations, we evaluate the uncertainties from the perspective of the degree to which differences in center locations can vary γ . For each center in Fig. 3.1b, 3.1c, 3.1e and 3.1f, we prepare a total of 24 centers around the original center regularly spaced 0.1° apart and fill a $0.4^\circ \times 0.4^\circ$ square and then we calculate γ one by one to estimate the standard deviation of 25 γ values (including original γ). The results show that the standard deviation ranges from 0.02 to 0.11 (Table 3.1). For the second cause, there are systematic differences in γ reaching 0.25 between imager and sounder sensors (Table 3.2). For the third cause, γ tends to be higher when the temporal interpolation by IR data is applied (Table 3.2). For the fourth cause, there are differences in γ even among imager sensors and among sounder sensors (Table 3.2). Fortunately, when γ is averaged over 6 h (an average between 3 h before and 3 h after each time point), these fine-scale fluctuations disappear and there remains a time evolution of γ that

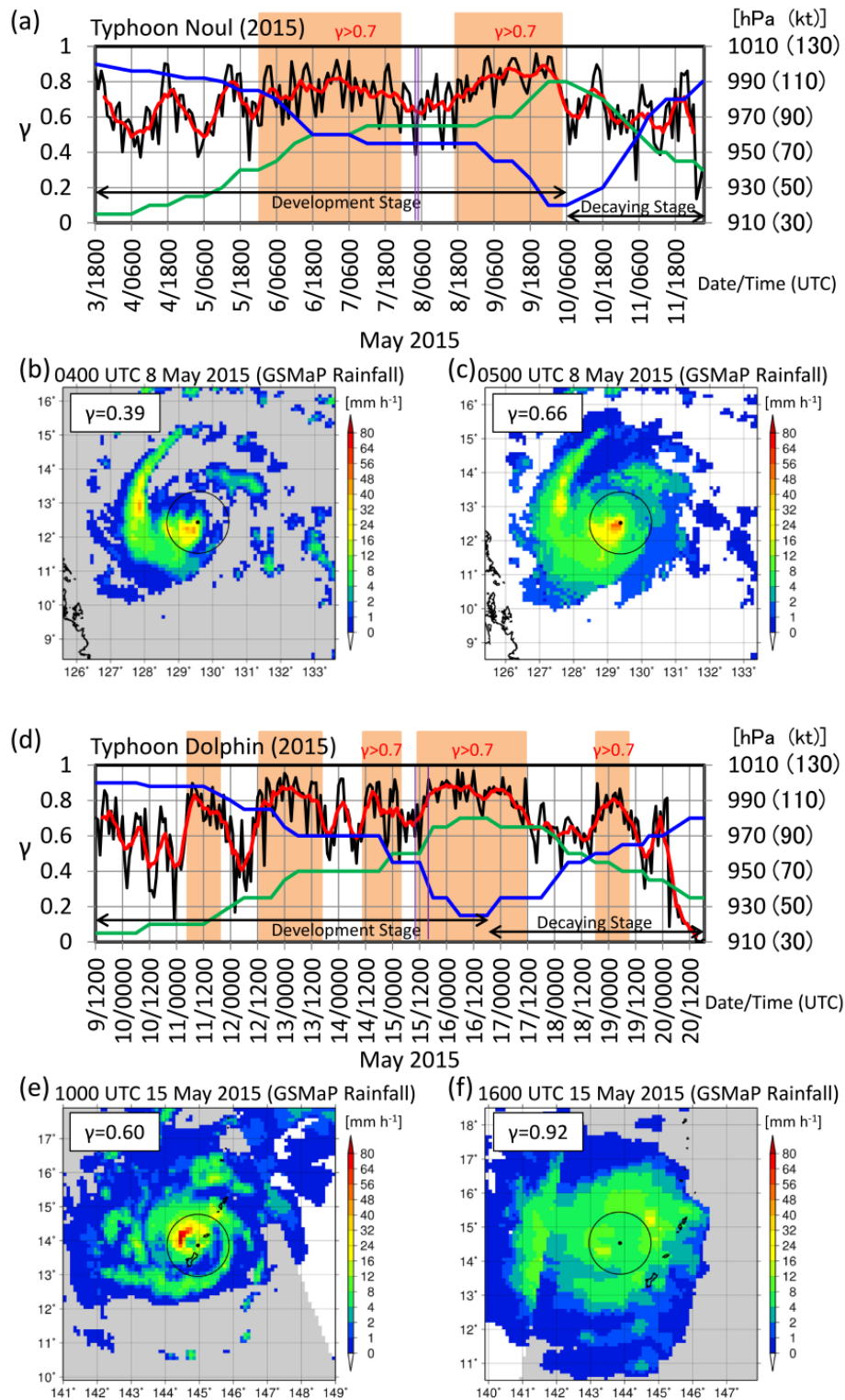


Fig. 3.1: (a) Time evolution of γ (hourly in black and 6-h mean in red), central pressure (blue) and maximum sustained wind (green) of Typhoon Noul (2015). The vertical purple lines indicate the time of the GSMaP images shown in (b) and (c). The orange shading indicates period when the 6-h mean γ was greater than 0.7 for at least 12 consecutive hours. (b) GSMaP image and the value of γ at 0400 UTC 8 May 2015. The circle is centered at the TC's center and has a 100 km radius. A gray background indicates data derived from microwave satellite data, and a white background indicates data derived by interpolation. (c) As (b), but at 0500 UTC 8 May 2015. (d) As (a), but for Typhoon Dolphin (2015). (e) As (b), but at 1000 UTC 15 May 2015. (f) As (b), but at 1600 UTC 15 May 2015.

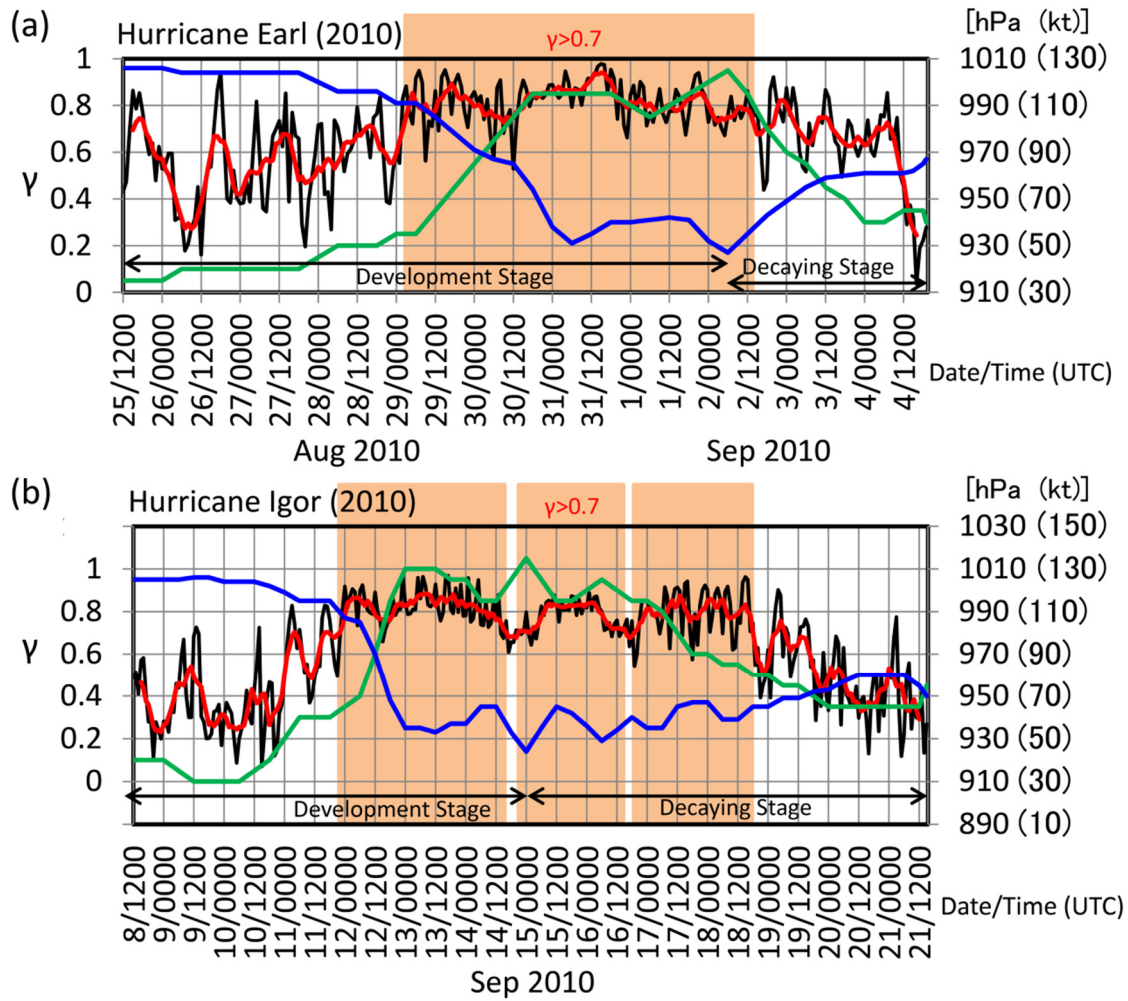


Fig. 3.2: (a) As Fig. 3.1a, but for Hurricane Earl (2010). (b) As Fig. 3.1a, but for Hurricane Igor (2010).

Table 3.1: Uncertainty evaluations of γ due to inaccurate TC center locations. Values of γ calculated by using the original center, and mean and standard deviation (Std dev) γ calculated by using the 25 centers (the 24 centers plus the original center) are provided. See text for details.

Case	γ	Mean γ	Std dev γ
Fig. 3.1b	0.39	0.38	0.08
Fig. 3.1c	0.66	0.64	0.11
Fig. 3.1e	0.60	0.55	0.05
Fig. 3.1f	0.92	0.92	0.02

Table 3.2: Differences in γ among satellites used in the GSMaP data. Here the hourly γ is classified according to which microwave satellite data mainly ($> 50\%$) covered a $2^\circ \times 2^\circ$ square area around a TC. Cases in which multiple microwave satellite covered the area simultaneously are excluded. The number of samples (N), mean and standard deviation (std dev) hourly γ , and mean and standard deviation of the 6-h mean γ at each satellite sensor are provided. The mean and standard deviation of the 6-h mean γ at each satellite sensor are computed by replacing the hourly γ with the 6-h mean γ . MHS stands for Microwave Humidity Sounder.

Satellite/Sensor	N	Mean γ	Std dev γ	Mean of 6-h mean γ	Std dev of 6-h mean γ
Temporal interpolation by IR imagery	25561	0.70	0.20	0.67	0.18
TRMM/TMI	1818	0.57	0.22	0.64	0.19
ADEOS-II/AMSR	48	0.51	0.22	0.60	0.20
Aqua/AMSR-E	746	0.53	0.21	0.66	0.18
GCOM-W/AMSR2	404	0.44	0.21	0.63	0.18
GPM-Core/GMI	150	0.48	0.21	0.61	0.18
DMSP-F13/SSM/I	778	0.57	0.22	0.65	0.18
DMSP-F14/SSM/I	742	0.58	0.22	0.65	0.18
DMSP-F15/SSM/I	953	0.58	0.21	0.66	0.18
DMSP-F16/SSMIS	1018	0.59	0.20	0.64	0.19
DMSP-F17/SSMIS	660	0.59	0.21	0.63	0.19
DMSP-F18/SSMIS	636	0.58	0.21	0.65	0.18
DMSP-F19/SSMIS	77	0.59	0.20	0.65	0.17
NOAA-15/AMSU-A/B	1270	0.68	0.19	0.67	0.18
NOAA-16/AMSU-A/B	1241	0.69	0.18	0.70	0.17
NOAA-17/AMSU-A/B	1168	0.68	0.20	0.67	0.18
NOAA-18/AMSU-A/MHS	1353	0.67	0.21	0.65	0.19
NOAA-19/AMSU-A/MHS	796	0.65	0.22	0.65	0.19
MetOp-A/AMSU-A/MHS	1344	0.65	0.21	0.65	0.19
MetOp-B/AMSU-A/MHS	588	0.67	0.21	0.65	0.18

fluctuates with a period of a few hours (Figs. 3.1a and 3.1d). When the hourly γ is replaced by the 6-h mean γ , differences in γ among sensors almost disappear (Table 3.2). Although the problems of data quality and TC center deviations are limitations of this study, we will use 6-h mean values of γ to examine the relationships between future TC intensity changes and current values of intensity and γ .

For the four cases shown in Figs. 3.1 and 3.2, during the development stage, the maximum sustained wind speed (central pressure) largely increases (decreases) when the 6-h mean γ (hereafter referred to as simply γ) persists above 0.7 for more than 12 h, whereas the maximum sustained wind speed (central pressure) stops increasing (decreasing) when γ temporarily decreases to less than 0.7. Although Rogers et al. (2015) reported that asymmetries, including convective bursts, persisted during RI of Hurricane Earl, γ in this study have in fact exceeded 0.7 immediately before the onset of RI (Fig. 3.2a). In the cases of Hurricane Earl and Igor, minor intensity changes such as those due to eyewall replacement cycles after RI show little correlation with changes of γ . During the decay stage, γ is not correlated to intensity changes.

Because the relationship between intensity changes and γ during the development stage is seen in TCs not only in the WNP basin but also in the North Atlantic basin, depending on the current intensity, the relationship is not likely to be dependent on either the basin in which TCs occur or the quality of the best track data used.

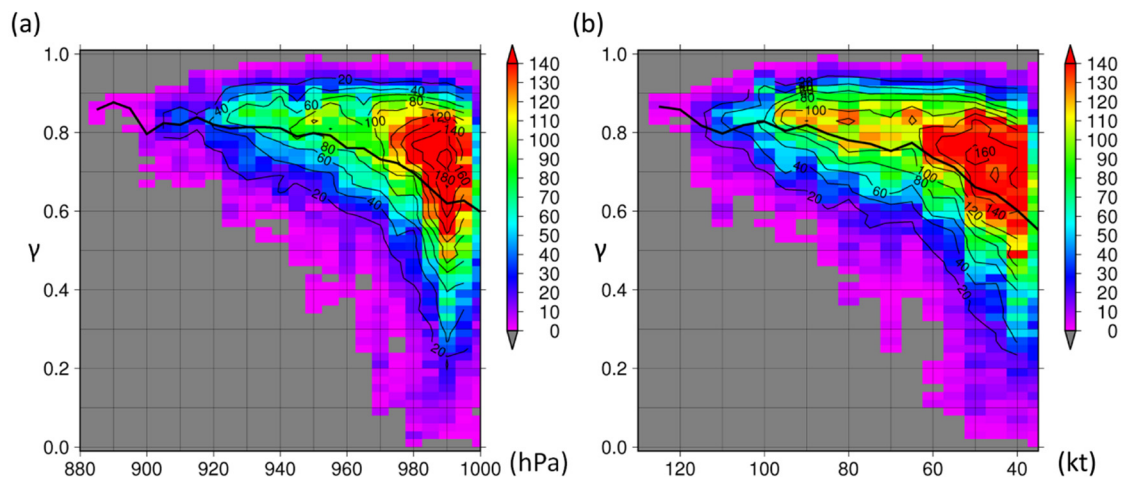


Fig. 3.3: Frequency distribution (number of samples, colors and contours) of the current intensity (horizontal axis) and γ (vertical axis) during the development stage: (a) central pressure and (b) maximum sustained wind. The black curve shows the averaged γ at each current intensity. Samples in (a) are the same as in Fig. 3.5b.

b. Relationship between TC intensity changes and axisymmetry

In this subsection, we first show the relationship between current intensity and γ , and the relationship between intensity change and γ . Then, we present the relative contribution of axisymmetric and asymmetric components of the rainfall rate to intensification. Finally, we present the relationship between RI and γ .

1) Current intensity versus axisymmetry

The frequency distribution of current intensity and γ during the development stage shows a peak around current intensities of 990 hPa or 50 kt and γ of ~ 0.73 (Fig. 3.3). Roughly speaking, averaged γ at each current intensity shows that within the current intensity range of 1000 hPa to 955 hPa (35 kt to 90 kt), γ increases with the current intensity, which implies that within these intensity ranges, the structure of many TCs changes from asymmetric to axisymmetric. In addition to this structural change, an increase in the azimuthally averaged rainfall rate contributes to the increase of γ at around these intensities. In contrast, at central pressure < 955 hPa (maximum sustained wind > 90 kt), mean γ is almost constant. The number of cases with current intensity < 920 hPa (> 110 kt) and the number of cases with γ greater than 0.95 are small. In addition, γ ranges widely at each current intensity.

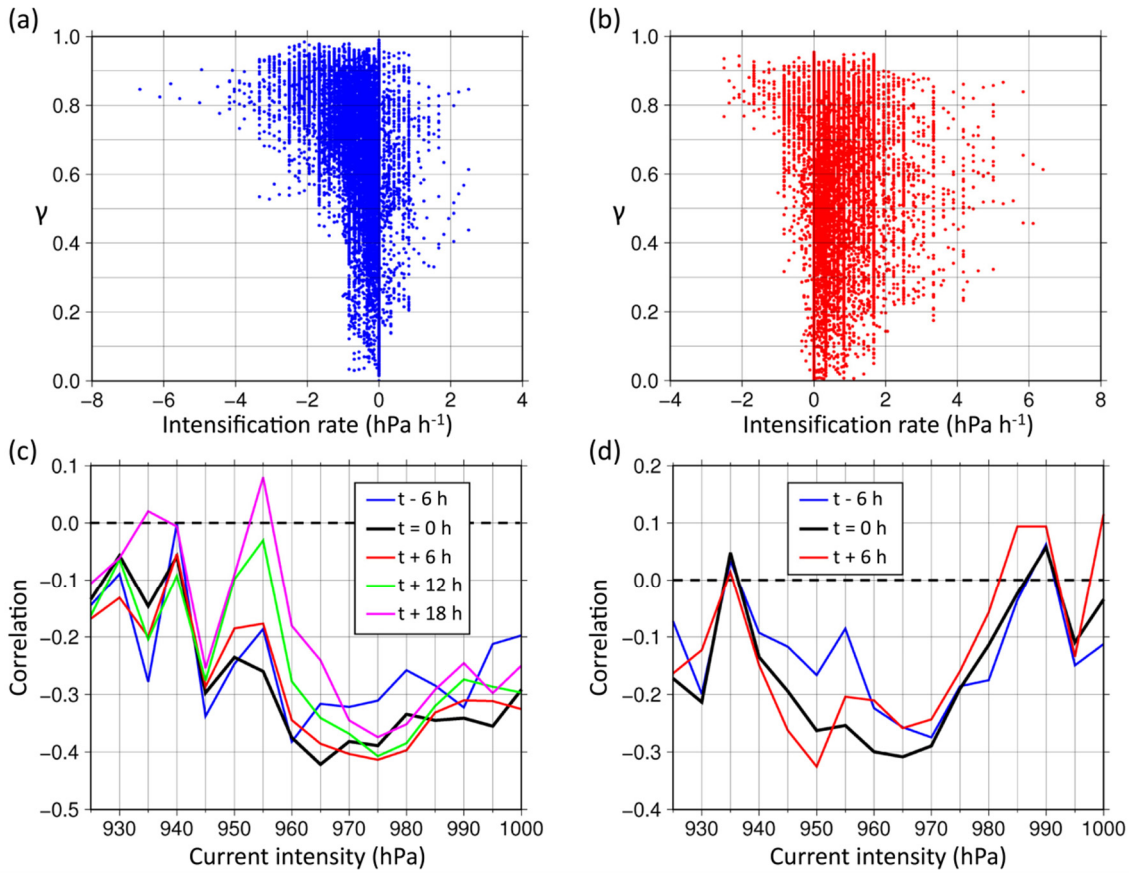


Fig. 3.4: (a) Scatter diagram of the intensification rate at $t = 0$ h versus γ during the development stage. (b) As (a), but for the decay stage. (c) Correlations between the intensification rate at $t - 6$ h, $t = 0$ h, $t + 6$ h, $t + 12$ h and $t + 18$ h, and γ at each current intensity during the development stage. The dashed line is drawn at zero. (d) As (b), but at $t - 6$ h, $t = 0$ h and $t + 6$ h during the decay stage. Note that the dataset used here includes temporary weakening periods during the development stage.

2) Intensity change versus axisymmetry

Next, we examine the intensification rate at different times in relation to the current intensity and γ during the development stage. Note that negative values of the intensification rate indicate the decrease in the central pressure. Here, we include temporary weakening periods during the development stage in the dataset of Figs. 3.4a and 3.4c to calculate correlations between the intensification rate and γ . The scatter diagram of the intensification rate at the current time ($t = 0$ h) and γ shows that the intensification rate is negatively correlated with γ , indicating that intensification tends to occur when γ is high, although the data are widely scattered (Fig. 3.4a). The intensification rate at $t = 0$, $t + 6$ h and $t + 12$ h has relatively high correlations with γ for intensities of 960–1000 hPa (Fig. 3.4c). In addition, this relationship continues to be relatively strong after $t + 12$ h for intensities > 970 hPa.

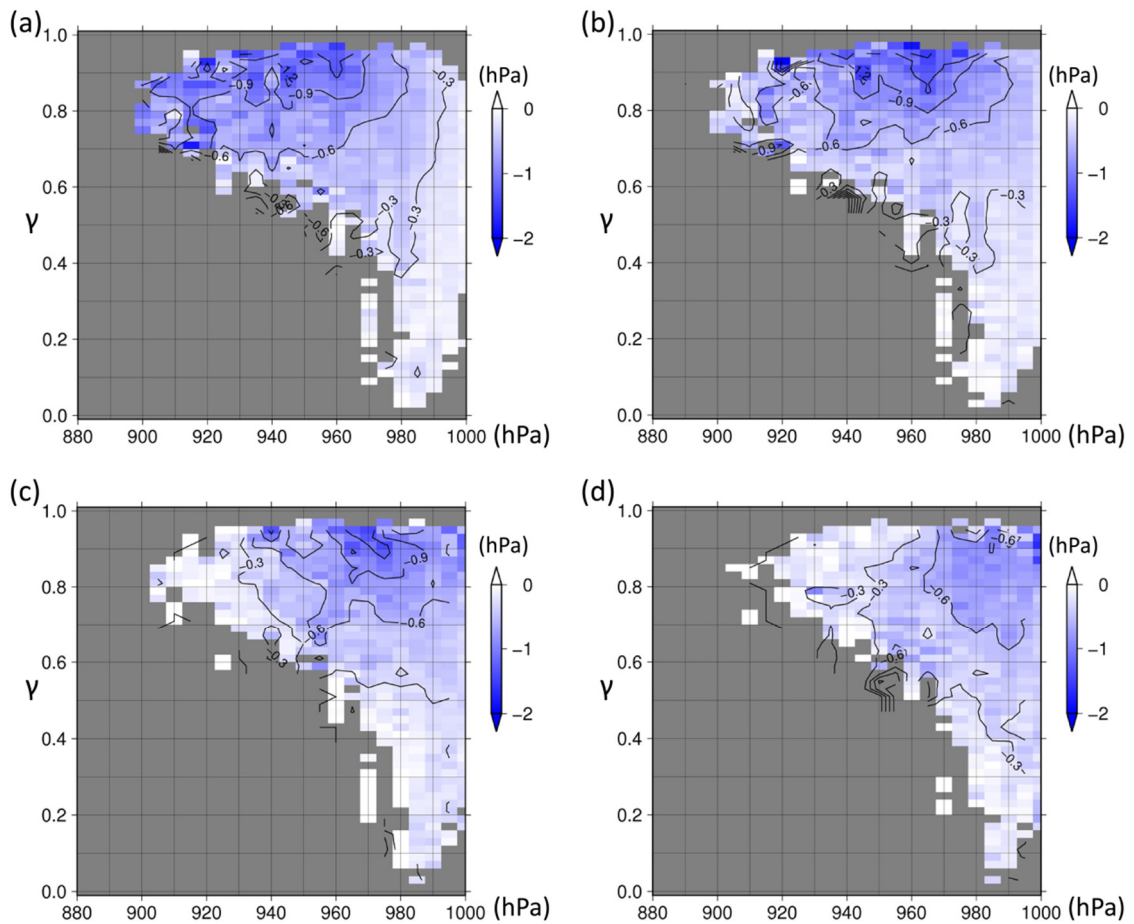


Fig. 3.5: Intensification rate (hPa per hour, colors and contours) relative to the current intensity (central pressure, horizontal axis) and γ (vertical axis) during the development stage: (a) $t - 6$ h, (b) $t = 0$ h, and (c) $t + 12$ h and (d) $t + 24$ h. Grids containing 5 or more cases are colored.

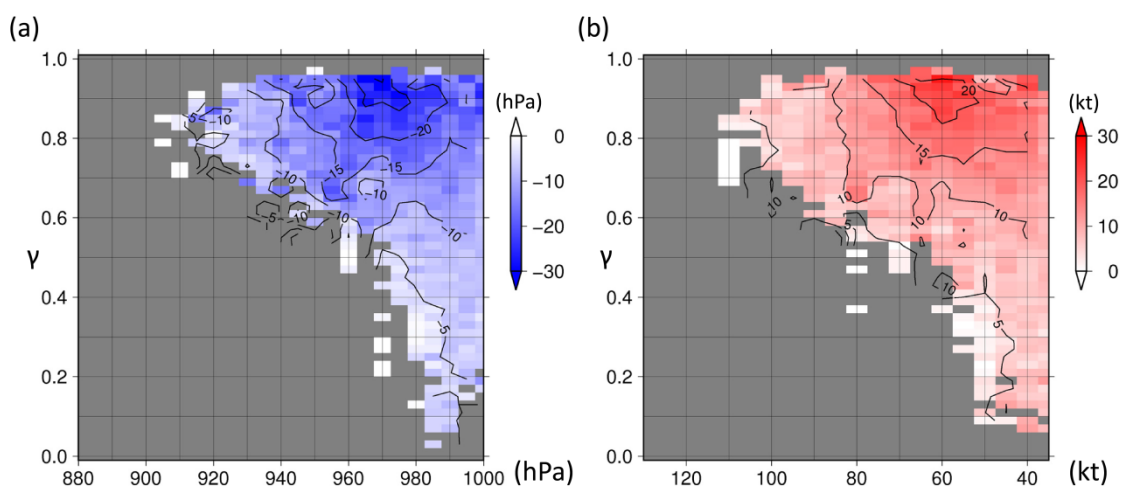


Fig. 3.6: Intensity changes in the next 24 h (colors and contours) relative to the current intensity (horizontal axis) and γ (vertical axis) during the development stage: (a) central pressure and (b) maximum sustained wind. Grids containing 5 or more cases are colored.

The scatter diagram during the decay stage shows that, compared with the development stage, the data are displaced in the x direction by about + 1 hPa h⁻¹ with a wider spread (Fig. 3.4b). Reintensifying TCs have relatively high γ (Fig. 3.4b) and the decay rate is slightly correlated with γ if including reintensifying TCs (Fig. 3.4d). However, within only weakening TCs there is little relationship between the decay rate and γ (Fig. 3.4b).

Figure 3.5 shows the relationship between the intensification rate at different times and current intensity and γ . On average, as γ becomes higher, the intensification rate at $t = 0$ h and $t + 12$ h tends to increase for TCs with current intensities of 945–995 hPa (Figs. 3.5b and 3.5c) (85–40 kt, not shown). This relationship, though less pronounced, can also be seen at $t - 6$ h, but at intensities < 945 hPa (> 85 kt, not shown) γ is uniformly relatively high (Fig. 3.5a). These findings show that when TCs finally reach their maximum intensity γ is relatively high because intensity and γ increase together. In other words, the intensification rate of most TCs that reach strong intensities < 945 hPa is relatively large at $t - 6$ h regardless of γ . Consistent with the correlations in Fig. 3.4c, the relationship still remains at $t + 24$ h for current intensities of 970–995 hPa (Fig. 3.5d) (60–40 kt, not shown).

Because during the development stage the intensification rate at $t = 0$ h, $t + 12$ h and $t + 24$ h is correlated to both current intensity and γ , there is also a relationship between the intensity change in the next 24 h and current intensity and γ (Fig. 3.6). This relationship is particularly clear for TCs with current central pressures (maximum winds) between 945 hPa and 995 hPa (85 kt and 40 kt) during the development stage. These intensity ranges are, in general, much weaker than the maximum potential intensity (MPI; e.g., Emanuel 1986; DeMaria and Kaplan 1994). Correlations are also relatively high for the intensity change in the next 12 and 24 h (Fig. 3.7). For intensities > 965 hPa and < 70 kt, the relationship of the intensity change in the next 36 h and 48 h with current intensity and γ continues to be relatively strong, as long as a TC is still in the development stage (Fig. 3.7), because the intensification rate at $t + 36$ h is still correlated to the current intensity and γ (not shown). These results suggest that once a TC becomes axisymmetric, it can keep its axisymmetric structure and can continue to intensify provided that a favorable environment for intensification exists.

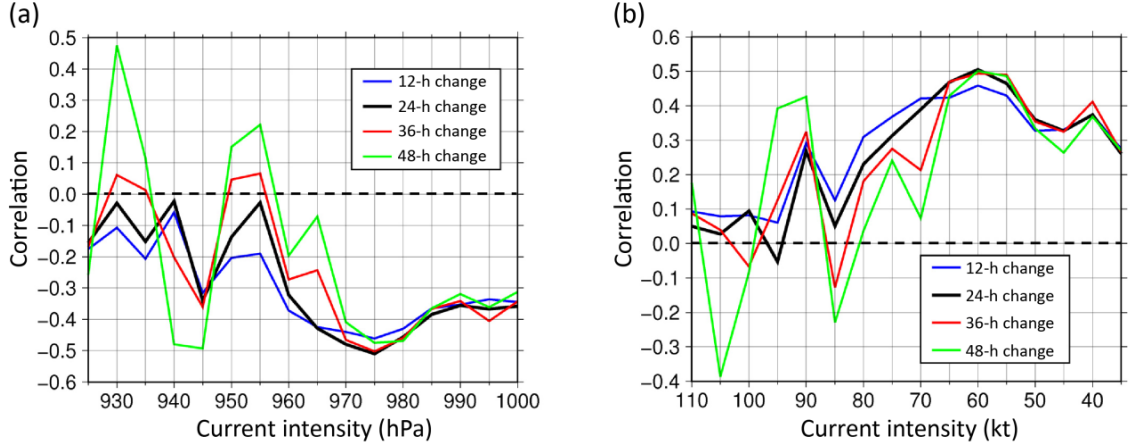


Fig. 3.7: Correlations between the intensity change in the next 12 h, 24 h, 36 h and 48 h, and γ at each current intensity during the development stage: (a) central pressure and (b) maximum sustained wind. Note that the dataset used here includes temporary weakening periods during the development stage. The dashed line is drawn at zero.

3) Relative contribution of axisymmetric and asymmetric components to intensification

Because γ used in this study depends not only on the magnitude of the asymmetric component (ϕ') of the rainfall rate but also on that of the axisymmetric component ($\bar{\phi}$) (Eq. (3.2)), we examine how these components contribute to intensification. Here, the asymmetric term, as a representative of the asymmetric component, is calculated as follows:

$$\int_0^{2\pi} |\phi'(r, \lambda, z, t)| d\lambda / 2\pi \quad (3.3)$$

We normalize values of the axisymmetric term (same as the axisymmetric component) to 19.1 mm h^{-1} , and those of the asymmetric term to 10.6 mm h^{-1} , determined as 98th percentiles of the distributions of axisymmetric and asymmetric values during the development stage to better illustrate grids containing 5 or more cases in Fig. 3.8. The distribution of intensity changes in the next 24 h relative to the 6-h mean axisymmetric and asymmetric terms in cases with a current intensity from 945 hPa to 995 hPa shows that the magnitudes of the asymmetric and axisymmetric terms generally increase concurrently (Fig. 3.8a). When the normalized axisymmetric term ranges from 0.1 to 0.7 and the normalized asymmetric term ranges from 0.1 to 0.6, in general, the larger the axisymmetric term and the smaller the asymmetric term are, the larger the intensity change is. The intensity changes in the next 24-h relative to current intensity (central pressure) and the axisymmetric term of the rainfall rate during the development stage (Fig. 3.8b) show that the axisymmetric term of the rainfall rate and the intensity change are

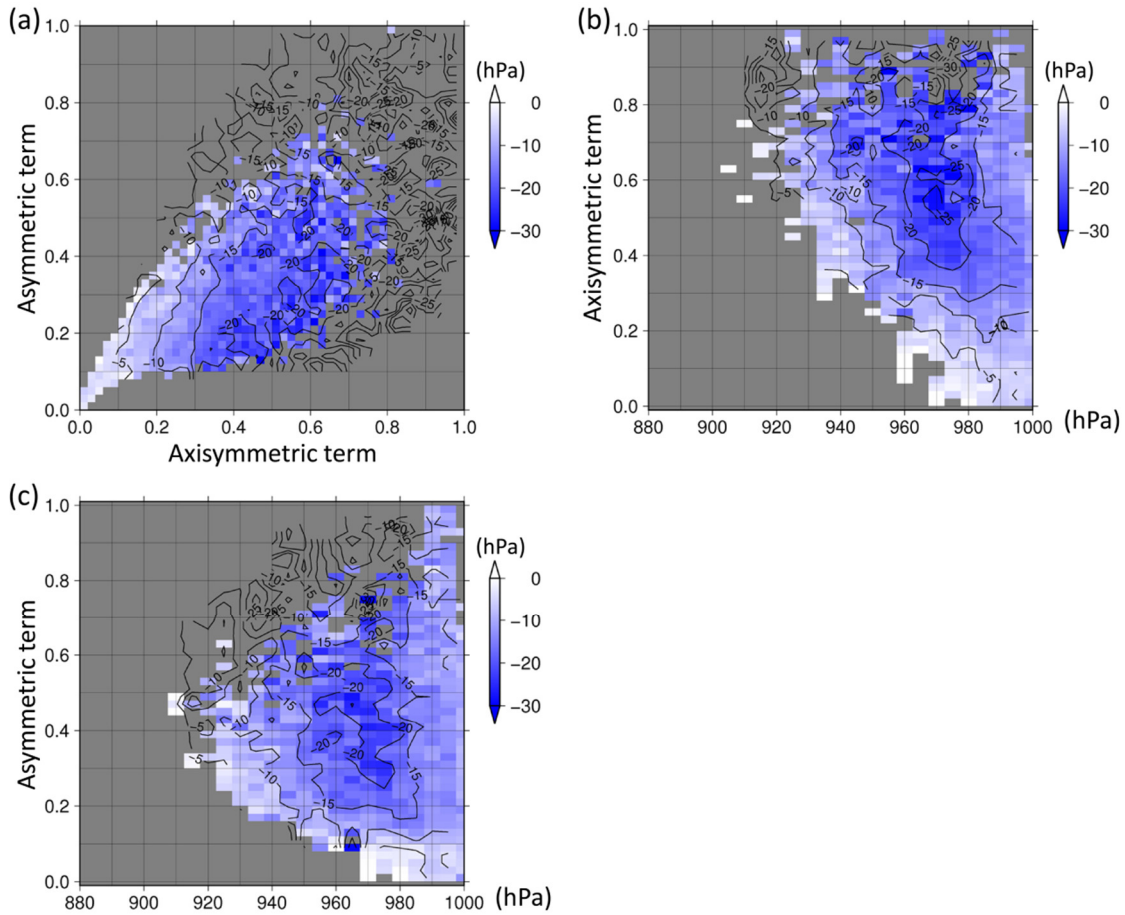


Fig. 3.8: Intensity changes (central pressure, colors and contours) in the next 24 h relative to (a) the 6-h mean axisymmetric (horizontal axis) and asymmetric (vertical axis) terms of the rainfall rate, (b) the current intensity (horizontal axis) and the 6-h mean axisymmetric term of the rainfall rate (vertical axis), and (c) the current intensity (horizontal axis) and the 6-h mean asymmetric term of rainfall rate (vertical axis), during the development stage. Only samples with a current intensity from 945 hPa to 995 hPa are included in (a). The values of axisymmetric term have been normalized to 19.1 mm h^{-1} , and those of the asymmetric term have been normalized to 10.6 mm h^{-1} . Grids containing 5 or more cases are colored.

correlated for current intensities of 935–980 hPa. It is also notable here that at a given current intensity, the intensity change also becomes larger as the asymmetric term becomes larger (Fig. 3.8c). This result follows from the fact that the asymmetric term increases with an increase in the axisymmetric term, although an increase in the asymmetric term is generally smaller than that in the axisymmetric term (Fig. 3.8a). Therefore, γ is a useful metric that can express the relative contribution of the axisymmetric and asymmetric terms to intensity changes.

Although Fig. 3.8 does not show if the relative contribution is associated with RI, the findings are similar to the results of Kaplan et al. (2010), who constructed an RI index by investigating differences in two

predictors between RI and non-RI cases; one predictor was the percentage of the area between radii of 50 km and 200 km from the TC center covered by IR TBs colder than $-30\text{ }^{\circ}\text{C}$ (PX30), and the other was the standard deviation of IR TBs in the same area (SDBT). They showed that the RI cases had higher PX30 values and lower SDBT values.

4) RI versus axisymmetry

The relationships during the development stage raise the following question: to what extent is γ associated with RI? We therefore investigate the relationship between RI and γ . We define RI as an intensification rate of at least 30 hPa over a 24-h period. This threshold is the 95th percentile of 24-h central pressure changes for WNP TCs, in the same way that Kaplan and DeMaria (2003) defined RI for Atlantic basin TCs using the maximum wind speed (see the Appendix B for details). In real cases, even if current environmental conditions and current inner-core structures are very favorable for RI, the favorable environmental conditions may not be maintained for very long. If the vertical wind shear suddenly becomes strong while the TC is developing, then both γ and the intensification rate will decrease. According to Miyamoto and Takemi (2013, 2015), the time after axisymmetrization of the PV field must be sufficient for the onset of RI. Thus, in real cases, it may be difficult to realize RI if high γ is only transient.

On the basis of this reasoning, we examine the relationship between RI and γ using the 24-h mean γ (i.e., an average between $t - 12$ h and $t + 12$ h), instead of the 6-h mean γ , though in hindsight. Figure 3.9c demonstrates that the 24-h mean γ has negative correlations < -0.4 with the 24-h intensity change with a time lag of 0–12 h for current intensities of 960–990 hPa. Then, we compare the frequency distributions of current intensity and the current 24-h mean γ between RI cases and non-RI cases (Figs. 3.9a and 3.9b). The 24-h intensity change used to classify each case is calculated as the difference between $t - 6$ h and $t + 18$ h (i.e., a 6-h lag). Most RI cases (~89%) are distributed between current intensities from 925 hPa to 985 hPa and 24-h mean γ values from 0.7 to 0.9. This result suggests that RI can occur when the current intensity is relatively far from the MPI but it rarely occurs when the current intensity is especially weak, as shown previously by Kaplan and DeMaria (2003). Although many non-RI cases are distributed within the same ranges as the RI cases, the average 24-h mean γ at each current intensity is much higher in RI cases than in non-RI cases for current intensities of 960–990 hPa. A scatter diagram (Fig. 3.9d) of the 24-h mean γ and intensity

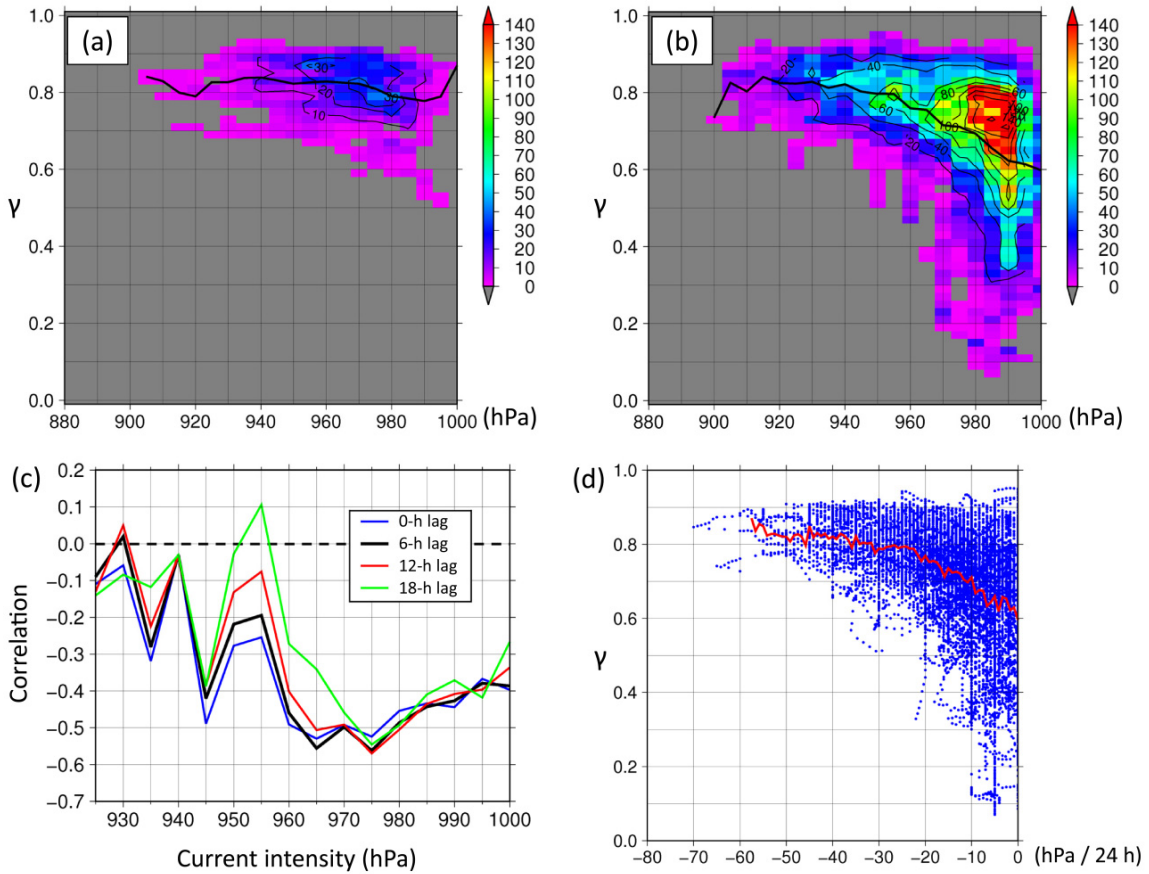


Fig. 3.9: (a) Frequency distribution (number of samples, colors and contours) of RI cases relative to the current intensity (central pressure, horizontal axis) and the 24-h mean γ (vertical axis). The black line indicates γ averaged over each current intensity. (b) As (a), but of non-RI cases. (c) Correlations between the 24-h mean γ and the 24-h intensity change with a time lag of 0 h (i.e., from $t - 12$ h to $t + 12$ h), +6 h, +12 h and +18 h at each current intensity during the development stage. Note that the dataset used here includes temporary weakening periods during the development stage. The dashed line is drawn at zero. (d) Scatter diagram of intensity changes from $t - 6$ h to $t + 18$ h versus the 24-h mean γ . Only samples with a current intensity from 945 hPa to 995 hPa are included. The red line indicates the average value of γ at each intensity change.

changes from $t - 6$ h to $t + 18$ h in cases with a current intensity from 945 hPa to 995 hPa (the range in which the relationship between intensity changes and γ is large; see Fig. 3.6) shows that, in general, as γ increases, the intensity change becomes larger, although the data are widely scattered.

One reason for the wide scatter may be differences in environmental conditions among cases. For example, even if vertical wind shear is weak and the internal conditions of a TC are favorable (i.e., relatively high γ), a TC that has almost reached its MPI cannot intensify further. In addition, TCs that intensify rapidly under relatively strong vertical wind shear with asymmetric structures (i.e., relatively low γ) (e.g., Molinari et al. 2004; Molinari and Vollaro 2010) might contribute to the wide scatter. Moreover, because γ is averaged within a 100 km radius, its value would depend on the horizontal scale of each TC; thus, differences in horizontal scale would also contribute to the wide scatter. Finally, a variety of observational errors by satellites, sensor biases among satellites, analysis errors in the GSMaP and the best track data could also cause the wide scatter.

3.3. Discussion

The relative relationship between the axisymmetric and asymmetric terms of the rainfall distribution and intensity changes during the development stage was such that the intensity change was larger when the axisymmetric term was larger and the asymmetric term was smaller (Fig. 3.8a). The axisymmetry, γ , of the rainfall distribution, which is a metric that reflects these relative relationships, could be correlated to subsequent intensity changes, but this relationship was strongly dependent on the current intensity. The results of this study strongly support from an observational perspective the finding of Miyamoto and Takemi (2013) that the axisymmetrization of a TC structure can lead subsequently to significant intensification. In addition, considering that the distribution of the rainfall rate is quite similar to that of diabatic heating (Zagrodnik and Jiang 2014), the results of this study are also very well consistent with the findings of Nolan and Grasso (2003) and Nolan et al. (2007) that the axisymmetric component of diabatic heating is much more important for vortex intensification than the asymmetric component, and that the efficiency of the intensification increases with the vortex strength, provided that the current intensity is well below the MPI. Because the asymmetric component increased along with the axisymmetric component, intense asymmetric convection may also contribute to intensification through an increase in the axisymmetric component of diabatic heating.

Axisymmetry is an indicator of a TC's inner-core structure, not an environmental parameter. However, axisymmetry can be changed by environmental vertical shear or by dry air intrusion (e.g., Riemer et al. 2010; Reasor et al. 2013) as well as by internal dynamics. In addition, a TC vortex can have resiliency against vertical shear that helps it retain its axisymmetry (e.g., Reasor and Montgomery 2001; Reasor et al. 2004). The degree of resiliency depends on the inertial stability, that is, TC intensity (e.g., DeMaria 1996; Jones 1995). Although it is difficult to determine if a change of γ should be attributed to internal TC dynamics or to environmental forcing, it might be interesting in a future study to further examine the relationship between γ and the magnitude of vertical wind shear.

Although individual intensification rates were widely scattered in relation to the parameter γ alone, it might be possible to explain intensity changes more adequately by using γ in combination with other parameters in a multiple regression analysis. For example, by adding γ -related predictors to

the Statistical Hurricane Intensity Prediction Scheme (SHIPS) model (DeMaria and Kaplan 1994, 1999; DeMaria et al. 2005) and to the RI index (Kaplan et al. 2010) might improve their forecast skill. We will investigate the possibility to improve intensity forecast by incorporating γ into the SHIPS model in Chapter 6. The SHIPS model has already incorporated IR TB-based parameters that represent axisymmetry to some extent (PX30 and SDBT; see section 3.2b; DeMaria et al. 2005). However, it should be noted that IR TBs, which are temperatures at cloud-top heights, cannot be assumed to be correlated with the amount of diabatic heating, whereas the rainfall rate used in this study can.

3.4. Summary

The relative relationship between axisymmetric and asymmetric components of TC rainfall distribution and TC intensity changes, including during the decay stage, has not been comprehensively investigated in real cases. Based on a study by Miyamoto and Takemi (2013), we investigated the relationship between TC future intensity change during the development and decay stages and both current intensity (both central pressure and maximum sustained wind) and axisymmetry deduced from hourly GSMaP data. The GSMaP data are satellite-derived rainfall estimates in the region from 60°S to 60°N with a resolution of 0.1°. As defined in this study, axisymmetry is a metric positively correlated with the magnitude of the axisymmetric component of the rainfall rate and negatively correlated with the magnitude of the asymmetric component. For samples, we used all 380 TCs that existed in the WNP basin from 2000 to 2015.

Case studies showed that a TC tended to intensify rapidly when the axisymmetry persisted at relatively high values for more than 12 h. In general, during the development stage, the intensification rate at $t = 0$ h, $t + 6$ h and $t + 12$ h was correlated to both the current intensity and axisymmetry. On average, the higher the axisymmetry of the TC, the larger the intensity change was in the next 24 h in the case of TCs with current central pressures (maximum sustained winds) between 945 hPa and 995 hPa (85 kt and 40 kt). In addition, for current intensities > 965 hPa and < 70 kt, the relationship of the intensity change in the next 36 h and 48 h with current intensity and axisymmetry continued to be relatively strong. These results suggest that once a TC becomes axisymmetric, it can keep its axisymmetric structure and can continue to intensify provided that a favorable environment for intensification exists. During the decay stage, although reintensifying TCs had relatively high axisymmetry, there was no relationship between the decay rate and axisymmetry. The mean axisymmetry of TCs experiencing RI was much higher than that of non-RI TCs for current intensities of 960–990 hPa. The relative relationship between axisymmetric and asymmetric terms showed that the larger the axisymmetric term and the smaller the asymmetric term, the larger the intensity change was, although the asymmetric term generally increased with the increase of the axisymmetric term. The metric of axisymmetry used in this study could properly express this relative relationship. The new observational evidence presented here is consistent with the findings of previous theoretical studies of

the intensification process, which emphasize the role of the axisymmetric component of diabatic heating.

Chapter 4: Reintensification and eyewall formation in strong shear: A Case Study of Typhoon Noul (2015)

4.1. Motivation

Typhoon Noul (2015) appeared to reintensify when it passed near Ishigaki Island from 1200 UTC 11 May to 1800 UTC 11 May 2015 (Fig. 1a). This reintensification was not captured in the best track data of the Regional Specialized Meteorological Center (RSMC) Tokyo (Fig. 4.1b). However, vigorous convection occurred downshear-left (Fig. 4.2), and then rainfall structure of the eyewall changed from asymmetry to symmetry (Fig. 4.3) in the presence of vertical wind shear greater than 10 m s^{-1} (Fig. 4.4). We will show evidence of the reintensification in section 4.3.

Strong vertical wind shear causes the structure of the eyewall to become asymmetric (e.g., Chen et al. 2006) and is generally a hostile environmental condition for TCs to intensify (e.g., Paterson et al. 2005; Wang et al. 2015). Why could Noul reintensify and have a symmetric eyewall despite vertical wind shear greater than 10 m s^{-1} ? To address this question, high-temporal observations are needed. Fortunately, surface observations around Ishigaki Island and data from a Japan Meteorological Agency (JMA) operational C-band Doppler radar installed at Ishigaki Island provided a great opportunity to examine Noul's reintensification.

The purpose of this study was to document the evolution of the inner-core structure of Noul and examine what processes were involved in Noul's reintensification and the formation of a symmetric eyewall in the presence of a relatively strong shear environment.

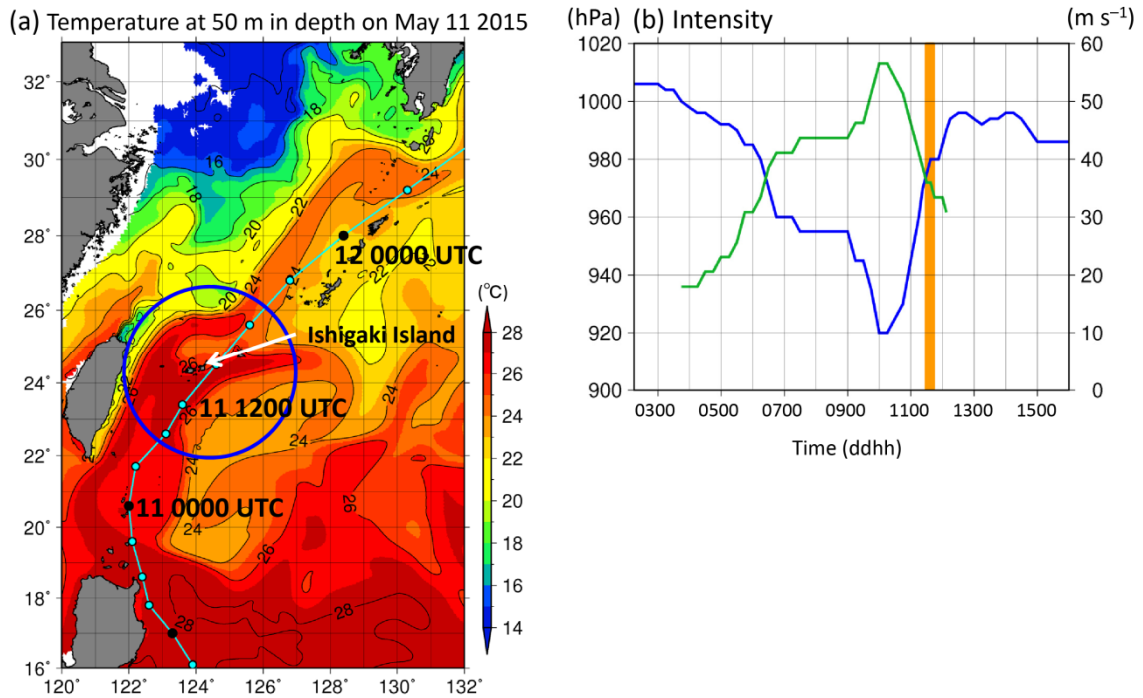


Fig. 4.1: (a) Ocean temperatures at 50 m depth on 11 May 2015 and Noul's track; light blue circles show the track at 6-h intervals, and black circles show the track at 1-day intervals. The large blue circle centered at Ishigaki Island denotes the range of the Ishigaki Doppler radar, ~ 200 km. The ocean temperature data were provided by the JMA. (b) Time evolution of Noul's intensity: green line, maximum wind; blue line, central pressure. RSMC Tokyo's best track data do not include maximum wind speeds for a TC categorized as a tropical depression. The vertical orange bar indicates the period focused on in this study.

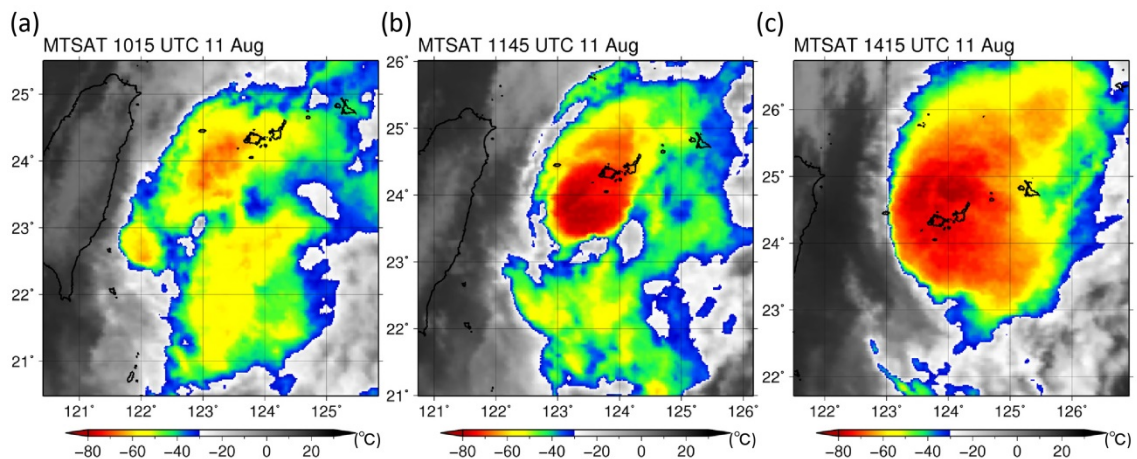


Fig. 4.2: Infrared brightness temperatures (at 10.3–11.3 μm) from the Multi-functional Transport Satellite (MTSAT-2) geostationary satellite.

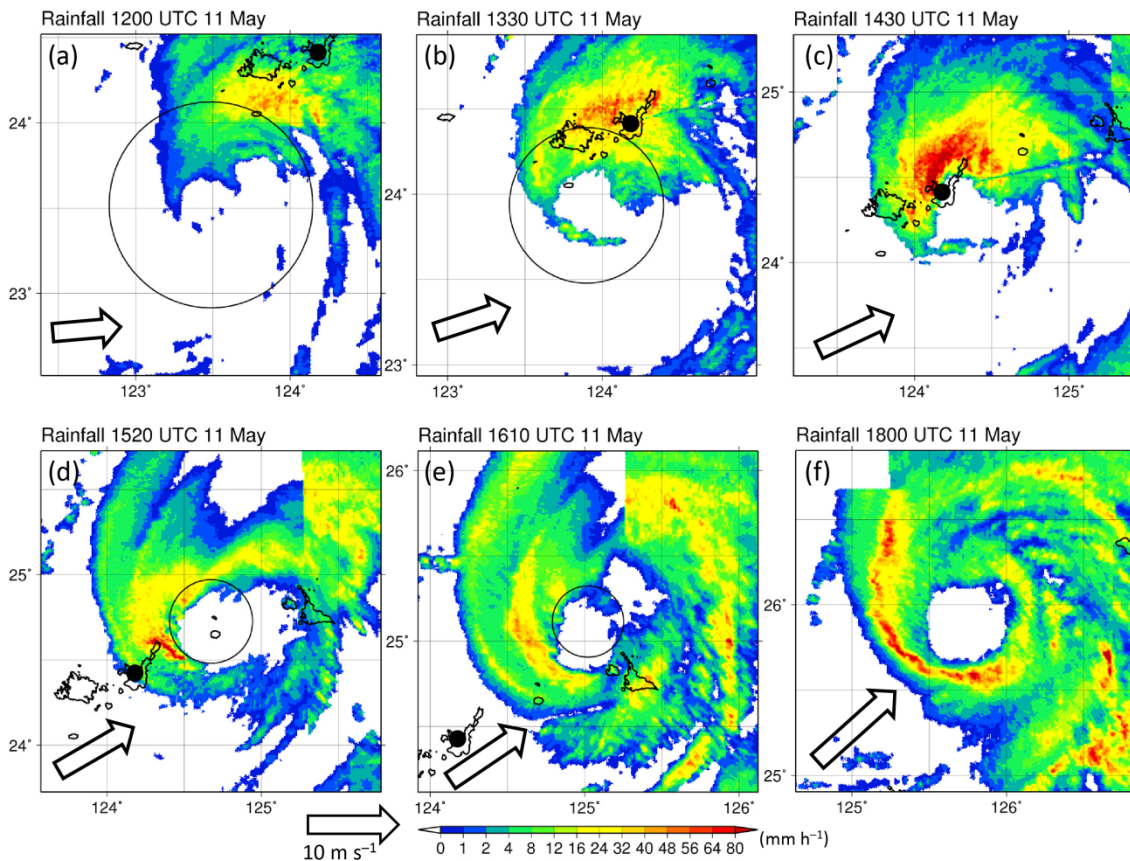


Fig. 4.3: Radar composite rainfall rate provided by the JMA. The black bold arrow shows the 850–200-hPa shear vector. The black dot indicates the radar site. The black circle denotes the 1-km RMW.

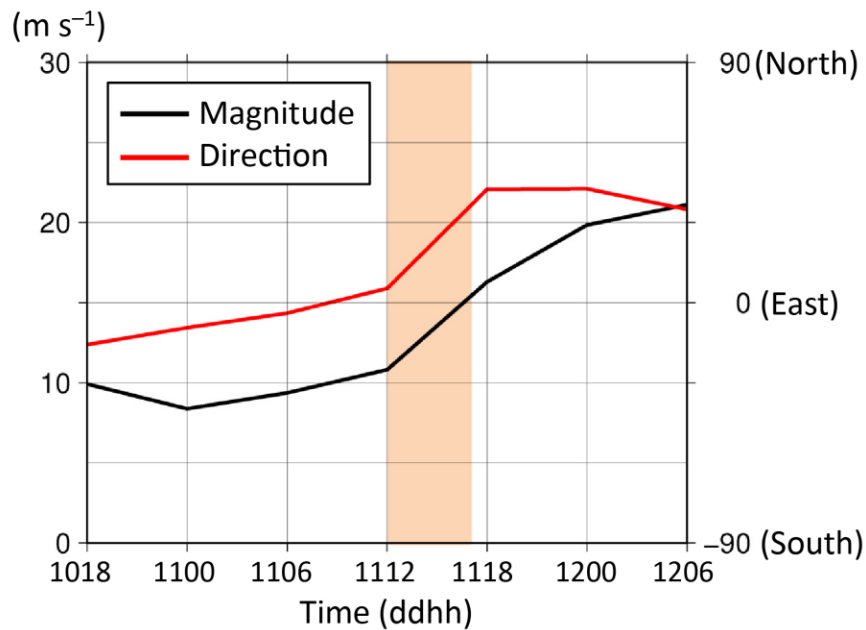


Fig. 4.4: Vertical wind shear (black line) and its heading direction (red line) between 200 and 850 hPa averaged within 500 km from the center. The shear was calculated by using JRA-55 data (Kobayashi et al. 2015). The shading indicates the radar observation period.

4.2. Data, method and accuracy evaluation

Data used in this study are surface observations provided by the JMA, C-band operational Doppler radar data observed at Ishigaki Island, radar composite rainfall data provided by the JMA, Infrared (IR) brightness temperatures (at 10.3–11.3 μm) from the Multi-functional Transport Satellite (MTSAT-2) geostationary satellite, and JRA-55 atmospheric reanalysis data (Kobayashi et al. 2015). The surface observations include maximum gust wind, temperature, dew-point temperature (or relative humidity), precipitation, station pressure and sea level pressure. Here, the maximum gust wind is a maximum of 3-sec mean wind observed during each 1-min period. As we show in subsection 4.2b, the maximum gust wind is informative to see the inner-core structure of Noul at the surface. Equivalent potential temperatures, θ_e , are calculated by using the formula of Bolton (1980). The Doppler observation parameters of the JMA radars are listed in Table 2.1.

We applied the ground-based velocity track display (GBVTD) technique (Lee et al. 1999) to Doppler velocity, V_D , data and retrieved the two-dimensional horizontal wind field at 1-km altitude intervals from 1 to 10 km of altitude for Noul. The dataset includes tangential winds with wavenumbers up to 3, and radial winds with wavenumbers up to 1 in storm-centered cylindrical coordinates. Details of the GBVTD-derived wind dataset are referred to Appendix A. The analysis period was from 1200 UTC 11 May to 1700 UTC 11 May 2015. The GBVTD technique can only retrieve the wind field at a range of radii between the storm center and the radar location and no V_D observations could be made in the eye region. For these reasons, no winds were retrieved while the radar site was located within the eye, which lasted about 1 h, from 1405 to 1450 UTC 11 May. For the GBVTD technique, the storm center is defined as the location that maximizes axisymmetric tangential wind, \bar{v} , on the scale of the RMW. We detected it by using the GBVTD-simplex center-finding method (Lee and Marks 2000; Bell and Lee 2012). In this method, the time continuity of the RMW, maximum \bar{v} , and center location is considered to find the center from candidates (for more details, see Bell and Lee 2012). The simplex search was performed at a range of radii between 30 and 60 km as a possible scale of the RMW. Note that there was uncertainty in the center-finding method when the TC approached the radar site within 60 km because the possible scale of the RMW was not sufficiently ensured. This is a limitation of finding the center in this study. In this study, we used the storm center at 1-km altitude for the GBVTD analysis

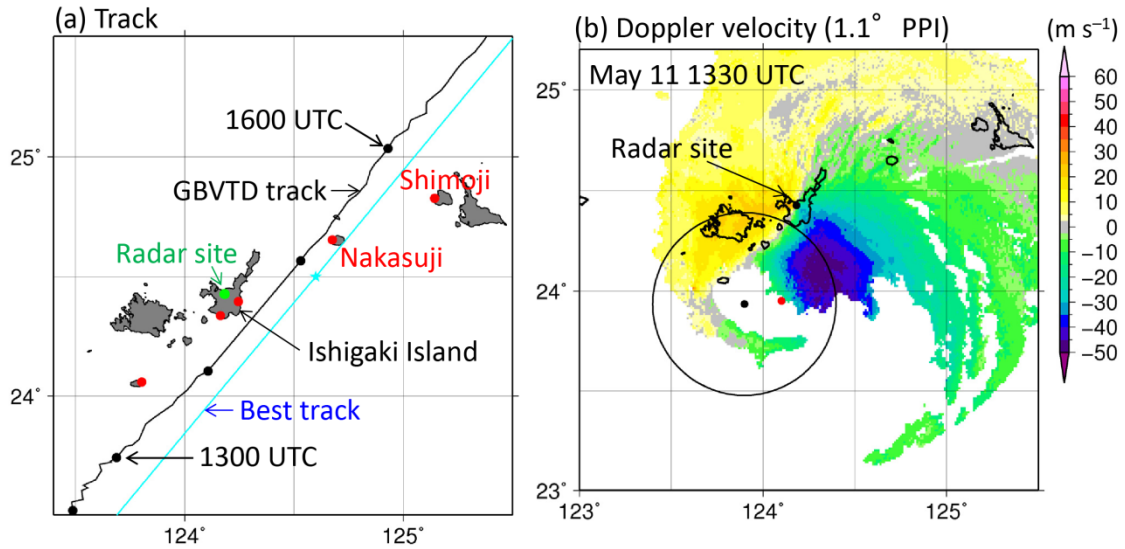


Fig. 4.5: (a) Noul's track; the black line shows the track from the GBVTD-simplex method at 5-min intervals and black circles are at 1-h intervals. The light blue line shows the track from RSMC Tokyo's best track data and the circle is the position at 1500 UTC 11 May. (b) The Doppler velocity PPI pattern at a 1.1° elevation angle at 1330 UTC 11 May. The black dot indicates the center detected in this study. The red dot indicates the temporally-interpolated center location of RSMC Tokyo's best track data. The black circle denotes the 1-km RMW.

at all altitudes to retrieve the axisymmetric component of the wind field.

Noul's track detected (Fig. 4.5a) was characterized as being displaced a few tens of kilometers westward from the location of the best track data. Here we'd like to justify the track we found in this study. Figures 4.3b and 4.5b confirm that the detected center lay in the center of a newly formed eyewall and in an appropriate location in V_D pattern. In contrast, the interpolated center position of the best track data was located just inside the eyewall, where V_D was $\sim 20 \text{ m s}^{-1}$ (Fig. 4.5b).

We evaluated the quality of the retrieved wind obtained by the GBVTD technique by defining a metric: the overall average of the root mean square difference (RMSD) between V_D resampled from the GBVTD-retrieved winds and observed V_D . Figure 4.6a shows that RMSDs generally range from 3 to 6 m s^{-1} , indicating larger values than those of other cases (e.g., Zhao et al 2012). Relatively poor quality of the GBVTD-retrieved winds is likely to stem from noise contamination including aliasing V_D , poor accuracy of the TC center finding, and complicated V_D pattern. For example, V_D pattern at 1621 UTC 11 May (Fig. 4.6b) shows that there were sea clutter around the radar site and noise throughout the V_D region, and that a dipole pattern associated with inbound and outbound Doppler velocities was distorted by complicated flow,

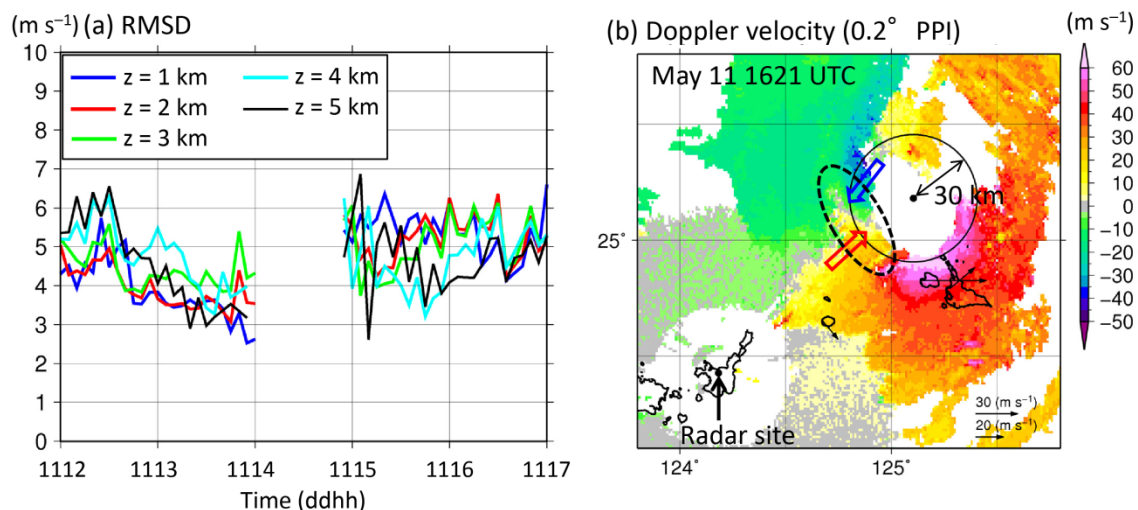


Fig. 4.6: (a) Time evolutions of the overall average of the RMSD between V_D resampled from the GBVTD-retrieved winds at altitudes from 1 to 5 km and observed V_D at altitudes from 1 to 5 km. (b) The Doppler velocity PPI pattern at a 0.2° elevation angle at 1621 UTC 11 May. The black circle denotes a radius of 30 km as a representative of the 1-km RMW. The small arrows show gust wind vector observed at around 1621 UTC. The red and blue bold arrows highlight directions of V_D . The dotted circle marks a convergence area that can be found in V_D field.

which can make the accuracy of the GBVTD-retrieved winds worse. Although we tried to remove all of clutter and noise, a fraction of them remained. Thus, the GBVTD-retrieved wind speed may have some uncertainty in this study. Because of that reason and limitations intrinsic in the GBVTD, we did not use GBVTD-retrieved asymmetric winds in this study. Instead, we used the maximum gust winds observed at weather stations.

4.3. Overview of Typhoon Noul

According to the best track data of RSMC Tokyo (Fig. 4.1b), Typhoon Noul attained a lifetime minimum central pressure of 920 hPa over the Philippine Sea at 0000 UTC 10 May 2015 (Fig. 4.1a). Then, it weakened rapidly while passing just northeast of Luzon Island. We focused the study on the period after 0900 UTC 11 May, a few hours before the increase in the P_{min} of Noul temporarily stopped, until 2100 UTC 11 May, when the weakening resumed.

Figure 4.7 shows that \bar{v} at 2-km altitude increased rapidly and attained $\sim 50 \text{ m s}^{-1}$ from 30 m s^{-1} during only 5 h from 1200 to 1700 UTC 11 May. This is evidence of Noul's reintensification. The reason why 1-km and 2-km \bar{v} were almost the same after 1545 UTC 11 May was that the number of plan position indicator (PPI) scans of the Ishigaki radar was limited when Noul was far from the radar site, which led to almost the same constant-altitude plan position indicator (CAPPI) data at 1-km and 2-km altitudes that were used for the GBVTD analysis.

Ocean temperatures at 50 m depth greater than 27°C prevailed south of Ishigaki Island (Fig. 4.1a). However, ocean temperatures at 50 m depth along the track after the passage near Ishigaki Island were less than 25°C . IR satellite imageries (Fig. 4.2) show that deep convections (convective bursts) started to occur on the north side of Noul, which was just on the downshear left side, at 1000 UTC 11 May just before sunset (1800 local time coordinated). Rainfall imageries (Fig. 4.3) show that eyewall structure transformed from asymmetry to symmetry within 6 h after the convective bursts. Noul was under an eastward shear of $10\text{--}12 \text{ m s}^{-1}$ around the onset of convective bursts (Fig. 4.4). Moving speed of Noul was very fast, greater than 10 m s^{-1} after 1300 UTC 11 May and exceeded 20 m s^{-1} after 1700 UTC 11 May. The gradual increase in shear and moving speed was caused by the influence of an upper-level jet associated with a deep trough over the mainland China (not shown).

It has been shown that TCs can intensify through interaction with an upper-level trough and associated jet (Molinari and Vollaro 1990; DeMaria et al. 1993; Hanley et al. 2001). A trough interaction involves that an upper-level jet preferably transfers negative angular momentum around a TC outward to spinup the outflow layer of a TC. The eddy momentum flux convergence (EFC) is often defined as follows:

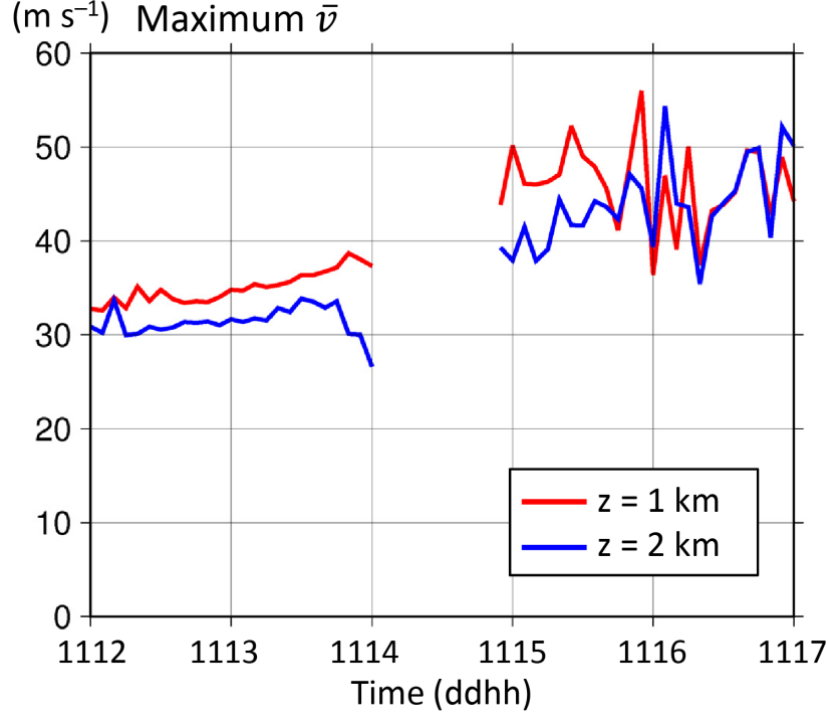


Fig. 4.7: Time evolutions of maximum azimuthal mean tangential wind speed at 1-km and 2-km altitudes.

$$\text{EFC} \equiv -\frac{1}{r^2} \frac{\partial}{\partial r} r^2 \overline{u'_{SR} v'_{SR}}, \quad (4.1)$$

where u_{SR} and v_{SR} are the radial and azimuthal components of storm-relative wind, respectively; r is the radius from the TC center; the overbar is an azimuthal mean; and the prime is the deviation from the azimuthal mean. To indicate a trough interaction objectively, Hanley et al. (2001) used an indicator of averaged EFC over a 300–600-km radius range at 200 hPa level that exceeds $10 \text{ s}^{-1} \text{ day}^{-1}$ continuously for more than 12 h. In the case of Noul, the upper-level jet axis associated with the deep trough was north ~ 1500 km far from Noul when the convection started around 1000 UTC 11 May. Calculating EFC using JRA-55 reanalysis data, the radius that exceeds $10 \text{ m s}^{-1} \text{ day}^{-1}$ was ~ 850 km from Noul's center as of 1200 UTC 11 May (not shown), which is too far to spinup Noul. Therefore, we do not conclude that from the perspective of EFC, Noul reintensified through interaction with the upper-level trough.

The magnitude of shear around Noul increased after 1800 UTC 11 May, reaching 20 m s^{-1} (Fig. 4.4). Low ocean temperatures and strong shear destroyed the eyewall and Noul weakened to be an extratropical cyclone at 0300 UTC 12 May.

4.4. Results

In this study, period I was defined as 1200–1400 UTC 11 May before the gap of the wind dataset and period II as 1500–1700 UTC 11 May after the gap. Period I is a period when convective bursts occurred in the downshear left quadrant, and period II is a period when the convection mainly lay in the upshear side. In the first half of this section, we present the evolution of axisymmetric structure. Then, we detail the evolution of asymmetric structure.

a. Axisymmetric structure

During period I, the vortex itself was on average still weak and Noul did not have a well-organized eyewall. Specifically, the height and radial width of the 30 m s⁻¹ contour of \bar{v} and the 10-dBZ contour of radar reflectivity were short and wide (Fig. 4.8a). However, the time evolution of axisymmetric structure at 1-km altitude shows that isopleths of azimuthal mean absolute angular momentum $\bar{M} \equiv (1/2)fr^2 + r\bar{v}$, where f is the Coriolis parameter, moved inward with time as the radial gradient of \bar{M} increased, indicating that inertial stability $I^2 \equiv \left(\frac{1}{r^3}\right)\frac{\partial\bar{M}^2}{\partial r}$ and absolute vorticity $\zeta_a \equiv \left(\frac{1}{r}\right)\frac{\partial\bar{M}}{\partial r}$ increased there (Fig. 4.9a). The RMW at 1-km altitude contracted from ~65 km at 1200 UTC to ~40 km at 1510 UTC (Fig. 4.9a). Below 4-km altitude, the inflow penetrated to a radius of 40 km well inside the RMW (Figs. 4.8b and 4.9b). The inflow exceeded 4 m s⁻¹ outside the RMW at 1-km altitude (Fig. 4.8b). Azimuthal mean reflectivity increased from 1315 UTC to 1430 UTC, with the radius of maximum reflectivity located inside the RMW (Fig. 4.9c). The configuration of maximum reflectivity inside the RMW and the low-level inflow in the vicinity of the RMW is known to be favorable for the increase in \bar{v} (Shapiro and Willoughby 1982; Pendergrass and Willoughby 2009; Nolan et al. 2007; Smith et al. 2009; Rogers et al. 2013; Smith and Montgomery 2016). Inside 40-km radius at 1-km altitude, outflow greater than 4 m s⁻¹ existed. The fact that \bar{M} increased inside 40-km radius despite the outflow and isopleths of \bar{M} sloped radially outward with height at low levels suggests that vertical advection of \bar{M} from the boundary layer greatly contributed to the increase in \bar{M} there.

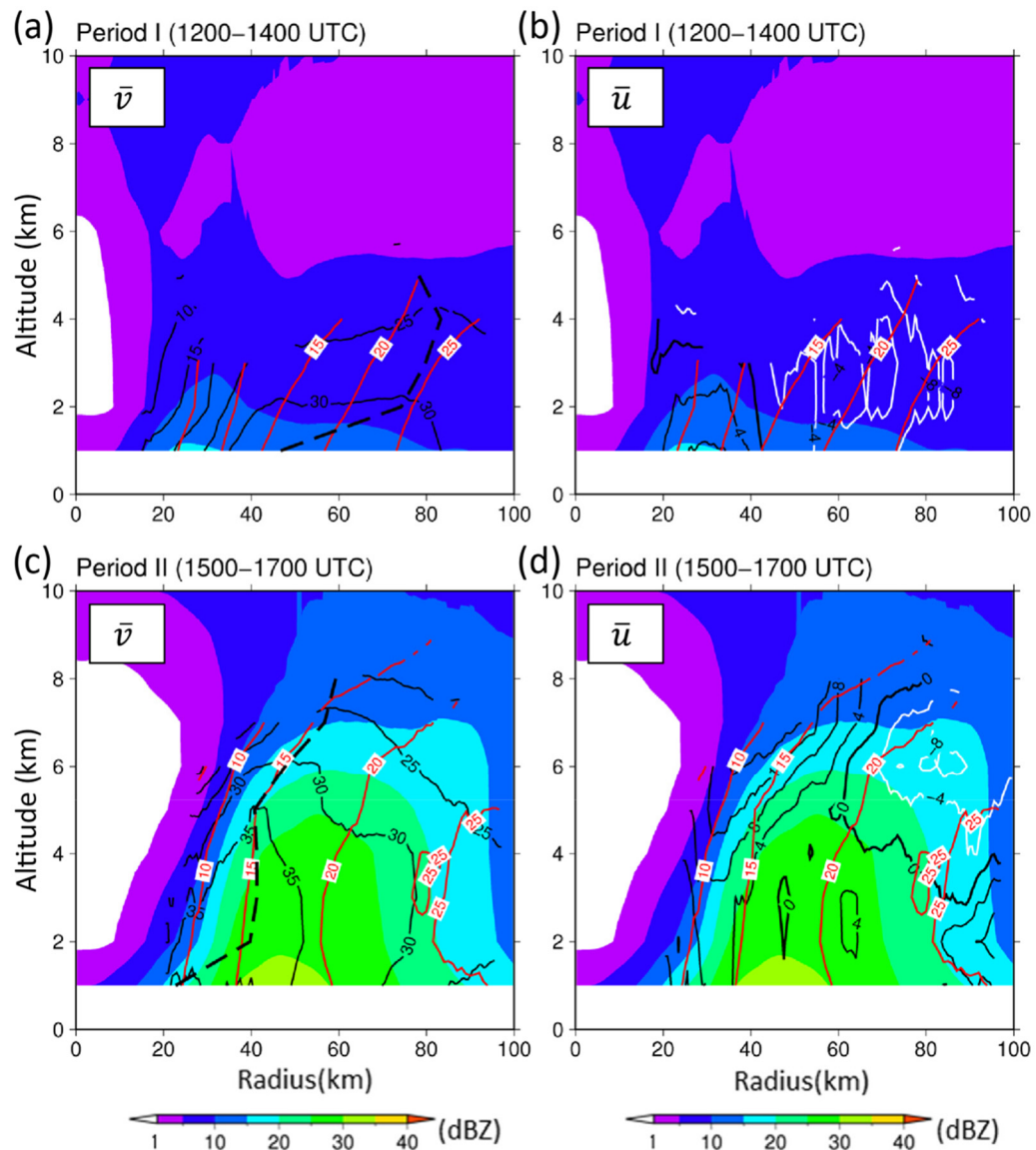


Fig. 4.8: Radius–height plots of (a) time-averaged \bar{v} (m s^{-1} , black contours), azimuthal mean radar reflectivity (color scale), and \bar{M} ($10^5 \text{ m}^2 \text{ s}^{-1}$, red contours), (b) time-averaged \bar{u} (m s^{-1} , black contours positive, white contours negative), azimuthal mean radar reflectivity (color scale), and \bar{M} ($10^5 \text{ m}^2 \text{ s}^{-1}$, red contours) during period I. The dashed line is the RMW. Contours were drawn in areas where there were observations averaged at least over 1 h in total. (c), (d) As in (a), (b), but for period II.

The accuracy of the GBVTD-retrieved winds during period II appears poorer than that of period I, because the distribution of both \bar{v} and \bar{u} was noisier (Figs. 4.9a, and 4.9b). \bar{v} erratically fluctuated, and inflow and outflow were mixed from 1530 to 1630 UTC 11 May (Fig. 4.9b). The RMW was sometimes within radii of 20–25 km where the retrieved \bar{v} was anomalously large (Fig. 4.9a). In spite of the uncertainty, \bar{v} definitely increased at least until 1600 UTC. Azimuthal mean reflectivity increased outside the RMW after 1500 UTC, and the outer radius of 20 dBZ broadened with time (Fig. 4.9c).

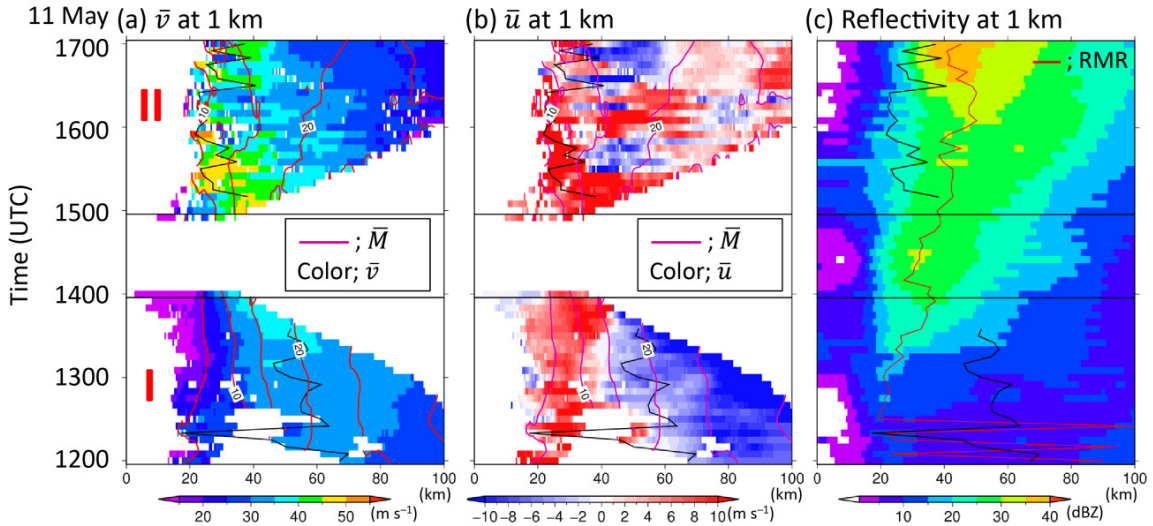


Fig. 4.9: (a) Radius–time Hovmöller diagram of \bar{v} at 1-km altitude (color scale), \bar{M} ($10^5 \text{ m}^2 \text{ s}^{-1}$, purple lines), and RMW (thick black line). The blank areas are where the GBVTD technique could not retrieve \bar{v} (i.e., during the Noul’s passage near Ishigaki Island). (b) Radius–time Hovmöller diagram of \bar{u} at 1-km altitude (color scale), \bar{M} ($10^5 \text{ m}^2 \text{ s}^{-1}$, purple lines), and RMW at 1-km altitude (thick black line). The blank areas are where the GBVTD technique could not retrieve \bar{u} . (c) Radius–time Hovmöller diagram of azimuthal mean radar reflectivity at 1-km altitude (color), radius of maximum radar reflectivity (red line), and RMW (thick black line). The black horizontal lines indicate the boundaries of the periods I and II.

b. Asymmetric structure

Just around the onset of reintensification, intense convection developed downshear left, a little far from the storm center (Fig. 4.3a). Then, this convection approached the storm center as the RMW contracted, and it moved cyclonically around the storm center from downshear to upshear as it was organized into the eyewall. The convection did not weaken when it moved into the upshear side of the eyewall, where downward motion generally dominates in the low-level troposphere in relatively strong shear (e.g., Reasor et al. 2013; DeHart et al. 2014). It was when the convection was active from 1315 UTC to 1600 UTC that \bar{v} at 1-km and 2-km altitude increased rapidly (Fig. 4.7). Finally, a symmetric eyewall formed by 1800 UTC (Fig. 4.3f).

To examine the wind field around the eyewall, storm-relative (hereafter, SR) surface winds were plotted at 4-min intervals at the relative location of weather stations to the storm center at a specific time (Fig. 4.10). The SR winds were derived from surface gust wind observations. The plots were made at 4 specific times (periods A–D) indicated in Table 4.1, assuming that the storm structure was in a steady state during each plot period. During periods A–D, surface inflow existed on the downshear side and surface outflow existed on the upshear side. Such a radial flow pattern is generally seen at the

Table 4.1: Periods of the plot of storm-relative (SR) surface winds at a specific time (Fig. 4.10). Note that not all SR winds observed at each weather station are plotted during plot periods. If a weather station was located in the eye during both periods, then SR winds during either period were excluded.

	Specific times	Plot periods
A	1330 UTC 11 May	1230–1430 UTC
B	1430 UTC 11 May	1330–1530 UTC
C	1520 UTC 11 May	1450–1600 UTC
D	1610 UTC 11 May	1530–1640 UTC

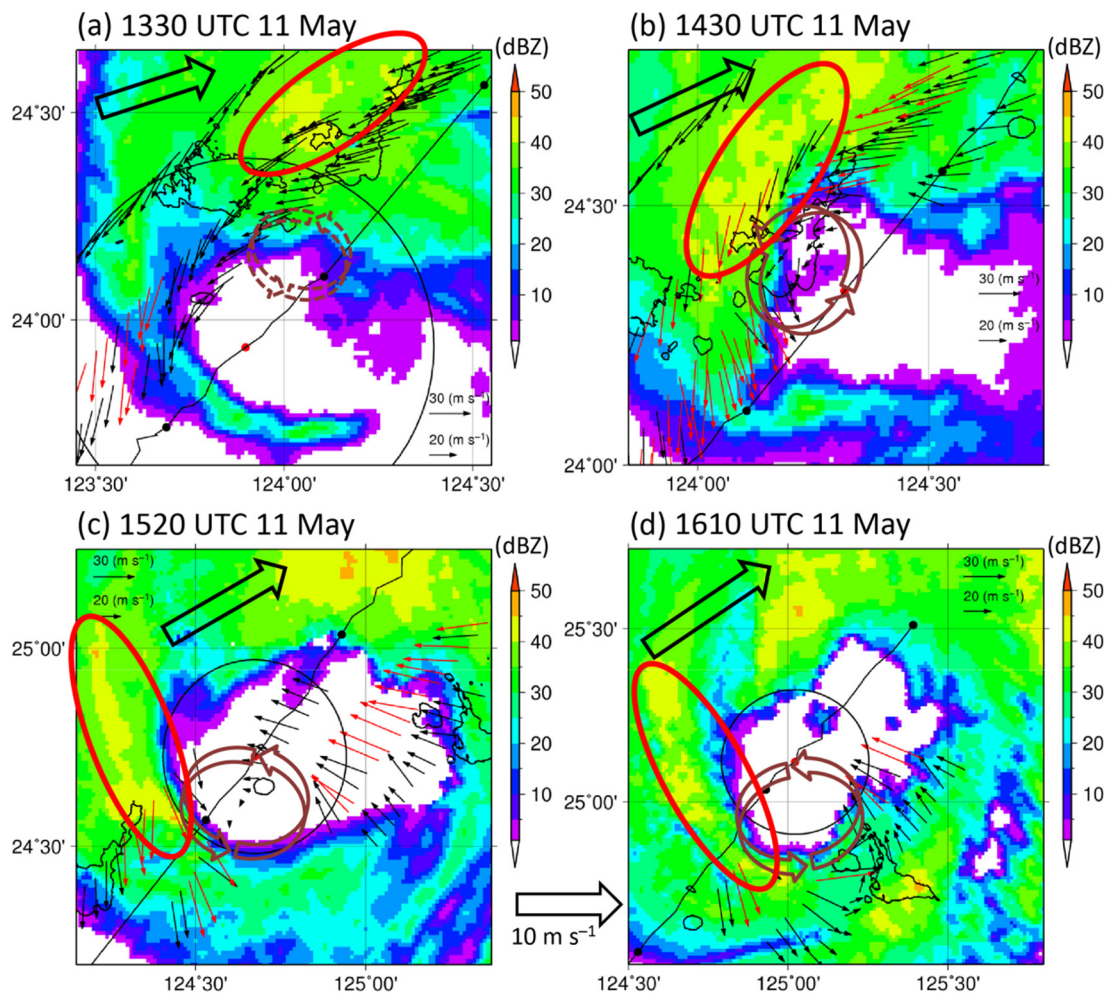


Fig. 4.10: Distribution of storm-relative (SR) surface winds (small arrows) and composite radar reflectivity (color scale) at (a) 1330 UTC 11 May, (b) 1430 UTC, (c) 1520 UTC, and (d) 1610 UTC. SR winds observed at each weather station during each period shown in Table 4.1 are plotted at the location relative to the TC center position at each specific time. The black line is the track from the GBVTD-simplex method until 1700 UTC 11 May. The red ellipse indicates the active asymmetric convection focused on in this study. The black bold arrow shows the 850–200-hPa shear vector. The black circle denotes the 1-km RMW. The dashed arrow circle indicates a concave portion of the inner edge of the eyewall. The brown arrow circle indicates the location of a mesovortex.

lower troposphere of TCs in shear (e.g., Braun et al. 2006; Reasor et al. 2013). During period A (Fig. 4.10a), around 20 km northwest of the center inside the eyewall, SR wind speed was $\sim 30 \text{ m s}^{-1}$. There was a concave portion inside the eyewall $\sim 20 \text{ km}$ northeast of the center. During period B (Fig. 4.10b), the concave portion existed northwest of the center, just inside the active convection with reflectivity greater than 40 dBZ extending from southwest to northeast, which corresponds to the convective asymmetry. Inside the concave portion around 20 km northwest of the center, SR wind speed was weak, below 10 m s^{-1} , forming a small-scale cyclonic circulation. Hereafter, we call this local circulation as a mesovortex. SR wind speed increased throughout the left side of the track except around the mesovortex. Then, the mesovortex moved inside the eyewall during periods of C and D (Figs. 4.10c, and 4.10d).

Because Noul moved northeastward with a speed of 18 m s^{-1} and passed very near Tarama Island (the location of the weather station named Nakasuji is indicated in Fig. 4.5a), the time evolution of surface observations at Tarama Island reflected the inner-core structure of Noul at the surface from downshear to upshear (Fig. 4.11). There was a minimum sea level pressure and a high θ_e peak around the mesovortex (from 1520 UTC to 1540 UTC) (Fig. 4.11c) where SR winds were below 10 m s^{-1} and the sign of SR tangential wind changed (Fig. 4.11a). The same feature was also observed when the mesovortex passed near Ishigaki Island (not shown). A steep radial gradient of θ_e reaching $15 \text{ K (10 km)}^{-1}$ from 1533 UTC to 1541 UTC existed in the area of outflow, which is indicative of positive θ_e advection from the eye into the inside of the convection. The V_D PPI pattern at a 0.2° elevation angle at 1621 UTC 11 May showed that the 0 m s^{-1} isopleth of V_D was nearly perpendicular to the radar range direction in the vicinity of the convective asymmetry on the western side of the Noul (the dotted circle shown in Fig. 4.6b), indicating the existence of horizontal convergence along the convection. The height of V_D around the convergence area in Fig. 4.6b was at 1–2-km altitude. The existence of the positive θ_e advection inside the eyewall and convergence along the asymmetric convection was a favorable configuration for the maintenance of the convection upshear.

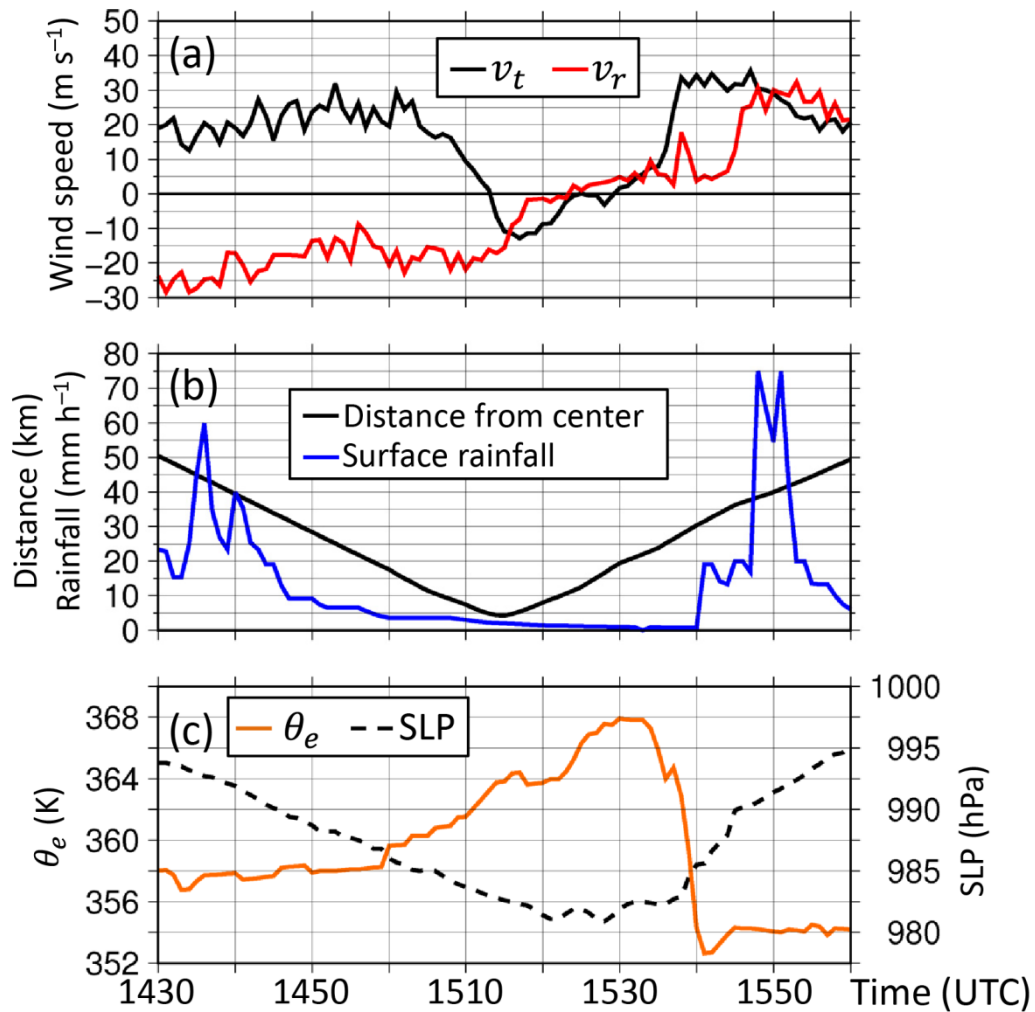


Fig. 4.11: Time evolutions of surface observations at Nakasuji, whose location is indicated in Fig. 4.5. (a) Storm-relative surface tangential wind speed (m s^{-1} , red line) and radial wind speed (m s^{-1} , black line) relative to the storm-scale center. (b) The distance between the storm-scale center and weather station (km , black line) and surface rainfall (mm h^{-1} , blue line). (c) Equivalent potential temperature θ_e (K , orange line) and sea level pressure (hPa , black dashed line).

A similar configuration of a mesovortex in the eye and convective bursts in the eyewall was shown by Guimond et al. (2016) who used aircraft observations. They showed that convective bursts occurred through the low-level convergence of outflow with warm buoyant air associated with mesovortices in the eye and vortex-scale flow. Eastin et al. (2005) reported using aircraft observations that the origin of buoyancy updrafts in the eyewall appeared to be high θ_e air advected by outflow of mesovortices from the eye, where θ_e is much (~ 10 K) greater than that in the eyewall. Reasor et al (2009) speculated that warm, moist air offsets negative influence associated with relatively strong shear, leading to the rapid intensification (RI) of Hurricane Guillermo (1997).

Relatively strong SR tangential winds greater than 30 m s^{-1} were present accompanied by low θ_e air underneath the convection (Figs. 4.11a, and 4.11c). By using SR tangential winds observed at Tarama Island and a formula of relative vorticity:

$$\zeta = \frac{\partial v_t}{\partial r} + \frac{v_t}{r},$$

where v_t is SR tangential wind, it is calculated that relative vorticity just inside the tip of the convection reached $0.8 \times 10^{-2} \text{ s}^{-1}$. When the mesovortex passed near Shimoji (Figs. 4.5a and 4.10d), a maximum gust wind speed of 58.6 m s^{-1} (ground-relative wind) was observed at Shimoji. This very strong wind inside the tip of the convection was also confirmed by V_D greater than 60 m s^{-1} at 1–2-km altitude near Shimoji in Fig. 4.6b. Such very strong wind speed just inside the eyewall was also observed in Hurricane Hugo (1989) (Marks et al. 2008).

As Fig. 4.10 showed the convective asymmetry rotating cyclonically, the wavenumber-1 asymmetry was characteristic before the formation of a symmetric eyewall in Noul. In fact, reflectivity in wavenumbers 0–7 averaged over 25–50 km in radius (around the RMW and outside the RMW) showed that the wavenumber-1 reflectivity asymmetry with the amplitude greater than 10 dBZ lasted until 1625 UTC 11 May while the wavenumber-0 reflectivity gradually increased (Fig. 4.12). After 1600 UTC, the wavenumber-1 asymmetry rapidly decreased and a symmetric eyewall was established by 1700 UTC. A wavenumber-1 distribution of reflectivity within 100-km radius showed that a positive wavenumber-1 anomaly propagated cyclonically at an almost single phase speed between radii of 25 and 50 km from 1300 to 1600 UTC (Fig. 4.13). Additionally, Noul persistently had convection downshear left at outer radii greater than $\sim 70 \text{ km}$ during reintensification. The wavenumber-1 asymmetry disappeared after 1630 UTC and there was no significant wavenumber-1 asymmetry within 70-km radius except for an asymmetry around 20-km radius due to the deviation from the symmetric eyewall center at 1700 UTC (Fig. 4.13e). There was another wavenumber-1 mode on the south-western side of the eyewall at 1800 UTC, which seemed a sheared wave with relatively large radial wavenumber (Fig. 4.3f). The wavenumber-1 reflectivity asymmetry rotated cyclonically after 1330 UTC from the downshear-left side to the upshear side (Fig. 4.14). At around 1630 UTC the propagation stopped and the magnitude decreased. Note that the wavenumber-1 asymmetry was mainly found in the downshear-left quadrant outside 50-km radius before 1330 UTC (Fig. 4.13a).

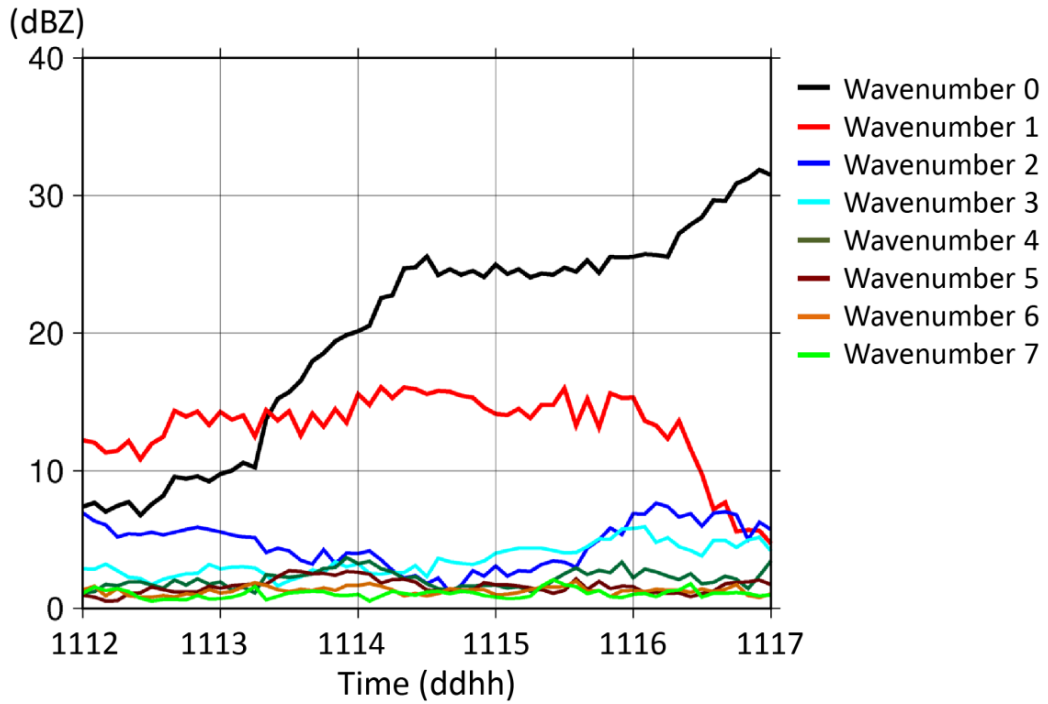


Fig. 4.12: Time evolution of radar reflectivity in wavenumbers 0–7 averaged over radii of 25–50 km (a simple average without considering the areal mean). The reflectivity is averaged between 1- and 2-km altitudes.

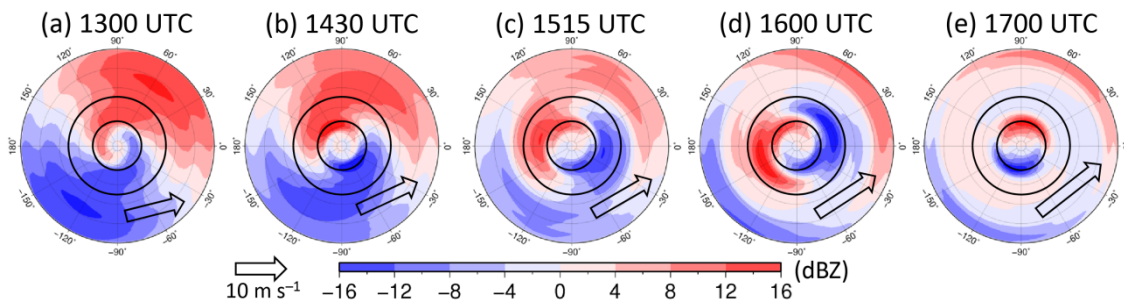


Fig. 4.13: Radar reflectivity distribution in wavenumber 1 within 100-km radius from the storm center. The reflectivity is averaged between 1- and 2-km altitudes. The black arrow shows the 850–200-hPa shear vector.

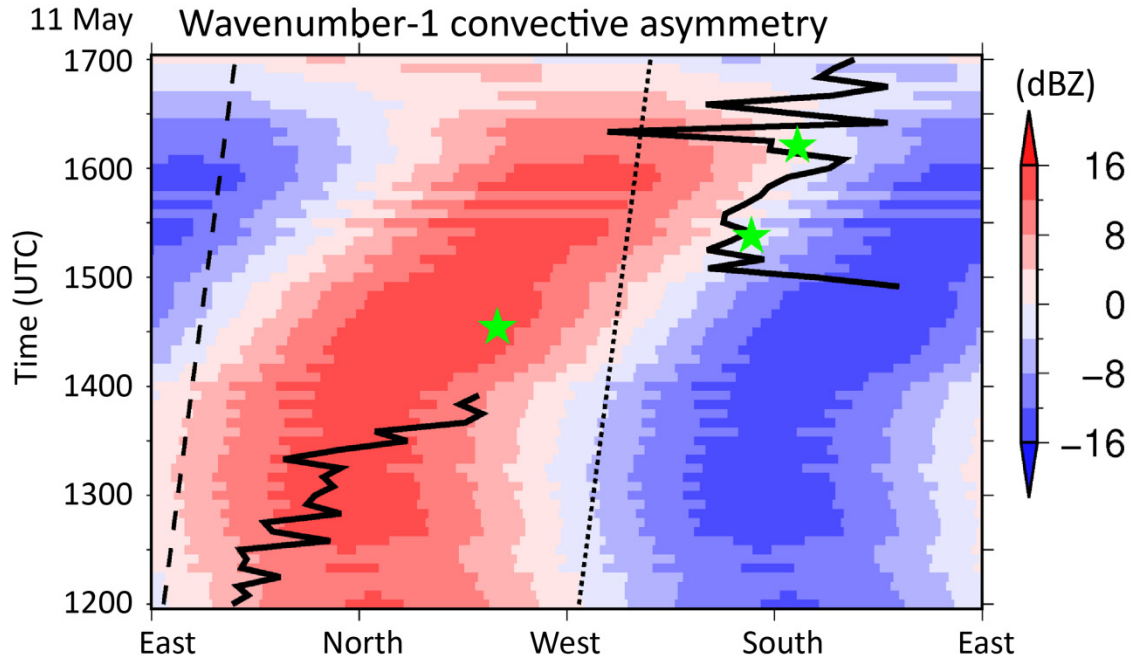


Fig. 4.14: Time–azimuth distribution of wavenumber-1 reflectivity averaged between radii of 25 and 50 km. The reflectivity is averaged between 1- and 2-km altitudes. The thick black line indicates the direction of the vortex tilt determined from the difference in the center between 1- and 5-km altitudes. The dashed line shows the direction of the 850–200-hPa shear vector and the dotted line shows the opposite direction of shear vector. The green stars indicate the direction of the mesovortex away from the storm center.

As described in Chapter 1, the tilt direction is related to the location of the upward motion maximum in the eyewall. In addition, Ueno (2007) found through numerical simulation that the amplitude of wavenumber-1 upward motion asymmetry in the eyewall is strongly correlated with that of wavenumber-1 rainfall asymmetry. Therefore, the wavenumber-1 convective asymmetry that rotated cyclonically around the eyewall in an environment of increasing shear implies that the vortex precessed as a tilt mode. The tilt mode is in phase to the direction of tilt (Reasor et al. 2004). To examine the vortex tilt of Noul, we detected the storm center at 5-km altitude in the same way as that at 1-km altitude described in section 4.2 and plotted the direction of the tilt between centers at 1-km and 5-km altitudes in Fig. 4.14. Centers above 5-km altitude could not be reliably detected because the density of Doppler velocity data was too sparse to find reasonable centers. The direction of vortex tilt was almost the same as that of the wavenumber-1 reflectivity before 1330 UTC and to 45–90° downstream of the wavenumber-1 reflectivity after 1330 UTC, reaching the upshear right quadrant. The direction of the tilt was coincided with that of the mesovortex, downstream of the peak of the reflectivity asymmetry. Note that there exists uncertainty in the analysis of

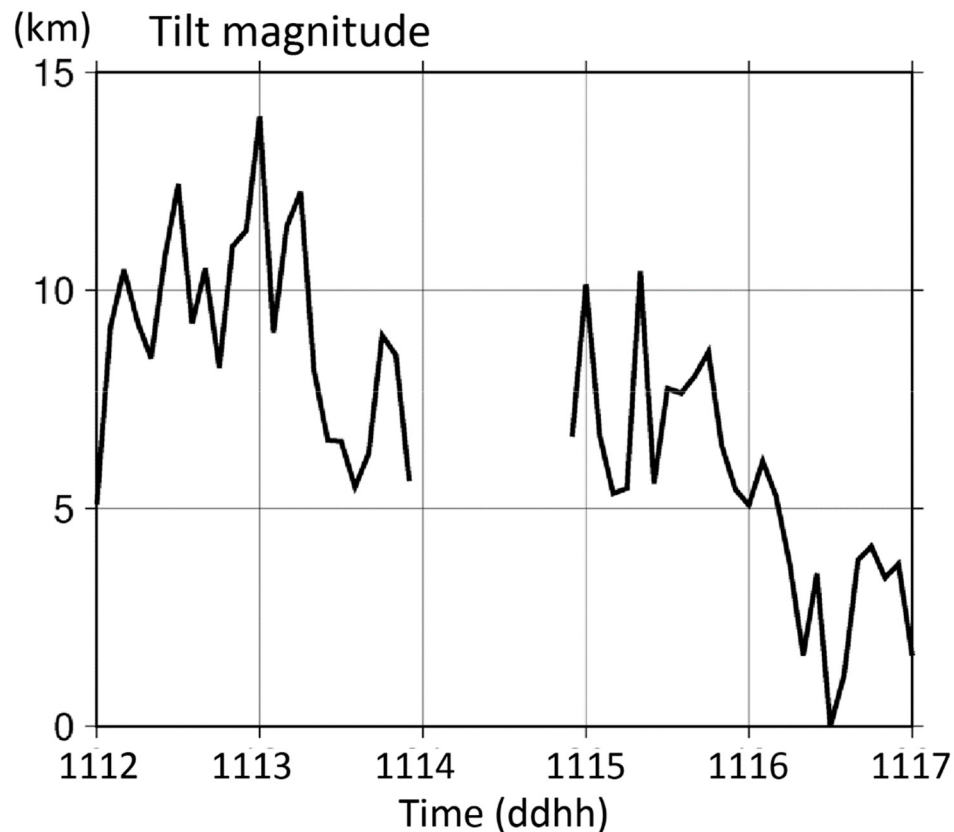


Fig. 4.15: Time evolution of the magnitude of the vortex tilt determined from the difference in the center between 1-km and 5-km altitudes.

the vortex tilt because the quality of the GBVTD analysis was poor, in particular, during period II. According to previous studies (e.g., Rogers et al. 2003; Reasor et al. 2013), the upward motion maximum and tilt direction tend to be found upstream of the reflectivity maximum. In this sense, there is a possibility that the direction of the tilt during period II contains systematic errors.

Figure 4.15 shows that the magnitude of the tilt was relatively large when the wavenumber-1 reflectivity was dominant (Fig. 4.12), but it decreased within 4 km after 1600 UTC when the amplitude of the reflectivity asymmetry became small. The evolution of the tilt indicates that the vortex was almost aligned after it precessed upshear from the downshear-left quadrant.

4.5. Discussion

Noul's reintensification is characterized as convective bursts, wavenumber-1 convective asymmetry, vortex tilt and its precession, and vertical alignment in an environment of increasing shear. Here, these characteristics are discussed below in reference to a theory of Reasor et al. (2004). Then, other intensifying TCs in shear are compared with Noul.

a. Vortex Precession

As described in Chapter 1, vortex precession can be projected onto a tilt mode of vortex Rossby waves (Reasor et al. 2004). Figure 4.16 shows that the radial gradient of relative vorticity at 1-km altitude was negative between radii of 25 and 50 km, where the wavenumber-1 convective asymmetry was primarily present. Assuming that the radial gradient of vorticity is the same in terms of sign as that of PV, vortex Rossby waves can propagate upwind relative to the tangential wind. A wavenumber-1 vortex Rossby wave propagating on the vorticity discontinuity on the Rankin vortex should be stationary relative to the ground (Lamb 1932), while a wavenumber-1 vortex Rossby wave on the vorticity gradient between radii of 25 and 50 km in Fig. 4.16 should propagate cyclonically at a slower speed than the corresponding tangential wind speed. The wavenumber-1 convective asymmetry at 37.5 km radius propagated cyclonically at an earth-relative speed of 8.9 m s^{-1} , which was $\sim 24\%$ of the corresponding \bar{v} at 1-km altitude (37.2 m s^{-1} , averaged over 25–50 km radius) during a period from 1330 to 1630 UTC. This behavior is consistent with a theory of vortex Rossby waves.

Why was Noul aligned through precession upshear without achieving a downshear-left tilt equilibrium? If the TC vortex precessed on the upshear side without any damping, then radial gradient of PV at the critical radius may have satisfied the condition of no damping. Unfortunately, the critical radius was located outside the analysis domain shown in Fig. 4.16 because even \bar{v} at 80-km radius was 26.3 m s^{-1} , much greater than the propagation speed (8.9 m s^{-1}).

According to a theory of vortex resilience in shear (e.g., Reasor et al. 2004; Schecter and Montgomery 2007; Schecter 2015; Reasor and Montgomery 2015), moist processes and associated vortex spinup can have positive impact on the vortex resiliency through the increase in the resonant damping rate. The moist processes lead to the reduction in the static stability, thereby the decrease in Rossby deformation radius. The decrease in the vortex scale and

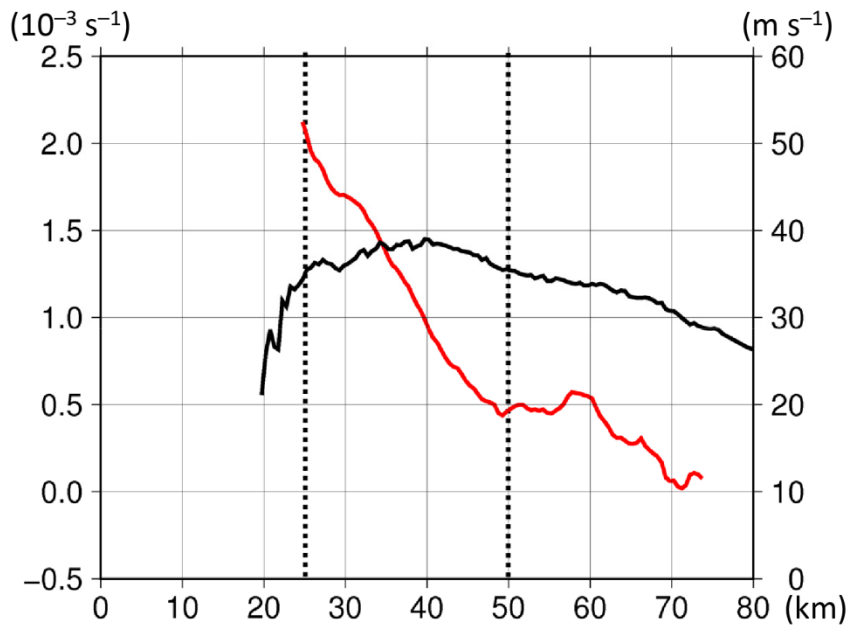


Fig. 4.16: Radial profile of time-averaged (from 1330 to 1630 UTC) azimuthal mean relative vorticity and \bar{v} at 1-km altitude. Values of relative vorticity are radially filtered using the 5-km running mean after the time average. The vertical dotted lines indicate the range of radii from 25 to 50 km.

the increase in inertial stability lead to the increase in Rossby number. The increase in the propagation speed of vortex Rossby waves relative to the ground moves the critical radius inward, leading to the increase in the rate of the resonant damping. This promotes to reach a tilt equilibrium.

For Noul, the fact that a symmetric eyewall was maintained after 1700 UTC (Fig. 4.3f) suggests that subsequent precession did not occur after the vertical alignment. Owing to the vortex spinup, the subsequent tilting may have been suppressed despite an environment of increasing shear.

b. Comparison with other intensifying storms in shear

Some previous studies have suggested that strong shear can favorably contribute to TC intensification through processes called downshear formation or asymmetric intensification. Nguyen and Molinari (2012) examined rapid intensification (RI) of Hurricane Irene (1999) and hypothesized that asymmetric forcing from strong shear and fast moving speed is responsible for RI. Molinari et al. (2006) and Molinari and Vollaro (2010) examined TS Gabrielle (2001) that intensified rapidly accompanied by a single intense mesovortex under strong shear, and speculated that there should be asymmetric dynamics for RI in strong shear through more diabatic heating to occur closer to the TC center. Nguyen and Molinari (2015) showed through

numerical simulation that during Gabrielle's intensification, an upright mesovortex formed downshear by the stretching and advection of vorticity in sufficient moisture environment, and that the intense mesovortex evolved into a TC vortex as its flow axisymmetrizes the original vortex. Musgrave et al. (2008) performed numerical experiments of Gabrielle and showed that the intensity simulated in an experiment in which vertical shear is reduced becomes weaker than the actual intensity. However, these cases of asymmetric intensification never had a closed eyewall during intensification, as Noul.

As for vertical alignment during intensification, Hurricane Earl (2010) might be a similar case to Noul in that the vortex was realigned after being largely tilted to 90° left of shear (Rogers et al. 2015; Stevenson et al. 2014). Earl had a shallow low-level circulation below 6-km altitude and an upper-level circulation above 5-km altitude with a displacement of ~ 50 km between circulation centers at 2- and 8-km altitudes prior to RI. In the next 12 h, RI started and the vortex became aligned in conjunction with convective bursts inside the RMW. However, the lack of high temporal resolution data prevented in-depth investigation of this event.

Noul was a TC that reintensified with the formation of a symmetric eyewall through precession upshear and vertical alignment in increasing shear. In spite of asymmetric convection, an axisymmetric view of the inner core of Noul showed that the timing of the increase in \bar{v} was consistent with that of the increase in azimuthal mean reflectivity inside the RMW, which was similar to other intensifying TCs. This suggests that the increase in the axisymmetric component of diabatic heating through asymmetric convection was important for Noul's intensification, as Molinari and Vollaro (2010) and Nguyen and Molinari (2012) described. In this sense, the vertical alignment was not the trigger for Noul's intensification, but the occurrence of convective bursts likely due to the increase in the vertical tilt in the environment where shear was increasing was the trigger.

4.6. Summary

Typhoon Noul (2015) underwent reintensification with vigorous asymmetric convection and then had a symmetric eyewall during the passage near Ishigaki Island, Okinawa, Japan, from 1200 to 1800 UTC May 11, 2015. During this period, westerly to southwesterly vertical wind shear increased from 11 to 16 m s⁻¹ and Noul speeded up northeastward from 10 to 20 m s⁻¹. Strong vertical wind shear greater than 10 m s⁻¹ is known to be unfavorable for storm's intensification and known to cause rainfall structure to be asymmetric. Therefore, the evolution of the inner-core structure of Noul during this period was unusual. Surface observations around Ishigaki Island and operational Doppler radar data provided an opportunity to document this reintensification. We focused, in particular, on the structural evolution of Noul.

An axisymmetric view of the inner core of Noul showed that the maximum \bar{v} at 2-km altitude retrieved from Doppler radar data by using the GBVTD technique increased from 30 m s⁻¹ to 50 m s⁻¹ during only 5 h, in association with the inflow penetrating to ~ 40 km radius well inside the RMW at least below 4-km altitude and the increase in azimuthal mean reflectivity inside the RMW. The 1-km RMW contracted from ~ 65 km to ~ 40 km. These features are consistent with those of intensifying TCs that have been revealed by many previous studies.

As for asymmetric structure, a wavenumber-1 convective asymmetry developed in the downshear-left quadrant at first. The asymmetry between radii of 25 and 50 km was organized into the eyewall and rotated cyclonically to the upshear side. Surface observations indicated that there was a mesovortex in the eye, located just inside the tip of the convective asymmetry. The mesovortex had warm moist air with a pressure minimum and radial gradient of θ_e between the mesovortex and the convection reaching 15 K (10 km)⁻¹. The configuration of the mesovortex and the convection was favorable for advecting high θ_e air from the eye to the convection. In conjunction with the convective asymmetry, the direction of vortex tilt between 1- and 5-km altitudes rotated cyclonically from the downshear-left to the upshear-right quadrant, although uncertainty existed in this analysis. It was when the magnitude of the tilt decreased below 4 km that the amplitude of the wavenumber-1 convective asymmetry became small and a symmetric eyewall formed. These features indicate that the vortex vertically aligned through vortex precession upshear in strong shear.

In a region between radii of 25 and 50 km from the storm center where the wavenumber-1 asymmetry was dominant, the radial gradient of relative vorticity was negative. This condition is consistent with the fact that the TC vortex precessed as a tilt mode of vortex Rossby waves. Convective bursts and vortex tilt were likely to occur triggered by the increase in shear. After the vertical alignment, Noul maintained a symmetric eyewall for a while. The effects of moist processes and vortex spinup may have enhanced vortex resilience in strong shear.

As far as we know, this is the first observational analysis of a TC that underwent vertical alignment through precession upshear in strong shear. Although many observational studies have examined the relationship between shear and asymmetric structure, none of them have found how a TC vortex behaves on a short time scale, ~ 6 h, in response to the increase in shear based on observations. In the case of Noul, intensity change was also dramatic. Further studies are needed to confirm whether the findings of this study are robust. More case studies and modeling studies with high temporal-resolution data are desired.

Chapter 5: Rapid Intensification of Typhoon Goni (2015)

After Eyewall Replacement

5.1. Motivation

To elucidate dynamical and thermodynamical processes of RI and eyewall replacement cycles (ERCs) of TCs, temporally and spatially dense observations are indispensable, because both RI and eyewall replacement cause drastic changes in the intensity and structure of TCs. Although observations by aircraft have provided invaluable clues to RI and ERC processes (e.g., Montgomery et al. 2006; Houze et al. 2007; Montgomery et al. 2014; Guimond et al. 2016), we have yet to obtain observations that are sufficiently dense both temporally and spatially. This lack of dense observations has prevented our full understanding of RI and ERCs.

The Ishigaki C-band Doppler radar (Fig. 5.1a) operated by the JMA observed Typhoon Goni (2015) at 5-min intervals for 24 h, while it was undergoing RI, just after completing an ERC, and reaching peak intensity. Like Goni, TCs can experience RI after an ERC (Sitkowski et al. 2011), as reviewed in subsection 1.3d. However, whether RI processes after an ERC differ from those not associated with an ERC has not yet been investigated.

The GBVTD technique can retrieve TC wind fields at 5-min intervals with a high spatial resolution of less than 1 km in horizontal grid spacing from single ground-based Doppler radar data. These data provide us with an invaluable opportunity to examine Goni's RI processes in detail.

The purpose of this chapter is to conduct an in-depth examination of processes occurring in Goni during RI just after the eyewall replacement using radar reflectivity and retrieved wind data with the aim of contributing to our understanding of the dynamical processes of RI. In particular, we focus on drastic structural changes around the onset of and during RI from an axisymmetric perspective and compared the kinematic structures of Goni with those that have been shown in observations and simulations for TCs that undergo RI without an ERC. To our knowledge, no case of RI just after an ERC has been examined by using both high-resolution temporal and high-resolution spatial observations obtained over a 24-h period.

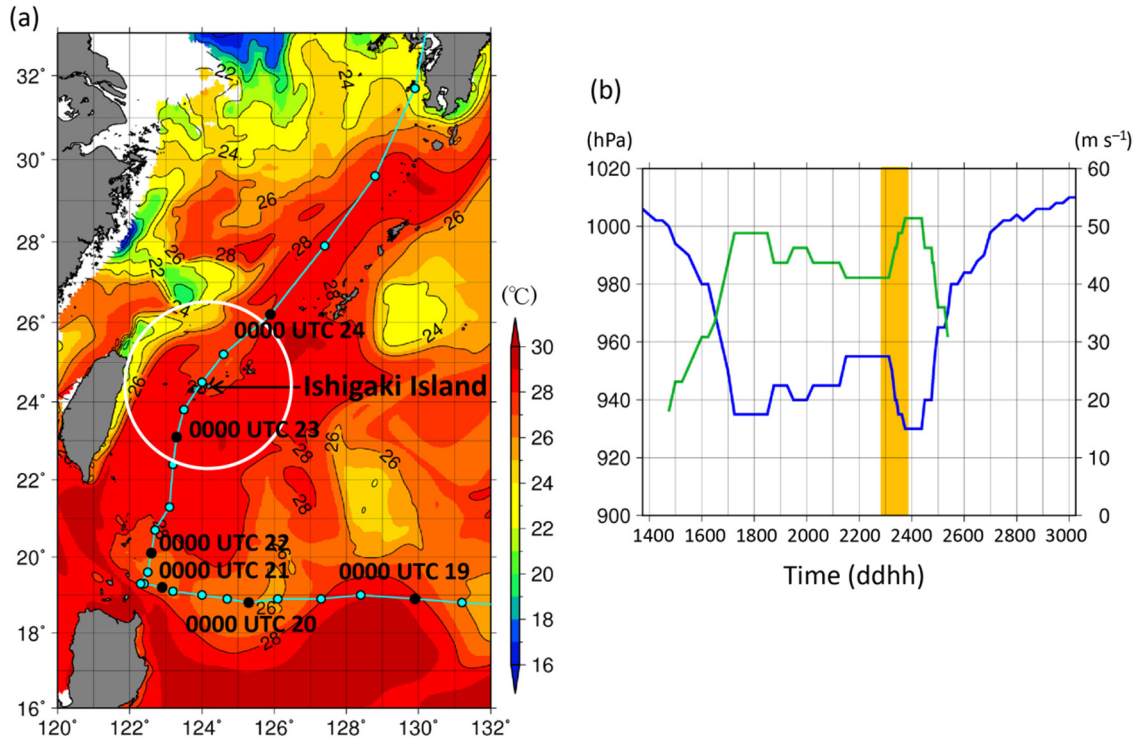


Fig. 5.1: (a) Ocean temperatures at 50 m depth on 22 August 2015 and Goni's track; circles show the track at 6-h intervals, and black circles show the track at 1-day intervals. The large white circle centered at Ishigaki Island denotes the range of the Ishigaki Doppler radar, ~ 200 km. The sea temperature data were provided by the JMA. (b) Time evolution of Goni's intensity: green line, maximum wind; blue line, central pressure. RSMC Tokyo's best track data do not include maximum wind speeds for a TC categorized as a tropical depression. The vertical orange bar indicates the period focused on in this study.

5.2. Data and methodology

a. Wind dataset

We apply the GBVTD technique to Doppler velocity, V_D , data observed by the Ishigaki C-band Doppler radar, and construct a two-dimensional wind dataset for Goni at 1-km altitude intervals from 1 to 10 km of altitude from 2200 UTC 22 August to 2200 UTC 23 August 2015 (see Appendix A for details). The Doppler observation parameters of the JMA radars are listed in Table 2.1. In this study, we set the retrieval resolution to 0.7° of azimuth and 500 m of radius in storm-centered cylindrical coordinates. The dataset includes tangential winds with wavenumbers up to 3, and radial winds with wavenumbers up to 1. Because radar coverage is sparse at high altitudes when Goni is far from the radar location, however, we are not able to obtain the wind field for all altitudes at all times. In addition, we obtain vertical

velocities, w , by upward integration of the mass continuity equation from the surface, where vertical velocity is 0. The mean hurricane season density profile of Jordan (1958) is used to compute w . Because there are no retrieved winds below 1-km altitude, 1-km winds are used as winds between the surface and 1-km altitude. This is a limitation of the vertical velocities used in this study.

The GBVTD technique uses the constant-altitude plan position indicator (CAPPI) data with a radial range of up to 200 km, to which plan position indicator (PPI) data with an elevation angle of less than 10.0° (specifically, 0.2° , 1.1° , 2.7° , 4.0° , 5.8° , 8.3°) are interpolated. For example, for radar ranges greater than ~ 60 km, V_D from the 0.2° elevation PPI scan, whose height is between 1 and 4 km, is projected onto the 1-km CAPPI. Because vertical profiles of wind speed in TCs generally increase downward from 3 km to below 1 km (e.g., Franklin et al. 2003), there is a possibility that this CAPPI method contributes to a negatively biased wavenumber-0 tangential wind, \bar{v} , when the TC center is far from the radar location. Similarly, the retrieved wavenumber-0 radial wind, \bar{u} , at 1-km altitude can be regarded as representing \bar{u} above 1-km altitude. In this study, we define a strong inflow layer as the boundary layer (BL), which is generally seen below 1-km altitude. Thus, we regard the wind field at 1-km altitude as virtually above the BL.

We summarize limitations and uncertainties in the GBVTD analysis in Appendix A. Based on those limitations and uncertainties, we focus mainly on the axisymmetric component of the retrieved winds in this study. In addition, because no TC centers are detected while the radar site is located within the TC's eye region, which lasted about 2 h, from 1140 to 1400 UTC 23 August 2015, we subjectively determine the center of the eye for that period while viewing radar reflectivity.

b. Data quality

The accuracy of the retrieved wind obtained by the GBVTD technique is defined as the overall average of the RMSD between V_D resampled from the GBVTD-retrieved winds and observed V_D , and it is identical to the RMSE in Zhao et al. (2012; their Fig. 3). In general, the RMSD at 2-km altitude was smaller than 3 m s^{-1} except when Goni passed near Ishigaki Island (Fig. 5.2). The horizontal distribution of the RMSD shows that it tends to be larger inside the RMW (not shown). It is likely that the presence of a small-scale extreme wind (e.g., Aberson et al. 2006) or small eyewall vorticity maximum

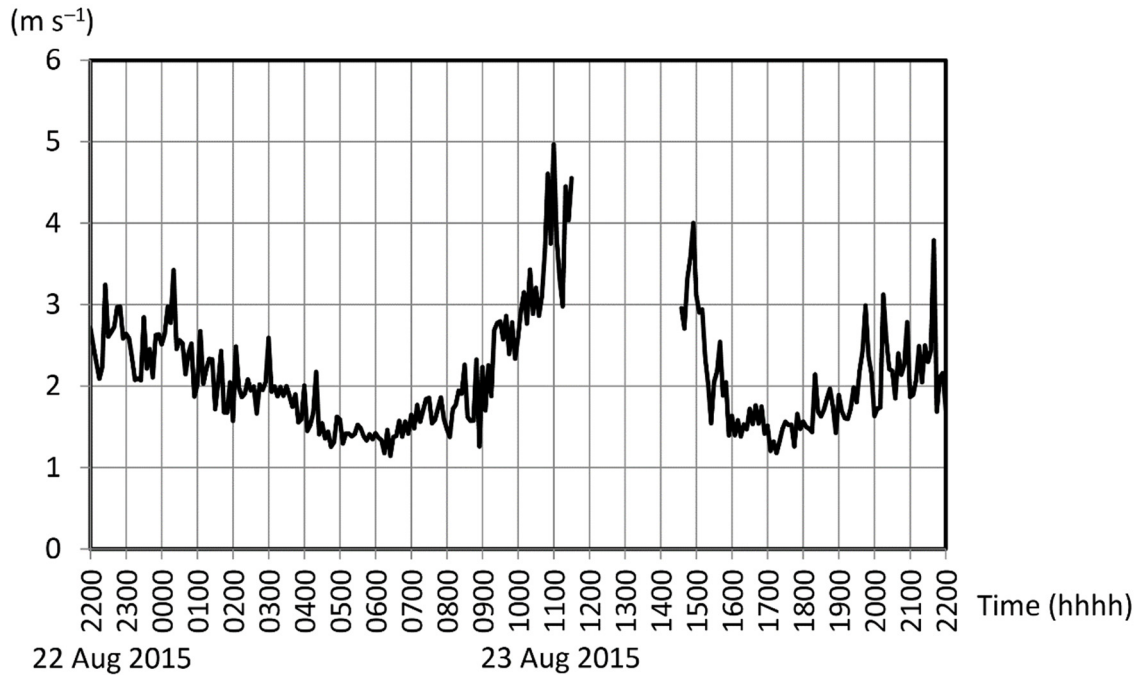


Fig. 5.2: Time evolution of the overall average of the RMSD between V_D resampled from the GBVTD-retrieved winds at 2-km altitude and observed V_D at 2-km altitude.

(e.g., Marks et al. 2008) along the inner edge of the eyewall, the existence of which is not taken account of by the GBVTD technique, lowered the accuracy of the GBVTD analysis result. In addition, if the retrieval range is inside the RMW, then there can be significant geometrical distortion in the GBVTD technique (Lee et al. 1999; Jou et al. 2008). Furthermore, noise contamination in the V_D field near the outermost range of the radar reduces the accuracy of the analysis (not shown). For these reasons, the overall average RMSD increased when Goni was located far from the radar site and when most of retrieval range was inside the RMW (i.e., when Goni approached the radar site). However, because the RMSD at 2-km altitude is generally less than 3 m s^{-1} where the wind speed is greater than 30 m s^{-1} , that is, because the RMSD is generally less than 10% of the actual wind speed, this level of accuracy is acceptable for the wind field analysis.

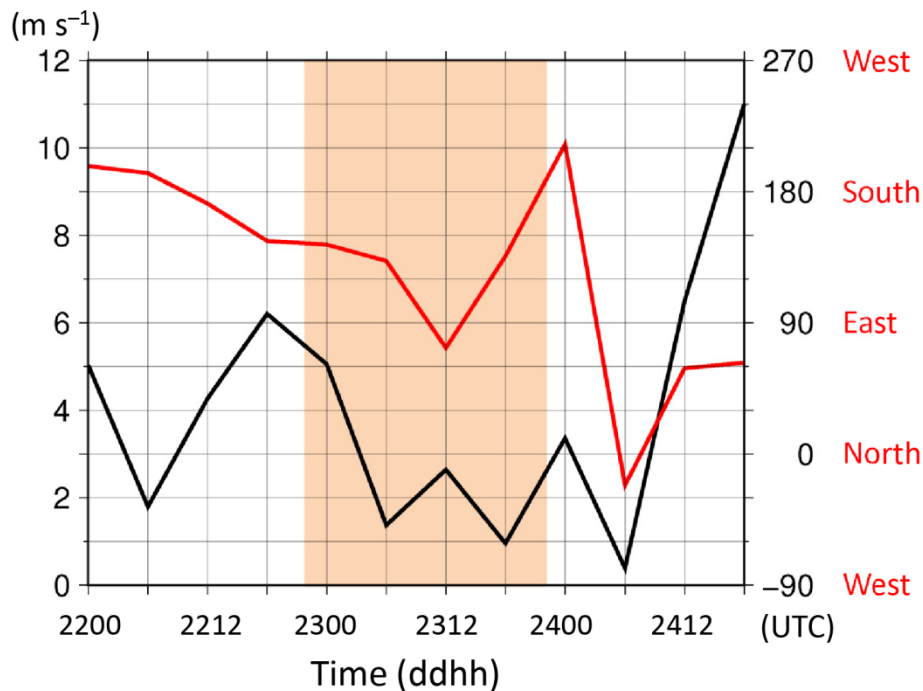


Fig. 5.3: Vertical wind shear (black line) and its heading direction (red line) between 200 and 850 hPa averaged within 500 km from the center. The shear was calculated by using JRA-55 data (Kobayashi et al. 2015). The shading indicates the radar observation period.

5.3. Overview of Goni

a. Storm history and environmental conditions

According to the best track data of RSMC Tokyo, Typhoon Goni moved westward along $\sim 19^\circ$ N from 18 to 20 August, and then remained nearly stationary just northeast of Luzon Island on 21 August before starting to move north–northeast after 1800 UTC 21 August (Fig. 5.1a). Goni weakened slightly just before the onset of intensification at 0300 UTC 23 August (Fig. 5.1b) and reached its lifetime-maximum intensity at 1800 UTC 23 August, just after it passed near Ishigaki Island. Subsequently, it moved northeastward over the East China Sea.

During the intensification beginning at 0300 UTC 23 August, the magnitude of vertical wind shear between 850 and 200 hPa was less than 6 m s^{-1} , with the direction of the shear being nearly southeastward (Fig. 5.3). In addition, ocean temperatures at 50 m depth east of Taiwan were greater than 28°C (Fig. 5.1a). These environmental conditions were favorable for TC intensification.

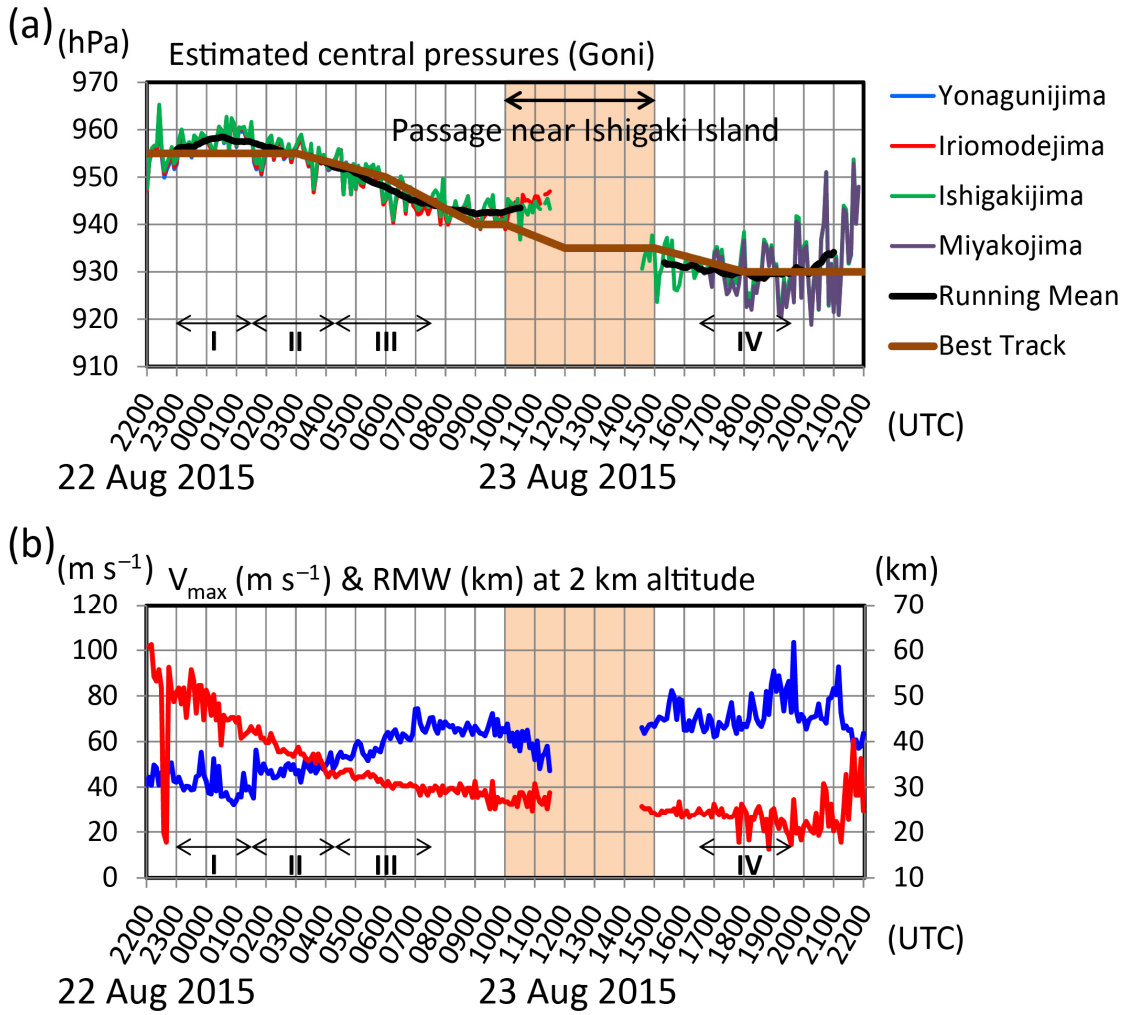


Fig. 5.4: (a) Time evolutions of estimated central pressures (blue, red, green and purple lines), their 2-h running mean (black line), and the best track central pressure (brown line) of Goni. The blue, red, green, and purple lines indicate central pressures derived from sea level pressure observations at Yonaguni, Iriomotejima, Ishigakijima, and Miyakojima, respectively. (b) Time evolutions of maximum wind speed (blue line) and RMW (red line) at 2-km altitude of Goni. Periods I–IV, defined in subsection 5.4 and Table 5.1, are also shown in each panel.

b. Intensity analysis

The intensity estimation results show that the evolution of central pressure estimated from Doppler radar data was consistent with that in the best track data (Fig. 5.4a). The 2-h running mean (black line) indicated that the central pressure first increased temporarily up to ~960 hPa at 0030 UTC 23 August, and then decreased rapidly by 30 hPa over the next 18 h. Thus, Goni’s intensification met the definition of RI, that is, a 30 hPa decrease in central pressure in 24 h (Appendix B). Hereafter, we define the period from 0030 UTC to 1830 UTC 23 August as the RI period. The temporary increase in

the central pressure at around 1030 UTC during Goni's passage near Ishigaki Island is due to the GBVTD-related limitations, as shown by the relatively large RMSDs at that time (Fig. 5.2). The central pressure decreased at an almost constant rate (-1.7 hPa h^{-1}) except for that temporary increase. In contrast, the maximum wind at 2-km altitude, despite some erratic fluctuations, rapidly increased by at least 30 m s^{-1} from 35 m s^{-1} during only 6 h from 0100 UTC to 0700 UTC 23 August while the RMW contracted greatly from 45 to 30 km (Fig. 5.4b). The maximum wind eventually reached at least 85 m s^{-1} at around 1900 UTC 23 August.

c. Structural evolution

Microwave satellite imagery shows that Goni had concentric eyewalls when it reached a point southeast of Taiwan at 0530 UTC 22 August (Fig. 5.5a). After 1700 UTC 22 August, there appeared to be active convection in both the inner and outer eyewalls because brightness temperatures became lower (Fig. 5.5b). Because 1700 UTC corresponds to 0100 local standard time, this temporary convective activity may have been associated with a diurnal cycle of convection as described by Dunion et al. (2014). Then, at 0435 UTC 23 August, Goni had a well-defined axisymmetric primary eyewall (Fig. 5.5c), suggesting that an eyewall replacement occurred.

Figures 5.6–5.8 show the structural evolution of the inner core before and after the eyewall replacement. At 2200 UTC 22 August, cloud-top temperatures associated with the inner eyewall were still low (Fig. 5.6a) and radar imagery showed a well-defined inner eyewall (Fig. 5.7a), but there was little evidence of a wind maximum at the inner eyewall (Fig. 5.8a), probably because of the limitations of the GBVTD analysis. Centers used in the GBVTD analysis are those determined relative to the RMW associated with the outer eyewall. Around that time, because the center of the inner eyewall wobbled relative to that of the outer eyewall, the centers were different, and as a result, the accuracy of the GBVTD retrieval around the inner eyewall was poor. After 0000 UTC 23 August, when Goni had reached a point ~ 200 km east of Taiwan, the storm underwent the eyewall replacement as the inner eyewall weakened and an outer eyewall developed (Fig. 5.7b). The disappearing inner eyewall merged with the outer eyewall on the southeast side at 0100 UTC 23 August (Fig. 5.7b). Brightness temperatures associated with the eyewall decreased, and a well-defined eye became visible on satellite imagery after 0330 UTC 23 August (Figs. 5.6b, c and d). Radar imagery showed a polygonal eyewall structure for a while after the replacement (Figs. 5.7c and d) and the wind

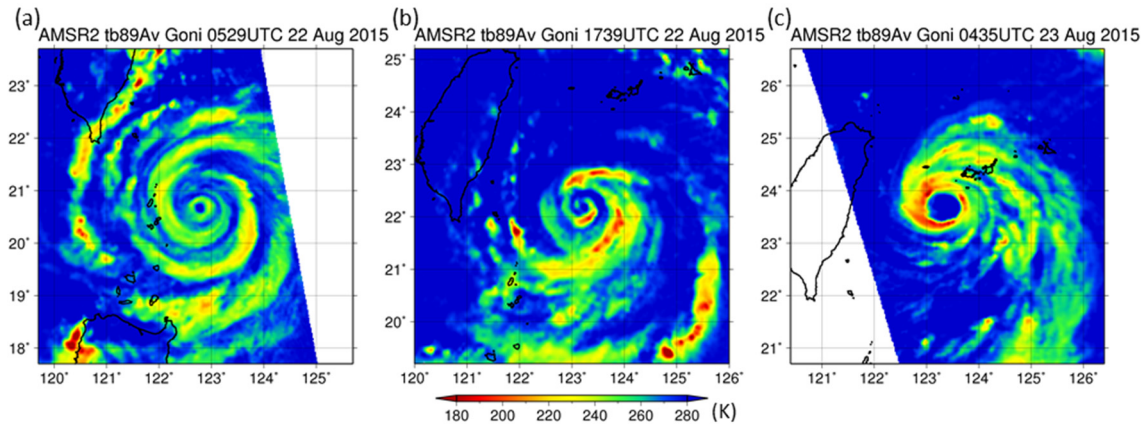


Fig. 5.5: Brightness temperatures from the Global Change Observation Mission 1st - Water (GCOM-W1) Advanced Microwave Scanning Radiometer 2 (AMSR2) (at 89 GHz A-horn, vertically polarized wave) polar-orbiting microwave satellite at (a) 0529 UTC 22 August, (b) 1739 UTC 22 August, and (c) 0435 UTC 23 August.

field at 2-km altitude showed local wind maxima near high reflectivity in the eyewall (Figs. 5.7c, 5.7d, 5.8c and 5.8d).

When Goni approached maturity, at 1730 UTC 23 August, there were many rainbands located outside the primary eyewall (Fig. 5.7f). Note that, due to radar attenuation, radar reflectivity distant from a radar site tends to be weaker than that near the site. Nonetheless, active rainbands were observed in the southeast quadrant where wind speed was also relatively strong (Fig. 5.8e).

After Goni reached maturity (1800 UTC 23 August), the storm had a concentric eyewall structure (Fig. 5.7g). However, no outer wind maximum was yet associated with the outer reflectivity maximum (~ 60 km) at that time (Fig. 5.8f).

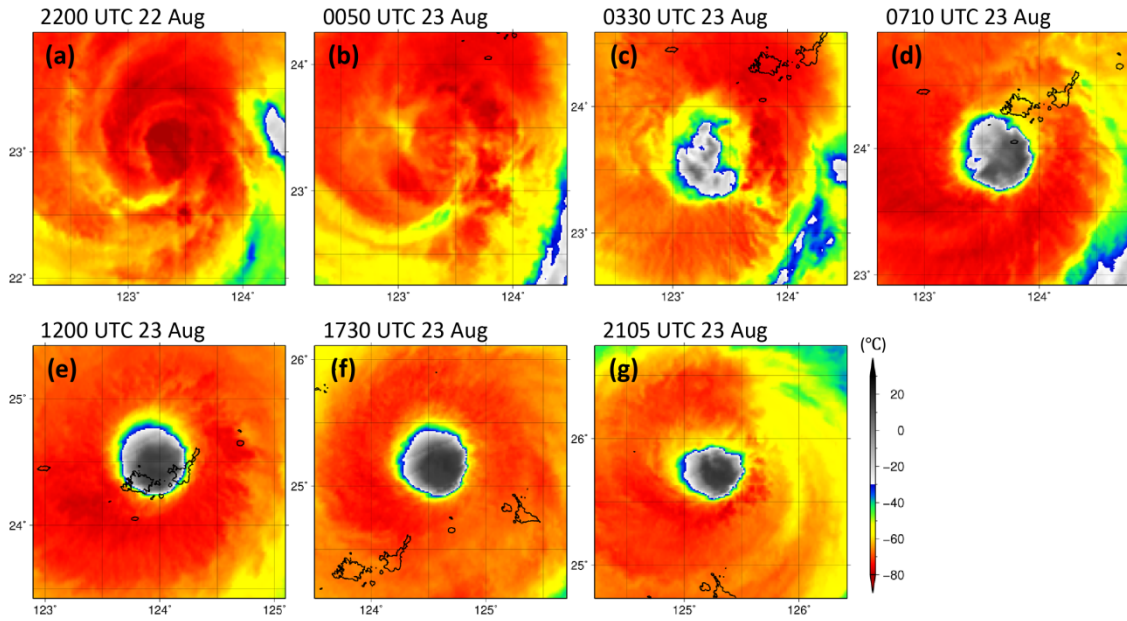


Fig. 5.6: Infrared brightness temperatures (at $10.4 \mu\text{m}$) from the Himawari-8 geostationary satellite.

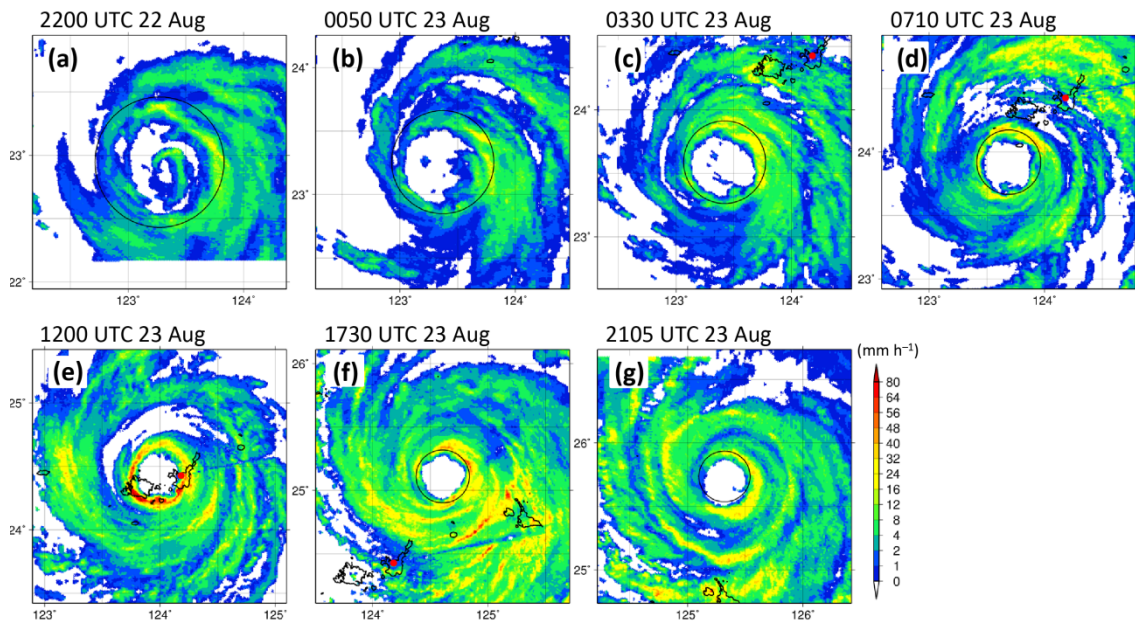


Fig. 5.7: Radar rainfall rate provided by the JMA. The red dot indicates the radar site. The black circle denotes the RMW.

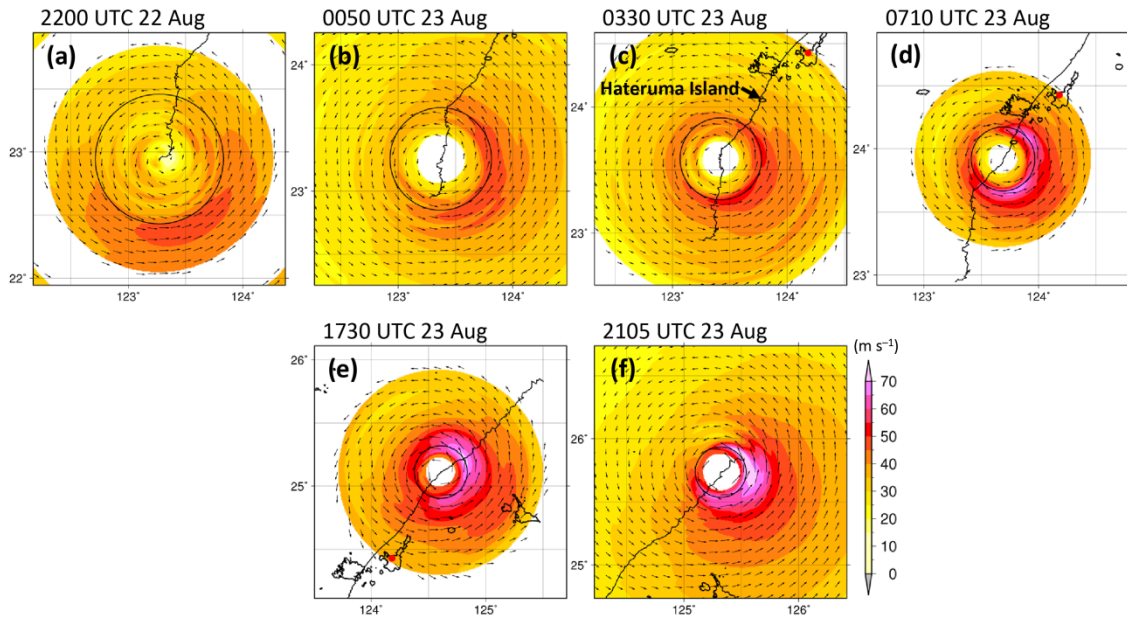


Fig. 5.8: Retrieved wind speed at 2-km altitude. The black line indicates the Goni's track, which is composed of the centers (from 2200 UTC 22 August to 2200 UTC 23 August) used in the GBVTD analysis and axisymmetric analyses. The red dot indicates the radar site. The black circle denotes the RMW. There was no GBVTD-retrieved wind field at 1200 UTC 23 August.

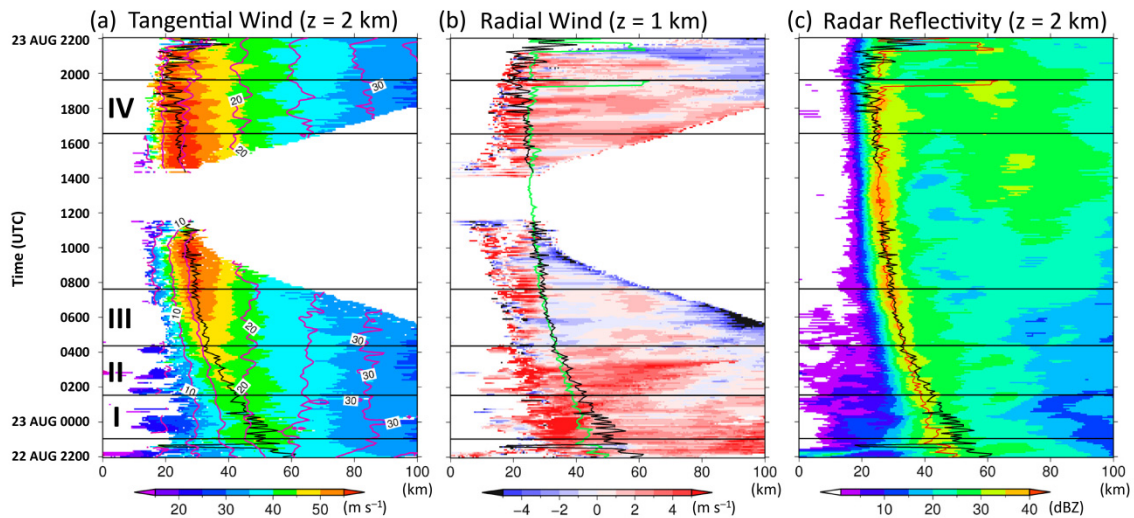


Fig. 5.9: (a) Radius–time Hovmöller diagram of \bar{v} at 2-km altitude (color scale), \bar{M} ($10^5 \text{ m}^2 \text{ s}^{-1}$, purple lines), and RMW (thick black line). The blank areas are where the GBVTD technique could not retrieve \bar{v} (i.e., during the TC's passage near Ishigaki Island and in the eye region). (b) Radius–time Hovmöller diagram of \bar{u} at 1-km altitude (color scale), radius of maximum radar reflectivity (green line), and RMW at 2-km altitude (thick black line). The blank areas are where the GBVTD technique could not retrieve \bar{u} . (c) Radius–time Hovmöller diagram of azimuthal mean radar reflectivity at 2-km altitude (color), radius of maximum radar reflectivity (red line), and RMW (thick black line). The black horizontal lines indicate the boundaries of the periods defined in Table 5.1.

Table 5.1: Definitions of the four periods.

	Period [UTC]	\bar{u} in the vicinity of the RMW at 1-km altitude
I	2300 22 Aug – 0125 23 Aug 2015	Relatively strong outflow
II	0130 23 Aug – 0415 23 Aug 2015	Outflow
III	0420 23 Aug – 0730 23 Aug 2015	Weak inflow immediately outside the RMW and outflow inside the RMW
IV	1630 23 Aug – 1930 23 Aug 2015	Outflow

5.4. Goni's RI

In this section, we document RI processes of Goni in detail. Radius–time Hovmöller diagrams of \bar{v} , \bar{u} , azimuthal mean radar reflectivity, and azimuthal mean absolute angular momentum \bar{M} (Fig. 5.9), where $\bar{M} = (1/2)fr^2 + r\bar{v}$, show the following:

- i) The 2-km RMW contracted from 60 to 25 km as \bar{v} in the vicinity of the RMW increased. Isopleths of \bar{M} inside the RMW moved inward with time such that the radial gradient of \bar{M} increased, whereas isopleths of \bar{M} outside the RMW moved outward during the first half of time period shown on the Hovmöller diagram.
- ii) While the RMW was rapidly contracting (from 2200 UTC 22 August to 0415 UTC 23 August), \bar{u} at 1-km altitude was outflow. After the contraction speed slowed down, \bar{u} just outside the RMW became inflow. Then, \bar{u} became outflow again at around 1800 UTC 23 August when Goni reached its peak intensity.
- iii) The radius of maximum reflectivity (RMR) at 2-km altitude was located inside the RMW during the period of rapid contraction. After Goni's passage near Ishigaki Island, the RMR was located outside the RMW and an outer reflectivity maximum formed around at radii of 60–80 km.

Hereafter, we focus on four specific periods (Table 5.1) during which enough wind data were retrieved to examine the processes at work. The boundary between periods I and II is determined by the difference in data density above 5-km altitude, and the boundary between periods II and III is determined by the timing of the change in \bar{u} at 1-km altitude from outflow to inflow just outside the RMW. Periods I and II encompass the onset of RI, period III falls within the period of RI, and during period IV, Goni is in its mature stage.

a. RI onset

During period I, the eyewall replacement had just been completed while the RMW rapidly contracted (Fig. 5.9a). There was relatively strong outflow of greater than 3 m s^{-1} inside the RMW at 1-km altitude (Fig. 5.9b). In radius–height plots of time-averaged \bar{v} , \bar{u} , azimuthal mean radar reflectivity, and \bar{M} (Fig. 5.10a–c), it can be seen that an axis of outflow was present that sloped radially outward with height at altitudes from 1 to 4 km (Fig. 5.10b). This structure may reflect the remnants of the low-level outflow above the inflow peak associated with the contracting RMW. The RMW sloped radially outward from 1- to 3-km altitude and inward from 3- to 5-km altitude (Fig. 5.10a). Stern et al. (2014) showed similar RMW slopes in their observations and numerical simulations and attributed these features to unbalanced flow in the vicinity of the RMW. During period I, the RMR was located 5 km inside the RMW and below 5-km altitude it was almost upright (Fig. 5.10a). Assuming that the reflectivity distribution is similar to the diabatic heating distribution, then this configuration was favorable for vortex spinup and RMW contraction (Shapiro and Willoughby 1982; Hack and Schubert 1986; Nolan et al. 2007; Pendergrass and Willoughby 2009; Rogers et al. 2013, 2015, 2016; Smith and Montgomery 2016), and likely led to the subsequent intensification, observed after this period.

During period II, Goni started to intensify again and the RMW continued to contract rapidly (Figs. 5.4 and 5.9a). The low-level outflow at and above 1-km altitude became weaker than it was during period I (Fig. 5.10e). The RMW was vertical up to 5-km altitude, and it sloped slightly outward above that altitude (Fig. 5.10d). The RMR was located a few kilometers inside the RMW and the slope of the RMR was more upright than slopes of \bar{M} surfaces in the vicinity of the RMR (Fig. 5.10d). This feature is consistent with the result of Hazelton et al. (2015), who showed the slopes of reflectivity and \bar{M} surfaces from composites of airborne Doppler radar and found that intensifying TCs tend to have dBZ surfaces that are more upright than \bar{M} surfaces. There was inflow just outside the RMW above 5-km altitude (Fig. 5.10e). Geostationary satellite imagery showed a well-defined eye from 0330 UTC 23 August (Fig. 5.6c) and a decrease over time in brightness temperatures associated with the eyewall (Figs. 5.6c and d). These features suggest that the secondary circulation driven by diabatic heating in the eyewall had started to strengthen.

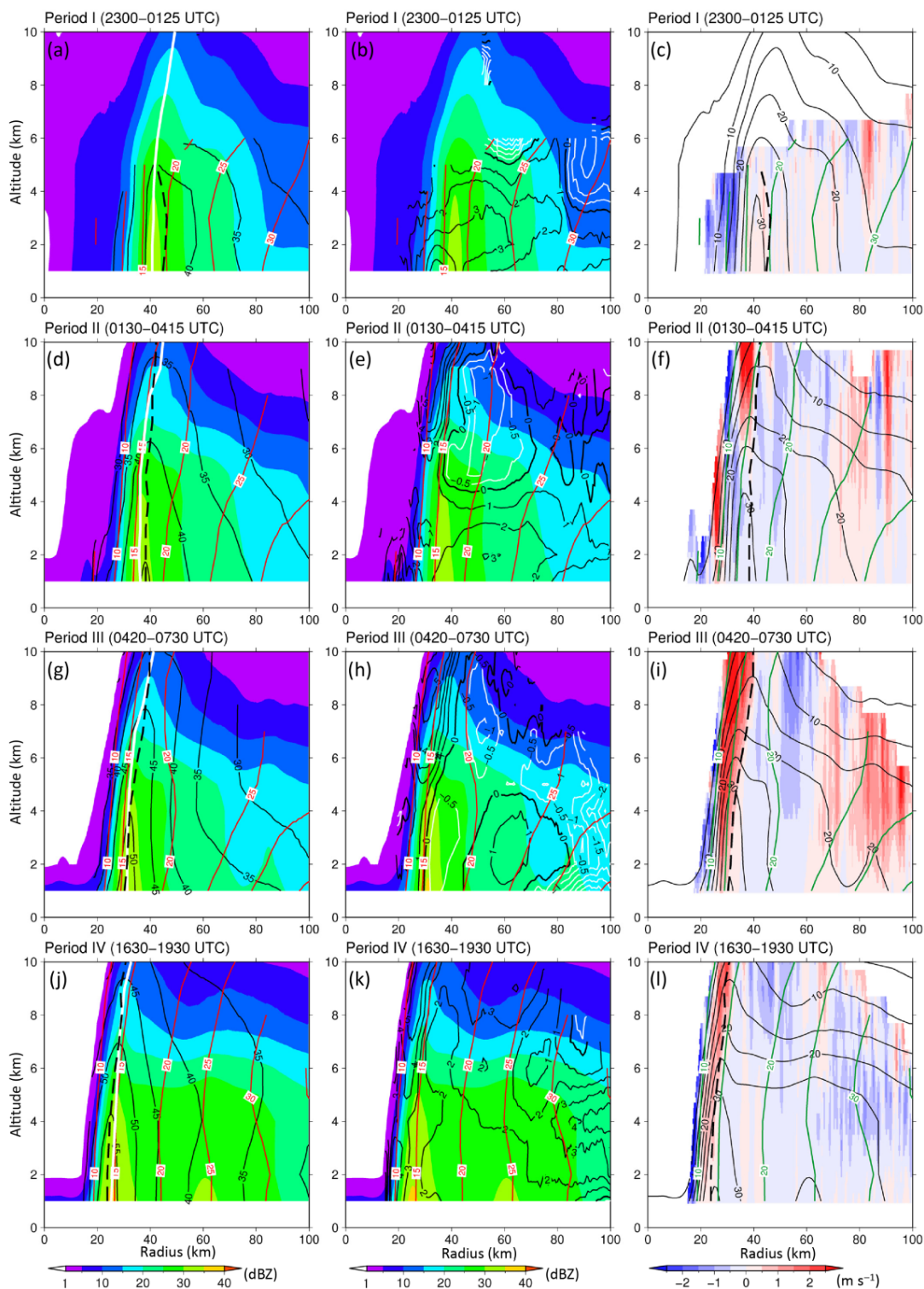


Fig. 5.10: Radius–height plots of (a) time-averaged \bar{v} (m s^{-1} , black contours), azimuthal mean radar reflectivity (color scale), and \bar{M} ($10^5 \text{ m}^2 \text{ s}^{-1}$, red contours), (b) time-averaged \bar{u} (m s^{-1} , black contours positive, white contours negative), azimuthal mean radar reflectivity (color scale), and \bar{M} ($10^5 \text{ m}^2 \text{ s}^{-1}$, red contours), (c) time-averaged \bar{w} (color scale), azimuthal mean radar reflectivity (black contours, but the zero contour is omitted), and \bar{M} ($10^5 \text{ m}^2 \text{ s}^{-1}$, green contours) during period I. The dashed line is the RMW and the white line is the RMR. Contours were drawn in areas where there were observations averaged at least over 1 h in total. (d), (e), (f) As in (a), (b), (c), but for period II. (g), (h), (i) As in (a), (b), (c), but for period III. (j), (k), (l) As in (a), (b), (c), but for period IV.

However, the distribution of \bar{w} calculated from upward integration of the mass continuity equation showed downdrafts just inside the RMW below 6-km altitude (Fig. 5.10f). Because BL models for TCs predict that a frictionally forced updraft lies near the RMW (e.g., Kepert 2001; Kepert and Wang 2001; Kepert and Nolan 2014) and because observations have shown that there are azimuthal-mean updrafts near the RMW (Bell and Montgomery 2008; Reasor et al. 2009; Rogers et al. 2012, 2013; Bell et al. 2012; Sanger et al. 2014; Stern et al. 2014), these downdrafts are most likely artificial products of the analysis. Using numerical simulation results as truth, Nolan (2013) revealed that, in the case of tornadoes, vertical velocities derived from Doppler radar data are problematic. He demonstrated that both the lack of a BL mass flux into the core region in the radar data and a positive bias of \bar{u} caused by outward centrifuging of debris by a tornado are likely to produce anomalously large downward motion inside the RMW. In the case of Goni, no inflow was retrieved in the vicinity of the RMW even at 1-km altitude during period II, leading to a lack of the BL convergence that should be present around the RMW (e.g., Kepert and Wang 2001). As a result, updrafts that should exist in and just above the BL were not calculated. Instead, downdrafts were computed because at altitudes from 1 to 4 km around the RMW divergence was mainly retrieved. For comparison, if it is assumed that the vertical velocity at 4-km altitude just inside the RMW is 0.5 m s^{-1} , then downward integration of the mass continuity equation from 4-km altitude yields a vertical velocity of $\sim 0.8 \text{ m s}^{-1}$ at 1-km altitude.

From period I to period II, the 2-km RMW rapidly contracted from 50 to 33 km. Along with this contraction, the tangential wind field contracted. For example, the 40 m s^{-1} isopleth outside the RMW contracted from a radius of 60 to 50 km (Fig. 5.9a). Weak reflectivity ranging from 25 to 30 dBZ was distributed from the 60 km to the 70 km radius in isolation from the eyewall (Fig. 5.9c). This reflectivity may be inner rainbands moving with the outflow in the lower troposphere, as shown by Moon and Nolan (2015).

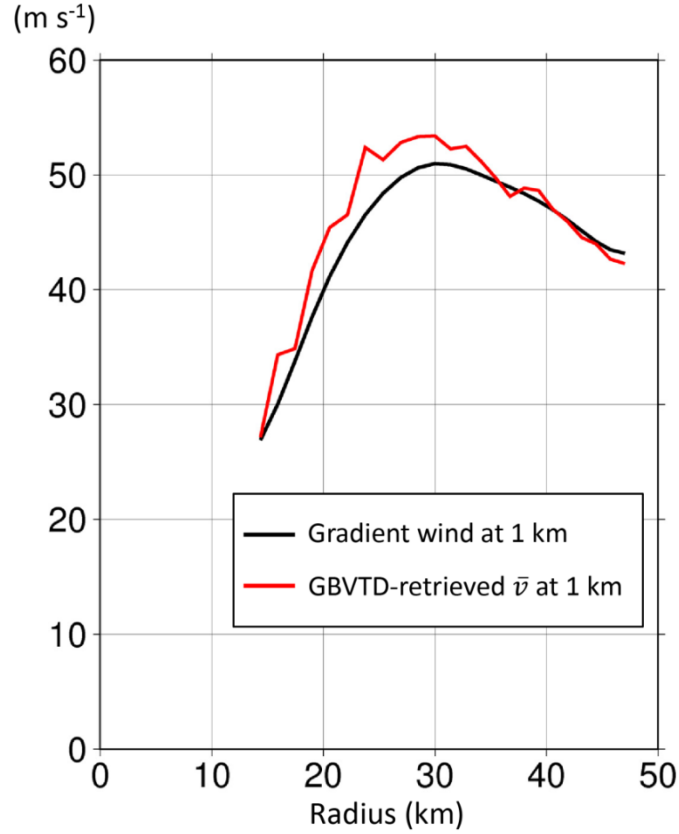


Fig. 5.11: Radial profile of gradient wind and GBVTD-retrieved \bar{v} at 1-km altitude.

Table 5.2: Contraction speed of the RMW at 1- and 10-km altitude. The speed was calculated from the difference between the mean RMWs of two periods.

	$z = 1 \text{ km}$	$z = 10 \text{ km}$
I \rightarrow II	-2.44 km h^{-1}	–
II \rightarrow III	-2.63 km h^{-1}	-0.82 km h^{-1}
III \rightarrow IV	-0.54 km h^{-1}	-0.74 km h^{-1}

Table 5.3: Values of the numerator and denominator of the term on the right-hand side of Eq. (5.1) and the diagnosed time tendency of the RMW at altitudes of 1 and 10 km between periods II and III, computed by using time-averaged \bar{v} during periods II and III. Values of $\partial^2 \bar{v} / \partial r^2$ were radially filtered using the 10-km running mean.

	$z = 1 \text{ km}$	$z = 10 \text{ km}$
$(\partial/\partial r)(\partial \bar{v}/\partial t)$	$-0.104 \times 10^6 \text{ s}^{-2}$	$-0.014 \times 10^6 \text{ s}^{-2}$
$\partial^2 \bar{v} / \partial r^2$	$-0.138 \times 10^6 \text{ m}^{-1} \text{ s}^{-1}$	$-0.093 \times 10^6 \text{ m}^{-1} \text{ s}^{-1}$
$-\frac{(\partial/\partial r)(\partial \bar{v}/\partial t)}{\partial^2 \bar{v} / \partial r^2} \Big _{\text{RMW}}$	-2.73 km h^{-1}	-0.54 km h^{-1}

b. RI phase

During period III, Typhoon Goni continued to intensify, but the contraction speed of the RMW slowed down (Figs. 5.4 and 5.9a). Just outside the RMW, \bar{u} at 1-km altitude changed to inflow, although weak outflow remained at around 60-km radius in the lower troposphere (Figs. 5.9b and 5.10h). At the same time, the 45 m s⁻¹ isopleth of \bar{v} outside the RMW started to expand radially outward (Fig. 5.9a). There was a strong updraft inside the RMW through the free atmosphere (Fig. 5.10i), and the magnitude of reflectivity in the eyewall increased during the second half of period III (Fig. 5.9c). These features are consistent with decrease in brightness temperatures in the satellite imagery (Figs. 5.5c, 5.6c, 5.6d, and 5.6e), though part of the increase in reflectivity is likely due to the effect of radar attenuation. The RMR at altitudes between 2 to 9 km was located inside the outward-sloping RMW (Fig. 5.10g). In contrast, reflectivity outside the RMW between 40 and 60 km radius became weaker with time, signaling the formation of a moat and the potential development of another secondary eyewall (Fig. 5.9c).

From 0530 UTC to 0725 UTC, Goni's eyewall passed over Hateruma Island (Fig. 5.8c), where there is a weather station operated by the JMA. We estimate the gradient wind speed at 1-km altitude from the gradient wind equation by using sea level pressure data at 5-min intervals observed at Hateruma Island during that period, under the assumption that radial pressure gradients at the surface and 1-km altitude are almost the same and that the pressure observations are representative of axisymmetric pressure in the vicinity of the eyewall. Here, the radial pressure gradient at each time is derived from the pressure observation and the distance between the storm center and the weather station, both of which are smoothed in time (by applying a 1-2-1 filter 20 times). Estimated gradient winds are, in general, smaller than the corresponding GBVTD-retrieved \bar{v} at 1-km altitude (Fig. 5.11), indicating that the flow around and inside the RMW at 1-km altitude is supergradient. This result is consistent with the existence of outflow inside the RMW at 1-km altitude (Figs. 5.9b and 5.10h).

The slope of the RMW became more outward slanting, reaching ~45° from the vertical. This slanting was caused by the more rapid contraction of the RMW at 1-km altitude, from 38 km during period II to 30 km during period III, compared with its contraction at 10-km altitude, from 42 km during period II to 39.5 km during period III (Table 5.2). Stern et al. (2015) demonstrated by using a diagnostic equation for RMW contraction that the speed of RMW contraction can be determined from the radial gradient of the

time rate of change of \bar{v} , $(\partial/\partial r)(\partial\bar{v}/\partial t)$, and the sharpness of peak in the radial profile of \bar{v} , $\partial^2\bar{v}/\partial r^2$, at the RMW:

$$\frac{d\text{RMW}}{dt} = - \left. \frac{(\partial/\partial r)(\partial\bar{v}/\partial t)}{\partial^2\bar{v}/\partial r^2} \right|_{\text{RMW}}. \quad (5.1)$$

Contraction is faster when $(\partial/\partial r)(\partial\bar{v}/\partial t)$ has a larger negative value and the \bar{v} peak is broader. From period I to period II, the outflow just outside the RMW in the lower troposphere above the BL suppressed the increase in \bar{v} there (see subsection 5.4d for more details), causing $(\partial/\partial r)(\partial\bar{v}/\partial t)$ to become more negative and leading to the more rapid contraction at 1-km altitude than at 10-km altitude (Table 5.3).

c. Mature stage

Goni reached its peak intensity after it passed near the Ishigaki radar (Fig. 5.4). An outer reflectivity maximum was formed from the radius of 60 to 80 km after 1000 UTC 23 August (Figs. 5.9c and 5.10j). Maximum \bar{v} at 2-km altitude peaked from 1430 UTC to 1700 UTC 23 August (Fig. 5.9a). The tangential wind field expanded radially outward, and isopleths of \bar{M} greater than $25 \times 10^5 \text{ m}^2 \text{ s}^{-1}$ moved radially inward from 1430 UTC to 2130 UTC. \bar{u} again became outflow above the BL (Figs. 5.9b and 5.10k). The RMR was located outside the RMW (Figs. 5.9c and 5.10j). The updraft axis associated with the eyewall was located just inside the RMW (Fig. 5.10l), but weakened. This weakening is consistent with increase in brightness temperatures in the satellite imagery (Figs. 5.6f and 5.6g). From period III to period IV, the contraction speed of the RMW in the upper level was the same as before, whereas the speed in the lower troposphere slowed down (Table 5.2). As a result, the RMW sloped less outward with height ($\sim 38^\circ$ from the vertical) in the mature stage (Fig. 5.10j). After 1800 UTC, the region with \bar{v} greater than 35 m s^{-1} expanded radially outward from 70 to 80 km, and isopleths of \bar{M} around the outer reflectivity peak moved radially inward (Fig. 5.9a). However, there was no local maximum in \bar{v} around the outer reflectivity peak at this time (Fig. 5.9a).

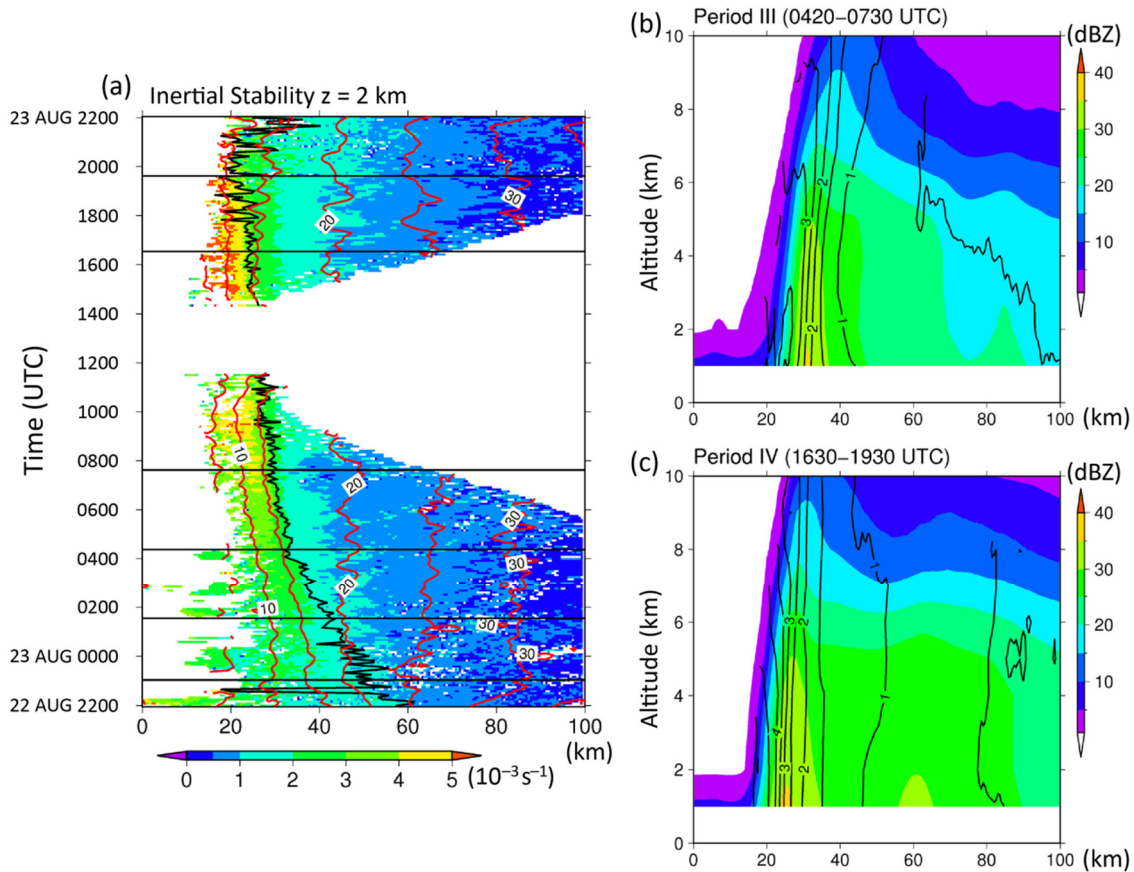


Fig. 5.12: (a) Hovmöller diagram of I (10^{-3} s^{-1} , color scale), \bar{M} ($10^5 \text{ m}^2 \text{ s}^{-1}$, red lines), and RMW (thick black line) at 2-km altitude. The blank areas are where the GBVTD technique could not retrieve \bar{v} (i.e., during the TC's passage near Ishigaki Island and in the eye region). The black horizontal lines indicate the boundaries of the periods defined in Table 5.1. (b, c) Radius–height plot of time-averaged I (10^{-3} s^{-1} , black contours) and azimuthal mean radar reflectivity (color scale) during (b) period III and (c) period IV.

A region of inertial stability, I (where $I^2 \equiv \left(\frac{1}{r^3}\right) \frac{\partial \bar{M}^2}{\partial r}$), of more than $1 \times 10^{-3} \text{ s}^{-1}$ ($\sim 20f$) at 2-km altitude outside the eyewall expanded from 40 to 50 km from 0800 UTC to 2200 UTC 23 August (Fig. 5.12a), whereas I at 2-km altitude outside the outer reflectivity maximum decreased (Figs. 5.12b and c). I in the middle troposphere increased (Figs. 5.12b and c) in the vicinity of the outer reflectivity maximum because \bar{v} increased greatly there (Fig. 5.10j). This increase in I is expected to increase the ratio of energy retained as wind kinetic energy to injected heat energy around the outer reflectivity peak (Rozoff et al. 2012), although the GBVTD analysis did not confirm the development of an outer wind maximum during the analysis period.

d. Absolute angular momentum budget

As described in subsection 1.3a, because absolute angular momentum is, to good approximation, materially conserved except in the BL, examining changes in the distribution of \bar{M} through the secondary circulation is useful for understanding the evolution of a TC vortex. We here examine changes in \bar{M} during the onset of and during RI by performing a budget analysis of \bar{M} .

The angular momentum budget equation can be expressed as follows (e.g., Rozoff et al. 2012):

$$\frac{\partial \bar{M}}{\partial t} = -r\bar{u}\bar{\zeta}_a - \bar{w} \frac{\partial \bar{M}}{\partial z} - \overline{ru'\zeta'_a} - \overline{w' \frac{\partial M'}{\partial z}} - \frac{1}{\rho'} \frac{\partial p'}{\partial \lambda} + r\bar{F}_\lambda, \quad (5.2)$$

where ζ_a is the vertical component of absolute vorticity, ρ is density, p is pressure, λ is the azimuthal angle, and F_λ is the tangential component of friction/diffusion. The azimuthal mean (axisymmetric component) of each variable is denoted by an overbar, and the deviation from the azimuthal mean (storm-relative asymmetric flow) is denoted by a prime. We calculate the first four terms on the right-hand side of Eq. (5.2). Additionally, because the sum of the four terms is inconsistent with the actual local time tendency, $\partial \bar{M} / \partial t$, the residual difference between the actual local time tendency and the sum from the first term to the fourth term is computed to evaluate analysis errors. We do not focus on the \bar{M} distribution at radii greater than 80 km because the retrieval accuracy is not good near the edge of the analysis field, as shown in Fig. 5.9b.

In general, although values of the eddy terms (the third and fourth terms) were much smaller than those of the azimuthal mean terms (the first and second terms), they were nonnegligible (Figs. 5.13d and e, and Figs. 5.14d and e). This is consistent with previous studies (Reasor et al. 2009; Rozoff et al. 2012; Sun et al. 2013; Persing et al. 2013; Miyamoto and Takemi 2015). Note that in the GBVTD technique, asymmetric radial winds are aliased into the other wind components (Lee et al. 1999), which introduces uncertainty into the values of the eddy terms. Also, note that the uncertainty in the vertical velocity calculation leads to uncertainty in the \bar{M} budget.

During period II (Fig. 5.13), \bar{M} increased greatly inside the RMW. Outside the RMW, \bar{M} increased at and above 5-km altitude, whereas \bar{M} decreased below 5-km altitude. The residual difference shows a lack of a positive advective tendency inside the RMW, and outside the RMW below 3-km altitude. The lack of both updrafts around the RMW during period II (Fig. 5.10f) and \bar{v} data in the BL most likely led to incorrect distribution of the second term and thus the budget inconsistency. A local time tendency of \bar{M}

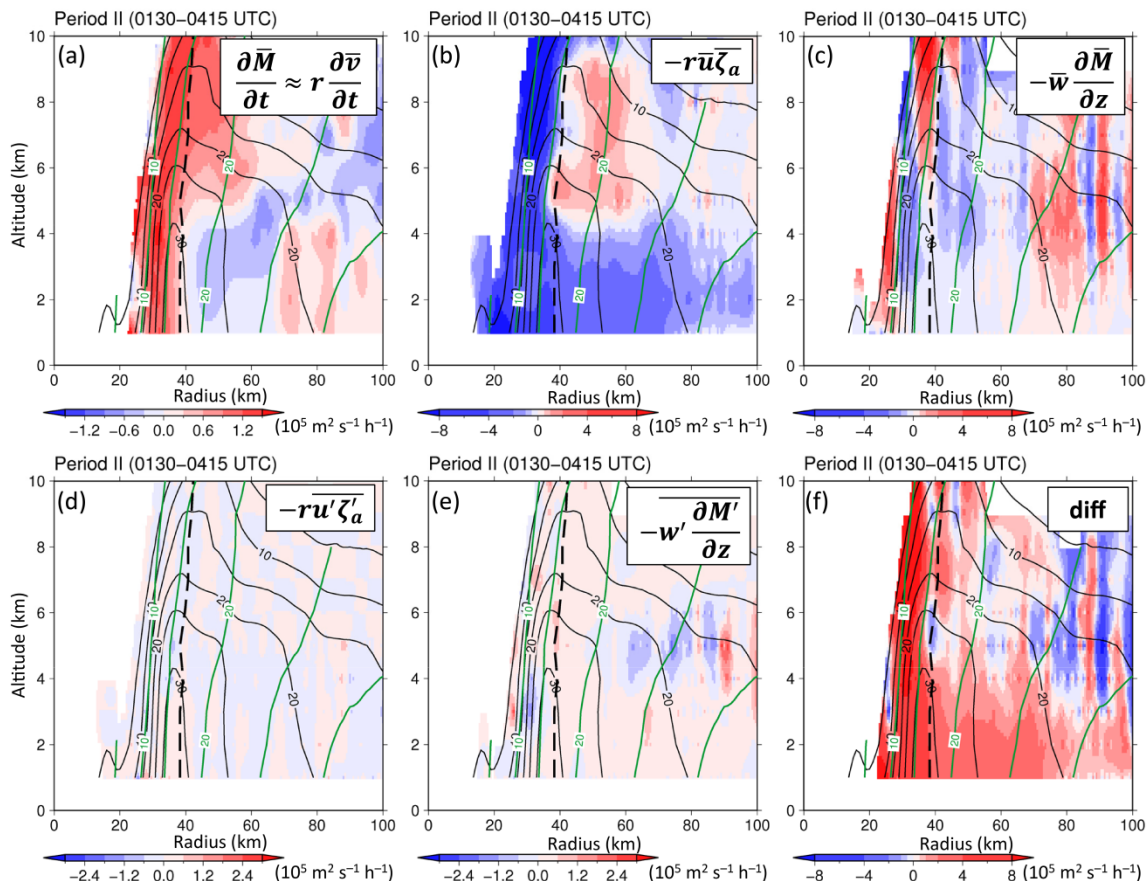


Fig. 5.13: Radius–height plots of time-averaged (a) local time tendency, $\partial \bar{M} / \partial t$, (color scale) (b) axisymmetric radial advection (color scale), (c) axisymmetric vertical advection (color scale), (d) eddy radial advection (color scale), (e) eddy vertical advection (color scale), and (f) residual difference between the local time tendency and the sum from the first term to the fourth term (color scale) during period II. The black contours are azimuthal mean radar reflectivity (the zero contour is omitted), the dashed line is the RMW, and the green contours are \bar{M} ($10^5 \text{ m}^2 \text{ s}^{-1}$).

outside the RMW was consistent with the distribution of the first term in terms of sign: the low-level outflow above the BL contributed to the decrease in \bar{M} below 5-km altitude; and upper-level inflow contributed to the increase in \bar{M} at and above 5-km altitude. In addition, this local decrease in \bar{M} outside the RMW below 5-km altitude led to the maintenance of relatively low I outside the RMW (Fig. 5.12a) through the decrease in the radial gradient of \bar{M} ,

$$\text{because } I^2 \equiv \left(\frac{1}{r^3} \right) \frac{\partial \bar{M}^2}{\partial r}.$$

During period III (Fig. 5.14), both \bar{M} just outside the RMW and \bar{M} inside the RMW increased. Inside the RMW, the first term was negative because of outflow, the second term was positive, and both eddy terms were slightly positive. The residual difference shows two large positive regions: just

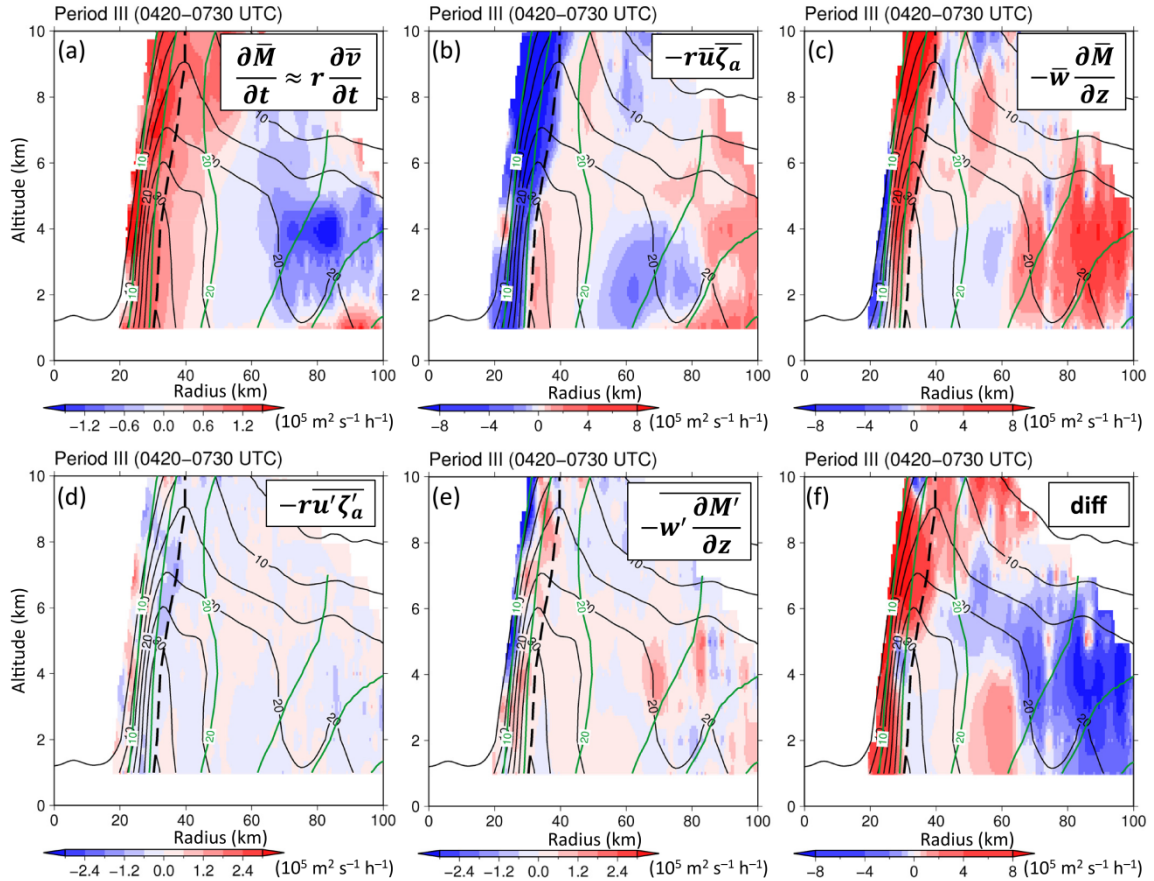


Fig. 5.14: As in Fig. 5.13, but for period III.

inside the RMW below 4-km altitude and above 5-km altitude. The lack of a positive advective tendency at low levels was likely caused by insufficient updrafts at low levels (Fig. 5.10i) and the lack of \bar{v} data in the BL, as in period II. If vertical velocities were $\sim 1.0 \text{ m s}^{-1}$ and $\partial \bar{M} / \partial z (= r \partial \bar{v} / \partial z)$ was 1.6 times as large at 1-km altitude as that calculated from the difference in \bar{v} between 1- and 2-km altitude just inside the RMW, then the tendency of the second term just inside the RMW at 1-km altitude would offset that of the first term. Just outside the RMW, the local time tendency is consistent with the distribution of the first term in terms of sign: that is, inflow just outside the RMW contributed to the increase in \bar{M} there, leading to the expansion of the tangential wind field.

Upward advection of high \bar{M} from the BL may have contributed to the actual increase in \bar{M} just inside the RMW during periods II and III in spite of the negative horizontal advective tendency in \bar{M} due to the outflow there. Zhang et al. (2001) performed a numerical simulation of Hurricane Andrew (1992) and demonstrated that upward advection of \bar{M} from the BL

overwhelms the decrease in \bar{M} owing to outflow associated with supergradient flow in the BL during RI. Schmidt and Smith (2016) also showed similar processes of vortex spinup and concluded that eyewall spinup occurs by upward advection of \bar{M} from the BL. Smith et al. (2009) and Smith and Montgomery (2016) have emphasized the importance of unbalanced flow in the BL to spin up a TC vortex.

5.5. Discussion

There were two notable features in our analysis results. During the onset of RI, just after the completion of an ERC, Goni had a broad region of outflow from the inside of the RMW to 100-km radius at altitudes between 1 to 5 km. As RI proceeded, \bar{u} changed from outflow to inflow just outside the RMW. These features are discussed below.

Relatively strong outflow just above the BL around the RMW suggests that there was supergradient flow in and above the BL. A low-level outflow jet associated with supergradient winds has been shown by many previous studies (Zhang et al. 2001; Kepert and Wang 2001; Kepert 2006a, b, 2013; Zhang et al. 2011). In particular, the existence of unbalanced flow in the BL during intensification and SEF has been demonstrated (Smith et al. 2009; Huang et al. 2012; Bell et al. 2012; Abarca and Montgomery 2013, 2014, 2015; Abarca et al. 2016). Abarca and Montgomery (2013) showed by numerical simulation that there is outflow above the BL around and outside the newly formed secondary eyewall in the presence of a strong BL inflow and supergradient flow during SEF. Meanwhile, in the Sawyer–Eliassen diagnostic model, outflow just above the BL can be represented by the response to the frictional forcing (Fudeyasu and Wang 2011).

In the case of Goni, however, the outflow outside the RMW around the onset of RI occupied a broad region from the inside of the RMW to 100-km radius at altitudes between 1 and 5 km. This feature is different from the distribution of \bar{u} that is generally seen in intensifying TCs. Observational and modeling studies have shown that an outflow jet associated with supergradient flow is confined to a narrow layer around the RMW just above the BL inflow, that intensifying TCs have weak inflow outside the RMW above the BL, and that this inflow advects \bar{M} radially inward to spin up a TC vortex (Reasor et al. 2009; Persing et al. 2013; Rogers et al. 2013, 2015; Wang and Wang 2014; Stern et al. 2015; Kilroy et al. 2016; Zhang et al. 2017). Such weak inflow is represented by the secondary circulation induced by imposed diabatic heating in the eyewall (Shapiro and Willoughby 1982; Hack and Schubert 1986; Pendergrass and Willoughby 2009). The existence of weak inflow above the BL has been theoretically modeled to explain vortex spinup, although roles of weak inflow in intensification differ among theories (Ooyama 1969; Emanuel 1989; Smith et al. 2009).

There is a possibility that the wide outflow region was partly due to analysis errors. The number of PPI scans observed by the operational Doppler

radar may be insufficient to resolve a narrow outflow jet just above the BL and insufficient to retrieve weak inflow in a broad region outside the RMW. Meanwhile, Wu et al. (2012) and Huang et al. (2012) showed that a broad outflow region exists from 1- to 5-km altitude outside the secondary eyewall up to ~ 180 -km radius just after SEF. Zhang et al. (2011) showed from a composite dropsonde dataset that for cat 4–5 hurricanes, an outflow region exists up to the $3 \times \text{RMW}$ just above 1.5-km altitude, although the number of samples was too few for the results to be considered robust. Liu et al. (1999) and Zhang et al. (2001) showed that outflow associated with supergradient flow exists within radii of more than the $3 \times \text{RMW}$ just above the BL during RI. In addition, recent studies have shown that supergradient flow exists not only in the BL but also at around 2-km altitude (Montgomery et al. 2014; Rogers et al. 2015). In such a case, outflow may occur at altitudes up to 4 km.

In Goni, the outflow just outside the RMW at low levels played a role in decreasing \bar{M} (Fig. 5.13) and lowering I there (Fig. 5.12a) around the onset of RI, just after the ERC, but not during RI. Rogers et al. (2013, 2015) hypothesized that low I outside the RMW is favorable for strong inflow, and thus greater mass fluxes into the eyewall region, because of less resistance to radial displacement, and this strong inflow and greater mass fluxes can lead to intensification. Whether such outflow is present in other intensifying TCs around the onset of RI just after the ERC, and what roles such outflow might play in subsequent intensification, should be addressed in a future study.

During RI, \bar{u} just outside the RMW at low levels above the BL became inflow. An updraft peak and the RMR between 2- and 9-km altitude were located inside the RMW. Thus, the secondary circulation became well-established. These features were consistent with those of intensifying TCs (Rogers et al. 2013, 2015). In addition, the increasing outward slope of the RMW during the first half of RI may have led to updrafts inside the RMW in the free atmosphere, provided that environmental conditions were favorable for intensification, because previous studies have shown that there is an updraft peak near the low-level RMW.

5.6. Summary

An operational ground-based Doppler radar located at Ishigaki Island observed Typhoon Goni (2015) for 24 h just after it completed an ERC. During this observation period, Goni experienced RI and then reached peak intensity. We examined a series of RI processes of Goni mainly from an axisymmetric perspective by using radar reflectivity and retrieved wind by the GBVTD technique with high resolution in both time and space. The P_{min} was estimated to fall by 30 hPa from 960 hPa at an almost constant rate during 18 h by using the retrieved tangential wind at 2-km altitude, sea level pressure observations near the radar site and the gradient wind equation, whereas the V_{max} at 2-km altitude increased by 30 m s⁻¹ from 35 m s⁻¹ during the first 6 h of RI and increased by 20 m s⁻¹ during the subsequent 12 h.

Around the onset of RI, during periods I and II when Goni temporarily weakened and started to intensify again, and when the inner eyewall disappeared, the following features were observed:

- i) Relatively strong outflow (>2 m s⁻¹) was present both inside and outside the RMW above the BL.
- ii) Immediately before RI onset, the RMW sloped radially outward from 1- to 3-km altitude and sloped inward from 3- to 5-km altitude.
- iii) Despite the outflow, \bar{M} inside the RMW was increased.
- iv) The maximum wind at 2-km altitude started to increase after the inner eyewall disappeared.
- v) The 2-km RMW rapidly contracted from 50 to 33 km within ~5 h.
- vi) The tangential wind field and high I region at 2-km altitude also contracted.
- vii) The RMR was located a few kilometers inside the RMW below 9-km altitude.

The outflow in the vicinity of the RMW suggests that there was supergradient flow in and just above the BL. The absolute angular momentum budget analysis showed that the outflow just outside the RMW above the BL contributed to the decrease in \bar{M} , that is, the contraction of the tangential wind field and high I region.

During RI, period III, the following features were seen:

- i) The RMW sloped more outward with height, reaching ~45° from the vertical.
- ii) The contraction speed of the low-level RMW slowed down.

- iii) \bar{u} in the lower troposphere changed from outflow to inflow immediately outside the RMW.
- iv) An updraft axis associated with the eyewall was located inside the RMW.
- v) The RMR was located inside the RMW at altitudes between 2 to 9 km.
- vi) A well-defined eye appeared, and active convection was enhanced in the eyewall.
- vii) Reflectivity outside the RMW between 40 and 60 km radius became weaker with time, leading to the formation of a moat and signaling the potential development of another secondary eyewall.
- viii) The tangential wind field around the RMW started to expand.

The absolute angular momentum budget analysis showed that the inflow above the BL immediately outside the RMW transported \bar{M} inward and contributed to the expansion of the tangential wind field.

During the mature stage, period IV, the following features were found:

- i) The RMR was located outside the RMW.
- ii) The outward slope of the RMW became less ($\sim 38^\circ$ from the vertical).
- iii) The tangential wind field expanded.
- iv) I outside the RMW was increased in the middle troposphere.
- v) An outer reflectivity maximum was formed at twice the RMW.

Although we could examine Goni's RI using high-resolution observations for 24 h, which is one of the novel features of this study, the study has some limitations. We lacked observations of BL flow, and the wind field immediately before the maturity of Goni. In addition, there are also some limitations inherent in the GBVTD technique. Furthermore, we lacked thermodynamic observations. These limitations made it difficult to capture completely the RI processes of Goni. In a future study, we will examine the detailed processes of RI associated with ERCs by using numerical simulations to reproduce the RI observed in Goni. In particular, we are interested in the roles of outflow and supergradient wind in the onset of RI, the reason that \bar{u} changed from outflow to inflow immediately outside the RMW, and how BL processes interact with the intensification of the interior vortex.

Chapter 6: Further Improvement in the SHIPS Using Rainfall and Structural Information

6.1. Motivation

The SHIPS predicts intensity changes mainly using environmental predictors, based on the idea that intensity change and maximum potential intensity (MPI) primarily depend on environmental conditions. However, intensity change is also dependent highly on convective activity and diabatic heating distribution of a TC. Observational studies have shown that brightness temperatures (T_b) and rainfall amounts from microwave satellites have the relationship with the current and future intensity (e.g., Rao and MacArthur 1994; Rao and McCoy 1997; Cecil and Zipser 1999; Bankert and Tag 2002; Keiper and Jiang 2012). 85-GHz T_b provides information about inner-core structure and convective activity, and 19-GHz and 37-GHz T_b provide rainfall information. Cecil and Zipser (1999) presented that the azimuthal mean 85-GHz T_b is related to the subsequent intensity change. Keiper and Jiang (2012) showed by using satellite observations that the formation of an eyewall ring that consists of low-level water clouds and warm rain is related to the subsequent rapid intensification (RI). In Chapter 3, we examined the relationship between the axisymmetry of rainfall distribution within 100-km radius from the TC center and future intensity change using a satellite-derived rainfall product, Global Satellite Mapping of Precipitation (GSMaP, Kubota et al. 2007, 2009), and showed that the larger the axisymmetry, the larger the subsequent intensification.

The importance of inner-core structure associated with internal processes to intensity change has been also verified from other perspectives. Hendricks et al. (2010) showed that there is little difference in environmental conditions between TCs that experienced RI and those that intensified at a normal rate, and concluded that the intensification rate is controlled mostly by internal dynamical processes, provided that environmental conditions are favorable for intensification. Miyamoto and Takemi (2013, 2015) performed an idealized numerical simulation and demonstrated that the axisymmetrization of potential vorticity field around a TC is important for a transition to RI and then an eyewall ring starts to form.

Based on these studies, the addition of predictors associated with TC

structure to SHIPS may improve its accuracy, in particular for the following two types of TCs; i) large-sized, unorganized TCs that are formed in the center region of monsoon gyres (Lander 1994), and ii) RI TCs defined as the 95th percentile of intensity changes over a 24-h period (Kaplan and DeMaria 2003, Appendix B). The former “monsoon gyre” type TCs can be characterized as a large-scale vortex relative to the maximum wind speed, a lack of a distinct cloud system center, and little intensification even in a favorable environment for intensification. Because the current version of SHIPS is not given structural information explicitly, it predicts intensification even for such type of TCs provided that environmental conditions are favorable, which can lead to an overforecast. As for RI TCs, the current version of SHIPS tends to underforecast their intensity. Predictors associated with the inner-core structure may increase the rate of intensity change, leading to a better forecast of RI.

Previous studies have shown that the addition of some microwave T_b predictors (e.g., mean T_b and maximum T_b within 100 km radius from the TC center) derived from 19-GHz T_b and 85-GHz T_b data to SHIPS (referred to SHIPS-MI) can improve its accuracy (Jones et al. 2006, 2007a, 2007b). Jones et al. (2006) presented that a 2%–8% improvement was obtained in SHIPS-MI compared with SHIPS without those predictors. However, issues of temporally sparse microwave satellite observations and their latency available to operational centers make operationalizing SHIPS-MI difficult so far. In this study, we resolve these issues by using data that are available to operational centers at least in near-real time at constant time intervals and that are available for a long period more than 10 years to calculate coefficients of a regression equation. The hourly GSMaP product meets these criteria. This product covers the area from 60°S to 60°N, available since 2000, and has a family of reanalysis version, near-real time version (about 4-h latency) and real-time version (almost no latency, Japan Aerospace Exploration Agency (JAXA) 2017a). We derive new predictors associated with TC rainfall and structure from the GSMaP data.

The purpose of this chapter is to examine the degree to which the accuracy can be improved if rainfall and structural information is added to SHIPS. In other words, the purpose is to examine how much the rainfall and structural information at the initial time is statistically related to the subsequent intensity change in the framework of a multiple regression model. For this purpose, we mainly use a GSMaP reanalysis product, which has the highest accuracy among the GSMaP family products. Then, we use a near-real

time GSMaP product to examine the feasibility for operational use.

6.2. Data and methodology

In this section, we describe data sources of both training samples from 2000 to 2012 used for computing coefficients of the regression model and independent samples from 2013 to 2016 used for forecast experiments in this study. Then, we introduce new predictors associated with rainfall distribution and structural features, followed by procedures of forecast experiments and their verification.

a. Data

For training samples, best track data at 6-h intervals from the RSMC Tokyo are used, including the intensity (both P_{min} and V_{max}), the center position, and the radius of 15 m s⁻¹ wind speed. Wind speeds in the best track data are based on 10-min sustained wind speeds. The best track data do not provide V_{max} information during tropical depressions ($V_{max} < 34$ kt, 1 kt = 0.514 m s⁻¹). Thus, the training samples include TCs at tropical storm strength and above ($V_{max} > 34$ kt), TCs just before they intensified into tropical storms, and storms just after they weakened to tropical depressions or extratropical cyclones. In the latter two cases, V_{max} is assumed as 30 kt.

Training samples of atmospheric environmental predictors are derived from JRA-55 reanalysis data (Kobayashi et al. 2015). Predictors related to infrared satellite T_b are derived from successive geostationary satellite data that have been used in the JMA. An SST dataset to calculate an empirical MPI (DeMaria and Kaplan 1994) is Centennial Observation-Based Estimates of SST (COBE-SST, Ishii et al. 2005) because it is used for JRA-55 data as the ocean boundary condition. Ocean heat content (OHC) is calculated using ocean data (MOVE/MRI.COM, Usui et al. 2006).

Table 6.1: SHIPS predictors list used in SHIPS-Base. Predictors retained in the P_{min} and V_{max} models are denoted with a P or V, respectively.

Predictor	Description	Model
MSLP	P_{min} at ft = 0	P, V
VMAX	V_{max} at ft = 0	
VMA2	Square of VMAX	V
PER	12-h change in P_{min} or V_{max}	P, V
OSLP	Absolute of (MSLP minus 970)	P
PMPE	(MSLP minus 880) times PER	P
VMPE	VMAX times PER	V
POT	Maximum potential intensity (MPI) minus VMAX	P, V
POT2	Square of POT	P, V
COHC	Ocean heat content	P, V
OHC2	Square of COHC	P, V
T200	200-hPa temperature (r=200–800 km)	P, V
T250	250-hPa temperature (r=200–800 km)	P, V
ZNAL	Zonal storm motion	P, V
RHMD	700–500 hPa relative humidity (%) (r=200–800 km)	P, V
EPOS	θ_e difference between lifted surface parcel and environment	P, V
SHDC	850–200-hPa vertical shear magnitude (r=0–1000 km)	P, V
SHGC	Generalized 850–200-hPa shear (average over all levels)	P, V
SHSH	Square of SHDC	P, V
SHLT	SHDC times the sine of latitude	P, V
SHVM	SHDC divided by VMAX	P, V
VMSH	VMAX times SHDC	V
PMSH	(MSLP minus 880) times SHDC	P
Z850	850-hPa absolute vorticity (r=0–1000 km)	P, V
D200	200-hPa divergence (r=0–1000 km)	P, V
TWAT	Tendency of 850 hPa tangential wind (r=0–500 km)	P, V
TADV	The temperature advection between 850 and 700 hPa (r=0–500 km)	P, V
TGRD	The magnitude of the temperature gradient between 850 and 700 hPa (r=0–500 km)	P, V
PC30	Percent area of infrared brightness temperature $T_b < -30^\circ\text{C}$ (r=300 km)	P, V
SDIR	Standard deviation of T_b (r=300 km)	P, V

GSMaP data used to extract rainfall and structural information for training samples are hourly reanalysis data (version 6 algorithm without the gauge correction), which are composed of satellite-based rainfall rate (mm h^{-1}) estimates with a resolution of 0.1° . These data are processed and provided by JAXA (JAXA 2017b). Because a temporal resolution of microwave satellite-based rainfall estimates at each point is about 3–6 h, hourly estimates are obtained by two temporal interpolation methods; the morph method and rainfall correction by a Kalman filter (Ushio et al. 2009). Details of GSMaP data for TC research are referred to Chapter 3. For inner-core structure such as eye size, radial distribution of convection, and concentric eyewalls, 0.1° resolution may be too coarse to resolve it completely. This is the limitation in this study.

For independent samples in forecast experiments (also see section 2.3), we prepare data that had been available to an RSMC Tokyo in real time. Real time analysis data at 6-h intervals from the RSMC Tokyo are used, including the intensity, the center position, and the radius of 15 m s^{-1} wind speed. JMA GSM forecast data are used. The GSM runs 4 times a day at 0000, 0600, 1200 and 1800 UTC, among which the GSM initialized at 1200 UTC runs up to 11 days, and others run up to 84 h from 2013 to 2015 and up to 132 h in 2016. Thus, the number of our forecast samples up to 5 days ahead decreases after 96-h forecast time ($ft = 96 \text{ h}$). For a SST dataset, Merged satellite and in situ data Global Daily Sea Surface Temperature (MDGSST, Kurihara et al. 2006) is used because it is used for the GSM as the ocean boundary condition. As for GSMaP data, both the GSMaP reanalysis product and near-real time product are used. Rainfall estimates of the reanalysis product are based on both past and future satellite data, while estimates of the near-real time product are based on only past data. Thus, data quality is much better for the former than for the latter. We examine the impact of GSMaP data used on intensity forecast.

b. New predictors

Most of predictors used in the current version of SHIPS with the GSM output (hereafter SHIPS-Base) are the same as those of SHIPS used in the United States (Table 6.1). We newly add five predictors listed in Table 6.2 to SHIPS-Base (hereafter SHIPS-GSMaP). IR T_b -related predictors are removed because the accuracy gets worse when they remain. Among the five new predictors, four predictors are mainly derived from GSMaP data; axisymmetry, rainfall areal coverage, radius of maximum rainfall, and total volumetric rain. Rossby number is derived from TC analysis data.

These five predictors were selected by performing stepwise regression (forward, backward, and stepwise selections) using IMSL libraries. Initially, we prepared 26 conventional predictors listed in Table 6.1 and 14 possible predictors associated with rainfall amount and structural features. These predictors were fed into the regression. We counted the number of times each predictor was retained during the forecast period up to 120 h at 6 h intervals in processes of three kinds of stepwise regressions. Then, predictors that had relatively high frequency of selection in the stepwise regressions were determined as new predictors. The selected new predictors are defined below.

The definition of axisymmetry γ is the same as that of Miyamoto and Takemi (2013) and Section 3.2 as follows;

$$\gamma(r, z, t) \equiv \frac{\bar{\phi}^{\lambda}(r, z, t)^2}{\bar{\phi}^{\lambda}(r, z, t)^2 + \int_0^{2\pi} \phi'(r, \lambda, z, t)^2 d\lambda / 2\pi} * 100, \quad (6.1)$$

where ϕ is a variable, and r , λ , and z are the radial, tangential, and axial direction, and t is time, respectively. As a variable in this study, we use the rainfall rate from the GSMaP dataset. The azimuthal mean (axisymmetric component) of a variable is denoted by an overbar, and the deviation from the azimuthal mean is denoted by a prime. We prepared 3 kinds of axisymmetry; an average over 0–300-km radius from the center, an average over 0–100-km radius, and an average over 100–300-km radius. Among three predictors, we found that the first one had the highest frequency of selection in the stepwise regression.

Rainfall areal coverage is defined as a percent area of rainfall over 0.1 mm h⁻¹ in a specific region. As with axisymmetry, three regions were prepared; a region over 0–300-km radius from the center, a region over 0–100-km radius, and a region over 100–300-km radius. For P_{min} forecast, a radius of 100–300 km from the center, whose region is approximately the outside of the radius of maximum wind (RMW), was selected in the stepwise regression. For V_{max} forecast, a radius of 0–300 km from the center was

selected. This parameter expresses the density of rainfall area.

The radius of maximum rainfall is defined as the radius of azimuthal mean maximum rainfall within 400-km radius from the center. This parameter is extracted as a proxy of the RMW.

Total volumetric rain is the sum of rainfall in a specific region. The same three regions as the rainfall areal coverage were prepared. For P_{min} forecast, a radius of 0–100 km from the center was selected in the stepwise regression. For V_{max} forecast, a radius of 100–300 km from the center was selected. This parameter can be a proxy of the magnitude of diabatic heating.

The amplitudes of a wavenumber-1 rainfall asymmetry averaged over each three region described above were also examined. However, none of the three parameters were retained with relatively high frequency of selection in the stepwise regression.

The parameters derived from the GSMaP data are obtained at 1-h intervals, but we apply a 5-h running mean (ft = $-5 \sim 0$ h) to eliminate biases dependent on satellite data used in the hourly GSMaP data. Section 3.2 presented that biases between satellites can be eliminated if a 6-h running mean is applied, and that effective signal related to intensity change can be detected by the running mean.

Miyamoto and Takemi (2015) demonstrated that the time taken for RI onset depends on Rossby numbers, R_o , of vortices at the initial time, and that intensification starts earlier when initial Rossby numbers are larger. R_o is defined as follows:

$$R_o \equiv \frac{V_{max}}{R_m f}, \quad (6.2)$$

where R_m is the RMW, f is the Coriolis parameter. Unfortunately, the best track data used in this study do not have RMW information. Instead, we use the radius of 15 m s^{-1} wind speed as a proxy of the RMW to compute R_o .

Because the new parameters are values at the initial forecast time, they are not dependent on forecast times. However, no matter how favorable rainfall and structural conditions at the initial time are for subsequent intensification, a TC does not intensify unless favorable environmental conditions are maintained along the future track. To overcome this limitation, values of the axisymmetry and total volumetric rainfall are multiplied by OHC along a forecast track. This modification adds time dependency to those parameters and adds nonlinearity of those parameters to a multiple regression model.

Table 6.2: Added predictors to SHIPS-GSMaP and excluded predictors. Predictors retained in the P_{min} and V_{max} models are denoted with a P or V, respectively.

In/Out	Predictor	Description	Model
In	AXIS	Axisymmetry of rainfall structure within 300-km radius times COHC	P, V
In	RCOV	Rain percent area coverage between 100- and 300-km radius	P
In	RCOV	Rain percent area coverage within 300-km radius	V
In	RMAX	Radius of maximum azimuthal mean rainfall	P, V
In	RVOL	Total volumetric rain within 100-km radius times COHC	P
In	RVOL	Total volumetric rain between 100- and 300-km radius times COHC	V
In	ROSB	Rosby number	P, V
Out	PC30	Percent area of infrared brightness temperature $T_b < -30^\circ\text{C}$ ($r=300$ km)	–
Out	SDIR	Standard deviation of T_b ($r=300$ km)	–

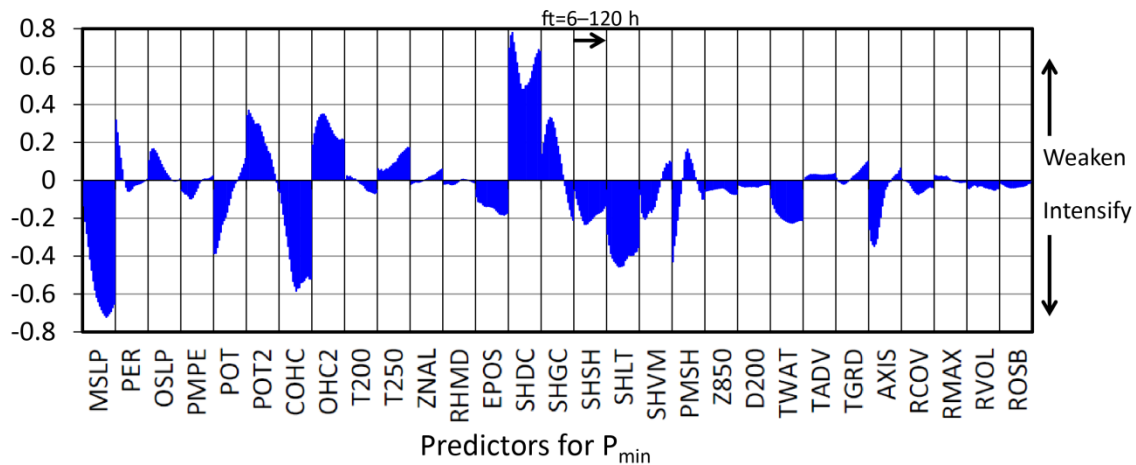


Fig. 6.1: Normalized SHIPS-GSMaP predictor coefficients for P_{min} from $ft = 6$ to 120 h. All predictor coefficients of $ft = 6-120$ h are plotted in each predictor box. A negative coefficient contributes to the decrease in P_{min} when the corresponding predictor value is above average.

Training samples for the period from 2000 to 2012 are used to calculate coefficients of SHIPS-Base and SHIPS-GSMaP. In this process, values of predictors are normalized by subtracting their means and dividing by their standard deviations. This normalization enables us to compare the magnitude of coefficients relatively. Normalized SHIPS coefficients for P_{min} (Fig. 6.1) indicate relative contribution of the new predictors to intensity change. In Fig. 6.1, a negative coefficient contributes to the decrease in P_{min} when the corresponding predictor value is above average. The magnitude of AXIS coefficients in the first half of the forecast period is generally greatest among the new predictors. AXIS contributes to intensification from $ft = 6$ to $ft = 84$ when its value is above average, whereas it contributes to weakening after $ft = 90$ when its value is above average. Other new predictors slightly contribute to intensity change. RCOV, RVOL and ROSB contribute to intensification when each value is above average. RMAX contributes to weakening from $ft = 6$ h to $ft = 66$ and contributes to intensification after $ft = 72$ when its value is above average, although the magnitude of RMAX coefficients are quite small.

The sign of coefficients of some new predictors is generally physically reasonable and consistent with previous studies. AXIS is consistent with the results of Miyamoto and Takemi (2013), Zagrodnik and Jiang (2014), and section 3 of this study, which showed that axisymmetric structure is related to intensification. RCOV and RVOL are consistent with the results of Jiang and Ramirez (2013), who found that rainfall in the inner-core region is at least moderate to heavy (i.e., total raining area $> 3000 \text{ km}^2$, total volumetric water $> 5000 \text{ mm h}^{-1} \text{ km}^2$) in TCs before the onset of RI. ROSB is consistent with the findings of Miyamoto and Takemi (2015).

c. Forecast experiments and their verification

Forecast experiments are performed for TCs over the ocean from 2013 to 2016, completely independent of the training samples. Two kinds of SHIPS-GSMaP forecasts are done. One uses the reanalysis GSMaP product to examine how much the accuracy improves provided that the quality of rainfall and structural information is as good as possible. Center positions used to extract parameters from GSMaP data are from the best track data. Similarly, the Rossby number is computed by using the best track data. The other uses the near-real time product to examine the feasibility of SHIPS-GSMaP for operational use in real time (hereafter “real-time SHIPS-GSMaP” to discriminate between two SHIPS-GSMaP forecasts). In real time SHIPS-GSMaP, center positions used are from the real time analysis data and the Rossby number is also computed by using the real time analysis data. Because the latency of the near-real time GSMaP product and the GSM output is almost the same (~4 h), it is possible to run real-time SHIPS-GSMaP operationally.

Forecasts are done for TCs that are recorded in the best track data. The forecasts include tropical depressions that subsequently evolved into tropical storms. A forecast is performed while the GSM predicts the existence of the storm within 5 days ahead even though it is forecast to evolve into an extratropical cyclone in the GSM forecast during forecast times. However, the forecast is stopped after it makes landfall in the GSM forecast. For practical use of SHIPS, when P_{min} is forecast to be above 1010 hPa, P_{min} forecast is corrected to 1010 hPa. Similarly, when V_{mas} is forecast to be below 30 kt, V_{max} forecast is corrected to 30 kt. This correction is justified because the GSM still forecast the existence of the TC at that time.

For verification, SHIPS forecasts are compared to the best track data. If there are no reference data in the best track, such forecasts are excluded from the verification. For P_{min} forecasts, the verification includes all TCs and extratropical cyclones that are recorded in the best track data, provided that SHIPS forecasts them. The reason why we include extratropical cyclones comes from the timing of extratropical transition. In general, the timing tends to be delayed in real time analysis. We consider that for operational use of SHIPS, it is convenient for verification to include storms that have already experienced extratropical transition in the best track data. For V_{max} forecasts, the verification does not include tropical depressions because the best track data used do not provide V_{max} information at tropical depression stage.

We conduct a paired Student’s t -test statistics with a one sided test to

confirm the improvement of the accuracy, given null hypothesis that there is no difference in the average of mean absolute errors (MAEs) between SHIPS-Base and SHIPS-GSMaP. Here, we have to consider the number of samples, i.e., sample size. As pointed out by Aberson and DeMaria (1994), we cannot say that all forecast samples are completely independent because forecast samples in the same TC can be correlated. For example, a forecast error at $ft = 48$ h initialized at a particular time can be correlated to that at $ft = 48$ h initialized at 6 h later for the same TC. In this study, following a method by Wilks (2006) and Jones et al. (2006), we calculate lag-1 autoregression to forecast errors at a particular forecast time and we introduce the effective sample size, N_e , as follows;

$$N_e = N \frac{(1-\rho_1)}{(1+\rho_1)}, \quad (6.3)$$

where N is the actual sample size, ρ_1 is the lag-1 autoregression coefficient. Table 6.3 lists results of ρ_1 and N_e . The correlation coefficients lie between 0.4–0.9, which leads to the large decrease in the number of samples. Nevertheless, the number of samples is greater than 80 up to $ft = 96$ h, which is sufficient to perform a significance test.

Intensity change is classified as steady state TCs, intensifying TCs and weakening TCs, following the same definition used in Jones et al. (2006); TCs with intensity changes < -10 hPa over a particular forecast duration (from the initial time to each forecast time) are classified as intensifying TCs, TCs with intensity changes $> +10$ hPa are weakening TCs, and others are steady state TCs. Note that by definition, there are cases that are classified as steady state TCs that actually experience both intensification and weakening during the forecast period. However, because SHIPS is a model to predict intensity change over a particular period, this definition is reasonable to verify the performance of SHIPS.

Table 6.3: Actual sample sizes (N), effective sample sizes (N_e), lag-1 autocorrelation coefficients (ρ_1), differences in mean absolute errors between SHIPS-Base and SHIPS-GSMaP, student t -statistic (t) for P_{min} and V_{max} , respectively. Bold and italic values in the column of t -statistic are statistically significant at the 95% significant level with a one sided test.

ft (h)	N (P_{min})	N_e (P_{min})	ρ_1 (P_{min})	Diff		N (V_{max})	N_e (V_{max})	ρ_1 (V_{max})	Diff	
				in MAE (P_{min})	t (P_{min})				in MAE (V_{max})	t (V_{max})
6	2294	684	0.54	0.07	<i>2.86</i>	1893	719	0.45	0.05	<i>1.84</i>
12	2225	583	0.58	0.21	<i>4.06</i>	1863	587	0.52	0.13	<i>2.74</i>
18	2142	508	0.62	0.36	<i>4.67</i>	1820	481	0.58	0.25	<i>3.75</i>
24	2049	364	0.70	0.54	<i>4.46</i>	1756	353	0.67	0.34	<i>3.48</i>
30	1958	285	0.75	0.68	<i>4.15</i>	1671	278	0.71	0.39	<i>3.08</i>
36	1875	220	0.79	0.73	<i>3.42</i>	1586	221	0.76	0.43	<i>2.81</i>
42	1783	180	0.82	0.81	<i>3.23</i>	1501	196	0.77	0.40	<i>2.30</i>
48	1706	162	0.83	0.78	<i>2.89</i>	1422	169	0.79	0.33	<i>1.77</i>
54	1625	149	0.83	0.75	<i>2.81</i>	1335	156	0.79	0.25	1.30
60	1550	133	0.84	0.73	<i>2.71</i>	1269	131	0.81	0.20	0.89
66	1475	115	0.86	0.73	<i>2.69</i>	1196	121	0.82	0.20	0.88
72	1407	112	0.85	0.66	<i>2.52</i>	1121	104	0.83	0.17	0.65
78	1341	105	0.86	0.59	<i>2.28</i>	1051	96	0.83	0.12	0.44
84	1266	98	0.86	0.49	<i>1.83</i>	984	98	0.82	0.12	0.39
90	427	90	0.65	0.71	<i>2.44</i>	335	89	0.58	0.39	1.22
96	395	81	0.66	0.55	<i>1.72</i>	314	80	0.60	0.30	0.91
102	372	73	0.67	0.50	1.53	295	74	0.60	0.38	1.15
108	349	89	0.59	0.49	<i>1.89</i>	269	74	0.57	0.29	0.96
114	323	92	0.56	0.38	1.54	248	67	0.57	0.17	0.56
120	299	64	0.65	0.18	0.68	227	54	0.62	0.15	0.59

6.3. Results

In this section, we show the model performance in a similar way to Jones et al. (2006). We mainly show the result of P_{min} forecast in which the addition of the new predictors has a larger impact on the improvement than in V_{max} forecast. First, we show the result when the reanalysis GSMaP product is used. Then, we present some forecast examples and discuss what is improved and what is unresolved. Finally, we show the result of real-time forecast.

a. Forecast performance

We compare SHIPS-GSMaP with SHIPS-Base. The performance of P_{min} and V_{max} at each forecast time in SHIPS-Base (Fig. 6.2a) shows that the MAE of P_{min} is ~ 13.2 hPa at $ft = 48$ h, ~ 15.2 hPa at $ft = 72$ h, and ~ 16.5 hPa after $ft = 90$ h. The MAE of V_{max} is ~ 11.4 kt at $ft = 48$ h, and ~ 13 kt after $ft = 72$ h. The MAEs of P_{min} and V_{max} in SHIPS-GSMaP are smaller than those in SHIPS-Base for all forecast times. The improvement rate (Fig. 6.2b) indicates that P_{min} forecast in SHIPS-GSMaP outperforms that of SHIPS-Base by 1%–7%, while V_{max} forecast improves by 1%–5%. The degree of the improvement in P_{min} is greater than that of V_{max} . The improvement is statistically significant at the 95% confidence level for P_{min} forecast up to $ft = 96$ h and $ft = 108$ h, and for V_{max} during a period of $ft = 6$ –48 h. Improvement is maximized at $ft = 30$ h for P_{min} up to near 7% and at $ft = 36$ h for V_{max} up to over 4%. Thus, rainfall and structural information at $ft = 0$ h definitely improves the accuracy of SHIPS mainly in the first half of the forecast period. This is consistent with that of Jones et al. (2006).

Next, to examine the improvement rate stratified by some conditions, MAEs of P_{min} forecasts at $ft = 48$ h are plotted relative to initial intensity in Fig. 6.3a. We consider that the improvement for 2 days forecast is important because MAEs greatly increase within 2 days (Fig. 6.2a). MAEs are decreased at initial intensities of 960 hPa and greater, where forecast samples account for 70% of the total. MAEs relative to the actual intensity change (Fig. 6.3b) indicate that improvement is seen at intensity changes between -15 and 10 hPa in 48 h, where the number of samples is greater than 100 in each bin. For intensifying TCs whose P_{min} fell by more than 25 hPa in 48 h, MAEs are not changed.

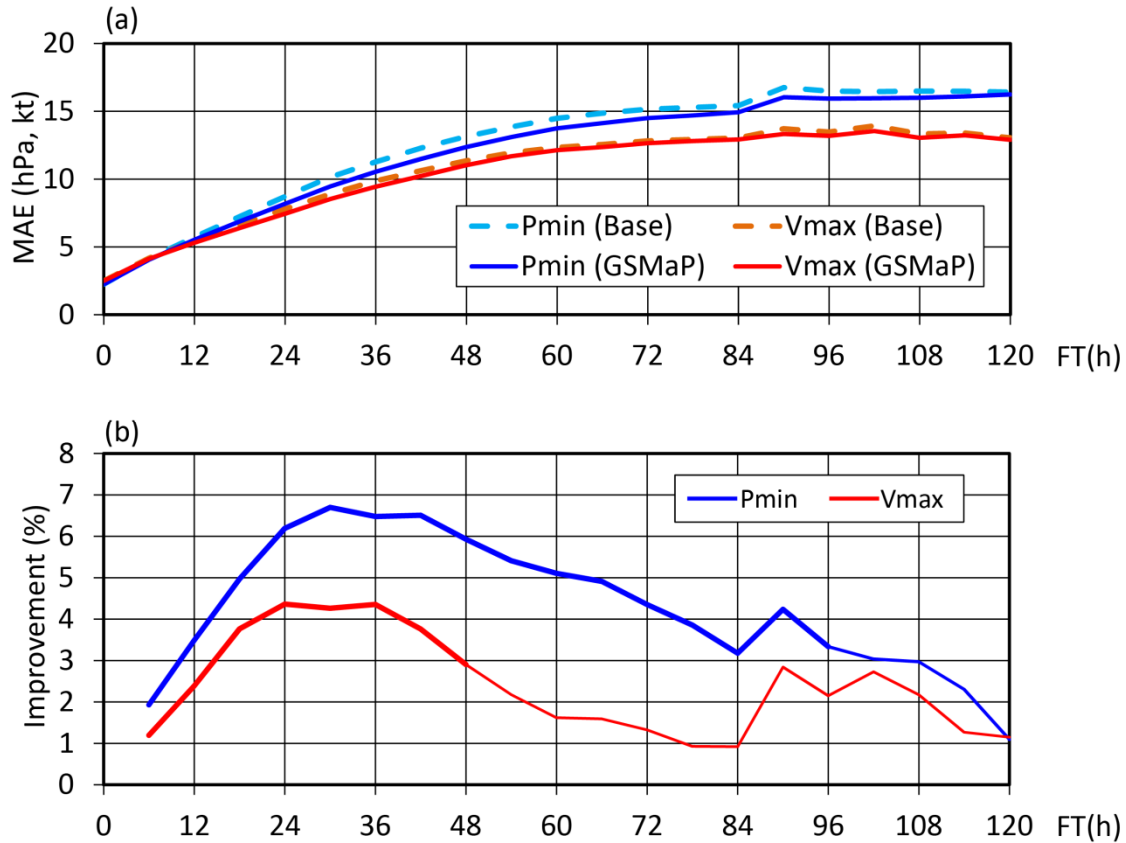


Fig. 6.2: (a) Mean absolute errors (hPa for P_{min} , kt for V_{max}) of the SHIPS-Base and SHIPS-GSMaP forecasts up to 5 days ahead for independent samples from 2013 to 2016 for the WNP basin. (b) Percent improvement of the SHIPS-GSMaP forecasts relative to the SHIPS-Base forecasts from 2013 to 2016 in the WNP basin. Bold lines indicate statistically significant differences at the 95% level.

Error frequency binned into 5-hPa intervals at $ft = 48$ h (Fig. 6.4a) shows that on the whole, the frequency of the 0 error bin is increased in SHIPS-GSMaP, indicating the improvement of forecast skill. While the frequency of positive errors is little changed, the frequency of negative errors from -20 to -40 hPa is decreased. This decrease is caused by the improvement for intensifying and steady state TCs (Figs. 6.4b and c). For intensifying TCs (Fig. 6.4b), the frequency peak in SHIPS-GSMaP is displaced in the positive direction by 10 hPa, indicating that SHIPS-GSMaP tends to underforecast P_{min} more than SHIPS-Base. Here, underforecasting means that P_{min} is forecast to be greater than the actual P_{min} . For steady state TCs, SHIPS-GSMaP contributes to the suppression of overforecasts. As a result, the error frequency distribution in SHIPS-GSMaP becomes more peaked than in SHIPS-Base. For weakening TCs (Fig. 6.4d), there is little difference in the frequency between SHIPS-GSMaP and SHIPS-Base.

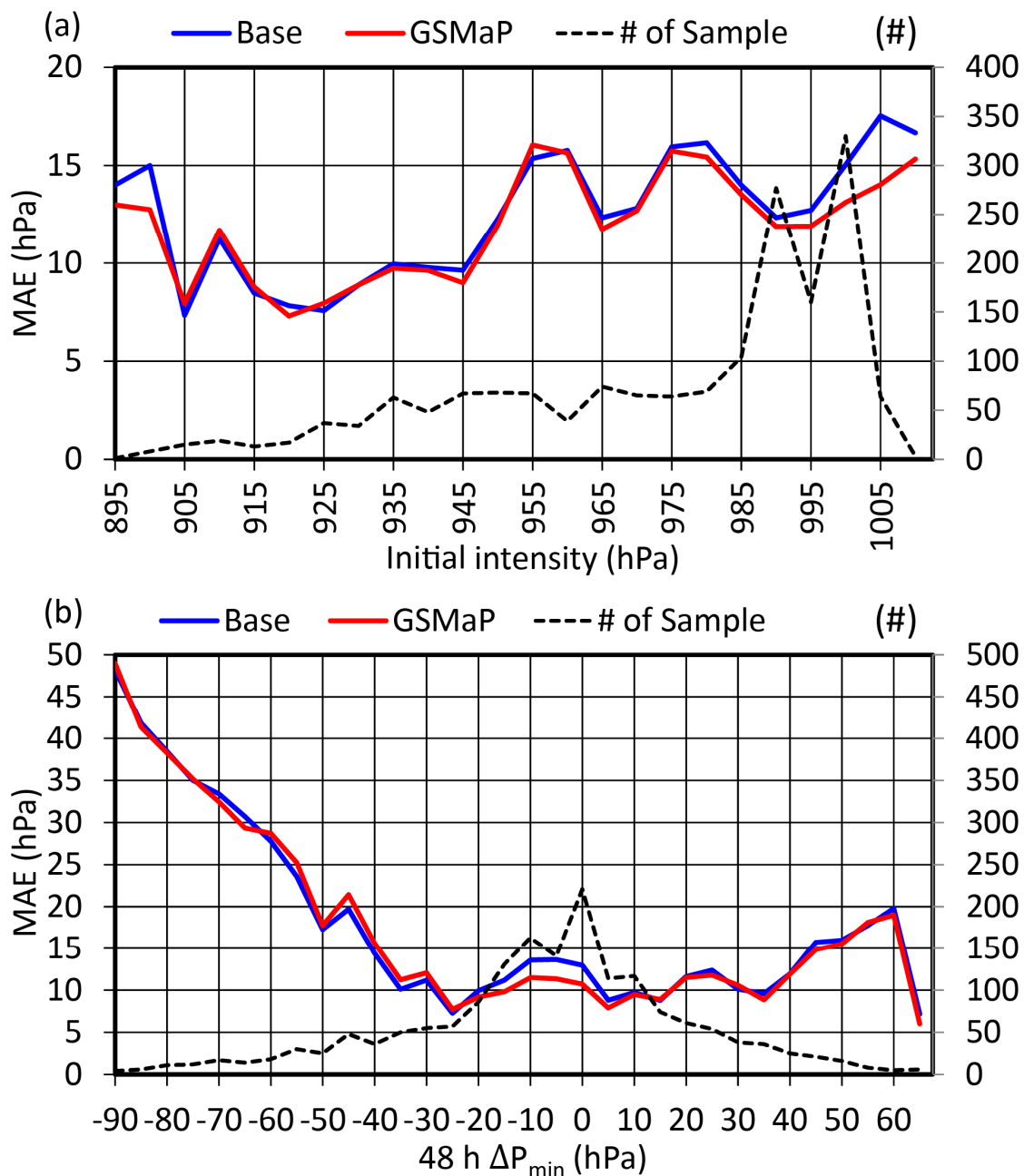


Fig. 6.3: SHIPS-Base and SHIPS-GSMaP mean absolute errors (a) stratified by best-track initial intensity in 5-hPa bins for 48-h forecasts and (b) stratified by subsequent intensity change in 5-hPa bins for 48-h forecasts. Dashed lines represent the number of samples within a particular bin.

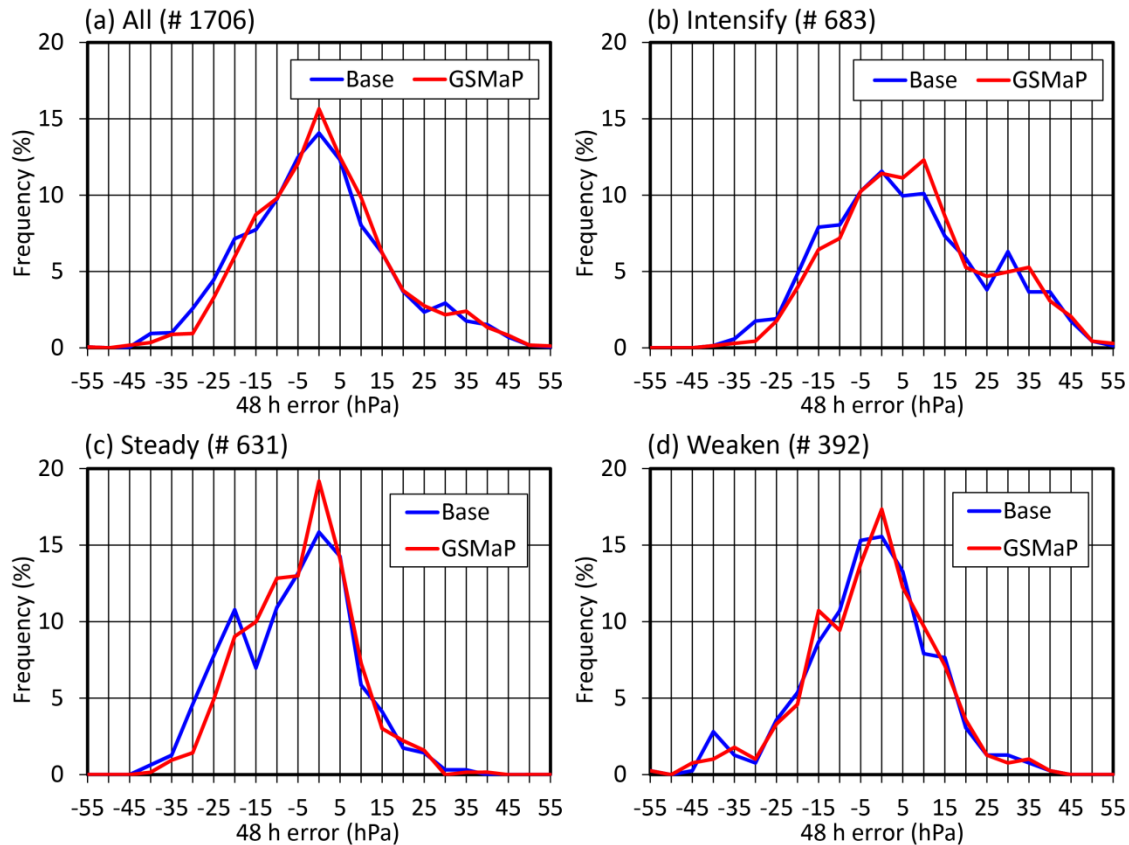


Fig. 6.4: SHIPS-Base and SHIPS-GSMaP 48-h P_{min} forecast errors binned in 5-hPa intervals and plotted relative to the total sample size for a particular type, indicated at the top of each figure. Types plotted include (a) all TCs, (b) intensifying TCs, (c) steady state TCs, and (d) weakening TCs. Positive values indicate underforecasting while negative values indicate overforecasting.

The evolution of bias stratified by types of intensity change (Fig. 6.5a) shows that for intensifying TCs, positive biases (i.e., underforecasting) of P_{min} forecasts are increased from $ft = 24$ h to 84 h. This result falls far short of our expectations that the addition of the new predictors may improve underforecasting of RI TCs. In contrast, biases are generally reduced for steady state TCs, for which overforecasting intensity is suppressed. The improvement rate of the MAE stratified by types of intensity change (Fig. 6.5b) shows that the performance of P_{min} forecast for steady state TCs is greatly improved by over 10% during a period of $ft = 24$ –66 h. The performance for intensifying and weakening TCs is little changed.

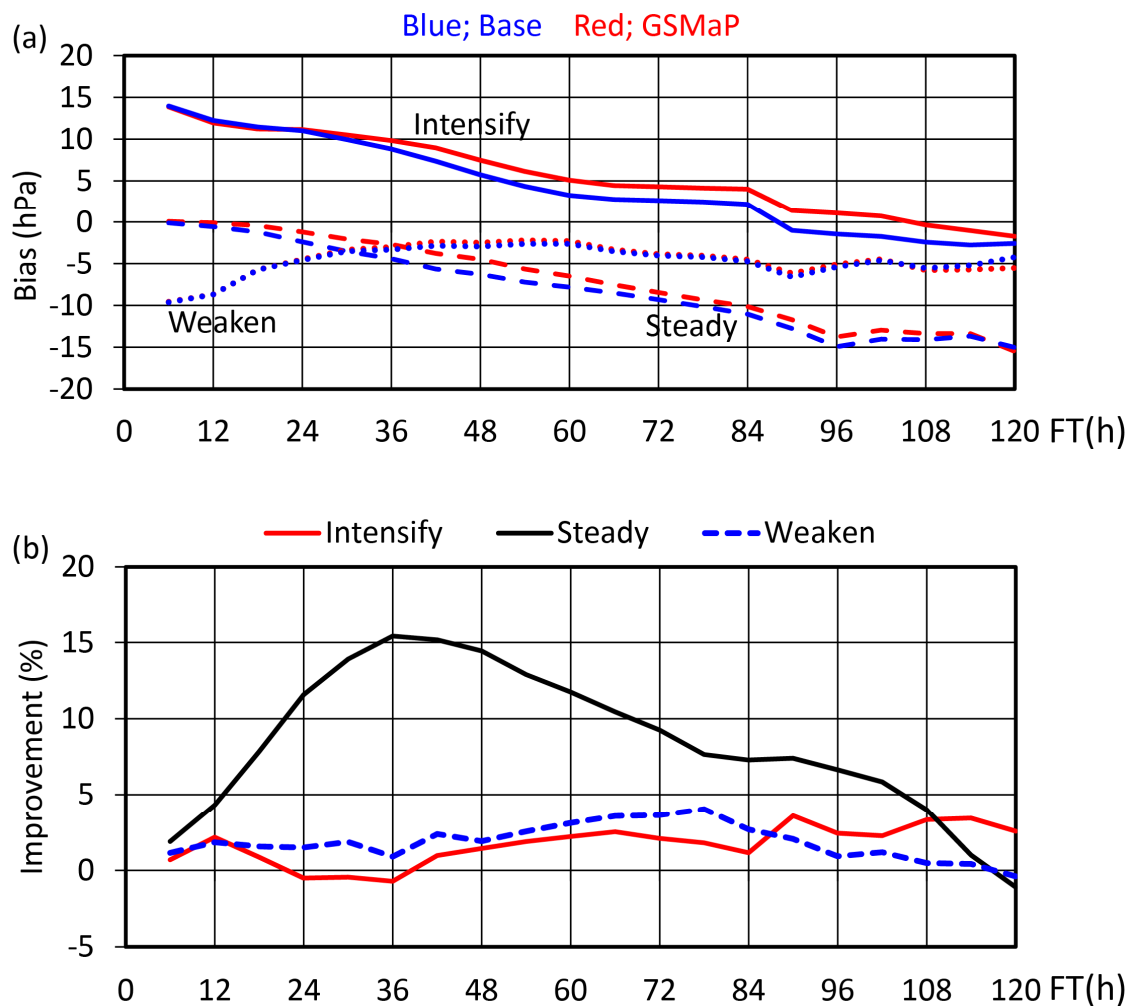


Fig. 6.5: (a) Biases of the SHIPS-GSMaP and SHIPS-Base forecasts classified as intensifying, weakening, and steady state TCs. (b) Percent improvement of the SHIPS-GSMaP forecasts relative to the SHIPS-Base forecasts classified as intensifying, weakening, and steady state TCs.

b. Case study

The great improvement for steady state TCs (Fig. 6.5) indicates that the use of rainfall and structural information contributes to the suppression of overforecasts. The case of Typhoon Nakri (2014) is a good example in this sense (Fig. 6.6). The intensity at 0000 UTC 31 July (0900 Japan standard time) was a P_{min} of 990 hPa, a 10-min V_{max} of 20 m s^{-1} , with a 15 m s^{-1} radius of 700 km to the southeast and 500 km to the northwest. Although the size was relatively large, there existed no organized convection around the center (24.4°N , 127.1°E) (Fig. 6.6b), and P_{min} fell by only 10 hPa after 0000 UTC 31 July (Fig. 6c). Nakri was typically a monsoon gyre type TC, which does not tend to intensify greatly. In spite of that, SHIPS-Base initialized at 1200 UTC 30 July forecasts intensification up to 967 hPa, because SSTs around the TC

(a) 0000 UTC 31 July

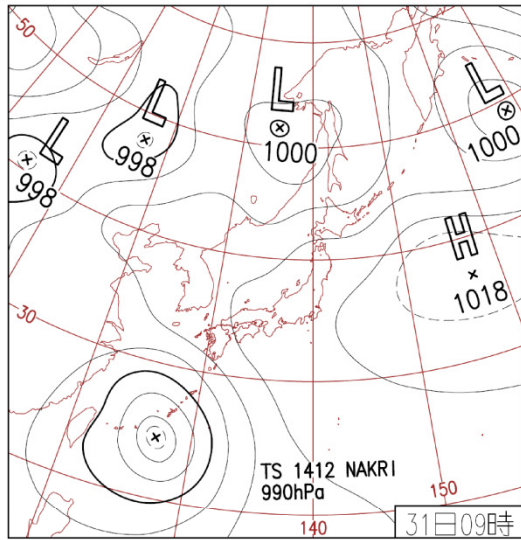
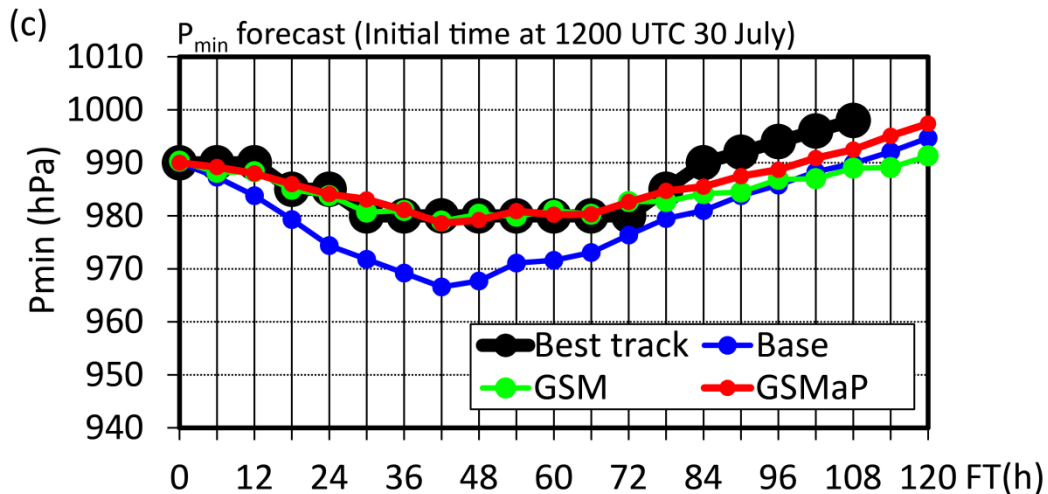
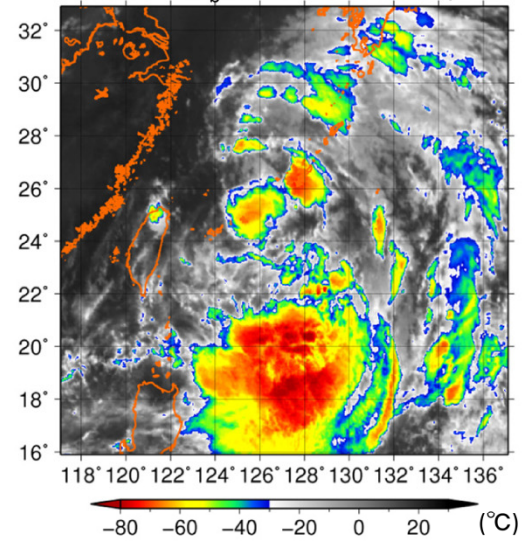
(b) MTSAT IR T_b 0000 UTC 31 July

Fig. 6.6: (a) Weather chart at 0000 UTC 31 July 2014 provided by the JMA. (b) Infrared brightness temperatures (at 10.3–11.3 μm) from the Multi-functional Transport Satellite (MTSAT-2) geostationary satellite at 0000 UTC 31 July 2014. (c) Intensity forecasts of the JMA GSM, SHIPS-Base and SHIPS-GSMaP for Typhoon Nakri (2014) initialized at 1200 UTC 30 July. Best-track intensity is also plotted. Because Nakri weakened to tropical depression at $ft = 90$ h (0600 UTC 3 August 2014) and dissipated at $ft = 108$ h (0000 UTC 4 August 2014), there was no best-track intensity after $ft = 108$ h.

are greater than 29 $^{\circ}\text{C}$, and the vertical wind shear (SHDC) along the track is ~ 5 m s^{-1} . In contrast, the forecast of SHIPS-GSMaP is very good. All newly added predictors contribute to the suppression of the decrease in P_{min} in the first half of the forecast period (not shown).

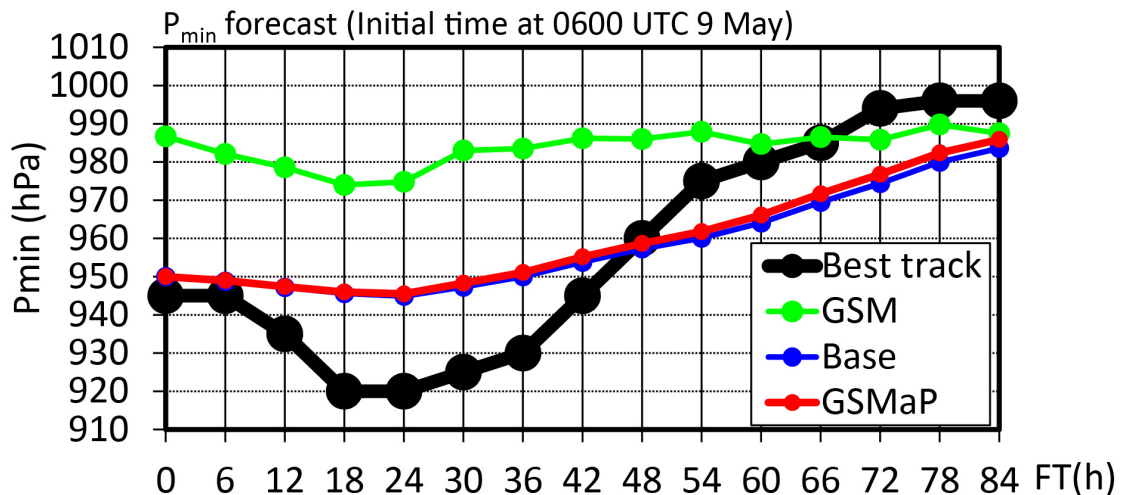


Fig. 6.7: Intensity forecasts of the JMA GSM, SHIPS-Base and SHIPS-GSMaP for Typhoon Noul (2015) initialized at 0600 UTC 9 May 2015. Best-track intensity is also plotted. Noul underwent extratropical transition at $ft = 72$ h (0600 UTC 12 May 2015).

In contrast, as shown in Figs. 6.3b and 6.5, SHIPS-GSMaP fails to improve forecast skill for intensifying TCs only with the addition of rainfall and structural information at $ft = 0$ h. For example, in the case of Typhoon Noul (2015) (Fig. 6.7), which started to intensify rapidly at $ft = 6$ h, then weakened after $ft = 24$ h, there is little difference in forecasts between SHIPS-GSMaP and SHIPS-Base. The improvement of forecast skill for intensifying TCs remains a challenging issue, which should be addressed in future work.

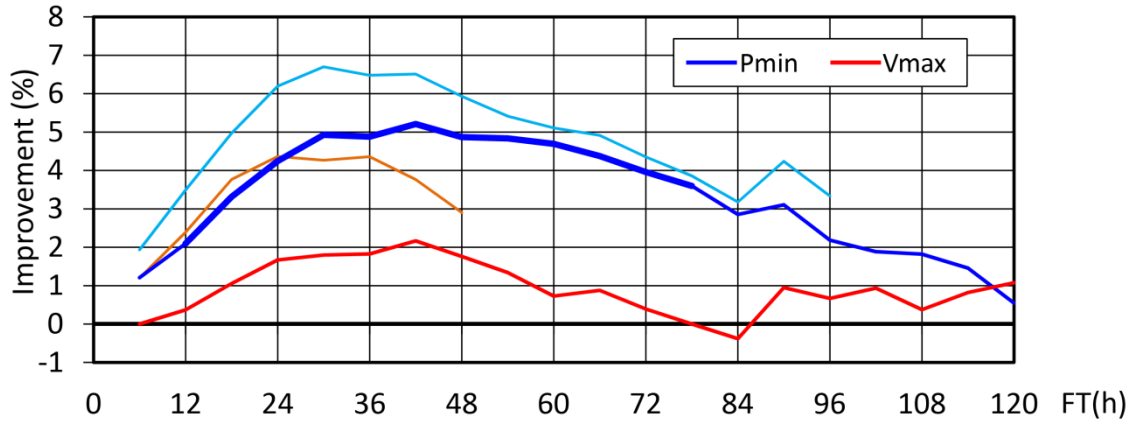


Fig. 6.8: Percent improvement of real-time SHIPS-GSMaP forecasts relative to SHIPS-Base forecasts from 2013 to 2016 in the WNP basin. Bold lines indicate statistically significant differences at the 95% level. For reference, the percent improvement shown in Fig. 6.2b is indicated by the thin light blue and brown lines.

c. Real time forecast

The result of real time forecast (Fig. 6.8) shows that the MAE of P_{min} forecast in SHIPS-GSMaP is reduced compared to SHIPS-Base. The improvement rate of 2–5% from $ft = 12$ h to $ft = 78$ h is statistically significant at the 95% confidence level. In contrast, the improvement of V_{max} forecast is not statistically significant at the 95% confidence level, but reaching up to 2%. These results indicate the feasibility of SHIPS-GSMaP for operational use in real time. The fact that SHIPS with the use of the reanalysis GSMaP product is superior to that with the use of the near-real time GSMaP product suggests that more accurate rainfall and structural information can lead to a better intensity forecast, and that the increase in the number of microwave satellites will lead to further improvement in SHIPS.

6.4. Summary

The current version of SHIPS predicts TC intensity mainly using predictors associated with environmental conditions, without using rainfall and structural features of TCs. However, recent studies have pointed out that inner-core structural conditions, such as the axial symmetry of rainfall distribution, also govern subsequent intensity change. What if rainfall and structural information is added to SHIPS? We examined the degree to which the accuracy could be improved when rainfall and structural features of TCs were added to SHIPS for the WNP basin. We derived new predictors mainly from the GSMaP hourly product, which is a microwave satellite-derived rainfall estimate dataset. This hourly dataset covers the area from 60°S to 60°N with a resolution of 0.1°, available since 2000, and is currently provided in near-real time. These characteristics are the advantage for SHIPS-GSMaP to be operationally used in real time. The predictors derived from the GSMaP product for P_{min} forecast include the axisymmetry of rainfall structure within 300 km of the TC center, rain areal coverage within a radius of 100–300 km, the radius of maximum azimuthal mean rainfall, and total volumetric rain within a radius of 100 km. Among these predictors, each value of the axisymmetry and the total volumetric rainfall was multiplied by a mean value of ocean heat content along a forecast track. In addition, Rossby number, defined as the maximum wind divided by the radius of 15 m s⁻¹ wind speed and the Coriolis parameter, was incorporated. Previous studies used predictors based on T_b data such as mean T_b and maximum T_b around the TC, whereas in this study we used predictors associated with physical features that were relevant to intensity change in previous studies. This may facilitate the interpretation of SHIPS forecast.

SHIPS coefficients indicated that among the five new predictors, a predictor associated with the axisymmetry had the largest impact on intensity change. We compared the mean absolute error between SHIPS with (SHIPS-GSMaP) and without (SHIPS-Base) the new predictors. First, we examined the degree to which the new predictors could improve the accuracy. In this examination, the new predictors were derived from the GSMaP reanalysis product and best track data. The forecast results up to 5 days ahead for TCs over the ocean showed that the addition of the new predictors for P_{min} forecast produced a 2–7% improvement up to $ft = 114$ h with a maximum improvement of near 7% at 30 h. The improvement for V_{max} forecast was also achieved by up to over 4% during a period of $ft = 6–48$ h. For P_{min}

forecast, the improvement was greatest for steady-state TCs. The use of rainfall and structural information contributed to the suppression of overforecasting for steady-state TCs. In contrast, little improvement was found for intensifying TCs. Then, we performed a real-time forecast experiment, in which the new predictors were derived from the hourly GSMaP near-real time product and real-time TC analysis data. The result demonstrated that even the use of the near-real time product can improve the accuracy of SHIPS, confirming the feasibility of real-time SHIPS-GSMaP for operational use.

Chapter 7: Conclusions

Numerical models have been sophisticated enough to reproduce various atmospheric phenomena with acceptable accuracy so far, and are a useful tool to promote our understanding of them. However, regarding TCs, numerical models do not accurately reproduce realistic structures and intensity changes of TCs, and thus currently have many issues to be addressed. As a result, the forecast skill of TC intensity in the JMA has not been improved at least for a decade or more. To improve TC intensity forecast, the development of a more sophisticated numerical model is required. In addition, the enhancement of techniques associated with structural and intensity analysis, and the documentation of processes involved in structural and intensity changes in TCs based on observations are greatly needed because findings from those observational studies can be used as ground truth for verification of numerical models.

On the basis of those backgrounds and motivations, in this study we stuck to observational studies of TC intensity. Specifically, we have developed an intensity estimation system by using Doppler radar data, have investigated intensity change processes by using observations including radar and satellite data, and have conducted a feasibility study to improve the skill of TC intensity forecasts.

In the WNP basin, TC intensity has been primarily estimated since aircraft observations ceased in 1987 by the Dvorak technique. This technique is an empirical method based on cloud patterns and thus has a large margin of errors. To understand features of TCs as they really are and of rapidly intensifying TCs, a physically-based method for intensity estimation was needed to be developed. In Chapter 2, we developed an intensity estimation system, where GBVTD-retrieved \bar{v} at 2-km altitude, SLP observations near the radar site, and the gradient wind equation were used to estimate the central pressure at 5-min intervals. The RMSE and bias of this method were 8.37 and 1.51 hPa, respectively, compared with the best track data of the RSMC Tokyo. In particular, for TCs with an RMW of 20–70 km, the estimation accuracy was outstanding, with an RMSE of only 5.55 hPa relative to the best track data. This level of accuracy is comparable to or better than the accuracies of Dvorak and satellite microwave-derived estimates, which are used operationally for TC intensity estimation. This system enabled us to

obtain TC intensity at 5-min intervals and thus to investigate rapid structural and intensity changes in real TCs.

From Chapter 3 to 5, we investigated the statistical relationship between TC rainfall structure and intensity change, and two intensifying TCs. One was a TC that reintensified in relatively strong shear, and the other was a TC that underwent RI just after an ERC. Remarkable findings are summarized as follows:

- It has been theoretically shown that the axisymmetric component of diabatic heating is much more efficient for TC intensification than the asymmetric component. To test whether this theory can be applied to real TCs, the relationship between axisymmetry (the degree of axial symmetry) derived from hourly satellite-based rainfall estimates and future intensity change was examined. The results showed that, during the development stage, the higher the axisymmetry, the larger the intensity change in the next 24 h for TCs with a current central pressure (maximum sustained wind) between 945 hPa and 995 hPa (85 kt and 40 kt). The relative relationship between axisymmetric and asymmetric components of rainfall showed that the larger the axisymmetric term and the smaller the asymmetric term, the larger the intensity change was, although the asymmetric term generally increased with the increase of the axisymmetric term. This study presented new observational evidence of the theory and provided an important knowledge for intensity forecast.
- Strong vertical wind shear causes the structure of the eyewall to become asymmetric and is generally a hostile environmental condition for TCs to intensify. However, Typhoon Noul (2015) reintensified with the formation of a symmetric eyewall despite shear increasing from 11 to 16 m s^{-1} in 6 h. The reintensification began with convective bursts in the downshear-left quadrant, which constituted a wavenumber-1 convective asymmetry in the eyewall. Then, the convective asymmetry moved to the upshear quadrant. During this period (only 5 h), azimuthal mean tangential wind at 2-km altitude increased from 30 to 50 m s^{-1} , in association with the increase in azimuthal mean reflectivity inside the RMW. It was when the vortex vertically aligned through vortex precession upshear that the amplitude of the wavenumber-1 convective asymmetry became small and a symmetric eyewall formed in strong shear. The radar analysis suggest that the vortex tilt, convective bursts,

and subsequent intensification occurred triggered by the increase in shear in the presence of environmental conditions favorable for convection.

- After the completion of an ERC, a TC often continues to intensify and in some cases RI occurs. However, RI processes after an ERC have not yet been investigated. An operational ground-based Doppler radar observed the RI of Typhoon Goni (2015) for 24 h immediately after it completed an ERC. We examined Goni's RI processes by using radar reflectivity and wind fields retrieved by the GBVTD technique. The maximum wind at 2-km altitude increased by 30 m s^{-1} during the first 6 h of RI, and it further increased by 20 m s^{-1} during the subsequent 12 h. Around the onset of RI, relatively strong outflow ($>2 \text{ m s}^{-1}$) was present both inside and outside the RMW above the boundary layer (BL), suggesting the existence of supergradient flow in and just above the BL. Despite this outflow, angular momentum increased inside the RMW. In contrast, a budget analysis of absolute angular momentum (AAM) showed that the outflow contributed to the decrease in AAM just outside the RMW below 5-km altitude. As a result, the low-level RMW contracted rapidly from 50 to 33 km, causing the RMW to slope greatly outward with height. The radial profile of tangential wind became more peaked with time. The peaked wind profile is consistent with that of other intensifying TCs. During RI, the low-level outflow changed into inflow immediately outside the RMW. Thus, the secondary circulation became well established. Then the tangential wind field and high inertial stability region expanded radially outward, followed by the formation of an outer reflectivity maximum at twice the RMW. The contraction speed of the low-level RMW slowed down.

While numerical models are used for track forecast, multiple linear regression models such as SHIPS are currently mainly used for intensity forecast owing to the poor performance of numerical models. In Chapter 6, the possibility of further improvement in TC intensity forecast was examined based on the findings in this study. Five new predictors associated with rainfall distribution and structural features, which were mainly derived from satellite-based rainfall estimates, were added to SHIPS. The results showed that the mean absolute error of the central pressure forecast in SHIPS with the new predictors produced a 2–7% improvement in the first half of 5 days forecast period. Regarding the central pressure forecast, the improvement was

greatest for steady-state TCs, whereas the improvement was much less for intensifying TCs.

Appendix A: GBVTD technique

A.1. GBVTD formulation

The GBVTD technique (Lee et al. 1999) is based on the assumption that there is one primary circular vortex around the TC center and that the asymmetric radial wind is much smaller than the corresponding tangential wind. These assumptions allow the retrieval of a two-dimensional TC wind field from single-Doppler velocities.

The GBVTD technique utilizes a coordinate system shown in Fig. A.1. Symbols are summarized in Table A.1. With this coordinate system, Doppler velocity can be expressed by the environmental wind, tangential wind, radial wind, and vertical wind as follows:

$$V_d = V_M \cos(\gamma - \theta_M) \cos\phi - V_T \sin\psi \cos\phi \\ + V_R \cos\psi \cos\phi + (w - v_t) \sin\phi.$$

Ignoring the vertical wind component, we obtain

$$\frac{V_d}{\cos\phi} = V_M \cos(\gamma - \theta_M) - V_T \sin\psi + V_R \cos\psi. \quad (\text{B.1})$$

V_T and V_R can be decomposed in terms of a Fourier series on the ψ coordinates.

$$V_T(\psi) = \sum_{n=0}^M (V_T C_n \cos n\psi + V_T S_n \sin n\psi), \quad (\text{B.2})$$

$$V_R(\psi) = \sum_{n=0}^N (V_R C_n \cos n\psi + V_R S_n \sin n\psi). \quad (\text{B.3})$$

Meanwhile, V_d can also be decomposed.

$$\frac{V_d}{\cos\phi} = \sum_{n=0}^L (A_n \cos n\psi + B_n \sin n\psi). \quad (\text{B.4})$$

Using Eqs. (B.1)–(B.4) with some arrangements, we can obtain an identity in ψ . Then, the following equations are derived:

$$V_M \cos(\theta_T - \theta_M) = A_0 + A_2 + A_4 - V_R C_1 - V_R C_3$$

$$V_T C_0 = -B_1 - B_3 - V_M \sin(\theta_T - \theta_M) \sin\alpha_{max} + V_R C_2$$

$$V_R C_0 = A_1 + A_3 - V_R C_2$$

$$V_T S_1 = A_2 - A_0 + A_4 + (A_0 + A_2 + A_4 - V_R C_1 - V_R C_3) \cos \alpha_{max} + V_R C_3$$

$$V_T C_1 = -2(B_2 + B_4) + V_R S_1 + V_R S_3$$

$$V_T S_2 = 2A_3 - V_R C_2$$

$$V_T C_2 = -2B_3 + V_R S_2$$

$$V_T S_3 = 2A_4 - V_R C_3$$

$$V_T C_3 = -2B_4 + V_R S_3$$

If it is assumed that the asymmetric radial wind is much smaller than the corresponding tangential wind ($V_T \gg V_R$), we can obtain the TC wind field by ignoring V_R terms with wavenumbers 1–3.

With this assumption, the GBVTD technique provides tangential winds with wavenumbers up to 3, radial wind with only wavenumber 0, and the component of the mean environmental wind parallel to a line connecting the TC center with the radar location at each TC radius in GBVTD nonlinear coordinates. The technique does not provide the cross-beam component of the mean environmental wind, $V_{M\perp}$. Instead, $V_{M\perp}$ is aliased into the wavenumber-0 (i.e., the azimuthal mean) tangential wind, \bar{v} ; as a result, the retrieval accuracy of \bar{v} is decreased at outer TC radii (Lee et al. 1999; Harasti et al. 2004; Chen et al. 2013). To resolve this aliasing issue, following Harasti et al. (2004), we use the cross-beam component of the TC translational speed as a proxy for $V_{M\perp}$ to dealias \bar{v} . Chapter 2 in this study demonstrates that dealiasing of \bar{v} in this way can greatly decrease its biases.

Finally, the retrieved winds in GBVTD nonlinear coordinates are converted into winds in storm-centered cylindrical coordinates. The retrieved V_M is decomposed into wavenumber-1 tangential and radial winds. In our retrieval procedure, tangential winds with wavenumbers higher than 3 in storm-centered cylindrical coordinates were azimuthally filtered out. The GBVTD technique has been successfully applied to the data of many TCs (Lee et al. 2000; Harasti et al. 2004; Lee and Bell 2007; Zhao et al. 2008, 2012, 2016).

Table A.1: Symbols used in the GBVTD formulation.

Symbols	Description
V_d	Doppler velocity from a ground-based radar
V_M	Environmental wind speed
V_T	Tangential wind speed centered at the TC
V_R	Radial wind speed centered at the TC
w	Vertical wind speed
v_t	Terminal fall speed of raindrops
ϕ	Elevation angle of the radar beam
C_n	Amplitude of the cosine component of V_T or V_R for wavenumber n
S_n	Amplitude of the sine component of V_T or V_R for wavenumber n

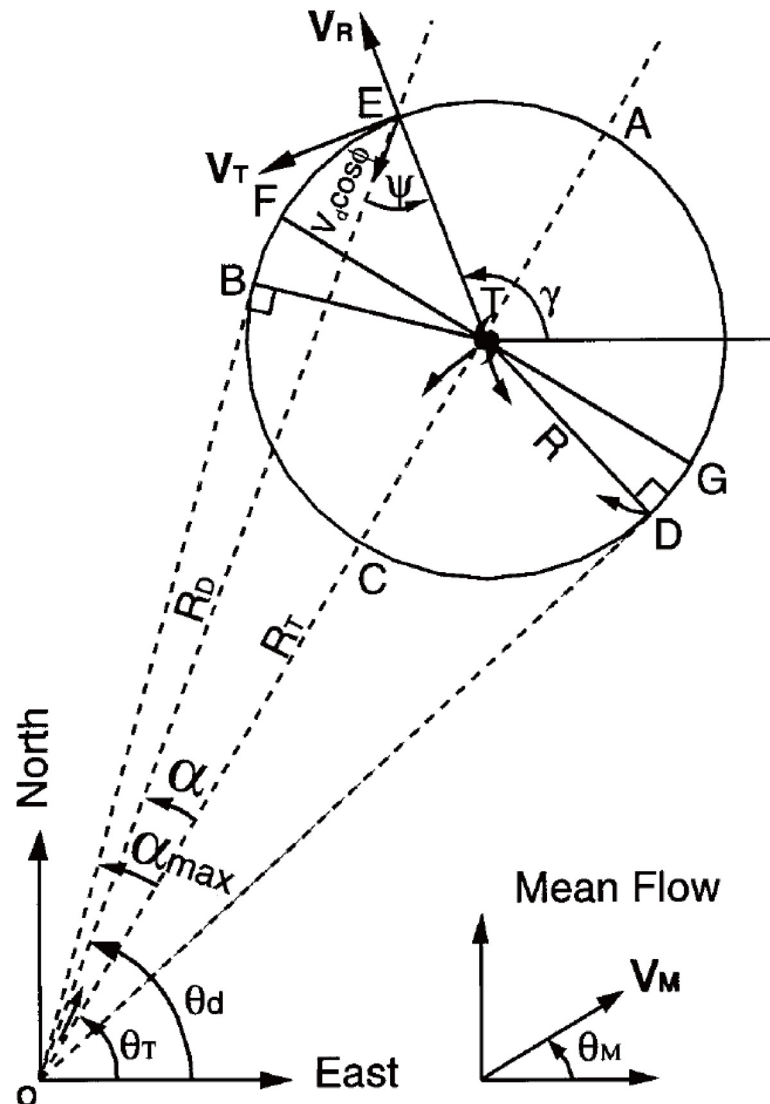


Fig. A.1: The geometry and symbols used in the GBVTD formulation. Adapted from Lee et al. (1999).

A.2. Limitations of the GBVTD technique

The GBVTD technique has some intrinsic limitations with respect to retrieval accuracy because it retrieves two-dimensional winds from only one component of the near-horizontal wind (i.e., V_D). The accuracy of the GBVTD-retrieved \bar{v} and \bar{u} is affected by the aliasing of the wavenumber-2 radial wind into \bar{v} and \bar{u} (Lee et al. 1999; Lee et al. 2006; Murillo et al. 2011; Bell and Lee 2012). The GBVTD technique assumes that the asymmetric radial wind is much smaller than the corresponding tangential wind. However, if the wavenumber-2 radial wind is dominant within the eye region and its distribution moves around the eyewall cyclonically together with mesovortices (e.g., Kossin and Schubert 2004; Braun et al. 2006) or vortex Rossby waves (e.g., Montgomery and Kallenbach 1997; Wang 2002), an artificial fluctuation in the retrieved \bar{v} and \bar{u} with a period of a few hours may be found. Because of this possibility, in our analysis we ignore fluctuations in \bar{v} and \bar{u} with a period of a few hours.

The accuracy of the GBVTD technique is also sensitive to the position accuracy of the TC center. We use the GBVTD-simplex algorithm (Lee and Marks 2000; Bell and Lee 2012) to detect the TC center at 1-km (Chapter 4) or 2-km (Chapter 5) altitude at 5-min intervals, and then we use the 1-km or 2-km TC center for the TC center at other altitudes. For maximum accuracy of the GBVTD analysis, it is actually desirable to use TC centers derived from V_D at each altitude. However, because there are few radar scatterers at upper altitudes, using the simplex algorithm, we are unable to detect centers at every altitude. Lee and Marks (2000) showed that the accuracy of the GBVTD-retrieved \bar{v} is less sensitive to the deviation from the true center than that of asymmetric tangential wind. Although a TC vortex generally tilts to the left of the downshear with height and the difference between centers at 2 and 10 km can be up to several kilometers (e.g., Reasor et al. 2013), this range of vortex tilt may not significantly affect the accuracy of \bar{v} . Moreover, because the magnitude of \bar{v} often changes drastically during RI, those changes can be captured despite the retrieval errors that may exist.

Furthermore, the GBVTD technique can only retrieve the wind field within the interval between the TC center and the radar location. For this reason, no winds are retrieved while the radar site is located within the TC's eye region, because no V_D observations can be made.

Appendix B: Definition of RI for WNP TCs

Kaplan and DeMaria (2003) defined RI as the 95th percentile of intensity changes over a 24-h period for Atlantic basin TCs, which is a maximum sustained wind speed increase of 30 kt. For WNP TCs, Holliday and Thompson (1979) used a 42 hPa threshold over a 24-h period. However, in the recent RSMC Tokyo's best track data (e.g., 2000–2015), this threshold can capture very few samples (above 98.5th percentile).

In this study, we determine an RI threshold using the central pressure from the RSMC Tokyo's best track data (2000–2015, at 6-h intervals) in the same way as in Kaplan and DeMaria (2003). Namely, intensity change is evaluated from $t = 0$ h to $t + 24$ h after provided that the TC remains over-water and a tropical cyclone from $t - 12$ h to $t + 24$ h. Note that the RSMC Tokyo's best track data do not include disturbances whose lives ended without evolving into, at least, tropical storms.

Fig. B.1 shows the cumulative frequency distributions of 24-h central pressure change (ΔP_{24}). The 95 percentile of the ΔP_{24} distribution is 30 hPa. Details of the samples are shown in Table B.1 and B.2.

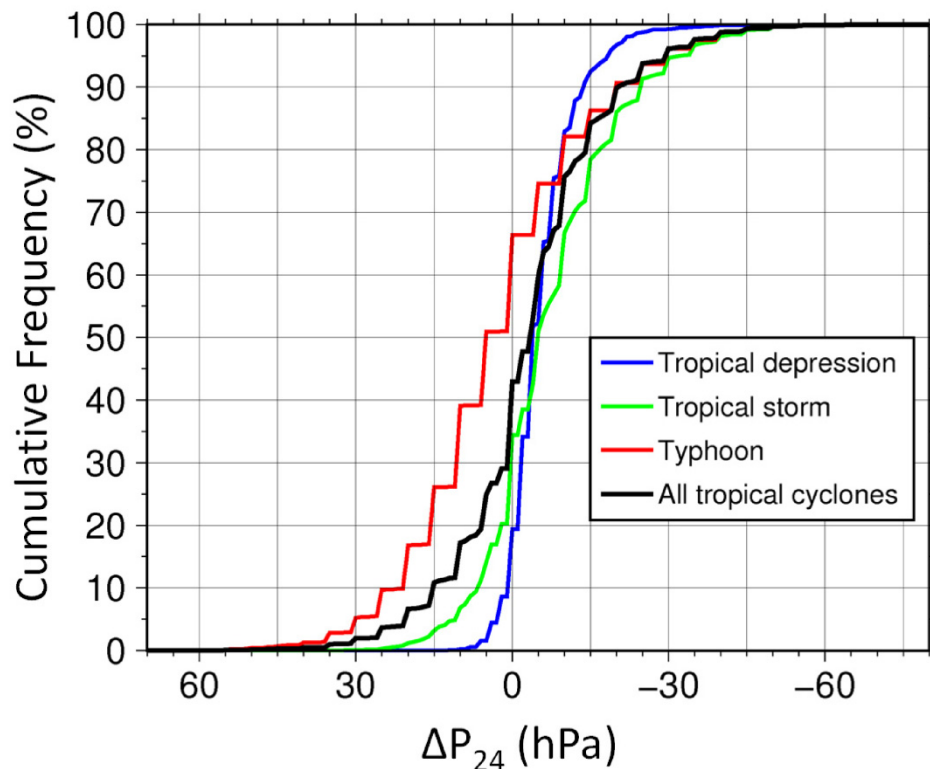


Fig. B.1: The frequency distributions of 24-h central pressure change (ΔP_{24}) stratified by TC intensity at $t = 0$ h. The distributions are provided for tropical depressions, tropical storms (both tropical storms and severe tropical storms), typhoons, and all TCs.

Table B.1: Statistics of central pressure changes over a 24-h period (ΔP_{24}) for tropical depressions, tropical storms, typhoons, and all TCs. The number of samples (N), mean and standard deviation (std dev), minimum (min), and maximum (max) ΔP_{24} are provided.

Intensity class	N	Mean (hPa)	Std dev (hPa)	Min (hPa)	Max (hPa)
Typhoon	2753	2.0	17.4	-65	60
Tropical storm	3237	-7.8	13.2	-75	34
Tropical depression	1562	-5.9	6.6	-61	12
All TCs	7552	-3.9	14.6	-75	60

Table B.2. The distribution of central pressure change over a 24-h period (ΔP_{24}) for the 437 RI cases. The number of RI cases is stratified by intensity class.

(hPa)	Tropical depressions	Tropical storms	Typhoons	All TCs
$-35 < \Delta P_{24} \leq -30$	5	96	67	168
$-40 < \Delta P_{24} \leq -35$	4	68	38	110
$-45 < \Delta P_{24} \leq -40$	1	37	37	75
$-50 < \Delta P_{24} \leq -45$	1	25	14	40
$-55 < \Delta P_{24} \leq -50$	0	13	8	21
$-60 < \Delta P_{24} \leq -55$	0	7	7	14
$-65 < \Delta P_{24} \leq -60$	1	3	1	5
$-70 < \Delta P_{24} \leq -65$	0	1	1	2
$-75 < \Delta P_{24} \leq -70$	0	1	0	1
$-80 < \Delta P_{24} \leq -75$	0	1	0	1
Total cases (%)	12 (2.7)	252 (57.7)	173 (39.4)	437 (100.0)

Appendix C: Basic formula

We here present three basic formulas that are often referred to in this study.

Absolute angular momentum, M , is, to good approximation, materially conserved above the boundary layer. Azimuthal mean absolute angular momentum, \bar{M} , is expressed as follows:

$$\bar{M} = (1/2)fr^2 + r\bar{v}.$$

Normally, \bar{M} increases with increasing radius.

The relationship between absolute vorticity $\bar{\zeta}_a$ and absolute angular momentum \bar{M} is written as follows:

$$\bar{\zeta}_a \equiv \left(f + \frac{\bar{v}}{r} + \frac{\partial \bar{v}}{\partial r}\right) = (f + \bar{\zeta}) = \left(\frac{1}{r}\right) \frac{\partial \bar{M}}{\partial r}.$$

Inertial stability is expressed as follows:

$$I^2 \equiv \bar{\zeta}_a \left(f + \frac{2\bar{v}}{r}\right) = \left(\frac{1}{r^3}\right) \frac{\partial \bar{M}^2}{\partial r}.$$

Normally, I^2 increases with decreasing radius. If $I^2 < 0$, the parcel is inertially unstable.

List of reference papers

This dissertation is based on the five papers listed below.

1. Shimada, U., M. Sawada, and H. Yamada, 2016: Evaluation of the accuracy and utility of tropical cyclone intensity estimation using single ground-based Doppler radar observations. *Mon. Wea. Rev.*, **144**, 1823-1840, doi:10.1175/MWR-D-15-0254.1.
2. Shimada, U., K. Aonashi, and Y. Miyamoto, 2017a: Tropical cyclone intensity change and axisymmetry deduced from GSMaP. *Mon. Wea. Rev.*, **145**, 1003-1017, doi: 10.1175/MWR-D-16-0244.1.
3. Shimada, U., M. Sawada, and H. Yamada, 2017b: Doppler radar analysis of the rapid intensification of Typhoon Goni (2015) after eyewall replacement. *J. Atmos. Sci.*, doi:10.1175/JAS-D-17-0042.1, in press.
4. Shimada, U., and T. Horinouchi, 2017c: Reintensification and eyewall formation in strong shear: a case study of Typhoon Noul (2015). In preparation.
5. Shimada, U., H. Owada, M. Yamaguchi, T. Iriguchi, M. Sawada, K. Aonashi, and M. DeMaria, 2017d: Further improvement in the SHIPS using rainfall and structural information. In preparation.

Dr. Sawada performed some numerical simulations in the paper of Shimada et al. (2016). The development of the intensity estimation system, satellite analyses, and radar analyses in all papers are performed by Udai Shimada with the assistance and guidance from co-authors.

References

- Abarca, S. F., and M. T. Montgomery, 2013: Essential dynamics of secondary eyewall formation. *J. Atmos. Sci.*, **70**, 3216–3230, doi:10.1175/JAS-D-12-0318.1.
- Abarca, S. and M. Montgomery, 2014: Departures from axisymmetric balance dynamics during secondary eyewall formation. *J. Atmos. Sci.*, **71**, 3723–3738, doi: 10.1175/JAS-D-14-0018.1.
- Abarca, S. F., and M. T. Montgomery, 2015: Are eyewall replacement cycles governed largely by axisymmetric balance dynamics? *J. Atmos. Sci.*, **72**, 82–87, doi:10.1175/JAS-D-14-0151.1.
- Abarca, S., M. Montgomery, S. Braun, and J. Dunion, 2016: On the secondary eyewall formation of Hurricane Edouard (2014). *Mon. Wea. Rev.*, **144**, 3321–3331, doi: 10.1175/MWR-D-15-0421.1.
- Aberson, S. D., and M. DeMaria, 1994: Verification of a nested barotropic hurricane track forecast model (VICBAR). *Mon. Wea. Rev.*, **122**, 2804–2815, doi:10.1175/1520-0493(1994)122<2804:VOANBH>2.0.CO;2.
- Aberson, S. D., M. T. Montgomery, M. Bell, and M. Black, 2006: Hurricane Isabel (2003): New insights into the physics of intense storms. Part II: Extreme localized wind. *Bull. Amer. Meteor. Soc.*, **87**, 1349–1354, doi:10.1175/BAMS-87-10-1349.
- Aonashi, K., and G. Liu, 2000: Passive microwave precipitation retrievals using TMI during the baiu period of 1998. Part I: Algorithm description and validation. *J. Appl. Meteor.*, **39**, 2024–2037, doi:10.1175/1520-0450(2000)039<2024:PMPRUT>2.0.CO;2.
- Aonashi, K., and Coauthors, 2009: GSMP passive microwave precipitation retrieval algorithm: Algorithm description and validation. *J. Meteor. Soc. Japan*, **87A**, 119–136, doi:10.2151/jmsj.87A.119.
- Bankert, R. L., and P. M. Tag, 2002: An automated method to estimate tropical cyclone intensity using SSM/I imagery. *J. Appl. Meteor.*, **41**, 461–472, doi:10.1175/1520-0450(2002)041<0461:AAMTET>2.0.CO;2.
- Bell, M. M., and W. Lee, 2012: Objective tropical cyclone center tracking using single-Doppler radar. *J. Appl. Meteor. Climatol.*, **51**, 878–896, doi:10.1175/JAMC-D-11-0167.1.
- Bell, M. M., and M. T. Montgomery, 2008: Observed structure, evolution, and potential intensity of category 5 Hurricane Isabel (2003) from 12 to 14

- September. *Mon. Wea. Rev.*, **136**, 2023–2046, doi:10.1175/2007MWR1858.1.
- Bell, M. M., M. T. Montgomery, and W.-C. Lee, 2012: An axisymmetric view of concentric eyewall evolution in Hurricane Rita (2005). *J. Atmos. Sci.*, **69**, 2414–2432, doi:10.1175/JAS-D-11-0167.1.
- Bender, M. A., 1997: The effect of relative flow on the asymmetric structure in the interior of hurricanes. *J. Atmos. Sci.*, **54**, 703–724, doi:10.1175/1520-0469(1997)054<0703:TEORFO>2.0.CO;2.
- Black, M. L., J. F. Gamache, F. D. Marks, C. E. Samsury, and H. E. Willoughby, 2002: Eastern Pacific Hurricanes Jimena of 1991 and Olivia of 1994: The effect of vertical shear on structure and intensity. *Mon. Wea. Rev.*, **130**, 2291–2312, doi:10.1175/1520-0493(2002)130<2291:EPHJOA>2.0.CO;2.
- Bolton, D., 1980: The computation of equivalent potential temperature. *Mon. Wea. Rev.*, **108**, 1046–1053, doi:10.1175/1520-0493(1980)108<1046:TCOEPT>2.0.CO;2.
- Braun, S. A., and L. Wu, 2007: A numerical study of Hurricane Erin (2001). Part II: Shear and the organization of eyewall vertical motion. *Mon. Wea. Rev.*, **135**, 1179–1194, doi:10.1175/MWR3336.1.
- Braun, S. A., M. T. Montgomery, and Z. Pu, 2006: High-resolution simulation of Hurricane Bonnie (1998). Part I: The organization of eyewall vertical motion. *J. Atmos. Sci.*, **63**, 19–42, doi:10.1175/JAS3598.1.
- Brueske, K. F., and C. S. Velden, 2003: Satellite-based tropical cyclone intensity estimation using the NOAA–KLM series Advanced Microwave Sounding Unit (AMSU). *Mon. Wea. Rev.*, **131**, 687–697, doi:10.1175/1520-0493(2003)131<0687:SBTCIE>2.0.CO;2.
- Cecil, D. J., and E. J. Zipser, 1999: Relationships between tropical cyclone intensity and satellite based indicators of inner core convection: 85-Ghz ice-scattering and lightning. *Mon. Wea. Rev.*, **127**, 103–123, doi:10.1175/1520-0493(1999)127<0103:RBTCIA>2.0.CO;2.
- Chen, S., J. A. Knaff, and F. D. Marks Jr., 2006: Effects of vertical wind shear and storm motion on tropical cyclone rainfall asymmetries deduced from TRMM. *Mon. Wea. Rev.*, **134**, 3190–3208, doi:10.1175/MWR3245.1.
- Chen, X., K. Zhao, W.-C. Lee, B. J.-D. Jou, M. Xue, and P. R. Harasti, 2013: The improvement to the environmental wind and tropical cyclone circulation retrievals with Modified GBVTD (MGBVTD) technique. *J. Appl. Meteor. Climatology*, **52**, 2493–2508,

- doi:10.1175/JAMC-D-13-031.1.
- Corbosiero, K. L., and J. Molinari, 2002: The effects of vertical wind shear on the distribution of convection in tropical cyclones. *Mon. Wea. Rev.*, **130**, 2110–2123, doi:10.1175/1520-0493(2002)130<2110:TEOVWS>2.0.CO;2.
- Corbosiero, K. L., and J. Molinari, 2003: The relationship between storm motion, vertical wind shear, and convective asymmetries in tropical cyclones. *J. Atmos. Sci.*, **60**, 366–376, doi:10.1175/1520-0469(2003)060<0366:TRBSMV>2.0.CO;2.
- DeHart, J. C., R. A. Houze, and R. F. Rogers, 2014: Quadrant distribution of tropical cyclone inner-core kinematics in relation to environmental shear. *J. Atmos. Sci.*, **71**, 2713–2732, doi:10.1175/JAS-D-13-0298.1.
- DeMaria, M., 1996: The effect of vertical shear on tropical cyclone intensity change. *J. Atmos. Sci.*, **53**, 2076–2088, doi:10.1175/1520-0469(1996)053,2076:TEOVSO.2.0.CO;2.
- DeMaria, M., 2009: A simplified dynamical system for tropical cyclone intensity prediction. *Mon. Wea. Rev.*, **137**, 68–82, doi:10.1175/2008MWR2513.1.
- DeMaria, M., and J. Kaplan, 1994: A statistical hurricane intensity prediction scheme (SHIPS) for the Atlantic basin. *Wea. Forecasting*, **9**, 209–220, doi:10.1175/1520-0434(1994)009<0209:ASHIPS>2.0.CO;2.
- DeMaria, M., and J. Kaplan, 1999: An updated Statistical Hurricane Intensity Prediction Scheme (SHIPS) for the Atlantic and eastern North Pacific basins. *Wea. Forecasting*, **14**, 326–337, doi:10.1175/1520-0434(1999)014<0326:AUSHIP>2.0.CO;2.
- DeMaria, M., J.-J. Baik, and J. Kaplan, 1993: Upper-level eddy angular momentum flux and tropical cyclone intensity change. *J. Atmos. Sci.*, **50**, 1133–1147, doi:10.1175/1520-0469(1993)050<1133:ULEAMF>2.0.CO;2.
- DeMaria, M., C. R. Sampson, J. A. Knaff, and K. D. Musgrave, 2014: Is tropical cyclone intensity guidance improving? *Bull. Amer. Meteor. Soc.*, **95**, 387–398, doi:10.1175/BAMS-D-12-00240.1.
- DeMaria, M., M. Mainelli, L. K. Shay, J. A. Knaff, and J. Kaplan, 2005: Further improvements to the Statistical Hurricane Intensity Prediction Scheme (SHIPS). *Wea. Forecasting*, **20**, 531–543, doi:10.1175/WAF862.1.
- Demuth, J. L., M. DeMaria, J. A. Knaff, and T. H. Vonder Haar, 2004: Validation of an Advanced Microwave Sounding Unit tropical cyclone

- intensity and size estimation algorithm. *J. Appl. Meteor.*, **43**, 282–296, doi:10.1175/1520-0450(2004)043<0282:EOAMSU>2.0.CO;2.
- Dunion, J. P., C. D. Thorncroft, and C. S. Velden, 2014: The tropical cyclone diurnal cycle of mature hurricanes. *Mon. Wea. Rev.*, **142**, 3900–3919, doi:10.1175/MWR-D-13-00191.1.
- Dvorak, V. F., 1975: Tropical cyclone intensity analysis and forecasting from satellite imagery. *Mon. Wea. Rev.*, **103**, 420 – 430, doi:10.1175/1520-0493(1975)103<0420:TCIAAF>2.0.CO;2.
- Dvorak, V. F., 1984: Tropical cyclone intensity analysis using satellite data. NOAA Tech. Rep. **11**, 45 pp.
- Eastin, M. D., W. M. Gray, and P. G. Black, 2005: Buoyancy of convective vertical motions in the inner core of intense hurricanes. Part II: Case studies. *Mon. Wea. Rev.*, **133**, 209–227, doi:10.1175/MWR-2849.1.
- Emanuel, K. A., 1986: An air-sea interaction theory for tropical cyclones. Part I: Steady-state maintenance. *J. Atmos. Sci.*, **43**, 585–605, doi:10.1175/1520-0469(1986)043<0585:AASITF>2.0.CO;2.
- Emanuel, K. A., 1989: The finite-amplitude nature of tropical cyclogenesis. *J. Atmos. Sci.*, **46**, 3431–3456, doi:10.1175/1520-0469(1989)046<3431:TFANOT>2.0.CO;2.
- Foerster, A. M., M. M. Bell, P. A. Harr, and S. C. Jones, 2014: Observations of the eyewall structure of Typhoon Sinlaku (2008) during the transformation stage of extratropical transition. *Mon. Wea. Rev.*, **142**, 3372–3392, doi:10.1175/MWR-D-13-00313.1.
- Frank, W. M., and E. A. Ritchie, 1999: Effects of environmental flow upon tropical cyclone structure. *Mon. Wea. Rev.*, **127**, 2044–2061, doi:10.1175/1520-0493(1999)127<2044:EOEFUT>2.0.CO;2.
- Frank, W. M., and E. A. Ritchie, 2001: Effects of vertical wind shear on the intensity and structure of numerically simulated hurricanes. *Mon. Wea. Rev.*, **129**, 2249–2269, doi:10.1175/1520-0493(2001)129<2249:EOVWSO>2.0.CO;2.
- Franklin, J. L., M. L. Black, and K. Valde, 2003: GPS dropwindsonde wind profiles in hurricanes and their operational implications. *Wea. Forecasting*, **18**, 32–44, doi:10.1175/1520-0434(2003)018<0032:GDWPIH>2.0.CO;2.
- Frisius, T., and M. Lee, 2016: The Impact of Gradient Wind Imbalance on Tropical Cyclone Intensification within Ooyama’s Three-Layer Model. *J. Atmos. Sci.*, **73**, 3659–3679, doi:10.1175/JAS-D-15-0336.1.
- Fudeyasu, H., and Y. Wang, 2011: Balanced contribution to the intensification

- of a tropical cyclone simulated in TCM4: Outer-core spinup process. *J. Atmos. Sci.*, **68**, 430–449, doi:<https://doi.org/10.1175/2010JAS3523.1>.
- Guimond, S. R., G. M. Heymsfield, P. D. Reasor, and A. C. Didlake, 2016: The Rapid Intensification of Hurricane Karl (2010): New Remote Sensing Observations of Convective Bursts from the Global Hawk Platform. *J. Atmos. Sci.*, **73**, 3617–3639, doi:10.1175/JAS-D-16-0026.1.
- Hack, J. J., and W. H. Schubert, 1986: Nonlinear response of atmospheric vortices to heating by organized cumulus convection. *J. Atmos. Sci.*, **43**, 1559–1573, doi:10.1175/1520-0469(1986)043<1559:NROAVT>2.0.CO;2.
- Hanley, D., J. Molinari, and D. Keyser, 2001: A Composite of the interactions between tropical cyclones and upper-tropospheric troughs. *Mon. Wea. Rev.*, **129**, 2570–2584, doi:10.1175/1520-0493(2001)129<2570:ACSOTI>2.0.CO;2.
- Harasti, P. R., 2014: An Expanded VVP Technique to Resolve Primary and Environmental Circulations in Hurricanes. *J. Atmos. Oceanic Technol.*, **31**, 249–271, doi:10.1175/JTECH-D-13-00030.1.
- Harasti, P. R., W.-C. Lee, and M. Bell, 2007: Real-time implementation of VORTRAC at the National Hurricane Center. Preprints, *33rd Conf. on Radar Meteorology*, Cairns, Australia, Amer. Meteor. Soc., P11A.6. [Available online at <https://ams.confex.com/ams/33Radar/webprogram/Paper123747.html>]
- Harasti, P. R., C. J. McAdie, P. P. Dodge, W.-C. Lee, J. Tuttle, S. T. Murillo, and F. D. Marks, 2004: Real-time implementation of single-Doppler radar analysis methods for tropical cyclones: Algorithm improvements and use with WSR-88D display data. *Wea. Forecasting*, **19**, 219–239, doi:10.1175/1520-0434(2004)019<0219:RIOSRA>2.0.CO;2.
- Hazelton, A. T., R. Rogers, and R. E. Hart, 2015: Shear-relative asymmetries in tropical cyclone eyewall slope. *Mon. Wea. Rev.*, **143**, 883–903, doi:10.1175/MWR-D-14-00122.1.
- Hendricks, E. A., M. S. Peng, B. Fu, and T. Li, 2010: Quantifying environmental control on tropical cyclone intensity change. *Mon. Wea. Rev.*, **138**, 3243–3271, doi:10.1175/2010MWR3185.1.
- Herndon, D., and C. Velden, 2004: Upgrades to the UW-CIMSS AMSU-based TC intensity algorithm. Preprints, *26th Conf. on Hurricanes and Tropical Meteorology*, Miami, FL, Amer. Meteor. Soc., 118–119.
- Holliday, C. R., and A. H. Thompson, 1979: Climatological characteristics of

- rapidly intensifying typhoons. *Mon. Wea. Rev.*, **107**, 1022–1034, doi:10.1175/1520-0493(1979)107<1022:CCORIT>2.0.CO;2.
- Hoshino, S. and T. Nakazawa, 2007: Estimation of tropical cyclone's intensity using TRMM/TMI brightness temperature data. *J. Meteor. Soc. Japan*, **85**, 437 – 454, doi:10.2151/jmsj.85.437.
- Houze, R. A., Jr., S. S. Chen, B. F. Smull, W.-C. Lee, and M. M. Bell, 2007: Hurricane intensity and eyewall replacement. *Science*, **315**, 1235–1239, doi:10.1126/science.1135650.
- Huang, Y.-H., M. T. Montgomery, and C.-C. Wu, 2012: Concentric eyewall formation in Typhoon Sinlaku (2008). Part II: Axisymmetric dynamical processes. *J. Atmos. Sci.*, **69**, 662–674, doi:10.1175/JAS-D-11-0114.1.
- Ishii, M., A. Shouji, S. Sugimoto, and T. Matsumoto, 2005: Objective analyses of sea-surface temperature and marine meteorological variables for the 20th century using ICOADS and the Kobe Collection. *Int. J. Climatol.*, **25**, 865–879, doi:10.1002/joc.1169.
- Ito, H., 2007: Dynamics of the tropics and tropical cyclogenesis (in Japanese). *Kaiyo monthly*, **39**, 136-144.
- Ito, K., 2016: Errors in tropical cyclone intensity forecast by RSMC Tokyo and statistical correction using environmental parameters. *SOLA*, **2**, 92-95, doi:10.2151/sola.2016-049.
- Japan Aerospace Exploration Agency, 2017a: JAXA global rainfall watch. [Available online at <http://sharaku.eorc.jaxa.jp/GSMaP/index.htm>.]
- Japan Aerospace Exploration Agency, 2017b: JAXA realtime rainfall watch. [Available online at http://sharaku.eorc.jaxa.jp/GSMaP_NOW/index.htm.]
- Japan Meteorological Agency, 2017a: Tropical cyclone genesis, approach, landfalls, and tracks (in Japanese). [Available online at <http://www.jma.go.jp/jma/kishou/known/typhoon/1-4.html>.]
- Japan Meteorological Agency, 2017b: Numerical weather prediction at the Japan Meteorological Agency. [Available online at <http://www.jma.go.jp/jma/jma-eng/jma-center/nwp/nwp-top.htm>.]
- Jarvinen, B. R., and C. J. Neumann, 1979: Statistical forecasts of tropical cyclone intensity for the North Atlantic basin. NOAA Tech. Memo. NWS NHC-10, 22 pp. [Available online at <http://www.nhc.noaa.gov/pdf/NWS-NHC-1979-10.pdf>.]
- Jiang, H., 2012: The relationship between tropical cyclone intensity change and the strength of inner-core convection. *Mon. Wea. Rev.*, **140**,

- 1164–1176, doi:10.1175/MWR-D-11-00134.1.
- Jiang, H., and E. M. Ramirez, 2013: Necessary conditions for tropical cyclone rapid intensification as derived from 11 years of TRMM data. *J. Climate*, **26**, 6459–6470, doi:10.1175/JCLI-D-12-00432.1.
- Jones, S. C., 1995: The evolution of vortices in vertical shear. I: Initially barotropic vortices. *Quart. J. Roy. Meteor. Soc.*, **121**, 821–851, doi:10.1002/qj.49712152406.
- Jones, T. A., and D. J. Cecil, 2007a: SHIPS-MI forecast analysis of Hurricanes Claudette (2003), Isabel (2003), and Dora (1999). *Wea. Forecasting*, **22**, 689–707, doi:10.1175/WAF1016.1.
- Jones, T. A., D. J. Cecil, and M. DeMaria, 2006: Passive-microwave-enhanced Statistical Hurricane Intensity Prediction Scheme. *Wea. Forecasting*, **21**, 613–635, doi:10.1175/WAF941.1.
- Jones, T. A., D. J. Cecil, and J. Dunion, 2007b: The environmental and inner-core conditions governing the intensity of Hurricane Erin (2007). *Wea. Forecasting*, **22**, 708–725, doi:10.1175/WAF1017.1.
- Jordan, C. L., 1958: Mean soundings for the West Indies area. *J. Meteor.*, **15**, 91–97, doi:10.1175/1520-0469(1958)015<0091:MSFTWI>2.0.CO;2.
- Jou, B. J.-D., W. C. Lee, S. P. Liu, and Y. C. Kao, 2008: Generalized VTD retrieval of atmospheric vortex kinematic structure. Part I: Formulation and error analysis. *Mon. Wea. Rev.*, **136**, 995–1012, doi:10.1175/2007MWR2116.1.
- Joyce, R. J., J. E. Janowiak, P. A. Arkin, and P. Xie, 2004: CMORPH: A method that produces global precipitation estimates from passive microwave and infrared data at high spatial and temporal resolution. *J. Hydrometeor.*, **5**, 487–503, doi:10.1175/1525-7541(2004)005<0487:CAMTPG>2.0.CO;2.
- Kaplan, J., and M. DeMaria, 2003: Large-scale characteristics of rapidly intensifying tropical cyclones in the North Atlantic basin. *Wea. Forecasting*, **18**, 1093–1108, doi:10.1175/1520-0434(2003)018<1093:LCORIT>2.0.CO;2.
- Kaplan, J., M. DeMaria, and J. A. Knaff, 2010: A revised tropical cyclone rapid intensification index for the Atlantic and eastern North Pacific basins. *Wea. Forecasting*, **25**, 220–241, doi:10.1175/2009WAF2222280.1.
- Keperter, J., 2001: The dynamics of boundary layer jets within the tropical cyclone core. Part I: Linear theory. *J. Atmos. Sci.*, **58**, 2469–2484, doi:10.1175/1520-0469(2001)058<2469:TDOBLJ>2.0.CO;2.
- Keperter, J. D., 2006a: Observed boundary layer wind structure and balance in

- the hurricane core. Part I: Hurricane Georges. *J. Atmos. Sci.*, **63**, 2169–2193, doi:10.1175/JAS3745.1.
- Kepert, J. D., 2006b: Observed boundary layer wind structure and balance in the Hurricane core. Part II: Hurricane Mitch. *J. Atmos. Sci.*, **63**, 2194–2211, doi:10.1175/JAS3746.1.
- Kepert, J. D., 2013: How does the boundary layer contribute to eyewall replacement cycles in axisymmetric tropical cyclones? *J. Atmos. Sci.*, **70**, 2808–2830, doi:10.1175/JAS-D-13-046.1.
- Kepert, J., and Y. Wang, 2001: The dynamics of boundary layer jets within the tropical cyclone core. Part II: Nonlinear enhancement. *J. Atmos. Sci.*, **58**, 2485–2501, doi:10.1175/1520-0469(2001)058<2485:TDOBLJ>2.0.CO;2.
- Kepert, J. D., and D. S. Nolan, 2014: Reply to “Comments on ‘How does the boundary layer contribute to eyewall replacement cycles in axisymmetric tropical cyclones?’” *J. Atmos. Sci.*, **71**, 4692–4704, doi:10.1175/JAS-D-14-0014.1.
- Kieper, M., and H. Jiang, 2012: Predicting tropical cyclone rapid intensification using the 37 GHz ring pattern identified from passive microwave measurements. *Geophys. Res. Lett.*, **39**, L13804, doi:10.1029/2012GL052115.
- Kieu, C., V. Tallapragada, and W. Hogsett, 2014: Vertical structure of tropical cyclones at onset of the rapid intensification in the HWRF model. *Geophys. Res. Lett.*, **41**, 3298–3306, doi:10.1002/2014GL059584.
- Kilroy, G., R. K. Smith, and M. T. Montgomery, 2016: Why do model tropical cyclones grow progressively in size and decay in intensity after reaching maturity? *J. Atmos. Sci.*, **73**, 487–503, doi:10.1175/JAS-D-15-0157.1.
- Knaff, J. A., C. R. Sampson, and M. DeMaria, 2005: An operational statistical typhoon intensity prediction scheme for the western North Pacific. *Wea. Forecasting*, **20**, 688–699, doi:10.1175/WAF863.1.
- Knaff, J. A., M. DeMaria, B. Sampson, and J. M. Gross, 2003: Statistical, 5-day tropical cyclone intensity forecasts derived from climatology and persistence. *Wea. Forecasting*, **18**, 80–92, doi:10.1175/1520-0434(2003)018<0080:SDTCIF>2.0.CO;2.
- Koba, H., T. Hagiwara, S. Osano, and S. Akashi, 1990: Relationship between the CI-number and central pressure and maximum wind speed in typhoons (in Japanese). *J. Meteor. Res.*, **42**, 59–67.
- Kobayashi, S., and Coauthors, 2015: The JRA-55 Reanalysis: General

- specifications and basic characteristics. *J. Meteor. Soc. Japan.*, **93**, 5–48, doi:10.2151/jmsj.2015-001.
- Kossin, J. P., and W. H. Schubert, 2004: Mesovortices in Hurricane Isabel. *Bull. Amer. Meteor. Soc.*, **85**, 151–153, doi:10.1175/BAMS-85-2-151.
- Kubota, T., S. Shige, K. Aonashi, K. Okamoto, 2009: Development of nonuniform beamfilling correction method in rainfall retrievals for passive microwave radiometers over ocean using TRMM observations. *J. Meteor. Soc. Japan*, **87A**, 153–164, doi:10.2151/jmsj.87A.153.
- Kubota, T., and Coauthors, 2007: Global precipitation map using satelliteborne microwave radiometers by the GSMaP project : Production and validation, *IEEE Trans. Geosci. Remote Sens.*, **45**, 7, 2259–2275, doi:10.1109/MICRAD.2006.1677106.
- Kurihara, Y., T. Sakurai, and T. Kuragano, 2006: Global daily sea surface temperature analysis using data from satellite microwave radiometer, satellite infrared radiometer and in-situ observations (in Japanese). *Wea. Bull.*, **73**, S1–S18.
- Lamb, H., 1932: *Hydrodynamics*. 6th ed. Dover, 738 pp.
- Lander, M. A., 1994: Description of a monsoon gyre and its effects on the tropical cyclones in the western North Pacific during August 1991. *Wea. Forecasting*, **9**, 640–654, doi:10.1175/1520-0434(1994)009<0640:DOAMGA>2.0.CO;2.
- Lee, W.-C., and M. M. Bell, 2007: Rapid intensification, eyewall contraction, and breakdown of Hurricane Charley (2004) near landfall. *Geophys. Res. Lett.*, **34**, L02802, doi:10.1029/2006GL027889.
- Lee, W.-C., and F. D. Marks Jr., 2000: Tropical cyclone kinematic structure retrieved from single-Doppler radar observations. Part II: The GBVTD-simplex center finding algorithm. *Mon. Wea. Rev.*, **128**, 1925–1936, doi:10.1175/1520-0493(2000)128<1925:TCKSRF>2.0.CO;2.
- Lee, W.-C., B. J.-D. Jou, P.-L. Chang, and S.-M. Deng, 1999: Tropical cyclone kinematic structure retrieved from single-Doppler radar observations. Part I: Interpretation of Doppler velocity patterns and the GBVTD technique. *Mon. Wea. Rev.*, **127**, 2419–2439, doi:10.1175/1520-0493(1999)127<2419:TCKSRF>2.0.CO;2.
- Lee, W.-C., B. J.-D. Jou, P.-L. Chang, and F. D. Marks Jr, 2000: Tropical cyclone kinematic structure retrieved from single-Doppler radar observations. Part III: Evolution and structure of Typhoon Alex (1987). *Mon. Wea. Rev.*, **128**, 3892–4001,

- doi:10.1175/1520-0493(2000)129<3982:TCKSRF>2.0.CO;2.
- Lee, W.-C., P. R. Harasti, M. Bell, B. J.-D. Jou, and M.-H. Chang, 2006: Doppler velocity signatures of idealized elliptical vortices. *Terr. Atmos. Oceanic Sci.*, **17**, 429–446.
- Liu, Y., D. Zhang, and M. Yau, 1999: A multiscale numerical study of Hurricane Andrew (1992). Part II: Kinematics and inner-core structures. *Mon. Wea. Rev.*, **127**, 2597–2616, doi:10.1175/1520-0493(1999)127<2597:AMNSOH>2.0.CO;2.
- Marks, F. D., P. G. Black, M. T. Montgomery, and R. W. Burpee, 2008: Structure of the eye and eyewall of Hurricane Hugo (1989). *Mon. Wea. Rev.*, **136**, 1237–1259, doi:10.1175/2007MWR2073.1.
- Martin, J. D., and W. M. Gray, 1993: Tropical cyclone observation and forecasting with and without aircraft reconnaissance. *Wea. Forecasting*, **8**, 519–532, doi:10.1175/1520-0434(1993)008<0519:TCOAFW>2.0.CO;2.
- Menelaou, K., M. K. Yau, and Y. Martinez, 2014: Some aspects of the problem of secondary eyewall formation in idealized three-dimensional nonlinear simulations, *J. Adv. Model. Earth Syst.*, **6**, 491–512, doi:10.1002/2014MS000316.
- Miyamoto, Y., and T. Takemi, 2013: A transition mechanism for the axisymmetric spontaneous intensification of tropical cyclones. *J. Atmos. Sci.*, **70**, 112–129, doi:10.1175/JAS-D-11-0285.1.
- Miyamoto, Y., and T. Takemi, 2015: A Triggering Mechanism for Rapid Intensification of Tropical Cyclones. *J. Atmos. Sci.*, **72**, 2666–2681, doi:10.1175/JAS-D-14-0193.1.
- Molinari, J., and D. Vollaro, 1990: External influences on hurricane intensity. Part II: Vertical structure and response of the hurricane vortex. *J. Atmos. Sci.*, **47**, 1902–1918, doi:10.1175/1520-0469(1990)047<1902:EIOHIP>2.0.CO;2.
- Molinari, J., and D. Vollaro, 2010: Rapid intensification of a sheared tropical storm. *Mon. Wea. Rev.*, **138**, 3869–3885, doi:10.1175/2010MWR3378.1.
- Molinari, J., D. Vollaro, and K. L. Corbosiero, 2004: Tropical cyclone formation in a sheared environment: A case study. *J. Atmos. Sci.*, **61**, 2493–2509, doi:10.1175/JAS3291.1.
- Molinari, J., P. Dodge, D. Vollaro, K. L. Corbosiero, and F. Marks, 2006: Mesoscale aspects of the downshear reformation of a tropical cyclone. *J. Atmos. Sci.*, **63**, 341–354, doi:10.1175/JAS3591.1.

- Montgomery, M. T., and R. J. Kallenbach, 1997: A theory for vortex Rossby waves and its application to spiral bands and intensity changes in hurricanes. *Quart. J. Roy. Meteor. Soc.*, **123**, 435–465, doi:10.1002/qj.49712353810.
- Montgomery, M. T., and R. K. Smith, 2014: Paradigms for tropical cyclone intensification. *Aust. Meteor. Oceanogr. J.*, **64**, 37–66.
- Montgomery, M. T., M. M. Bell, S. D. Aberson, and M. L. Black, 2006: Hurricane Isabel (2003): New insights into the physics of intense storms. Part I: Mean vortex structure and maximum intensity estimates. *Bull. Amer. Meteor. Soc.*, **87**, 1335–1347, doi:10.1175/BAMS-87-10-1335.
- Montgomery, M. T., J. Zhang, and R. K. Smith, 2014: An analysis of the observed low-level structure of rapidly intensifying and mature Hurricane Earl (2010). *Quart. J. Roy. Meteor. Soc.*, **140**, 2132–2146, doi:10.1002/qj.2283.
- Moon, Y., and D. S. Nolan, 2015: Spiral rainbands in a numerical simulation of Hurricane Bill (2009). Part II: Propagation of Inner Rainbands. *J. Atmos. Sci.*, **72**, 191–215, doi:10.1175/JAS-D-14-0056.1.
- Murillo, S. T., W.-C. Lee, M. M. Bell, F. D. Marks Jr., P. P. Dodge, and G. M. Barnes, 2011: Intercomparison of ground-based velocity track display (GBVTD)-retrieved circulation centers and structures of Hurricane Danny (1997) from two coastal WSR-88Ds. *Mon. Wea. Rev.*, **139**, 153–174, doi:10.1175/2010MWR3036.1.
- Musgrave, K. D., C. A. Davis, and M. T. Montgomery, 2008: Numerical simulations of the formation of Hurricane Gabrielle (2001). *Mon. Wea. Rev.*, **136**, 3151–3167, doi:10.1175/2007MWR2110.1.
- National Centers for Environmental Prediction, Environmental Modeling Center, cited 2017: NCEP operational HWRP forecasting system. [Available online at http://www.emc.ncep.noaa.gov/gc_wmb/vxt/HWRP/index.php.]
- Nguyen, L. T., and J. Molinari, 2012: Rapid intensification of a sheared, fast-moving hurricane over the Gulf Stream. *Mon. Wea. Rev.*, **140**, 3361–3378, doi:10.1175/MWR-D-11-00293.1.
- Nguyen, L. T., and J. Molinari, 2015: Simulation of the downshear reformation of a tropical cyclone. *J. Atmos. Sci.*, **72**, 4529–4551, doi:10.1175/JAS-D-15-0036.1.
- Nolan, D. S., 2013: On the use of Doppler radar-derived wind fields to diagnose the secondary circulations of tornadoes. *J. Atmos. Sci.*, **70**, 1160–1171,

- doi:10.1175/JAS-D-12-0200.1.
- Nolan, D. S., and L. D. Grasso, 2003: Nonhydrostatic, three-dimensional perturbations to balanced, hurricane-like vortices. Part II: Symmetric response and nonlinear simulations. *J. Atmos. Sci.*, **60**, 2717–2745, doi:10.1175/1520-0469(2003)060<2717:NTPTBH>2.0.CO;2.
- Nolan, D. S., Y. Moon, and D. P. Stern, 2007: Tropical cyclone intensification from asymmetric convection: Energetics and efficiency. *J. Atmos. Sci.*, **64**, 3377–3405, doi:10.1175/JAS3988.1.
- Nolan, D. S., J. A. Zhang, and D. P. Stern, 2009: Evaluation of planetary boundary layer parameterizations in tropical cyclones by comparison of in situ observations and high-resolution simulations of Hurricane Isabel (2003). Part I: Initialization, maximum winds, and the outer-core boundary layer structure. *Mon. Wea. Rev.*, **137**, 3651–3674, doi:10.1175/2009MWR2785.1.
- Olander, T.L., and C.S. Velden, 2007: The Advanced Dvorak Technique (ADT): Continued development of an objective scheme to estimate TC intensity using geostationary IR satellite imagery. *Wea. Forecasting*, **22**, 287–298, doi:10.1175/WAF975.1.
- Olander, T.L., C.S. Velden, and J. P. Kossin, 2004: The Advanced Objective Dvorak Technique (AODT)—Latest upgrades and future directions. Preprints, *26th Conf. on Hurricanes and Tropical Meteorology*, Miami, FL, Amer. Meteor. Soc., 294–295.
- Ooyama, K. V., 1969: Numerical simulation of the life cycle of tropical cyclones. *J. Atmos. Sci.*, **26**, 3–40, doi:10.1175/1520-0469(1969)026,0003:NSOTLC.2.0.CO;2.
- Oyama, R., 2014: Estimation of tropical cyclone central pressure from warm core intensity observed by the Advanced Microwave Sounding Unit-A (AMSU-A), *Pap. Meteor. Geophys.*, **65**, 35–56, doi:10.2467/mripapers.65.35.
- Paterson, L. A., B. N. Hanstrum, N. E. Davidson, and H. C. Weber, 2005: Influence of environmental vertical wind shear on the intensity of hurricane-strength tropical cyclones in the Australian region. *Mon. Wea. Rev.*, **133**, 3644–3660, doi:10.1175/MWR3041.1.
- Pendergrass, A. G., and H. E. Willoughby, 2009: Diabatically induced secondary flows in tropical cyclones. Part I: Quasi-steady forcing. *Mon. Wea. Rev.*, **137**, 805–821, doi:10.1175/2008MWR2657.1.
- Persing, J., M. T. Montgomery, J. C. McWilliams, and R. K. Smith, 2013: Asymmetric and axisymmetric tropical cyclone dynamics. *Atmos.*

- Chem. Phys.*, **13**, 12299–12341, doi:10.5194/acp-13-12299-2013.
- Powell, M. D., E. W. Uhlhorn, and J. D. Kepert, 2009: Estimating maximum surface winds from hurricane reconnaissance measurements. *Wea. Forecasting*, **24**, 868–883, doi:10.1175/2008WAF2007087.1.
- Rao, G. V., and P. D. MacArthur, 1994: The SSM/I estimated rainfall amounts of tropical cyclones and their potential in predicting the cyclone intensity changes. *Mon. Wea. Rev.*, **122**, 1568–1574, doi:10.1175/1520-0493(1994)122<1568:TSERAO>2.0.CO;2.
- Rao, G. V., and J. H. McCoy, 1997: SSM/I measured microwave brightness temperatures (TB's), anomalies of TB's and their relationship to typhoon intensification. *Nat. Hazards*, **15**, 1–19.
- Reasor, P. D., and M. T. Montgomery, 2001: Three-dimensional alignment and corotation of weak, TC-like vortices via linear vortex Rossby waves. *J. Atmos. Sci.*, **58**, 2306–2330, doi:10.1175/1520-0469(2001)058<2306:TDAACO>2.0.CO;2.
- Reasor, P. D., and M. D. Eastin, 2012: Rapidly intensifying Hurricane Guillermo (1997). Part II: Resilience in shear. *Mon. Wea. Rev.*, **140**, 425–444, doi:10.1175/MWR-D-11-00080.1.
- Reasor, P. D., and M. T. Montgomery, 2015: Evaluation of a heuristic model for tropical cyclone resilience. *J. Atmos. Sci.*, **72**, 1765–1782, doi:10.1175/JAS-D-14-0318.1.
- Reasor, P. D., M. D. Eastin, and J. F. Gamache, 2009: Rapidly intensifying Hurricane Guillermo (1997). Part I: Low-wavenumber structure and evolution. *Mon. Wea. Rev.*, **137**, 603–631, doi:10.1175/2008MWR2487.1.
- Reasor, P. D., M. T. Montgomery, and L. D. Grasso, 2004: A new look at the problem of tropical cyclones in vertical shear flow: Vortex resiliency. *J. Atmos. Sci.*, **61**, 3–22, doi:10.1175/1520-0469(2004)061<0003:ANLATP>2.0.CO;2.
- Reasor, P. D., R. Rogers, and S. Lorsolo, 2013: Environmental flow impacts on tropical cyclone structure diagnosed from airborne Doppler radar composites. *Mon. Wea. Rev.*, **141**, 2949–2969, doi:10.1175/MWR-D-12-00334.1.
- Riemer, M., M. T. Montgomery, and M. E. Nicholls, 2010: A new paradigm for intensity modification of tropical cyclones: Thermodynamic impact of vertical wind shear on the inflow layer. *Atmos. Chem. Phys.*, **10**, 3163–3188, doi:10.5194/acp-10-3163-2010.
- Riemer, M., M. T. Montgomery, and M. E. Nicholls, 2013: Further examination

- of the thermodynamic modification of the inflow layer of tropical cyclones by vertical wind shear. *Atmos. Chem. Phys.*, **13**, 327–346, doi:10.5194/acp-13-327-2013.
- Rios-Berrios, R., and R. D. Torn, 2017: Climatological analysis of tropical cyclone intensity changes under moderate vertical wind shear. *Mon. Wea. Rev.*, **145**, 1717–1738, doi: 10.1175/MWR-D-16-0350.1.
- Rogers, R. F., P. Reasor, and S. Lorsolo, 2013: Airborne Doppler observations of the inner-core structural differences between intensifying and steady-state tropical cyclones. *Mon. Wea. Rev.*, **141**, 2970–2991, doi:10.1175/MWR-D-12-00357.1.
- Rogers, R. F., P. Reasor, and J. Zhang, 2015: Multiscale structure and evolution of Hurricane Earl (2010) during rapid intensification. *Mon. Wea. Rev.*, **143**, 536–562, doi:10.1175/MWR-D-14-00175.1.
- Rogers, R. F., S. S. Chen, J. Tenerelli, and H. E. Willoughby, 2003: A numerical study of the impact of vertical shear on the distribution of rainfall in Hurricane Bonnie (1998). *Mon. Wea. Rev.*, **131**, 1577–1599, doi:10.1175//2546.1.
- Rogers, R. F., S. Lorsolo, P. D. Reasor, J. Gamache, and F. D. Marks Jr., 2012: Multiscale analysis of tropical cyclone kinematic structure from airborne Doppler radar composites. *Mon. Wea. Rev.*, **140**, 77–99, doi:10.1175/MWR-D-10-05075.1.
- Rogers, R., J. Zhang, J. Zawislak, H. Jiang, G. Alvey, E. Zipser, and S. Stevenson, 2016: Observations of the structure and evolution of Hurricane Edouard (2014) during intensity change. Part II: Kinematic structure and the distribution of deep convection. *Mon. Wea. Rev.*, **144**, 3355–3376, doi:10.1175/MWR-D-16-0017.1.
- Rogers, R., S. Aberson, M. Bell, D. Cecil, J. Doyle, T. Kimberlain, J. Morgerman, L. Shay, and C. Velden, 2017: Re-Writing the tropical record books: The extraordinary intensification of Hurricane Patricia (2015). *Bull. Amer. Meteor. Soc.*, doi:10.1175/BAMS-D-16-0039.1, in press.
- Rozoff, C. M., D. S. Nolan, J. P. Kossin, F. Zhang, and J. Fang, 2012: The roles of an expanding wind field and inertial stability in tropical cyclone secondary eyewall formation. *J. Atmos. Sci.*, **69**, 2621–2643, doi:10.1175/JAS-D-11-0326.1.
- Saito, K., and Coauthors, 2006: The operational JMA nonhydrostatic mesoscale model. *Mon. Wea. Rev.*, **134**, 1266–1298, doi:10.1175/MWR3120.1.

- Saito, K., J. Ishida, K. Aranami, T. Hara, T. Segawa, M. Narita, and Y. Honda, 2007: Nonhydrostatic atmospheric models and operational development at JMA. *J. Meteor. Soc. Japan*, **85B**, 271–304, doi:10.2151/jmsj.85B.271.
- Sakuragi, T., S. Hoshino and N. Kitabatake, 2014: Development and verification of a tropical cyclone intensity estimation method reflecting the variety of TRMM/TMI brightness temperature distribution. RSMC Tokyo - Typhoon Center Tech. Rev., No. **16**.
- Sampson, C. R., and J. A. Knaff, 2014: Advances in intensity guidance. *8th International Workshop on Tropical Cyclones*, Jeju, Republic of Korea. [Available online at https://www.wmo.int/pages/prog/arep/wwrp/new/documents/Topic2.7_AdvancesinIntensityGuidance.pdf.]
- Sanger, N. T., M. T. Montgomery, R. K. Smith, and M. M. Bell, 2014: An observational study of tropical cyclone spinup in Supertyphoon Jangmi (2008) from 24 to 27 September. *Mon. Wea. Rev.*, **142**, 3–28, doi:10.1175/MWR-D-12-00306.1.
- Schechter, D. A., 2015: Response of a simulated hurricane to misalignment forcing compared to the predictions of a simple theory. *J. Atmos. Sci.*, **72**, 1235–1260, doi:10.1175/JAS-D-14-0149.1.
- Schechter, D. A., and M. T. Montgomery, 2003: On the symmetrization rate of an intense geophysical vortex. *Dyn. Atmos. Oceans*, **37**, 55–88, doi:10.1016/S0377-0265(03)00015-0.
- Schechter, D. A., and M. T. Montgomery, 2007: Waves in a cloudy vortex. *J. Atmos. Sci.*, **64**, 314–337, doi:10.1175/JAS3849.1.
- Schechter, D. A., M. T. Montgomery, and P. D. Reasor, 2002: A theory for the vertical alignment of a quasigeostrophic vortex. *J. Atmos. Sci.*, **59**, 150–168, doi:10.1175/1520-0469(2002)059<0150:ATFTVA>2.0.CO;2.
- Schmidt, C. W., and R. K. Smith, 2016: Tropical cyclone evolution in a minimal axisymmetric model revisited. *Quart. J. Roy. Meteor. Soc.*, **142**, 1505–1516, doi:10.1002/qj.2753.
- Schubert, W. H., and J. J. Hack, 1982: Inertial stability and tropical cyclone development. *J. Atmos. Sci.*, **39**, 1687–1697, doi:10.1175/1520-0469(1982)039<1687:ISATCD>2.0.CO;2.
- Schubert, W. H., J. J. Hack, P. L. Silva Dias, and S. R. Fulton, 1980: Geostrophic adjustment in an axisymmetric vortex. *J. Atmos. Sci.*, **37**, 1464–1484, doi:10.1175/1520-0469(1980)037<1464:GAIAAV>2.0.CO;2.

- Schumacher, A., M. DeMaria, and J. Knaff, 2013: Summary of the new statistical-dynamical intensity forecast models for the Indian Ocean and Southern Hemisphere and resulting performance. JTWC Project Final Report. [Available online at http://rammb.cira.colostate.edu/research/tropical_cyclones/ships/docs/JTWC_project_final_report_oct_2013.docx.]
- Shapiro, L., and H. E. Willoughby, 1982: The response of balanced hurricanes to local sources of heat and momentum. *J. Atmos. Sci.*, **39**, 378–394, doi:10.1175/1520-0469(1982)039<0378:TROBHT>2.0.CO;2.
- Shige, S., T. Yamamoto, T. Tsukiyama, S. Kida, H. Ashiwake, T. Kubota, S. Seto, K. Aonashi, and K. Okamoto, 2009: The GSMaP precipitation retrieval algorithm for microwave sounders. Part I: Over-ocean algorithm. *IEEE Trans. Geosci. Remote Sens.*, **47**, 3084–3097.
- Shimada, U., H. Kubota, H. Yamada, E. O. Cayan, and F. D. Hilario, 2017: Intensity and inner-core structure of Typhoon Haiyan (2013) near landfall: Doppler radar analysis. *Mon. Wea. Rev.*, in revision.
- Sitkowski, M., J. Kossin, and C. M. Rozoff, 2011: Intensity and structure changes during hurricane eyewall replacement cycles. *Mon. Wea. Rev.*, **139**, 3829–3847, doi:10.1175/MWR-D-11-00034.1.
- Smith, R.K., and M. T. Montgomery, 2016: The efficiency of diabatic heating and tropical cyclone intensification. *Quart. J. Roy. Meteor. Soc.*, **142**, 2081–2086, doi:10.1002/qj.2804.
- Smith, R. K., M. T. Montgomery, and V. S. Nguyen, 2009: Tropical cyclone spin-up revisited. *Quart. J. Roy. Meteor. Soc.*, **135**, 1321–1335, doi:10.1002/qj.428.
- Stern, D. P., J. R. Brisbois, and D. S. Nolan, 2014: An expanded dataset of hurricane eyewall sizes and slopes. *J. Atmos. Sci.*, **71**, 2747–2762, doi:10.1175/JAS-D-13-0302.1.
- Stern, D. P., J. L. Vigh, D. S. Nolan, and F. Zhang, 2015: Revisiting the relationship between eyewall contraction and intensification. *J. Atmos. Sci.*, **72**, 1283–1306, doi:10.1175/JAS-D-14-0261.1.
- Stevenson, S.N., K. L. Corbosiero, and J. Molinari, 2014: The Convective Evolution and Rapid Intensification of Hurricane Earl (2010). *Mon. Wea. Rev.*, **142**, 4364–4380, doi:10.1175/MWR-D-14-00078.1.
- Sun, Y. Q., Y. Jiang, B. Tan, and F. Zhang, 2013: The governing dynamics of the secondary eyewall formation of Typhoon Sinlaku (2008). *J. Atmos. Sci.*, **70**, 3818–3837, doi:10.1175/JAS-D-13-044.1.
- Susca-Lopata, G., J. Zawislak, E.J. Zipser, and R.F. Rogers, 2015: The Role of

- Observed Environmental Conditions and Precipitation Evolution in the Rapid Intensification of Hurricane Earl (2010). *Mon. Wea. Rev.*, **143**, 2207–2223, doi:10.1175/MWR-D-14-00283.1.
- Tallapragada, V., C. Kieu, Y. Kwon, S. Trahan, Q. Liu, Z. Zhang, and I. Kwon, 2014: Evaluation of storm structure from the operational HWRF model during 2012 implementation. *Mon. Wea. Rev.*, **142**, 4308–4325, doi:10.1175/MWR-D-13-00010.1.
- Tang, B., and K. A. Emanuel, 2010: Midlevel ventilation's constraint on tropical cyclone intensity. *J. Atmos. Sci.*, **67**, 1817–1830, doi:10.1175/2010JAS3318.1.
- Tao, C. and H. Jiang, 2015: Distributions of shallow to very deep precipitation-convection in rapidly intensifying tropical cyclones. *J. Climate.*, **28**, 8791–8824, doi:10.1175/JCLI-D-14-00448.1.
- Ueno, M., 2007: Observational analysis and numerical evaluation of the effects of vertical wind shear on the rainfall asymmetry in the typhoon inner-core region. *J. Meteor. Soc. Japan*, **85**, 115–136, doi:10.2151/jmsj.85.115.
- Ueno, M., 2008: Effects of ambient vertical wind shear on the inner-core asymmetries and vertical tilt of a simulated tropical cyclone. *J. Meteor. Soc. Japan*, **86**, 531–555, doi:10.2151/jmsj.86.531.
- Ushio, T., and Coauthors, 2009: A Kalman filter approach to the Global Satellite Mapping of Precipitation (GSMaP) from combined passive microwave and infrared radiometric data. *J. Meteor. Soc. Japan*, **87A**, 137–151, doi:10.2151/jmsj.87A.137.
- Usui, N., S. Ishizaki, Y. Fujii, H. Tsujino, T. Yasuda, and M. Kamachi, 2006: Meteorological Research Institute multivariate ocean variational estimation (MOVE) system: Some early results. *Adv. Space Res.*, **37**, 806–822, doi:10.1016/j.asr.2005.09.022.
- Velden, C. S., T. Olander, and R. M. Zehr, 1998: Development of an objective scheme to estimate tropical cyclone intensity from digital geostationary satellite imagery. *Wea. Forecasting*, **13**, 172–186, doi:10.1175/1520-0434(1998)013<0172:DOAOST>2.0.CO;2.
- Velden, C., D. Herndon, J. Kossin, J. Hawkins, and M. DeMaria, 2007: Consensus estimates of tropical cyclone (TC) intensity using integrated multispectral (IR and MW) satellite observations. *Joint 2007 EUMETSAT Meteorological Satellite & 15th AMS Satellite Meteorology and Oceanography conference*, Amsterdam, The Netherlands. [Available online at

- http://www.ssec.wisc.edu/meetings/jointsatmet2007/pdf/velden_satcon.pdf
- Vigh, J. L., and W. H. Schubert, 2009: Rapid development of the tropical cyclone warm core. *J. Atmos. Sci.*, **66**, 3335–3350, doi:10.1175/2009JAS3092.1.
- Wang, H., and Y. Wang, 2014: A numerical study of Typhoon Megi (2010): Part I: Rapid intensification. *Mon. Wea. Rev.*, **142**, 29–48, doi:10.1175/MWR-D-13-00070.1.
- Wang, Y., 2002: Vortex Rossby waves in a numerically simulated tropical cyclone. Part I: Overall structure, potential vorticity, and kinetic energy budgets. *J. Atmos. Sci.*, **59**, 1213–1238, doi:10.1175/1520-0469(2002)059<1213:VRWIAN>2.0.CO;2.
- Wang, Y., and G. J. Holland, 1996: The beta drift of baroclinic vortices. Part I: Adiabatic vortices. *J. Atmos. Sci.*, **53**, 411–427, doi:10.1175/1520-0469(1996)053<0411:TBD0BV>2.0.CO;2.
- Wang, Y., Y. Rao, Z.-M. Tan, and D. Schnemann, 2015: A statistical analysis of the effects of vertical wind shear on tropical cyclone intensity change over the western North Pacific. *Mon. Wea. Rev.*, **143**, 3434–3453, doi:10.1175/MWR-D-15-0049.1.
- Wang, M., K. Zhao, W. C. Lee, B. J.-D. Jou, and M. Xue, 2012: The Gradient Velocity Track Display (GrVTD) Technique for Retrieving Tropical Cyclone Primary Circulation from Aliased Velocities Measured by Single-Doppler Radar. *J. Atmos. Oceanic Technol.*, **29**, 1026–1041, doi:10.1175/JTECH-D-11-00219.1.
- Wilks, D. S., 2006: *Statistical Methods in the Atmospheric Sciences*. 2d ed. International Geophysics Series, Vol. 91, Academic Press, 627 pp.
- Willoughby, H. E., 1990: Gradient balance in tropical cyclones. *J. Atmos. Sci.*, **47**, 265–274, doi:10.1175/1520-0469(1990)047<0265:GBITC>2.0.CO;2.
- Wu, C.-C., Y.-H. Huang, and G.-Y. Lien, 2012: Concentric eyewall formation in Typhoon Sinlaku (2008). Part I: Assimilation of T-PARC data based on the ensemble Kalman filter (EnKF). *Mon. Wea. Rev.*, **140**, 506–527, doi:10.1175/MWR-D-11-00057.1.
- Wu, C.-C., K.-H. Chou, Y. Wang, and Y.-H. Kuo, 2006: Tropical cyclone initialization and prediction based on four-dimensional variational data assimilation. *J. Atmos. Sci.*, **63**, 2383–2395, doi:10.1175/JAS3743.1.
- Wu, L., S. A. Braun, J. Halverson, and G. Heymsfield, 2006: A numerical study

- of Hurricane Erin (2001). Part I: Model verification and storm evolution. *J. Atmos. Sci.*, **63**, 65–86, doi:10.1175/JAS3597.1.
- Yamauchi, H., O. Suzuki, and K. Akaeda, 2006: A hybrid multi-PRI method to Dealias Doppler velocities. *SOLA*, **2**, 92-95, doi:10.2151/sola.2006-024.
- Zagrodnik, J. P., and H. Jiang, 2014: Rainfall, convection, and latent heating distributions in rapidly intensifying tropical cyclones. *J. Atmos. Sci.*, **71**, 2789–2809, doi:10.1175/JAS-D-13-0314.1.
- Zawislak, J., H. Jiang, G. Alvey, E. Zipser, R. Rogers, J. Zhang, and S. Stevenson, 2016: Observations of the structure and evolution of Hurricane Edouard (2014) during intensity change. Part I: Relationship between the thermodynamic structure and precipitation. *Mon. Wea. Rev.*, **144**, 3333–3354, doi:10.1175/MWR-D-16-0018.1.
- Zhang, D.-L., Y. Liu, and M. K. Yau, 2001: A multiscale numerical study of Hurricane Andrew (1992). Part IV: Unbalanced flows. *Mon. Wea. Rev.*, **129**, 92–107, doi:10.1175/1520-0493(2001)129<0092:AMNSOH>2.0.CO;2.
- Zhang, J. A., R. F. Rogers, D. S. Nolan, and F. D. Marks Jr., 2011: On the characteristic height scales of the hurricane boundary layer. *Mon. Wea. Rev.*, **139**, 2523–2535, doi:10.1175/MWR-D-10-05017.1.
- Zhang, J. A., R. F. Rogers, and V. Tallapragada, 2017: Impact of Parameterized Boundary Layer Structure on Tropical Cyclone Rapid Intensification Forecasts in HWRF. *Mon. Wea. Rev.*, **145**, 1413–1426, doi:10.1175/MWR-D-16-0129.1.
- Zhao, K., W.-C. Lee, and B. J.-D. Jou, 2008: Single Doppler radar observation of the concentric eyewall in Typhoon Saomei ,2006, near landfall. *Geophys. Res. Lett.*, **35**, L07807, doi:10.1029/2007GL032773.
- Zhao, K., M. Xue, and W.-C. Lee, 2012: Assimilation of GBVTD-retrieved winds from single-Doppler radar for short-term forecasting of super typhoon *Saomai* (0608) at landfall. *Quart. J. Roy. Meteor. Soc.*, **138**, 1055–1071, doi:10.1002/qj.975.
- Zhao, K., Q. Lin, W.-C. Lee, Q. Sun, and F. Zhang, 2016: Doppler Radar Analysis of Triple Eyewalls in Typhoon Usagi (2013). *Bull. Amer. Meteor. Soc.*, **97**, 25–30, doi:10.1175/BAMS-D-15-00029.1.
- Zhu, T., D-L. Zhang, and F. Weng, 2004: Numerical simulation of Hurricane Bonnie (1998). Part I: Eyewall evolution and intensity changes. *Mon. Wea. Rev.*, **132**, 225–241, doi:10.1175/1520-0493(2004)132<0225:NSOHBP>2.0.CO;2.

Zhu, Z.-D., and P. Zhu, 2014: The role of outer rainband convection in governing the eyewall replacement cycle in numerical simulations of tropical cyclones, *J. Geophys. Res. Atmos.*, **119**, 8049-8072, doi:10.1002/2014JD021899.